

Photon-Upconversion Nanoparticles as Background-Free Luminescent Labels for Immunoanalytical Applications



DISSERTATION ZUR ERLANGUNG DES DOKTORGRADES DER
NATURWISSENSCHAFTEN (DR. RER. NAT.) DER FAKULTÄT CHEMIE
UND PHARMAZIE DER UNIVERSITÄT REGENSBURG

vorgelegt von

Matthias Jürgen Mickert

aus Nürnberg

im Jahr 2020

Promotionsgesuch eingereicht am: 06.05.2020

Die Arbeit entstand in der Zeit von Dezember 2015 bis März 2020 am Institut für Analytische Chemie, Chemo- und Biosensorik an der Universität Regensburg.

Die Arbeit wurde angeleitet von: PD Dr. Hans-Heiner Gorris.

Vorsitzender:	Prof. Dr. Oliver Tepner
Erstgutachter:	PD Dr. Hans-Heiner Gorris
Zweitgutachter:	Prof. Dr. Frank-Michael Matysik
Drittprüfer:	Prof. Dr. Reinhard Sterner
Promotionskolloquium:	30.04.2021

I.	ABBREVIATIONS	I-1
II.	DECLARATION OF COLLABORATIONS	II-5
III.	CURRICULUM VITAE	III-8
IV.	FUNDAMENTALS	IV-13
IV.1.	INTRODUCTION.....	IV-13
IV.2.	A SHORT HISTORICAL PERSPECTIVE ON IMMUNOASSAYS.....	IV-16
IV.3.	DIGITAL IMMUNOASSAYS.....	IV-17
IV.4.	ANTIBODIES.....	IV-19
IV.4.1.	Antibody Isotypes.....	IV-19
IV.4.2.	Antibody Structure.....	IV-20
IV.4.3.	Polyclonal Antibodies.....	IV-21
IV.4.4.	Monoclonal Antibodies.....	IV-22
IV.5.	ANTIBODY ALTERNATIVES.....	IV-23
IV.5.1.	Aptamers.....	IV-23
IV.5.2.	Molecularly Imprinted Polymers.....	IV-26
IV.6.	ENZYME LABELS.....	IV-28
IV.6.1.	Enzyme-linked Immunosorbent Assay.....	IV-28
IV.6.2.	Digital ELISA.....	IV-32
IV.7.	FLUORESCENT MOLECULAR LABELS.....	IV-33
IV.7.1.	Fluorescence Polarization Immunoassay.....	IV-33
IV.7.2.	Time-Resolved Fluorescence Immunoassay.....	IV-34
IV.7.3.	Immuno PCR.....	IV-34
IV.7.4.	Digital Fluorescence Affinity Assays.....	IV-35
IV.8.	NANOPARTICLE LABELS.....	IV-38
IV.8.1.	Gold Nanoparticles.....	IV-38
IV.8.2.	Quantum Dots.....	IV-40
IV.8.3.	Photon-Upconversion Nanoparticles.....	IV-42
IV.8.4.	Digital Affinity Assays with Nanoparticle Labels.....	IV-45
IV.9.	REFERENCES.....	IV-47
V.	REVIEW ARTICLE 1: ADVANCES IN OPTICAL SINGLE-MOLECULE DETECTION: EN ROUTE TO SUPERSENSITIVE BIOAFFINITY ASSAYS	V-57
V.1.	ABSTRACT.....	V-58
V.2.	INTRODUCTION.....	V-58
V.3.	ENZYME LABELS.....	V-63
V.3.1.	Assays Based on Product Precipitation.....	V-63
V.3.2.	Assays in Confined Environments.....	V-63
V.4.	DNA LABELS FOR PCR AMPLIFICATION.....	V-67
V.5.	FLUORESCENT MOLECULAR LABELS.....	V-68
V.5.1.	Detection of Surface-Bound Analytes.....	V-69
V.5.2.	Laser-Induced Fluorescence Detection Inside a Capillary.....	V-72
V.5.3.	Fluorescence Correlation Spectroscopy.....	V-74
V.6.	NANOPARTICLE LABELS.....	V-76
V.6.1.	Semiconductor Nanoparticles.....	V-77
V.6.2.	Photon-Upconversion Nanoparticles.....	V-80
V.7.	PLASMONIC NANOPARTICLES.....	V-82
V.8.	BEAD LABELS.....	V-88
V.8.1.	Fluorescence Microscopy.....	V-88
V.8.2.	Bright-Field Microscopy.....	V-90
V.8.3.	Dark-Field Microscopy.....	V-91

V.9.	LABEL-FREE DETECTION	V-93
V.10.	SUMMARY AND OUTLOOK	V-96
V.11.	ACKNOWLEDGEMENTS	V-101
V.12.	REFERENCES	V-102
VI.	RESEARCH ARTICLE 1: SINGLE-MOLECULE UPCONVERSION-LINKED IMMUNOSORBENT ASSAY WITH EXTENDED DYNAMIC RANGE FOR THE SENSITIVE DETECTION OF DIAGNOSTIC BIOMARKERS	VI-111
VI.1.	ABSTRACT	VI-112
VI.2.	INTRODUCTION	VI-112
VI.3.	EXPERIMENTAL SECTION	VI-114
VI.4.	RESULTS AND DISCUSSION	VI-117
VI.5.	CONCLUSIONS	VI-122
VI.6.	REFERENCES	VI-123
VI.7.	SUPPORTING INFORMATION	VI-126
VII.	RESEARCH ARTICLE 2: UPCONVERSION-LINKED IMMUNOSORBENT ASSAY MEASURES SUBFEMTOMOLAR CONCENTRATIONS OF PROSTATE-SPECIFIC ANTIGEN THROUGH SINGLE-MOLECULE COUNTING	VII-141
VII.1.	ABSTRACT	VII-142
VII.2.	INTRODUCTION	VII-142
VII.3.	MATERIALS AND METHODS	VII-144
VII.4.	RESULTS AND DISCUSSION	VII-146
VII.5.	CONCLUSIONS	VII-151
VII.6.	REFERENCES	VII-154
VII.7.	SUPPORTING INFORMATION	VII-157
VIII.	RESEARCH ARTICLE 3: SURFACE DESIGN OF PHOTON-UPCONVERSION NANOPARTICLES FOR HIGH-CONTRAST IMMUNOCYTOCHEMISTRY	VIII-179
VIII.1.	ABSTRACT	VIII-180
VIII.2.	INTRODUCTION	VIII-180
VIII.3.	MATERIALS AND METHODS	VIII-182
VIII.4.	RESULTS AND DISCUSSION	VIII-188
VIII.5.	CONCLUSIONS	VIII-198
VIII.6.	REFERENCES	VIII-200
VIII.7.	SUPPORTING INFORMATION	VIII-202
IX.	SINGLE-MOLECULE ENZYME MEASUREMENTS	IX-231
X.	RESEARCH ARTICLE 4: TRANSITION STATE ENSEMBLES NAVIGATE THE PATHWAYS OF ENZYME CATALYSIS	X-235
X.1.	ABSTRACT	X-236
X.2.	INTRODUCTION	X-236
X.3.	EXPERIMENTAL SECTION	X-239
X.4.	RESULTS AND DISCUSSION	X-242
X.5.	CONCLUSIONS	X-253
X.6.	APPENDICES	X-254
X.7.	REFERENCES	X-256
X.8.	SUPPORTING INFORMATION	X-260
XI.	SUMMARY AND CONCLUSIONS	XI-265
XII.	ZUSAMMENFASSUNG UND FAZIT	XII-269

XIII.	ACKNOWLEDGMENTS.....	XIII-273
XIV.	EIDESSTATTLICHE ERKLÄRUNG	XIV-275

I. Abbreviations

4-MUP	4-methyl-umbelliferylphosphate
Ab	antibody
AB	ammonium bicarbonate
AFP	α -fetoprotein
Alen	alendronate
APA	5-azidopentanoic acid
AS	assay buffer
AuNP	gold nanoparticle
BCN	bicyclononyne
BGG	bovine γ -globulins
bp	boiling point
BSA	bovine serum albumin
C	constant region
CEA	carcinoembryonic antigen
cBSA	cationized bovine serum albumin
CFI	chrome-free infinity corrected
CPS	counts per second
CV	coefficient of variance
DAB	diaminobenzidine
DAPI	4',6-diamidino-2-phenylindole
DDAO phosphate	(9H-(1,3-dichloro-9,9-dimethylacridin-2-one-7-yl) phosphate, diammonium salt)
ddH ₂ O	double-distilled water
DELFI	dissociation-enhanced lanthanide fluorescence immunoassay
DLS	dynamic light scattering
DMEM	Dulbecco's modified eagle's medium
DMF	dimethylformamide
DMSO	dimethylsulfoxide
dsDNA	double-stranded DNA

Abbreviations

<i>E. coli</i>	<i>Escherichia coli</i>
EC ₅₀	effective concentration that gives half maximal response
ECL	electrochemiluminescence
EDC	1-ethyl-3-(3-dimethylaminopropyl)carbodiimide
EDTA	ethylene diamine tetraacetic acid
ELASA	enzyme-linked apta-sorbent assay
ELISA	enzyme-linked immunosorbent assay
EM	electron microscopy
ErbB/HER2	human epidermal growth factor
F _{ab}	antigen-binding fragment
FAM	5(6)-carboxyfluorescein
F _c	crystallizable fragment
FCCS	fluorescence cross-correlation spectroscopy
FCS	fluorescence correlation spectroscopy
FFPE	formalin-fixed paraffin-embedded
FIA	fluorescent immunoassay
FPIA	fluorescence polarization immunoassay
FRET	Förster resonance energy transfer
FWHM	full width at half maximum
GAL	β-D-galactosidase
GUS	β-D-glucuronidase
H&E	hematoxylin and eosin
HBsAg	hepatitis B surface antigen
hCG	human chorionic gonadotropin
HEPES	4-(2-Hydroxyethyl)piperazine-1-ethanesulfonic acid
HIV	human immunodeficiency virus
HRP	horseradish peroxidase
ICC	immunocytochemistry
Ig	immunoglobulins
IGEPAL CO-520	polyoxyethylene (5) nonylphenylether
IHC	immunohistochemistry

LC-MS/MS	liquid chromatography with tandem mass spectrometry
LFA	lateral flow assay
LOD	limit of detection
LOQ	limit of quantification
LWD	long working distance
MES	sodium 2-(<i>N</i> -morpholino)ethanesulfonate
MIP	molecularly imprinted polymer
MWCO	molecular weight cut-off
NA	numerical aperture
NBT	nitro blue tetrazolium
Ner	neridronate
NFL	neurofilament light chain protein
NHS	<i>N</i> -hydroxysuccinimide
NIR	near-infrared
NPP	nitrophenyl phosphate
NTA	nanoparticle tracking analysis
o.n.	overnight
PBS	phosphate-buffered saline
PCR	polymerase chain reaction
PDI	polydispersity index
PDMS	polydimethylsiloxane
PEG	polyethylene glycol
PSA	prostate specific antigen
PVA	poly(vinyl alcohol)
QD	quantum dot
Q-TOF	quadrupole time of flight
RGP	resorufin- β -D-galactopyranoside
RIA	radioimmunoassay
RNA	ribonucleic acid
ROI	region of interest
RT	room temperature

Abbreviations

<i>S/B</i>	signal/background
SA	streptavidin
SB	SuperBlock
sCMOS	scientific complementary metal oxide semiconductor
SELEX	systematic evolution of ligands by exponential enrichment
SERS	surface-enhanced plasmon resonance
Simoa	single-molecule array platform
SPR	surface plasmon resonance
ssDNA	single-stranded DNA
TBS	tris-buffered saline
TBS-T	tris-buffered saline containing Tween 20
TEM	transmission electron microscopy
TIRFM	total internal reflection microscopy
TMB	tetramethylbenzidine
TNF- α	tumor necrosis factor- α
TR	time-resolved
Tris	tris(hydroxymethyl)aminomethane
TS	transition state
TST	transition state theory
UCL	upconversion luminescence
UCNP	photon-upconversion nanoparticle
ULISA	upconversion-linked immunosorbent assay
UV	ultraviolet
V	variable region
WI	working distance
ΔG^\ddagger	free energy of activation

II. Declaration of Collaborations

According to § 8 Abs. 1 Satz 2 Ziff. 7 of the “Ordnung zum Erwerb des akademischen Grades eines Doktors der Naturwissenschaften (Dr. rer. nat.) an der Universität Regensburg vom 18. Juni 2009”, the following paragraph states the collaborations for the experimental and theoretical results presented in this thesis.

Chapter V, Review Article 1: Advances in optical single-molecule detection: on the road to super-sensitive bioaffinity assays

M. J. Mickert and Dr. Z. Farka did the literature research for the article, created the first outline, and distributed the work among the authors. M. J. Mickert was evaluating and summarizing 75 of the original 258 articles and contributed to various chapters. M. J. Mickert and J. Brandmeier translated the Review to German. Table 1, and the cover were created by M. J. Mickert. All authors revised the manuscript. PD Dr. H.-H. Gorris was the corresponding author.

Chapter VI, Research Article 1: Single-Molecule Upconversion-Linked Immunosorbent Assay with Extended Dynamic Range for the Sensitive Detection of Diagnostic Biomarkers

Dr. Z. Farka and M. J. Mickert contributed equally to the article. The experiments were planned and conducted by Dr. Z. Farka and M. J. Mickert, under supervision of PD Dr. H.-H. Gorris, and Assoc. Prof. Dr. Petr Skládal. M. J. Mickert modified the epifluorescence microscope and optimized it for the detection of individual photon-upconversion nanoparticles. Characterization of the microscope laser and single-particle imaging of particles with different sized was done by M. J. Mickert. Illustrations were created by M. J. Mickert. Gel electrophoresis, immunoassays, and data evaluation was done by M. J. Mickert and Dr. Z. Farka. Nanoparticle synthesis, silanization, and gravimetric analysis was done by Dr. A. Hlaváček from the Czech Academy of Sciences in Brno, Czech Republic. Transmission electron microscopic images were conducted by Miroslav Peterek and Dr. Z. Farka at the CF Cryo-electron Microscopy and Tomography facilities at the CEITEC MU institute in Brno. Surface plasmon resonance measurements were done by M. Pastucha and Dr. Z. Farka at the CEITEC MU. Dynamic light scattering measurements were done by Dr. Z. Farka. All authors revised the manuscript, PD Dr. H.-H. Gorris was the corresponding author.

Chapter VII, Research Article 2: Upconversion-Linked Immunosorbent Assay Measures Subfemtomolar Concentrations of Prostate-Specific Antigen through Single-Molecule Counting

M. J. Mickert and Dr. Z. Farka contributed equally to the article. The experiments were planned and conducted by M. J. Mickert and Dr. Z. Farka under the supervision of PD Dr. H.-H. Gorris, and Assoc. Prof. Dr. Petr Skládal. Nanoparticle purification was done by M. J. Mickert. Illustrations were created by M. J. Mickert. Upconversion-linked immunosorbent assays were optimized, conducted, and evaluated by M. J. Mickert and Dr. Z. Farka. Surface plasmon resonance measurements were done by M. J. Mickert and Dr. Z. Farka with the help of M. Pastucha at the CEITIC MU institute in Brno. Optimization of the Click reaction for the immobilization of streptavidin on the nanoparticles was done by M. J. Mickert, Dr. Z. Farka and Dr. U. Kostiv. Photon-upconversion nanoparticles and the alkyne-PEG-neridronate-linker were synthesized by Dr. U. Kostiv at the Institute of Macromolecular Chemistry in Prague, Czech Republic. Kaivogen (Turku, Finland) provided commercial streptavidin-modified upconversion nanoparticles. Dynamic light scattering measurements were performed by Z. Farka, U. Kostiv, and M. J. Mickert. Transmission electron microscopic images were provided by Dr. U. Kostiv and Kaivogen. Patient samples were provided by Dr. M. Marečková. All authors revised the manuscript, PD Dr. H.-H. Gorris was the corresponding author.

Chapter VIII, Research Article 3: Surface Design of Photon-Upconversion Nanoparticles for High-Contrast Immunocytochemistry

Dr. Z. Farka and M. J. Mickert contributed equally to the article. The experiments were planned and conducted by Dr. Z. Farka and M. J. Mickert, under the supervision of PD Dr. H.-H. Gorris, and Assoc. Prof. Dr. Petr Skládal. M. J. Mickert did the synthesis of the alkyne-PEG-neridronate-linker, bleaching experiments, combination of H&E staining and upconversion staining, and staining of real samples. M. J. Mickert created all illustrations. Dr. Z. Farka and M. J. Mickert performed the immunostaining of FFPE cell-pellet slides. M. J. Mickert and Z. Mikušová stained the cell dispersions. A general procedure for the immunohistological staining of cells was provided by Dr. W. Xu from the company TTP (Cambridge, UK) and was optimized by Dr. Z. Farka and M. J. Mickert. Photon-upconversion nanoparticles were synthesized by Dr. A. Hlaváček from the Czech Academy of Science in Brno. Ligand exchange reactions and Click reactions for streptavidin immobilization were conducted and optimized by Dr. Z. Farka and M. J. Mickert. Cell dispersion were provided by Dr. P. Bouchalová and Assoc. Prof. Dr. P. Bouchal from the Masaryk University in Brno, Czech Republic. Nanoparticle tracking analysis was done by Dr. Z. Farka. Transmission electron microscopic images were made by Dr. V. Vykoukal and Dr. Z. Farka at the CF Cryo-electron Microscopy and Tomography facilities in Brno. Liquid chromatography with subsequent tandem mass

spectrometry was done by K. Mikulášek and Prof. Z. Zdráhal from CEITEC MU, Brno. All authors revised the manuscript, PD Dr. H.-H. Gorris was the corresponding author.

Chapter X, Research Article 4: Transition State Ensembles Navigate the Pathways of Enzyme Catalysis

Initial writing of the article was done by M. J. Mickert, PD Dr. H.-H. Gorris revised the manuscript. Single-molecule enzyme kinetic data was reinterpreted by M. J. Mickert and PD Dr. H.-H. Gorris from Liebherr, R. B., Hutterer, A., Mickert, M. J., Vogl, F. C., Beutner, A., Lechner, A., & Gorris, H.-H. Three-in-one enzyme assay based on single-molecule detection in femtoliter arrays. *Anal. Bioanal. Chem.*, 2015, 407 (24), 7443-7452. New experiments and data evaluation were done by M. J. Mickert. Calculation of ΔG^\ddagger was done by M. J. Mickert with initial the help of D. Gahler. The illustration in Figure 1 was adapted from Liebherr et al.; all other illustrations were created by M. J. Mickert. PD Dr. Hans-Heiner Gorris was the corresponding author.

List of Publications

1. U. Kostiv, Z. Farka, M. J. Mickert, H.-H. Gorris, N. Velychkivska, O. Pop-Georgievski, M. Pastucha, E. Odstrčilíková, P. Skládal, D. Horák, Facile Conjugation of Antibodies to PEG-Modified Upconversion Nanoparticles for Bioanalytical Applications, **2020, in revision.**
2. Z. Farka*, M. J. Mickert*, Z. Mikušová, A. Hlaváček, P. Bouchalová, W. Xu, P. Bouchal, P. Skládal, H.-H. Gorris, Surface Design of Photon-Upconversion Nanoparticles for High-Contrast Immunocytochemistry. *Nanoscale*, **2020, online**, DOI: 10.1039/C9NR10568A.
3. T. Raith, A. Kröninger, M. J. Mickert, H.-H. Gorris, F.-M. Matysik, Enhanced Resolution of Generator-Collector Studies of Enzymatic Structures by Means of Hydrodynamic Scanning Electrochemical Microscopy, *Talanta*, **2020**, *214*, 120844.
4. Z. Farka*, M. J. Mickert*, M. Pastucha, Z. Mikušová, P. Skládal, H.-H. Gorris, Fortschritte in der Optischen Einzelmoleküldetektion: Auf dem Weg zu Supersensitiven Bioaffinitätsassays, *Angew. Chem.* **2019, accepted.**
5. Z. Farka*, M. J. Mickert*, M. Pastucha, Z. Mikušová, P. Skládal, H.-H. Gorris, Advances in Optical Single-Molecule Detection: En Route to Super-Sensitive Bioaffinity Assays, *Angew. Chem. Int. Ed.* **2019, online**, DOI: 10.1002/anie.201913924.
6. M. J. Mickert*, Z. Farka*, U. Kostiv, A. Hlaváček, D. Horák, P. Skládal, H.-H. Gorris, Streptavidin-Coated Upconversion-Nanoparticles Enable Single-Molecule Immunosorbent Assays with Subfemtomolar Detection Limits. *Anal. Chem.* **2019**, *91*(15), 9425-9441.
7. V. Poláchová, M. Pastucha, Z. Mikušová, M. J. Mickert, A. Hlaváček, H. H. Gorris, Z. Farka, Click-Conjugated Photon-Upconversion Nanoparticles in an Immunoassay for Honeybee Pathogen *Melissococcus Plutonium*. *Nanoscale*, **2019**, *11*(17), 8343-8351.
8. A. Hlaváček, M. J. Mickert, T. Soukka, S. Lahtinen, T. Tallgren, N. Pizúrová, A. Król, H.-H. Gorris, Large-Scale Purification of Photon-Upconversion Nanoparticles by Gel Electrophoresis for Analog and Digital Bioassays. *Anal. Chem.* **2018**, *91*(2), 1241-1246.
9. K. Rustler, M. J. Mickert, J. Nazet, R. Merkl, H.-H. Gorris, B. Koenig, Development of Photoswitchable Inhibitors for β -D-Galactosidase. *Org. Biomol. Chem.* **2018**, *16*(40), 7430-7437.
10. M. J. Mickert, H.-H. Gorris, Transition State Ensembles Navigate the Pathways of Enzyme Catalysis. *J. Phys. Chem. B*, **2018**, *122*(22), 5809-5819.
11. Z. Farka*, M. J. Mickert*, A. Hlaváček, P. Skládal, H.-H. Gorris, Single-Molecule Upconversion-Linked Immunosorbent Assay with Extended Dynamic Range for the Sensitive Detection of Diagnostic Biomarkers. *Anal. Chem.* **2017**, *89*(21), 11825-11830.
12. A. Hlaváček, M. Peterek, Z. Farka, M. J. Mickert, L. Prechtel, D. Knopp, H.-H. Gorris, Rapid Single-Step Upconversion-Linked Immunosorbent Assay for Diclofenac. *Microchim. Acta.* **2017**, *184*(10), 4159-4165.
13. M. J. Mickert, H.-H. Gorris, Hohe Verdünnung, winzige Volumina-Einzelmolekülmethode, *Nachr. Chem.* **2016**, *64*, 412-415.
14. A. Sedlmeier, A. Hlaváček, L. Birner, M. J. Mickert, V. Muhr, T. Hirsch, P. L. A. M. Corstjens, H. J. Tanke, T. Soukka, H.-H. Gorris, Highly Sensitive Laser Scanning of Photon-upconverting Nanoparticles on a Macroscopic Scale. *Anal. Chem.* **2016**, *88*, 1835-1841.
15. R. B. Liebherr, A. Hutterer, M. J. Mickert, F. C. Vogl, A. Beutner, A. Lechner, H. Hummel, H.-H. Gorris, Three-in-one Enzyme Assay Based on Single-Molecule Detection in Femtoliter Arrays. *Anal. Bioanal. Chem.* **2015**, *407*, 744-7452.

*Authors contributed equally.

IV. Fundamentals

IV.1. Introduction

The first part of the present work describes the fundamental building blocks of immunoassays or more generally spoken affinity assays. Historical milestones that finally led to the development of highly sensitive digital (single-molecule) immunoassays are highlighted. According to the glossary for chemistry of terms used in biotechnology written by the International Union of Pure and Applied Chemistry (IUPAC) in 1992,¹ an immunoassay is defined as a ligand-binding assay that uses a specific antigen or antibody, capable of binding to the analyte to identify and quantify a substance. The antibody can be linked to a radioisotope (radioimmunoassay), or to an enzyme that catalyzes an easily monitored reaction (enzyme-linked immunosorbent assay, ELISA), or to a highly fluorescent compound by which the location of an antigen can be visualized (immunofluorescence). Hence, this definition is very specific regarding the labels and does not cover any sort of nanoparticle label, or label-free techniques like surface plasmon resonance (SPR), therefore more general definition is preferable. The IUPAC recommendations of 1994 about the nomenclature for radioanalytical chemistry provide a broader definition of immunoassays. Here, immunoassays are assays based on the immunological binding of a specific antigen or antibody with the component under study.²

The literature is describing countless variations of immunoassays. In the following text the fundamental assay schemes are briefly described. Immunoassays are divided into two main categories; (i) heterogeneous assays, which require a separation step of bound and free labels, and (ii) homogeneous assays where no separation step is needed.³ Both types can be either in a non-competitive (sandwich), or a competitive format. A basic heterogeneous sandwich immunoassay (**Figure 1A**) consists of a capture antibody bound to a solid surface like the bottom of a microplate, subsequent incubation with the analyte leads to the formation of the antigen-antibody immunocomplex. A second antibody—usually carrying a label that generates a measurable signal—called detection antibody is added and forms the final immunosandwich. Hence, the number of labeled detection antibodies increases with increasing analyte concentration, which leads to the increase of the detectable signal. The sandwich assay is only possible for analyte molecules that are big enough to allow for two antibodies to bind.

In a heterogeneous competitive assay (**Figure 1B**), the capture antibody is also bound to a solid substrate, but no detection antibody is needed. The competition for free binding sites of the capture antibody occurs between a tracer molecule and the analyte itself. The tracer molecule must be able to bind to the antibody with a comparable affinity as the analyte itself, and it must

Fundamentals

carry a label that generates the signal. The tracer molecule often consists of an analyte molecule bound to a label. The signal of tracer molecules bound to the capture antibody in a competitive sandwich assay decreases with increasing analyte concentration because more binding sites get occupied by the free analyte instead the tracer that generates the signal. Alternatively, the free tracer molecules in the supernatant can be measured, resulting in an increasing signal, with increasing analyte concentration. This form of an assay is also suitable for small analyte molecules that do not have two binding sites for antibodies.

Homogeneous assays do not require a solid support for the immobilization of a capture antibody. Instead, the signal is directly measured in solution without the need for an additional separation step. Omitting the washing step is possible because the free label generates no or a different signal than the bound label. In a sandwich-like homogeneous assay (**Figure 1C**), two antibodies carrying interacting labels are used. The quantitative signal is generated if both labels come into proximity and start interacting with each other. One commonly used interaction is the Förster resonance energy transfer (FRET), where one fluorophore absorbs the excitation light and transfers the energy through non-radiative dipole-dipole interactions to a second fluorophore, which then emits light.⁴

The competitive homogeneous immunoassay (**Figure 1D**)—analog to the competitive heterogeneous assay—requires a tracer molecule. If the tracer is bound to the labeled antibody, FRET can happen between both labels, and a high signal is observed. If the analyte is present, it can replace the tracer, which diffuses away from its FRET-partner, and the FRET-signal decreases.

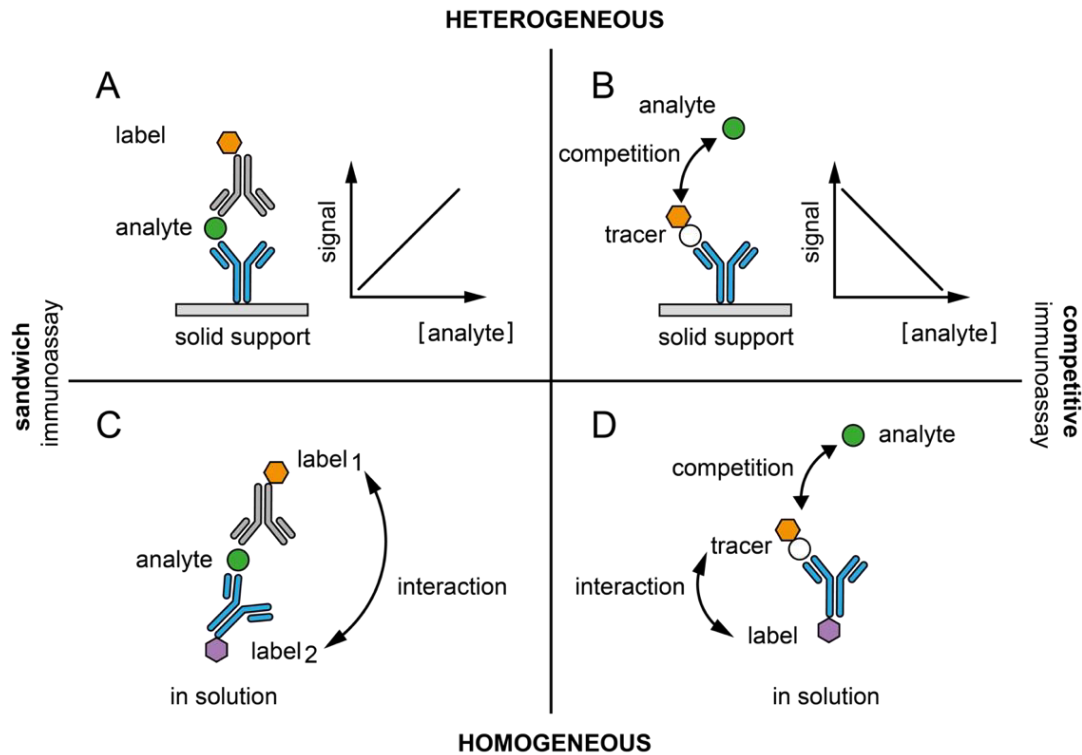


Figure 1: Generalized immunoassay schemes. **A)** In the heterogeneous sandwich immunoassay, a first antibody (capture antibody) is bound to a solid substrate and binds to the analyte molecules. A second antibody carrying a label (detection antibody) also binds to the analyte. After a washing step to remove unbound detection antibody, the signal, which is generated by the label is measured. **B)** In a competitive heterogeneous immunoassay, the analyte molecules compete with a labeled tracer molecule for free binding sites of a surface-immobilized capture antibody. With an increasing number of analyte molecules, fewer tracer molecules can bind to the surface, causing a decreasing signal. **C)** The homogeneous sandwich immunoassay requires two labeled antibodies where one label generates a measurable signal if it comes into proximity with the second label. **D)** In the homogeneous competitive immunoassay, a tracer molecule competes with the free analyte for the antibody binding sites. The label on the tracer can interact with the label on the antibody if both are in proximity. If free analyte is present, less of the tracer can bind to the antibody, and the signal changes.

IV.2. A Short Historical Perspective on Immunoassays

In 1959 the two U.S. researchers Rosalyn S. Yalow and Solomon Berson, developed one of the first immunoassay.⁵ They observed that patients suffering from diabetes who were treated with animal insulin developed globulins, freely circulating in the bloodstream.⁶ By injecting more insulin into the patient, Yalow and Berson observed a longer retention time of insulin in the blood compared to untreated patients. This finding suggested that the globulins they found can bind specifically to insulin. The insulin antibodies were purified and used in the first radioimmunoassay (RIA). To determine the insulin concentration in blood samples, purified insulin was labeled with the radionuclide ¹³¹I and added to the analyte sample. After adding the antibodies, labeled and unlabeled insulin competed for the antigen-binding sites of the antibodies. Bound and free insulin molecules were separated by paper chromatography and ¹³¹I was quantified with a scintillation counter. The invention of the RIA and the fact that Yalow and Berson did not patent the assay principle led to the rapid development of numerous different immunoassays.⁷ In 1977—five years after the death of Berson—Yalow was honored with the Nobel Prize for medicine.

In 1971 the Swedish scientists Eva Engvall and Peter Perlmann developed the first competitive enzyme-linked immunosorbent assay (ELISA). They determined the concentration of specific rabbit antibodies in rabbit serum. Polystyrene tubes were coated with the antigen of the target antibody, followed by incubation with rabbit serum. The antigen-specific antibodies in the rabbit serum bound to the antigen on the surface of the tube. Next, alkaline phosphatase-labeled anti-rabbit antibodies were added, which bound to the rabbit antibodies. After a washing step to separate unbound phosphatase-labeled antibodies, the chromogenic substrate *p*-nitrophenyl phosphate (NPP) was added. Alkaline phosphatase catalyzes the hydrolysis of NPP, leading to the formation of the yellow *p*-nitrophenol, which was monitored by measuring the absorbance at 400 nm.⁸ In the same year, B.K. Van Weemen and A.H.W.M. Schuurs from the Netherlands conducted a competitive ELISA assay using the enzyme horseradish peroxidase (HRP). HRP is a peroxidase that catalyzes the oxidation of a chromogenic substrate in the presence of hydrogen peroxide.⁹

One year later, in 1972, Kenneth E. Rubenstein et al. performed the first homogeneous immunoassay. Morphine was coupled to the enzyme lysozyme, binding of anti-morphine antibodies to these conjugates inhibited the enzyme activity. Free morphine was added and competed with the enzyme-coupled morphine for the antibody binding sites. The release of the morphine-lysozyme conjugate led to a reactivation of the enzyme, which was monitored by absorption measurements. At the presence of *Micrococcus luteus*, the reaction mixture was turbid, during the enzymatic reaction the bacterium got digested and the absorbance decreased.¹⁰⁻¹¹

Another milestone in the history of immunoassays was the development of a method to produce monoclonal antibodies in large quantities. In 1975 George Köhler and Cesar Milstein from the MRC Laboratory of Molecular Biology in Cambridge invented a technique to merge mouse cancer cells so-called myeloma cells with antibody-producing B-cells, extracted from the spleen of mice that were immunized with the antigen of interest.¹² For their accomplishments, Köhler and Milstein were awarded the Nobel Prize for medicine in 1984. Rapid reproduction and longevity of myeloma cells allowed the reproducible production of high amounts of monoclonal antibodies leading to numerous variations of immunoassays in the following decades.

IV.3. Digital Immunoassays

The typical detection limit of a standard immunoassays, like the ELISA, is in the picomolar range.¹³ Many clinical markers for infectious diseases,¹⁴ toxins,¹⁵ and cancer¹⁶ occur in lower concentrations, thus demanding for lower limits of detection. Increasing the sensitivity of affinity assays also opens access to novel clinical markers whose concentrations are undetectable using conventional methods. It is no wonder that assay development today aims for the highest possible sensitivity, which ultimately leads to the development of single-molecule immunoassays.

In single-molecule immunoassays, the analyte molecule is labeled in the same way as in conventional assays, but the readout and/or the assay design is more sophisticated in a way that it allows for the detection of an individual label. Many different readout schemes, even label-free, have reached single-molecule sensitivity. By using nanopipettes, it was, for example, possible to monitor the concentration of α -fetoprotein (AFP) in solution using an electrochemical readout.¹⁷ A force-based technique with molecular tuning forks was employed for the sensing of an anti-digoxigenin antibody.¹⁸ However, the most sensitive single-molecule assays rely on optical readout methods of nanoparticles, the (luminescent) product of an enzymatic reaction, or fluorescent molecules.

All three label-types are shown in **Figure 2** and finally resulted in assays with single-molecule sensitivity. The ability to detect an individual label that is bound to an analyte molecule does not mean that the assay has the highest possible sensitivity. Factors like the non-specific binding of the label or the antibodies and the affinity of the antibodies are vital elements that limit the assay sensitivity. The clear advantage of the digital readout is that each label gives one signal well above the measurement background making the readout independent of the measurement noise and variations in the optical background. By lowering the errors and making the assay more robust, digital readout methods are less prone to background

interference. These advantages contribute to the (often) higher sensitivity compared to analog readout methods.

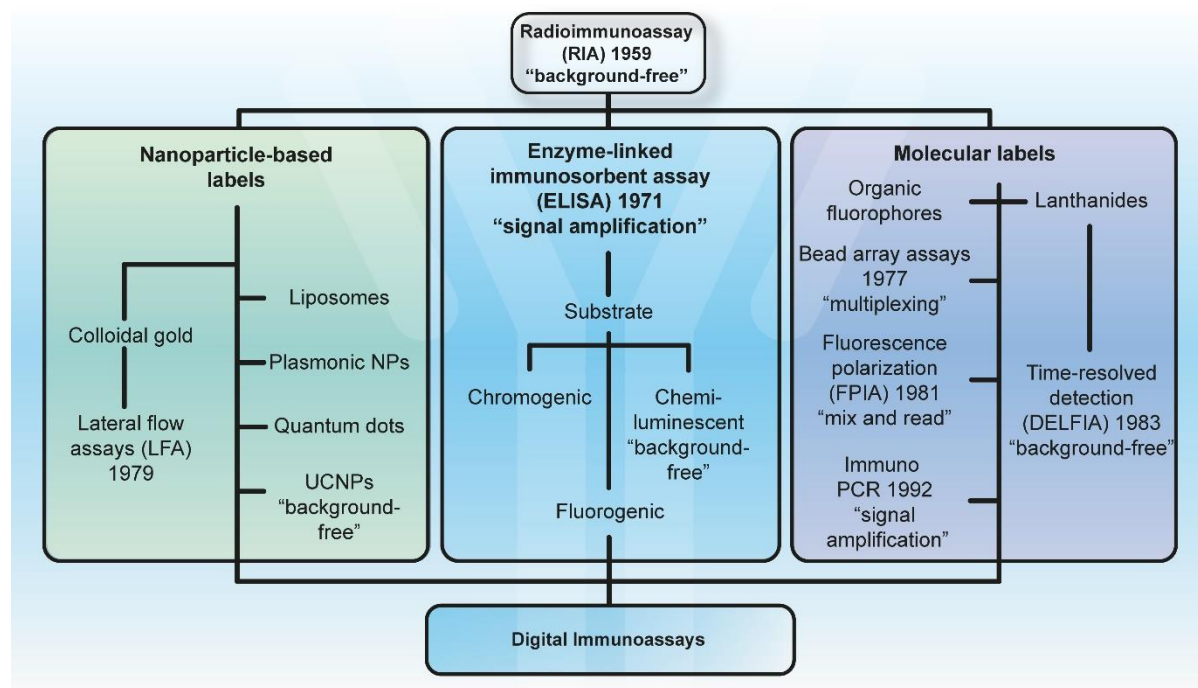


Figure 2: Overview of the development of different immunoassays with optical readout sorted by the label type.

A fluorophore can emit up to 10^6 photons before it bleaches, but the excitation light also causes optical background interferences due to light scattering and autofluorescence. Considering that the measured signal in digital assays is generated by a single label, achieving single-molecule sensitivity is only possible by reducing the background signal, which is generally done by decreasing the detection volume to a few femtoliters. Techniques like total internal reflection microscopy (TIRFM), confocal microscopy, or fluorescence correlation microscopy are commonly used to decrease the background signal. Lowering the detection volume also lowers the number of labels that can be detected at the same time, increasing the sampling error (also Poisson noise, \sqrt{n}/n), which depends on the number of detected labels (n). To compensate for this, either the measurement time or a high parallelization is necessary.

IV.4. Antibodies

IV.4.1. Antibody Isotypes

The most critical element in an immunoassay is the antibody. It provides specificity and— together with the label—translates the presence of an analyte molecule into a measurable signal. Antibodies, or immunoglobulins (Ig) of vertebrates, exist in five different isotypes classified according to the structures of their heavy chain (**Figure 3**). IgA plays a pivotal role in the immune response at the mucosal surfaces and appears in a monomeric, dimeric, or rarely trimeric and tetrameric form, where the dimeric form is predominantly present in secretions like milk, tears or saliva.¹⁹ IgD only appears in its monomeric form, its exact role in the immune response is still unclear, but it is known that it works as an antigen receptor in the development of B-cells.²⁰ IgE is an almost only membrane-bound antibody, especially on mast cells, to protect against parasites and allergens. On contact with allergens, the IgE antibodies trigger the release of biologically active mediators from the mast cells.²¹ The most abundant type of antibody in human blood is the IgG, which accounts for 10–20% of the total protein content in human serum. It is a monomeric antibody and has four subclasses IgG1, IgG2, IgG3, and IgG4, which have structural differences in the constant region. IgG antibodies are glycoproteins that consist of 82–96% protein and 4–18% carbohydrates.²² The largest immunoglobulin is the pentameric IgM antibody, it is the first antibody that appears upon infection with an antigen and has a total of 10 antigen-binding sites and bind exceptionally strong onto their targets.²³

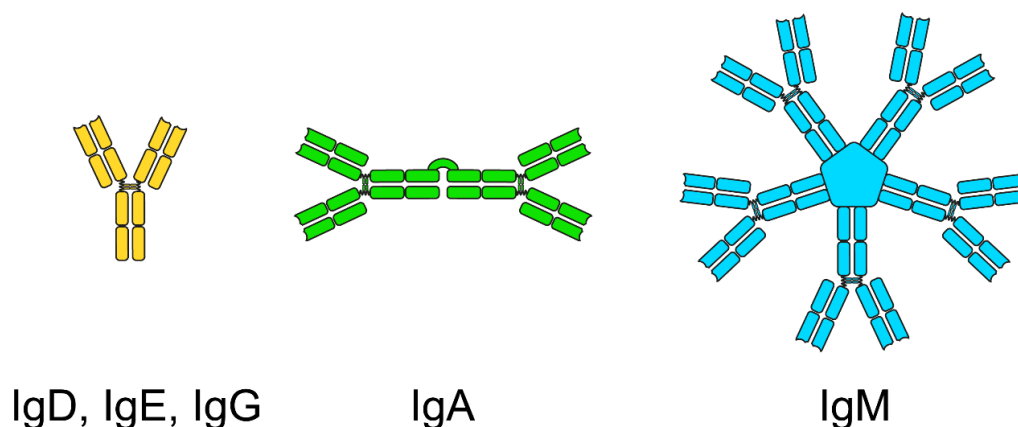


Figure 3: Different isotypes of antibodies sorted by their structure. IgD, IgE, and IgG antibodies are monomeric antibodies (green). The IgA antibody (purple) is dimeric. The biggest antibody isotype is the IgM antibody (blue), consisting of a total of 10 antigen-binding sites.

IV.4.2. Antibody Structure

The most frequently used antibody in immunoassays is the IgG antibody. The typical structure of an IgG (**Figure 4**) consists of two heavy chains (H, 50 kDa) and two light chains (L, 25 kDa) that are connected via disulfide bonds and result in a Y-shaped form. Incubating an antibody with the protease papain generates three fragments, each having a mass of 50 kDa. Two of these fragments are called antigen-binding fragments (F_{ab}). The third fragment is the crystallizable fragment (F_c). It has glycosylation sites for glycans, which serve as a communication element for the immune system.²⁴ The F_{ab} fragments consist of a full light chain and half of a heavy chain and are connected to the F_c region *via* flexible polypeptide segments called the hinge region. The heavy chains are again divided into different subclasses γ_1 , γ_2 , γ_3 , and γ_4 , which differ in the number and location of disulfide bonds and length of the hinge region.²⁵ Heavy and light chains consist of immunoglobulin domains that are formed by two β -sheets facing each other.²⁶ The top two immunoglobulin domains of the heavy and the light chain form the variable region (V), the flexibility in this part of the antibody is necessary to account for various antigens. In the V region of the heavy and light chains are highly variable chains located that form loops in the immunoglobulin structure. These loops are called complementary-determining regions (CDR1, CDR2, and CDR3) and form together a surface that causes the antigen specificity.²⁷ The remaining eight domains build the constant region (C), which is highly conserved and only differs between the isotypes.

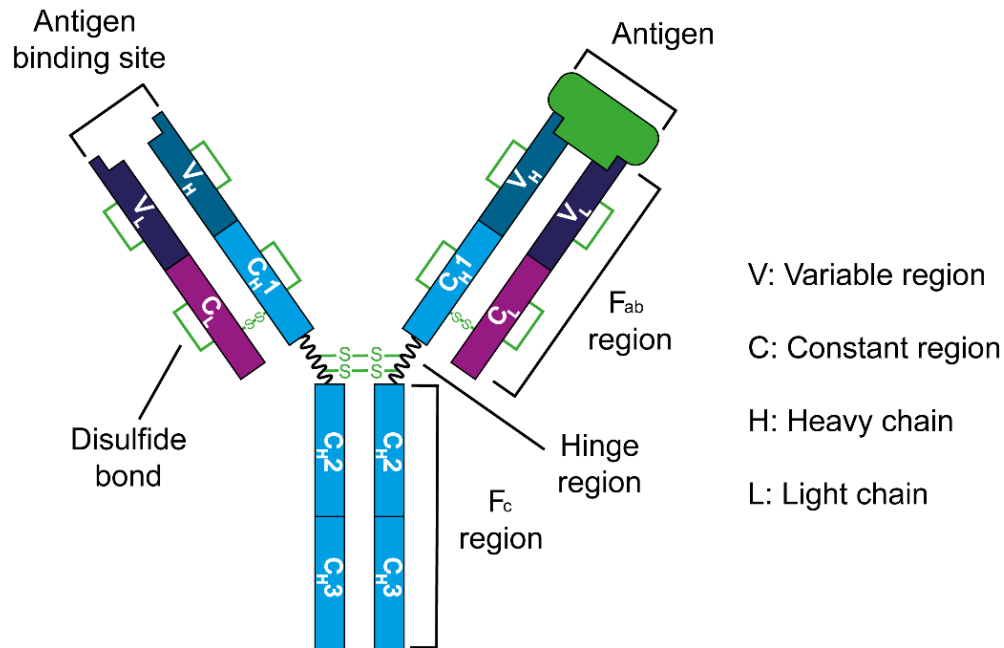


Figure 4: Structure of an IgG antibody. The antibody consists of two heavy chains (blue) and two light chains (purple). Upon incubation with papain three fragments (two F_{ab}, and one F_c region), each having a mass of 50 kDa. The upper part of the Y-shaped antibody contains the variable regions that contain highly variable CDR regions. CDR regions, form hyperloops that are responsible for the antigen specificity.

IV.4.3. Polyclonal Antibodies

B-lymphocytes are cells that produce antibodies. If different B-cells express an antibody against a specific antigen, then the antibodies are called polyclonal because they differ in their variable regions and bind to different sites—also called epitopes—of the antigen. For the preparation of polyclonal antibodies, the target antigen is injected into an animal like rabbit, goat, or mouse. The process is repeated several times over a defined period to trigger the animal's immune response, causing the B-cells to produce antibodies. The polyclonal antibody is then purified from the serum and often lyophilized in the presence of stabilizers like sugars, or polyols. In this form the antibodies are stable for several years if stored at low temperatures between -20 and -80 °C.²⁸⁻²⁹ Polyclonal antibodies are inexpensive, quick in production and especially suited for the detection of antigens that have slight variations in their epitopes. Because of the nature of the production process, there are always slight variations from batch to batch because different animal individuals are used. Also, the cross-reactivity can be higher because of the variable antigen-binding sites.

IV.4.4. Monoclonal Antibodies

The counterpart to the polyclonal antibody is the monoclonal antibody that binds to one specific epitope of the antigen. The first step in the production (**Figure 5**) of monoclonal antibodies is the immunization of an animal, typically a mouse. After a specific period, antibodies appear in the blood, and antibody-producing B-cells from the spleen of the animal are isolated. The next step is the preparation of hybridoma cells consisting of spleen cells fused with cancer cells from bone marrow, which are called myeloma cells.³⁰ Hybridoma cells combine the immortality of cancer cells with the production of specific antibodies against the desired target. Next, the hybridoma cells are highly diluted, and individual cells are grown in microtiter wells, followed by the screening for high-affinity antibodies against the antigen of interest. This step is repeated several times. The clone with the best antibody is amplified, the antibodies separated and purified. Monoclonal antibodies have a high specificity against a particular epitope and can be produced in large quantities with low batch-to-batch variations, but the development and production are costly and time-consuming.

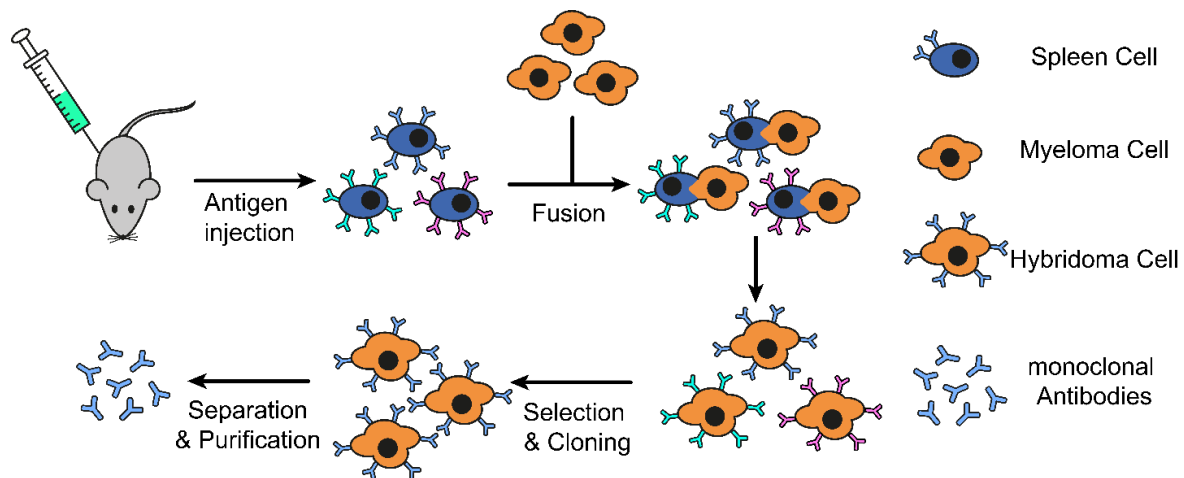


Figure 5: Production process of monoclonal antibodies. The antigen is injected into a mouse, triggering an immune response that leads to the production of antibody-producing B-cells from the spleen. The B-cells are fused with “immortal” myeloma cells and form hybridoma cells. The hybridoma cell-line with the best antibody is selected and cloned. In the last step, the antibodies are separated and purified.

IV.5. Antibody Alternatives

IV.5.1. Aptamers

Antibodies are not the only molecules used as recognition elements in affinity assays. In 1990, Andrew D. Ellington and Jack W. Szostak from the department of molecular biology of the Massachusetts General Hospital published a method to produce RNA molecules that specifically bound to target molecules. They called these molecules aptamers, which is derived from the Latin word *Aptus*, meaning “to fit”.³¹ Szostak later won the Nobel prize for medicine in 2009 not for his work on aptamers but for the discovery of “how chromosomes are protected by telomeres and the enzyme telomerase”.³² In the same year of the first publication of aptamers, Tuerk and Gold published a method called systematic evolution of ligands by exponential enrichment (SELEX).³³ This made it possible to select aptamers from a combinatorial library that specifically bind to a non-nucleic acid target with high affinity. A combinatorial library (**Figure 6**) of approximately 10^{15} different single-stranded DNA (ssDNA) molecules is amplified with polymerase chain reaction (PCR) to generate a large pool of double-stranded DNA (dsDNA), which is transcribed into RNA that has a more extensive repertoire of available spatial structures.³⁴ The RNA pool is incubated with the target analyte, which is, for example, immobilized on magnetic microspheres,³⁵ or on the solid phase of a chromatographic column,³⁶ and only RNA molecules with affinity to the target bind to the microbeads. The bound RNA is separated from unbound RNA and eluted from the magnetic spheres. The RNA is again transcribed into DNA and amplified with PCR. Now the whole process is usually repeated 8–15 times to get highly specific and strong-binding aptamers.³⁷ After the final SELEX round, the aptamers are cloned and sequenced. With the known aptamer sequence, the molecule can be synthesized *in vitro*—a significant advantage over antibodies—and further optimized, for example, by shortening the sequence. It is also possible to use ssRNA as aptamers. These have a lower intrinsic chemical stability,³⁸ but their 3D structures are considered to be more stable than the corresponding DNA structures.³⁹ Additionally, the commonly used T7 RNA polymerase is tolerant towards many modified ribonucleotides making the available structural pool even bigger.⁴⁰ To make aptamers more resistant towards degradation by nucleases the D-(deoxy)ribose can be exchanged by L-(deoxy)ribose generating an enantiomeric aptamer—also called Spiegelmer—that is not recognized by natural enzymes.⁴¹⁻⁴²

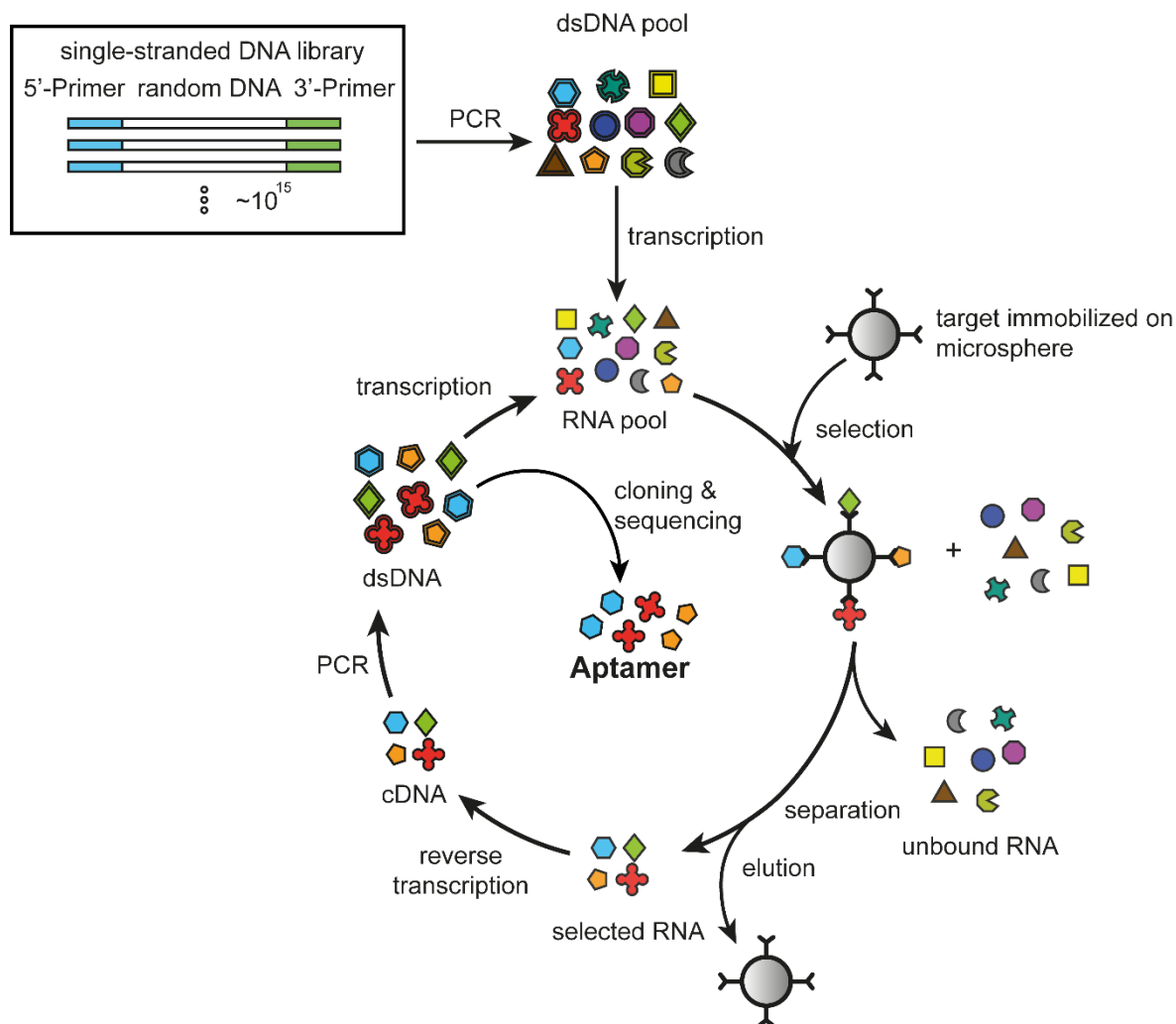


Figure 6: Illustration of the SELEX process. A combinatorial DNA library is amplified using PCR. The resulting dsDNA is transcribed into RNA and incubated with the analyte immobilized on magnetic beads. A washing step removes unbound RNA. RNA that bound to the magnetic beads is eluted and transcribed into DNA. The DNA is amplified with PCR and the cycle is repeated multiple times. At the end aptamers with the highest binding affinity to the analyte are cloned and sequenced.

Nowadays, aptamers found wide application in various kinds of affinity assays, the direct replacement of the ELISA is called the enzyme-linked apta-sorbent assay (ELASA).⁴³ Even combinations between aptamers and antibodies are reported.⁴⁴ A brief comparison of antibodies and aptamers is given in **Table 1**.

Table 1: Comparison of aptamers with antibodies.

	Aptamer	Antibody
Production	-tedious SELEX method - <i>in vitro</i> by chemical synthesis	- <i>in vivo</i> -difficult to produce antibodies for non-immunogenic molecules -with hybridoma cells, almost endless supply of monoclonal antibodies -with known gene sequence, <i>in vitro</i> synthesis of recombinant antibodies or fragments also possible
Size	-12–30 kDa for 30–80 nucleotides -access to tissue ⁴⁵	-normal IgG ~150 kDa -limited membrane permeability -90 kDa nanobodies with 15 kDa antigen binding fragments exist but are still rare ⁴⁶
Targets	-small targets like ions (Ni^{2+}) ⁴⁷ to epitopes of cells (cell-SELEX) ⁴⁸ -non-immunogenic targets	-small targets like ions (Hg^{2+}) ⁴⁹ -big proteins, viruses, bacteria, surface proteins of cells
Reproducibility	-low batch-to-batch variations	-different animals produce different antibodies -monoclonal antibodies have low batch to batch variations
Stability	-highly temperature stable -can be stored at room temperature -refold into active structure after heating -theoretically reusable after assay -sequence of aptamer is stored as data	-storage in refrigerator/freezer -irreversible denaturation after heating -usually one-time use -hybridoma cells must be stored frozen
Dissociation constants	-nanomolar to picomolar range ⁵⁰	-nanomolar to picomolar range ⁵¹

IV.5.2. Molecularly Imprinted Polymers

Linus Pauling postulated in 1940 a process of the formation of antibodies. He assumed that the antibody consists of at least two antigen-binding sites and a conformationally stable center. In his theory, the globulin chain forms around the antigen. Attracting groups like a positive charge of the antigen and a negative charge of the peptide chain will face each other while repelling groups with the same charge. These electrostatic interactions lead to a defined three-dimensional structure that is specific for the analyte molecule.⁵² While Pauling's hypothesis for the antibody formation turned out to be wrong, his idea explains the specificity of another promising recognition element for affinity assays so-called molecularly imprinted polymers (MIPs). MIPs are polymers formed from selected monomers polymerized in the presence of a template molecule. Synthesizing a MIP (**Figure 7**) starts with the selection of appropriate monomers that can interact with specific sites of the target molecule *via* hydrophobic interactions, metal coordination, electrostatic forces, hydrogen bonding, and more. The monomers and the template are dissolved in an inert solvent and interact with each other. The solvent in MIP synthesis called "porogen" plays a pivotal role in the formation of the pores in the polymer. The pores are essential for the access of the analyte when the polymer has formed.⁵³ The polymerization is often initiated by a radical polymerization of monomers with acryl or vinyl groups because they exist in large variations of functional groups.⁵⁴ After polymerization, the template molecule is eluted, and depending on the polymerization method and treatment afterward, MIPs can have various sizes and shapes.

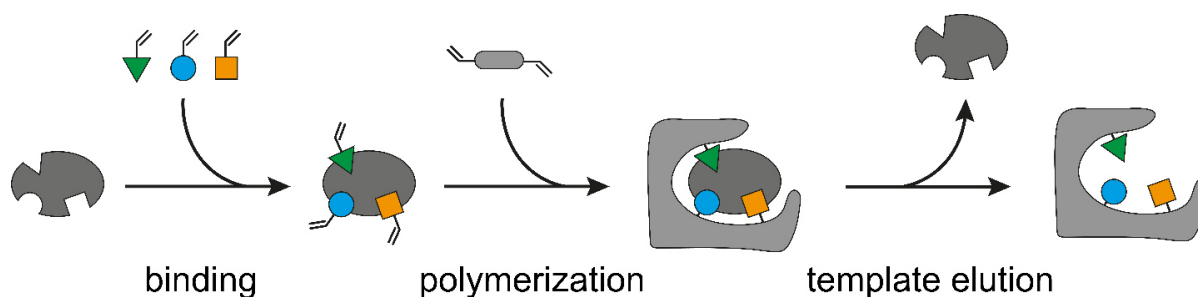


Figure 7: General procedure of MIP synthesis. The template molecule (dark grey) is incubated with functional monomers (colored). Some monomers interact with the template molecule via electrostatic, hydrophobic interaction, hydrogen bonding, and more. The polymerization of the monomers is initiated, and the template molecule eluted from the resulting MIP.

One of the easiest but also the crudest method is to mechanically grind the MIP after solution polymerization, which yields micrometer-sized particles often used as column material for chromatographic separations.⁵⁵ However, this top-down approach yields particles with different shapes and a broad size distribution. It is also possible to form the polymers directly

in chromatographic columns via *in situ* thermal-initiated copolymerization, which are then called monolithic MIPs. This method was used to separate enantiomeric D and L-phenylalanine derivatives, which would not be possible with commonly used C-18 columns.⁵⁶ Uniform MIP beads with an average diameter of 5.6 μm were synthesized by a two-step swelling and polymerization method with 1 μm polystyrene beads as a shape template.⁵⁷ Another way to synthesize spherical MIPs is the in-flight polymerization of an aerosol of the monomer, a photoinitiator, and the template molecule. The aerosol is sprayed into a box equipped with two UV lamps (400 W) that start the cationic polymerization. At the end of the flight path, the formed MIP beads are collected with an electrostatic precipitator.⁵⁸

The group of Mosbach performed one of the first affinity assays using MIPs as a recognition element in 1993.⁵⁹ They designed a competitive radio MIP assay where either theophylline or diazepam were radiolabeled and competed with the unlabeled analyte molecules in spiked human serum. Nowadays, spherical MIP nanoparticles (MIPNs) as an alternative to antibodies have attracted attention for affinity-based assays. MIPNs have a high surface to volume ratio, are easily dispersible, and many different methods for the functionalization of the polymer have been developed.⁶⁰ MIPNs were, for example, used in a competitive affinity assay for the determination of vancomycin.⁶¹ In this competitive assay format, a microwell was coated with vancomycin, and a mixture of MIPNs with a $\gamma\text{-Fe}_3\text{O}_4$ core that has a peroxidase-like activity and free vancomycin were added. In case of a low amount of free vancomycin the MIPNs could bind to the surface-immobilized vancomycin, whereas at high vancomycin concentrations, the binding sites of the MIPs were occupied. After a washing step to remove unbound MIPNs, a tetramethylbenzidine (TMB) substrate was added, and the catalytic core of the MIPNs converted the substrate to a colored product. The ability to produce MIPNs with an intrinsic enzymatic activity removes the need for an additional labeling procedure.

Xing et al. reported a sandwich-like affinity assay for neuron-specific enolase using MIPs.⁶² For the surface imprinting of the detection label, the group synthesized silica-coated silver nanoparticles with incorporated boronic acid. Coupling fructose to the N-terminus of the neuron-specific enolase template leads to a complex formation between the fructose and the boronic acid. The surface imprinting was performed by incubating the dispersion with different functional silanes for 40–70 min. After removing the template molecule, the particles had a specific affinity towards the N-terminus of the analyte molecule. For capturing the analyte, fructose was coupled to the C-terminus of the protein and bound to boronic acid-functionalized gold nanoparticles coated on a glass substrate. Surface imprinting was performed utilizing the same silanes used for imprinting the silver particles. The final MIP-complex consisted of the epitope imprinted gold nanoparticles on a glass substrate for capturing, the neuron-specific enolase, and the epitope imprinted silver nanoparticles as a detection label. Quantification of

the analyte was done by surface-enhanced Raman scattering, which resulted in a limit of quantification (LOQ) of 10 pg/mL.

MIPs are versatile tools for various applications such as affinity-based separation methods, or quantitative affinity assays. Main advantages are the easy production⁶³ and high stability, which renders MIPs as perfect recognition elements in biosensors. However, challenges including non-specific adsorption,⁶⁴ heterogeneity of target binding sites, and lower affinity and specificity compared to antibodies have to be overcome to establish MIPs as an alternative to antibodies.⁶⁵

IV.6. Enzyme Labels

IV.6.1. Enzyme-Linked Immunosorbent Assay

An enzyme is a protein that has an intrinsic catalytic ability that can be exploited to generate high signals if used with an appropriate substrate. Enzymes are the gold standard as signal generating elements in different kinds of affinity assays, including the widespread ELISA. The most common enzymes used for affinity assays are horseradish peroxidase (HRP), alkaline phosphatase, beta-D-galactosidase (GAL), and urease. Choosing the optimal enzyme for each application is an essential factor. High turnover numbers, availability of suitable substrates, and the absence of interfering compounds in the measurement environment are essential points for the assay design.⁶⁶ Sodium azide is, for example, often used as an additive in buffers because it is preventing bacterial growth, prolonging the shelf-life of the buffers. However, it is also known to inhibit the activity of HRP,⁶⁷ thus, potentially reducing the sensitivity of the assay. In this case, GAL might be a better option. Also, the pH of the used buffer dramatically influences the activity of an enzyme species. Alkaline phosphatase is well-suited for measurements in an alkaline environment and has its optimal activity at around pH 9.0.⁶⁸ In contrast, HRP has its pH optimum at around pH 6.5, depending on the substrate.⁶⁹ Some buffers contain ethylene diamine tetraacetic acid (EDTA), which complexes divalent metal ions like Mg^{2+} ; GAL is a glycoside hydrolase that has two Mg^{2+} ions bound per monomer⁷⁰ as cofactors that are crucial for the catalytic reaction. In the presence of EDTA, the activity of GAL decreases.⁷¹ For each application, a suitable substrate is needed; a few selected examples and typical applications are listed in **Table 2**.

Table 2: Common enzyme substrates for different applications.

Substrate	Enzyme	Detection	Application example
3,3',5,5'- Tetramethylbenzidine (TMB)/H ₂ O ₂	HRP	Colorimetric	ELISA, Western Blot
Diaminobenzidine (DAB)/H ₂ O ₂	HRP	Colorimetric	Immunocytochemistry, Western Blot
Amplex Red/H ₂ O ₂	HRP	Fluorescence	ELISA, Western Blot
Luminol/H ₂ O ₂	HRP	Chemiluminescence	Western Blot, ELISA
Nitro blue tetrazolium (NBT)	Alkaline phosphatase	Colorimetric	Western Blot
4-Methyl- umbelliferylphosphate (4-MUP)	Alkaline phosphatase	Fluorescence	ELISA
DDAO-phosphate	Alkaline phosphatase	Fluorescence	ELISA
<i>o</i> -Nitrophenol- β -D- galactopyranosid (oNPG)	GAL	Colorimetric	ELISA
Resorufin- β -D- galytopyranoside (RGP)	GAL	Fluorescence	ELISA, digital ELISA
Fluorescein di(β -D- galactopyranoside)	GAL	Fluorescence	ELISA
Bromocresol purple/urea ⁷²	Urease	Colorimetric	ELISA

Since Yalow and Berson performed the first immunoassay, many different assay designs have emerged. ELISAs are routinely conducted in microtiter plates. The most straightforward ELISA assay is the direct ELISA (**Figure 8A**). In the direct approach, the analyte is coated onto the bottom of a microplate *via* non-specific adsorption. Next, a blocking step is performed to decrease non-specific binding sites. For blocking, phosphate-buffered saline (PBS, pH 7.4) containing 1% bovine serum albumin (BSA) is often used. Other possible blocking agents are casein, skim milk powder, or commercial blocking buffers. Incubation with an enzyme-labeled detection antibody leads to the formation of an immunocomplex. Buffers used for antibody-antigen binding usually have a neutral pH and contain a small amount of a non-ionic detergent

like Tween 20, which occupies hydrophobic regions of the antibody to suppress non-specific binding. Unbound antibody conjugates are removed, and a substrate is added. During the enzymatic reaction, the substrate is converted, for example, to a colored product that can be detected in a microplate reader. To avoid time-consuming incubation times until a stable signal is achieved, it is advantageous to stop the enzymatic generation after a particular time. The HRP substrate TMB for example turns from colorless to blue upon the enzymatic oxidation, adding H_2SO_4 stops the reaction and turns the color to yellow, which can be quantified by measuring the absorbance at 450 nm. The direct approach is usually less sensitive than using a sandwich like-format. In biological fluids like blood serum, many proteins are present in higher concentrations than the analyte causing them to block the surface of the microplate, preventing the target from binding there.

A typical sandwich ELISA is shown in **Figure 8B**. Here, the analyte is captured by the capture antibody and a second antibody, the detection antibody that is labeled with an enzyme forms the final immunosandwich. The capture antibody is often non-specifically adsorbed to the microplate surface by incubation overnight (o.n.) in carbonate buffer at pH 9.6. The relatively high pH value ensures that the antibody has several hydrophobic binding sites, promoting adsorption to the polystyrene surface.

In indirect ELISAs (**Figure 8C**), a third antibody (called secondary antibody) is used that carries the label. Secondary antibodies are anti-species antibodies that specifically bind to immunoglobulins from the respective species. If a mouse antibody is used as a primary antibody, an anti-mouse secondary antibody will bind to it. In this case, the target is detected indirectly by detecting the presence of the primary antibody. The indirect approach can result in higher signals because, in theory, more than one secondary antibody can bind to the primary. Thus, more enzyme labels are present. Additionally, secondary antibodies can be used for different targets if the species of the primary and secondary antibody match. However, the capture antibody must be from a different species, or the secondary antibody will bind to it and cause a high non-specific signal.

Using secondary antibodies to immobilize the capture antibody is also possible (**Figure 8D**). A wide range of microplates coated with anti-species antibodies is commercially available or can be produced in the laboratory. The advantage of using anti-species plates is that the capture antibody—from the same species—can be immobilized much faster compared to the non-specific adsorption because the equilibrium of the immunoreaction is usually reached in less than an hour. Secondary antibodies that bind primarily to the heavy chains of the primary antibodies cause a directional binding of the capture antibody, potentially reducing the necessary coating concentration of the primary antibody. With a dissociation constant of 10^{-15} M, the biotin-streptavidin complex is the most robust known noncovalent bond between

protein and ligand.⁷³ The strong biotin-streptavidin interaction can be exploited for an indirect detection system (**Figure 8D**) if connecting the primary antibody to biotin and using an enzyme that is connected to streptavidin (SA).

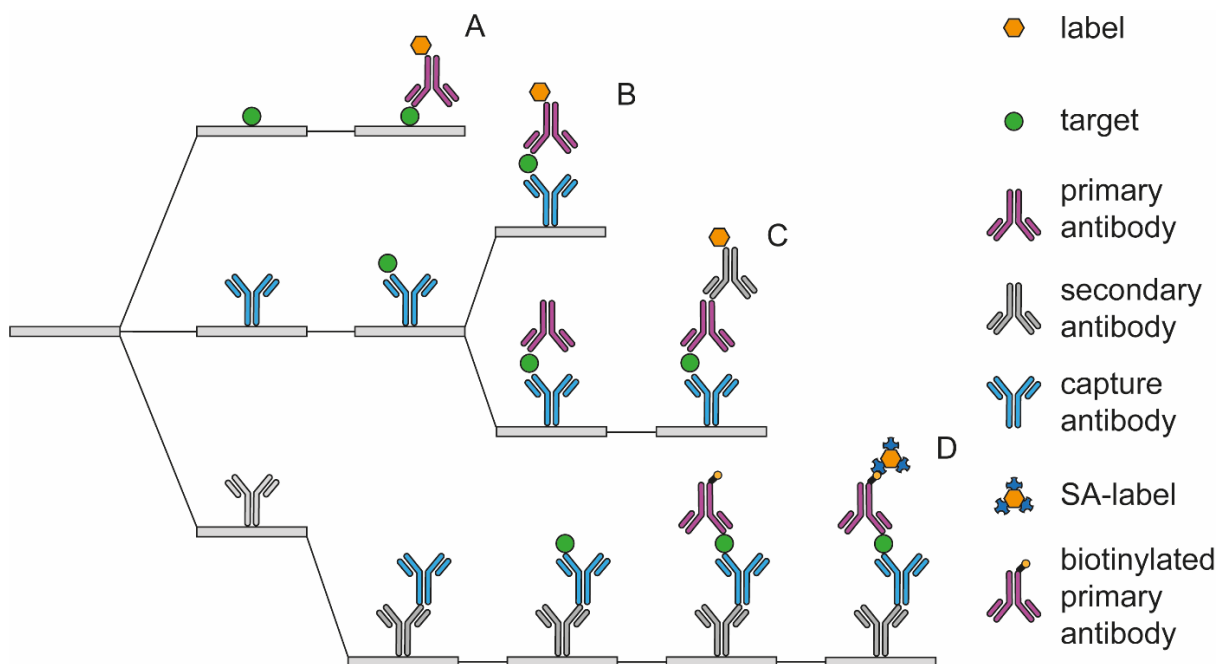


Figure 8: Different types of ELISA assay designs. **A)** In the direct ELISA the analyte is coated onto a surface and the detection antibody binds to it to generate a measurable signal. **B)** The typical sandwich ELISA includes a capture antibody to immobilize the target onto a surface. The detection antibody binds to a different epitope of the target and forms the immunosandwich. **C)** In an indirect sandwich ELISA, a labeled anti-species antibody is used to detect a target-bound primary antibody. **D)** An anti-species antibody can be used to achieve a directional immobilization of the capture antibody. Primary antibodies connected to biotin serve as an anchor for streptavidin, which is connected to the label.

IV.6.2. Digital ELISA

The ability of enzyme molecules to produce thousands of fluorophores in a short time, each emitting up to a million photons, enabled the development of one of the first digital ELISAs. In the digital ELISA, individual enzyme molecules are enclosed into so-called femtoliter arrays (fL-arrays) fabricated into polydimethylsiloxane (PDMS),⁷⁴ fused silica,⁷⁵ or optical fiber bundles.⁷⁶ The arrays consist of a high number of homogeneous wells (>50,000) with a volume of around 50 μm^3 (50 fL). The research group of David R. Walt paved the way for the commercialization of this technique by improving the limit of detection (LOD) for prostate-specific antigen (PSA) of conventional analog ELISAs by 1000 \times .⁷⁷ With the idea of developing a fully automated single-molecule ELISA system, the company Quanterix was founded in 2007. The commercial digital ELISA from Quanterix is called single-molecule array platform (Simoa) and uses several fL-arrays fabricated into microfluidic channels that are arranged in a circular pattern on a compact disc-like chip.

For the immunoassay, the capture antibody was immobilized onto magnetic microbeads with a diameter of 2.7 μm (**Figure 9A, B**). The antibody-coated beads were dispersed in excess into the analyte solution to capture the target. This step improves the overall capture efficiency compared to microplate assays, because the beads have a high surface area and diffuse freely in the analyte medium. In addition, the beads can be used to preconcentrate the analyte. Preconcentration is done by dispersing the beads in the analyte medium, followed by magnetic separation, and redispersion in a smaller volume. The high bead-to-analyte ratio resulted in a significant fraction of beads that did not capture an analyte molecule and a small fraction with an immobilized analyte molecule. Next, the beads were incubated with a biotinylated primary antibody and a streptavidin-GAL conjugate. A washing step followed by magnetic separation removed the unbound detection conjugate. The microspheres were loaded, together with the fluorogenic substrate RGP, into the femtoliter array and sealed by an oil film to prevent product diffusion. The size of the beads was chosen that exactly one bead fits into a fL-well (**Figure 9B**). Wells that contained a magnetic bead that captured a target molecule also contained a GAL label and showed increasing fluorescence over time that was monitored using epifluorescence microscopy. The analyte concentration was obtained by counting the number of fluorescent wells.

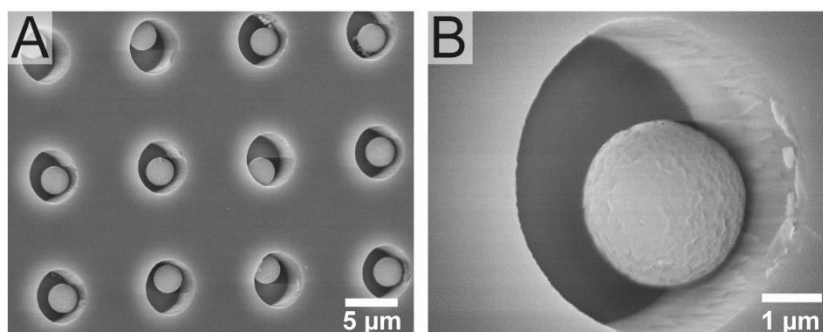


Figure 9: Scanning electron microscopic images of fused silica fL-arrays with a diameter of 4 mm and a depth of 3 μm (38 fL) loaded with magnetic beads with a diameter of 2.7 μm. **A)** Image with 3300× magnification and a 15° angle. **B)** Image of a single well with a 19000× magnification and a 15° angle.

The Simoa technology enabled measurements of PSA and tumor necrosis factor- α (TNF- α) with very low LODs of 50 aM for PSA and 150 aM for TNF- α .⁷⁷ The technology was further used to measure the concentrations of other clinical relevant analytes like the p24 protein of HIV,⁷⁸ urinary biomarkers⁷⁹, or the neurofilament light chain protein (NFL), an indicator of different neurodegenerative conditions and brain injuries.⁸⁰ NFL is traditionally measured in cerebrospinal fluid, which is obtained by a lumbar puncture. The high sensitivity of the digital ELISA superseded the need for this procedure and enabled NFL measurements in human serum.⁸¹

IV.7. Fluorescent Molecular Labels

Supposedly the immunological staining of cells is the earliest report about the use of fluorescent molecular labels in bioanalytical applications. Albert H. Coons described in 1942 a method of conjugating a fluorescein derivative onto antibodies and used these conjugates to stain mouse liver cells that had a pneumococcal 3 infection.⁸² Affordable, stable and bright excitation sources like laser diodes, stable fluorophores with large Stokes shifts, and sensitive detectors like photomultiplier tubes, and photodiodes accounted for the development of very sensitive fluorescent immunoassays (FIA).

IV.7.1. Fluorescence Polarization Immunoassay

The fluorescence polarization immunoassay (FPIA) is a prominent example of a competitive, homogeneous FIA. Fluorescent polarization occurs if a slowly rotating fluorescent molecule is excited with linear polarized light. Free fluorescent molecules undergo rapid rotations in solution. Upon binding to an antibody, the rotary diffusion of the fluorescent molecule strongly decreases, causing a polarized emission. Dandliker and Feigen described the first FPIA in 1961.⁸³ The two researchers synthesized fluorescein-labeled ovalbumin and used it to immunize rabbits. Rabbit γ -globulins were separated and used in an affinity assay for

fluorescently labeled ovalbumin. Binding of the fluorescein-ovalbumin conjugate resulted in an emission decrease and an increase in polarization that could be monitored in a cuvette. With their measurements, Dandliker and Feigen successfully demonstrated the potential of the FPIA for the determination of equilibrium constants and the quantification of biomarkers. FPIA systems were also commercialized, for example, by Abbot (AxSYM).⁸⁴

IV.7.2. Time-Resolved Fluorescence Immunoassay

The development of time-resolved (TR) detection methods marked another important milestone for FIAs. In 1983 Siitari et al.⁸⁵ from the company Wallac Oy (Turku, Finland) used lanthanide complexes for the quantification of hepatitis B surface antigen (HBsAg). The general assay design was similar to the sandwich ELISA, except that the detection antibody was directly labeled with a luminescent Eu^{3+} complex. An aminophenyl derivative of EDTA that strongly coordinates to lanthanide ions was synthesized. The aminophenyl was activated *via* diazotization and coupled to tyrosine and histidine groups of an anti-HBsAg antibody. A polystyrene tube was coated with a capture antibody, incubated with plasma containing the analyte, followed by the detection antibody. The advantage of the lanthanide luminescence is the long lifetime up to a few milliseconds depending on the ligand.⁸⁶ In the TR measurements, the Eu^{3+} complex was excited with a 0.5 μs light pulse of a xenon flashlamp at 330 nm. A delay of 50 μs ensured that the autofluorescence of the matrix was decayed before the 613 nm emission light was collected for 250 μs . The TR measurement significantly reduced the background caused by autofluorescence and light scattering. With the TR-FIA, Siitari et al. reached higher sensitivity for HBsAg (0.2 ng/mL) compared to the RIA (0.5 ng/mL) simultaneously eliminating the need to use radioactive isotopes.

In 1985 Wallac Oy successfully launched an improved version of the TR-FIA, the dissociation-enhanced lanthanide fluorescence immunoassay (DELFLIA).⁸⁷ The assay principle of the DELFLIA is the same as in the TR-FIA, but at the end, the lanthanide complex is dissociated from the antibody, and a highly fluorescent chelate in a micellar solution is formed, significantly enhancing the lanthanide emission.⁸⁸ Today Wallac Oy belongs to Perkin Elmer.⁸⁹

IV.7.3. Immuno PCR

In 1992, Sano et al.⁹⁰ published an FIA that uses a PCR amplification step called immuno PCR. The main difference to the ELISA was the detection conjugate. The group designed a chimeric molecule between SA and protein A, which specifically bound to the F_c -fragment of IgG molecules. The SA-side served to immobilize a biotinylated linear plasmid DNA. After the immunocomplex was formed, a 260 base pair sequence of the linear plasmid DNA was amplified *via* PCR using appropriate primers. Then, 15 μL of the amplified DNA was loaded onto an agarose gel that solidified in the presence of the intercalation dye ethidium bromide.

An electric field was applied, and the 260 base pair sequence migrated towards the positively charged anode. After electrophoresis, the gel was photographed under UV excitation. Ethidium bromide showed a significantly enhanced fluorescence upon intercalation into double-stranded DNA, which was proportional to the number of analyte molecules. At this time, digital cameras were still rare, so the group took a photo of the gel on a polaroid film and evaluated the emission using a densitometer, which was used to measure the optical density of transparent or reflective surfaces.⁹¹ The superior sensitivity of the immuno PCR was demonstrated with BSA as a model analyte and was able to detect 580 BSA molecules in a volume of 50 μL (20 aM), which was 10^5 more sensitive than the corresponding ELISA with alkaline phosphatase as a label (20 pM).

IV.7.4. Digital Fluorescence Affinity Assays

TIRF Microscopy

For the detection of individual fluorophores, the detection volume must be significantly reduced to distinguish the emission from the background. Therefore, techniques like TIRF microscopy are the method of choice for digital fluorescence affinity assays. In TIRF microscopy, the excitation light is directed in a total reflection angle to a coverslip or prism. At the boundary surface, an evanescent field develops, decaying exponentially with the distance from the coverslip or prism. This causes that only fluorophores in proximity (few 100 nm) to the surface get excited, decreasing the measurement background.⁹²

Weng et al.⁹³ reported a digital fluorescence affinity assay for the quantification of the three small molecules; adenosine, the insecticide acetamiprid, and the toxin PCB-77. As a recognition element, a hairpin-shaped aptamer was used that was attached to the surface of a glass slide *via* biotin-SA interaction. The analyte solution was applied together with a short fluorescent DNA probe. Binding of the analyte to the aptamer changed the conformation of the hairpin-like structure to an open form, which allowed for the binding of the fluorescent DNA probe. The binding event of the fluorescent DNA probe took place inside the evanescent field of the TIRF illumination, leading to the excitation of the fluorophore. Unbound DNA probes were on average too far away and were not excited by the evanescent field. The LODs were 0.3 pM for adenosine, 0.35 pM for acetamiprid and 0.72 pM for PCB-77. Weng et al. demonstrated that aptamers are valid options for affinity assays, especially if small analyte molecules are the targets of interests.

Laser-induced Fluorescence

While TIRF illumination is a powerful tool for background reduction for microscopic applications, it is challenging to implement this technique in automated fluorescence readers in routine applications. Here a different single-molecule technique based on laser-induced fluorescence detection in capillaries, the Erenna platform proved to be the leading technique. Originally the Erenna was invented by the American company Singulex, which shut down in 2019. Merck took over the distribution and is selling the device along with kits for the detection of various analytes like cardiac troponin I, tumor necrosis factor- α , or interleukin 1- α .⁹⁴ During the assay procedure, capture antibody-coated magnetic microbeads are used to immobilize and preconcentrate the target. A fluorescently labeled detection antibody forms an immunosandwich with the antigen and capture bead. Unbound detection antibody is removed by magnetic separation of the beads, and the spheres are resuspended in a small volume of 20 μ L. The detection antibody is eluted from the particles and loaded into a capillary. For single-molecule counting, a small volume inside the capillary is illuminated by a highly focused laser through an objective. If a fluorescently labeled molecule passes the excitation volume, a fluorescence burst is detected and counted if it is above a fixed threshold. In the specifications of the Erenna: an LOD for a fluorescently labeled antibody of less than 1 fM is given, which would correspond to approx. 12,000 antibodies in a volume of 200 μ L.⁹⁴ The Erenna system was used to determine cardiac troponin I (LOD of 8 pM),⁹⁵ soluble amyloid-beta oligomers (0.18 pM),⁹⁶ or mutant huntingtin protein (40 fM).⁹⁷

Fluorescence Correlation Spectroscopy

Fluorescence correlation spectroscopy (FCS) is an experimental technique for the detection of individual fluorophores, which is based on statistical fluctuations of the fluorescence intensity in solution. For FCS, a tiny observation area is needed, rendering microscopic techniques like TIRF microscopy, confocal microscopy, stimulated emission depletion microscopy, or two-photon microscopy as suitable methods to measure FCS. In confocal microscopy, the excitation laser is focused to a diffraction-limited spot, and a pinhole in front of the detector further confines the detection along the axial direction.⁹⁸ The emission light of fluorophores traveling through the excitation volume is measured by highly sensitive photon avalanche diodes capable of detecting single photons in real-time.⁹⁹ The time-dependent fluctuations in the fluorescence intensity contain the information needed to quantify the target. Extraction of the relevant data is done by applying the appropriate auto-correlation function, which depends among other things on the shape of the excitation beam, photophysical properties of the fluorophore, and the orientation of the fluorophore in the sample.¹⁰⁰

Chatterjee et al.¹⁰¹ used FCS to develop a single-molecule sandwich immunoassay for the detection of the neuronal cell adhesion molecule contactin-2 in cerebrospinal fluid. A

fluorescently labeled anti-contactin-2 primary antibody formed an immunosandwich with anti-contactin-2 and a second primary antibody. The formation of the immunocomplex changed the diffusion rate of the labeled antibody, which was monitored *via* FCS.

The sensitivity of FCS in sandwich immunoassays is further increased by using two fluorescently labeled antibodies (two different colors). This technique is also called fluorescence cross-correlation spectroscopy (FCCS). Here, the cross-correlation curve compares the intensities of both fluorophores (**Figure 8**). If the sandwich immunocomplex is formed, the diffusion times of both fluorophores are equal.⁹⁸ Miller et al., for example, demonstrated the practical use of FCCS for the quantification of human chorionic gonadotropin (LOD of 100 pM) and prion protein (2 nM).¹⁰²

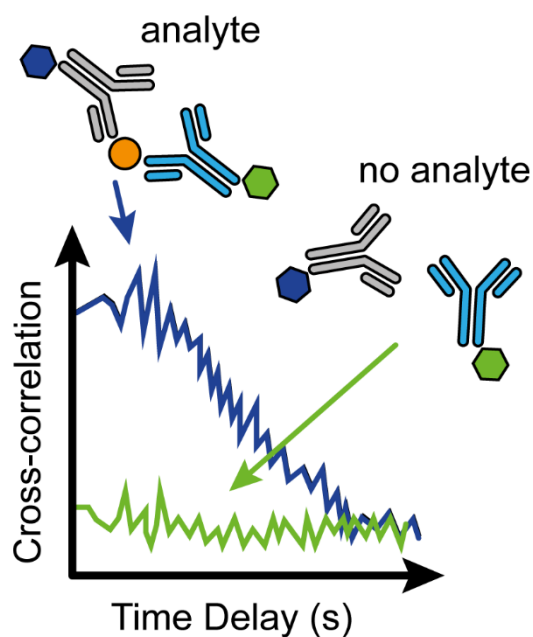


Figure 10: Schematic representation of the cross-correlation of two fluorescently labeled antibodies in the presence of the analyte (blue curve) and without analyte (green curve).

IV.8. Nanoparticle Labels

In recent years, many different bioaffinity assays using nanoparticles as a label were reported.¹⁰³ Well-established representatives are gold nanoparticles, nanozymes, photon-upconversion nanoparticles, and quantum dots. Nanoparticles generate higher signals than small molecular labels but are also bigger in size, potentially hindering the formation of immunocomplexes because of steric effects and promoting non-specific binding. Another problem is the colloidal stability of nanoparticles. If the surface of nanoparticles is not shielded by a suitable coating, nanoparticles tend to aggregate over time, resulting in poor performance in affinity assays. In contrast to small molecular fluorophores where techniques like confocal microscopy and TIRF microscopy are needed to detect a single label, individual nanoparticles can be detected with standard microscope methods. For example, individual gold nanoparticles larger than 20 nm can be imaged directly by phase-contrast microscopy or differential interference microscopy,¹⁰⁴ and the emission of photon-upconversion nanoparticles is visible using standard epilluminescence microscopy.¹⁰⁵

IV.8.1. Gold Nanoparticles

Gold nanoparticles (AuNPs) are plasmonic nanoparticles that can be synthesized in aqueous solution by reducing Au^{3+} in the presence of a stabilizer. A common way of AuNP synthesis is to reduce AuCl_3 with citric acid, which also acts as a stabilizer. After nucleation, a ligand exchange reaction can be performed to introduce functional groups like carboxyl groups that are suitable for the immobilization of biomolecules. The strong affinity of thiol groups to gold is often used to attach linkers like PEG onto gold nanoparticles.¹⁰⁶

AuNPs have various properties that can be exploited for analytical applications. Small AuNPs (~30 nm)¹⁰⁷ strongly absorb light causing the intense red color in colloidal dispersion. A popular application for colloidal AuNPs is the colorimetric lateral flow assay (LFA, **Figure 11**) for the pregnancy indicator human chorionic gonadotropin (hCG). In a typical lateral flow assay, the sample (blood or urine) is applied on the sample pad, and capillary forces cause the liquid to move towards the other end of the strip, where the adsorption pad is located. The sample first passes through the conjugate pad that contains the detection conjugate. The target is captured by the AuNPs conjugated with antibodies and travels towards the test-line. The test-line consists of immobilized capture antibodies that form a sandwich with the detection antibody and the analyte. The accumulation of gold particles causes a red color, which allows for a visual readout. At the end of the strip the control-line is located, which consists of immobilized secondary antibodies that bind the detection antibody independent of the analyte and indicates if the assay worked properly.

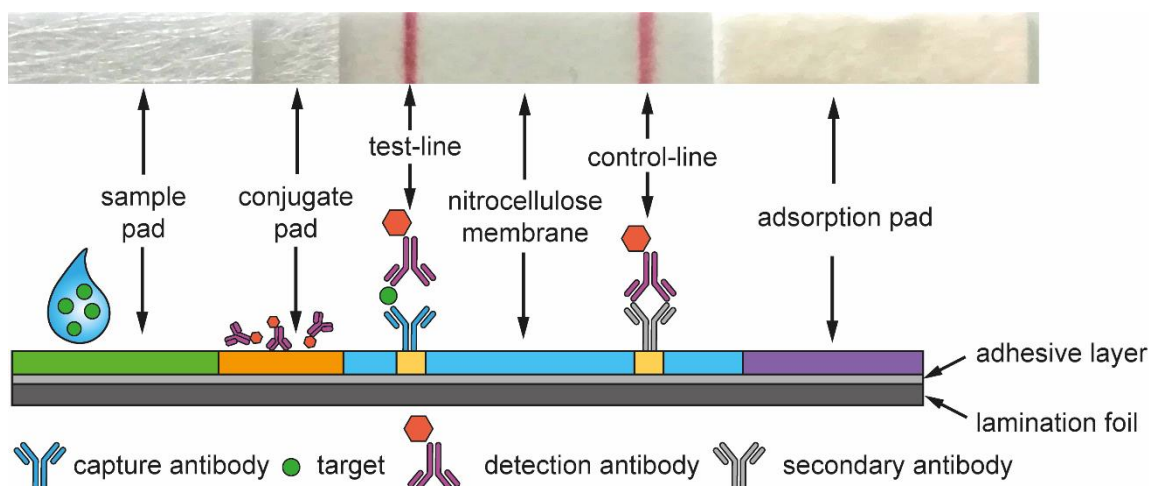


Figure 11: Top: Photograph of an LFA strip with AuNPs as a label. Bottom: Illustration of the different components of a typical lateral flow strip.

Small AuNPs also emit light with a maximum at a wavelength of about 610 nm. It was reported that the particle (38 nm diameter) brightness is high enough to detect individual AuNPs using epifluorescence microscopy for imaging of cancer cells.¹⁰⁸ After excitation, the electrons undergo a thermal relaxation causing the environment close to the AuNP to heat up, which is a critical factor for *in vivo* imaging, or if the AuNP is bound to a heat-sensitive molecule like a protein. Orrit et al.¹⁰⁹ exploited the photothermal effect to visualize individual AuNPs down to 10 nm by photothermal imaging and estimated the temperature increase during excitation of about 15 K for a 5 nm AuNP. Another method to image single AuNPs is the dark-field microscopy. It is based on the strong scattering properties of the nanoparticles that are also tunable because the wavelength of the scattered light depends on the size and shape of the nanoparticles.

Upon absorption of light, free electrons inside the AuNP are excited and start to oscillate collectively, which is referred to as a surface plasmon resonance.¹¹⁰ The surface plasmon resonance frequency is size-dependent and around 510–530 nm for particles between 4–40 nm.¹¹¹ The plasmonic effect is a powerful tool to enhance the sensitivity in Raman spectroscopy. In Raman spectroscopy, the inelastic scattering of vibrational and rotational states of molecules is measured. Scattered photons can take energy from the molecule causing the wavelength of the scattered light to shift to smaller values (anti-Stokes shift) or transfer energy to the molecule of interest, causing a redshift (Stokes shift). The Raman spectrum is characteristic for a given molecule and suitable for the label-free detection of analytes.¹¹² Attaching the molecule of interest onto a gold surface, for example, by the formation of an immunocomplex, enhances the Raman signal by several orders of magnitude and is called surface-enhanced Raman scattering (SERS). In label-free SERS the spectrum of the analyte is

directly measured. In the label-based SERS, for example, a Raman active dye coupled to a SERS-active nanoparticle. The label-based SERS effect was used in a sandwich immunoassay for the detection of cardiac troponin I. Magnetic beads were used to capture and preconcentrate the analyte. The detection label consisted of AuNPs coated with a Raman reporter and an anti-cardiac troponin I antibody, several of these conjugates were assembled on graphene oxide fragments and formed the reporter probe. The SERS-based assay achieved a LOD of 5 pg/mL suitable for real-world applications.¹¹³

Uniform AuNPs typically have a red color that rapidly changes to blue if the particles form aggregates. In 1996, Chad Mirkin first reported a colorimetric assay for DNA based on the color change of AuNPs during aggregation.¹¹⁴ De la Rica et al. used the color change of AuNPs to design a plasmonic ELISA, one of the most sensitive assays for PSA in existence.¹¹⁵ The target molecule was captured by the capture antibody, coated in a microwell. A primary anti-PSA antibody was added, followed by the addition of a biotinylated secondary antibody. For the detection, a streptavidin decorated with catalase was used. The enzyme catalase promotes the disproportionation reaction of H_2O_2 to H_2O and O_2 . If H_2O_2 was present in the solution, the AuNPs were stable because H_2O_2 reduces gold ions in solution, stabilizing the spherical AuNPs causing a red colored dispersion. In the presence of the analyte, the catalase-labeled streptavidin is also present and the H_2O_2 concentration decreases, causing the particles to aggregate, resulting in a color change from red to blue. The difference is visible with the bare eye. The plasmonic ELISA reached an LOD of 1 ag/mL (0.4 aM).

IV.8.2. Quantum Dots

The first report about semiconductor nanocrystals, also known as quantum dots (QDs), was by Alexei Ekimov in the early 1980s. He studied the color of glass doped with semiconductors such as CdSe, CdS, CuBr and CuCl. During his experiments with the glass, he found small nanometer-sized crystals that absorbed light at low wavelengths.¹¹⁶ Together with Alexander Efros, he developed a controlled growing technique for these nanocrystals in multicomponent silicate glass, and described their size-dependent optical properties.¹¹⁷ These particles were later named QDs. The intrinsic optical features that render QDs as exceptional labels for bioanalytical applications are high quantum yields, high molar extinction coefficients, a broad absorption range (**Figure 11A**, black line), narrow emission bands (**Figure 11A**) that are tunable by size (**Figure 11B**), large Stokes shifts, and a high chemical and optical stability.¹¹⁸

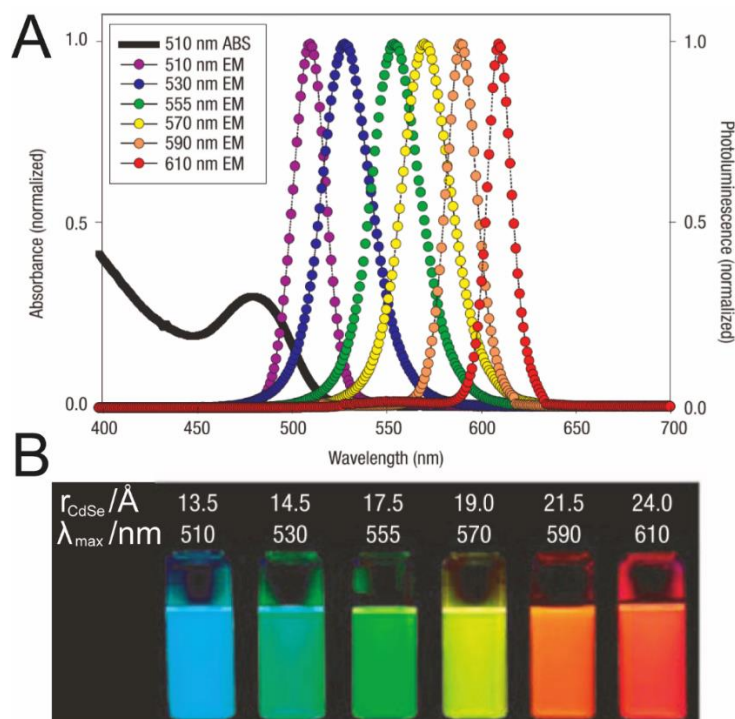


Figure 11: Spectral properties of QDs. **A**) Absorption and emission spectra of CdSe QDs with different radii. The black line indicates the absorption spectrum of CdSe particles with a radius of 13.5 Å. **B**) Photo of CdSe QD dispersions demonstrating the size-dependent emission of QDs. Adapted with permission from Springer Nature: Nature Materials¹¹⁸, Copyright 2005.

Today, colloidal synthesis routes are established for various QD types like CdSe, CdTe, ZnSe, ZnS, and CdS. The group of Bawendi¹¹⁹ was the first to establish a synthesis method for highly uniform QDs. The synthesis was based on the pyrolysis of organometallic compounds by injection into a hot coordinating solvent, which lead to a controlled crystal growth with a narrow size distribution. For QDs the size distribution is critical because a broader distribution also causes broader emission peaks.

Because of their small size, electrons in QDs are confined in all three dimensions resulting in quantized energy levels between the valence band and the conduction band. The energy gap between valence and conduction band depends on the size of the particle. Bigger particles have a smaller energy gap, leading to a red shifted emission. Smaller QDs have a larger energy gap causing the emission to be shifted to the blue.¹²⁰ The emission of available QDs covers the whole visible spectrum (**Figure 12**), even particles that emit in the ultraviolet (ZnS), and in the near-infrared (NIR) region (PbS, PbSe/Te) exist. Sharp emission bands with maxima at many different wavelengths make QDs especially interesting for multiplexed applications. The

company Intellicyt, for example, uses mixtures of QDs for the barcoding of microbeads in flow cytometry.¹²¹

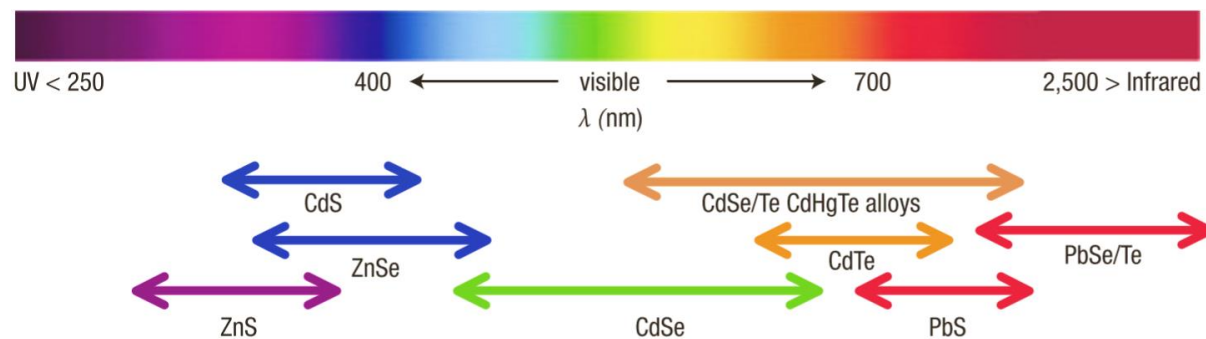


Figure 11: Schematic representation of the emission ranges of various kinds of QD materials.

Adapted with permission from Springer Nature: Nature Materials¹¹⁸, Copyright 2005.

QDs also found a wide range of applications in immunoassays. Kerman et al. developed a quantum dot-based immunosensor for the detection of PSA with a fluorescence microscope.¹²² A capture antibody was immobilized on a carbon electrode, followed by incubation with the sample to capture specifically PSA. A biotinylated primary antibody was used to immobilize SA-coated QDs. The readout was performed under a fluorescence microscope, and the integrated intensity in several defined regions of interest (ROIs) compared to a calibration was used to quantify the analyte concentration in human serum with an LOD of 0.25 ng/mL. A multiplexed analysis of four different toxins was reported by the group of Mattoussi.¹²³ A mixture of capture antibodies against the toxins was immobilized in microwells and incubated with mixtures of the analytes (ricin, cholera toxin, shiga like toxin 1, and staphylococcal enterotoxin B). Four different QDs were conjugated with detection antibodies specific for one of the toxins. The group demonstrated that all four toxins could be detected by measuring a whole spectrum in each well with subsequent deconvolution of the spectrum. The advantages of QDs for multi-analyte detection compared to organic fluorophores (small Stokes shifts, broad emission bands) were demonstrated with this experiment.

IV.8.3. Photon-Upconversion Nanoparticles

Photon-upconversion nanoparticles (UCNPs) are luminescent nanocrystals that can be excited by NIR light at 980 nm, whereupon the UCNPs emit light with higher energy. This process involves the sequential absorption of two or more photons by the nanoparticle (**Figure 13**).

The brightest known UCNPs today consist of a hexagonal NaYF₄ host lattice, a material that has low phonon energies, minimizing non-radiative relaxation pathways.¹²⁴ The host matrix is doped with Yb³⁺ sensitizer ions that absorb the excitation light and emitting ions like Er³⁺ (red and green emission, **Figure 13**, right) or Tm³⁺ (blue and NIR emission, **Figure 13**, left). The principles of using Yb-Er and Yb-Tm couples reach back to 1966, when François Auzel suggested that energy transfers can occur between excited rare earth metal ions.¹²⁵ It took more than three decades until Heer et al. reported on lanthanide upconversion in a transparent colloidal solution.¹²⁶

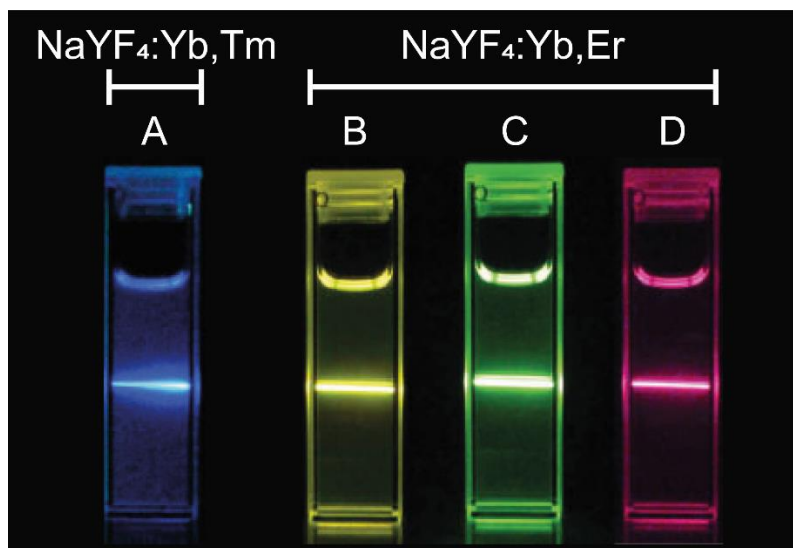


Figure 13: Photographic image of the upconversion luminescence of UCNPs in cyclohexane with excitation at 980 nm. **A)** Blue upconversion luminescence of Tm³⁺-doped UCNPs. **B)** Total upconversion luminescence of Er³⁺-doped UCNPs. **C)** Green upconversion luminescence (red filtered). **D)** Red upconversion luminescence (green filtered). Adapted with permission from John Wiley and Sons: *Advanced Materials*¹²⁷, Copyright 2008.

Any upconversion process can, by nature, never reach a higher quantum yield than 50%. For UCNPs, the highest achievable quantum yield resembles the yield of its bulk material, which lies for NaYF₄:Yb³⁺, Er³⁺, at around 10%.¹²⁸ The quantum efficiency of UCNPs is drastically reduced in aqueous environments. The quenching is caused by non-radiative relaxation pathways between the excited state and vibrational modes of the OH-groups of water (blue curled arrows in **Figure 14**).¹²⁹ To overcome the quenching effect, an inert NaYF₄ shell without emitting ions can be grown around the UCNPs.¹³⁰

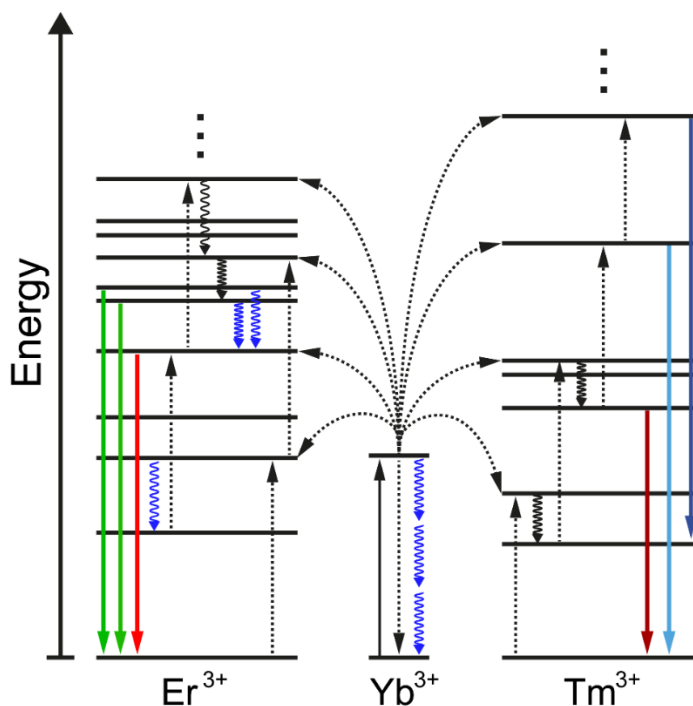


Figure 14: Simplified energy diagram for Er^{3+} -doped UCNPs (left) and Tm^{3+} -doped UCNPs (right). Dashed arrows indicate non-radiative energy transfers. Curled, black arrows represent multiphoton relaxations, and blue curled arrows denote increased multiphoton relaxations caused by vibrations of OH-groups. Solid arrows mark photon absorption (black) or emission (colored).

The generally low quantum yields of UCNPs are compensated by several factors. 1) Each particle consists of many simultaneously sensitizing and emitting ions. 2) UCNPs are extremely photostable, allowing for a powerful laser excitation to enhance the luminescence. 3) The NIR excitation prevents autofluorescence and minimizes light scattering, which enables almost background-free measurements. 4) UCNPs, unlike QDs, do not blink and show a constant emission, this is especially beneficial for imaging applications.

UCNPs can be synthesized in a controlled manner by a high-temperature coprecipitation method.¹³¹ In this method, lanthanide trichloride salts (YCl_3 , YbCl_3 , TmCl_3) in methanol are heated to 160° for 30 min in a mixture of oleic acid and 1-octadecene, cooled down to room temperature and a mixture of NH_4F and NaOH in methanol is added. The methanol is evaporated by heating to 160°C for 30 min, and the temperature is increased to 300°C for 90 min under argon or nitrogen atmosphere. At 300°C the UCNPs undergo a phase transition from cubic α -phase to the hexagonal β -phase. The particles are precipitated with ethanol and washed with methanol and ethanol several times. The purified UCNPs have a hydrophobic surface because a coating of oleic acid is formed around the particles during the synthesis.

For bioanalytical applications like immunoassays, water dispersible particles are required, which can be achieved by replacing the oleic with other surface coatings like PEG,¹³² a silica

shell,¹³³ or forming a polymer around the particles.¹³⁴ Two common methods exist to remove the oleic acid from the particles, a ligand exchange reaction with NOBF₄,¹³⁵ and protonation of oleic acid with subsequent washing.¹³⁶ Phosphonate groups strongly coordinate to lanthanide ions; this can be exploited to immobilize functional linkers onto the UCNP surface.¹³⁶

To specifically detect an analyte, UCNPs can be coupled to a recognition element like an antibody¹³⁷ or aptamer.¹³⁸ A common way to attach biomolecules to the nanoparticles is to modify them with carboxyl groups. UCNPs can be silanized with a carboxy silane, or carboxylated PEG can be used for surface coating. The carboxyl group is transformed into an active ester using EDC/NHS chemistry. Activated carboxyl groups react with amino groups in the side chains of lysine to form an amide bond. Hlaváček et al.¹³⁹ used EDC/NHS chemistry to build a tracer molecule for a competitive ULISA for diclofenac. In a first step, EDC/NHS was used to covalently bind diclofenac to bovine γ -globulin, then silica-coated UCNPs with free carboxyl groups were activated with EDC/NHS, and the diclofenac/bovine γ -globulin was attached. This tracer was used to compete with the free diclofenac for binding sites of a capture antibody. With an increasing amount of free analyte molecules, less of the tracer molecules could bind to the microplate, and the signal decreased. The assay resulted in an LOD of 70 pM for diclofenac.

IV.8.4. Digital Affinity Assays with Nanoparticle Labels

AuNPs were used in a single-particle scattering assay for the detection of the clinical marker molecules PSA, α -fetoprotein (AFP), and carcinoembryonic antigen (CEA). A gold nanoparticle was decorated with a primary capture antibody and immobilized in a flow cell on a microscope coverslip. The analyte was added and captured by the primary antibody, and the detection conjugate, consisting of a silver nanoparticle (AgNP); this was followed by the addition of a primary antibody. The binding of the detection conjugate led to a significantly enhanced scattering intensity, which was detected *via* darkfield microscopy for individual particles. The digital readout resulted in LODs of 3.3 pM for PSA, 5.9 pM for AFP, and 1.7 pM for CEA.¹⁴⁰

A homogeneous immunoassay was developed for CEA using QDs as a label. Two batches of the same kind of QD were coated with different antibodies against CEA. The particles formed immunosandwiches with the analyte and were subsequently immobilized on a microscope coverslip. Because of the small size of the particles below the diffraction limit, it was impossible to separate individual QDs from the immunocomplexes under a fluorescence microscope. The researches exploited the photooxidation of QDs (bleaching) that occurs after a certain irradiation time. The QD-emission was split into a zeroth-order dot (direct transmission) and a first-order streak (diffraction beam) using a diffraction grating in front of

Fundamentals

the detector. During the excitation, an asynchronous photooxidation of the two sandwiched QDs took place that led to a blue shift of the emission wavelength of the first order streak. Because the first order streak only split if two QDs were bound together, the analyte concentration could be determined by counting the number of the split streaks. The digital counting of split first order streaks resulted in an LOD of 6.7 fM for CEA and demonstrated that the same label could be used twice in an optical, homogeneous immunoassay.¹⁴¹

The next chapters will demonstrate the use of UCNPs for highly sensitive immunoassays. Research articles 1 & 2 describe digital sandwich immunoassays for PSA. The third article uses UCNP labels for the immunochemical staining of breast cancer cells.

IV.9. References

1. Nagel, B.; Dellweg, H.; Gierasch, L., Glossary for chemists of terms used in biotechnology (IUPAC Recommendations 1992). *Pure Appl. Chem.* **1992**, *64* (1), 143-168.
2. Van Grieken, R.; De Bruin, M., Nomenclature for radioanalytical chemistry (IUPAC Recommendations 1994). *Pure Appl. Chem.* **1994**, *66* (12), 2513-2526.
3. Engvall, E., Enzyme immunoassay ELISA and EMIT. *Method. Enzymol.* **1980**, *70*, 419-439.
4. Clapp, A. R.; Medintz, I. L.; Mattoussi, H., Förster resonance energy transfer investigations using quantum-dot fluorophores. *Chem. Phys. Chem.* **2006**, *7* (1), 47-57.
5. Yalow, R. S.; Berson, S. A., Assay of plasma insulin in human subjects by immunological methods. *Nature* **1959**, *184* (4699), 1648-1649.
6. Berson, S. A.; Yalow, R. S.; Bauman, A.; Rothschild, M. A.; Newerly, K., Insulin-¹³¹I metabolism in human subjects: demonstration of insulin binding globulin in the circulation of insulin treated subjects. *J. Clin. Invest.* **1956**, *35* (2), 170-190.
7. Wu, A. H., A selected history and future of immunoassay development and applications in clinical chemistry. *Clin. Chim. Acta.* **2006**, *369* (2), 119-124.
8. Engvall, E.; Perlmann, P., Enzyme-linked immunosorbent assay, ELISA: III. Quantitation of specific antibodies by enzyme-labeled anti-immunoglobulin in antigen-coated tubes. *J. Immunol.* **1972**, *109* (1), 129-135.
9. Van Weemen, B.; Schuurs, A., Immunoassay using antigen—enzyme conjugates. *FEBS lett.* **1971**, *15* (3), 232-236.
10. Rubenstein, K. E.; Schneider, R. S.; Ullman, E. F., “Homogeneous” enzyme immunoassay. A new immunochemical technique. *Biochem. Biophys. Res. Co.* **1972**, *47* (4), 846-851.
11. Shugar, D., The measurement of lysozyme activity and the ultra-violet inactivation of lysozyme. *Biochem. Biophys. Acta* **1952**, *8* (C), 302-309.
12. Köhler, G.; Milstein, C., Continuous cultures of fused cells secreting antibody of predefined specificity. *Nature* **1975**, *256* (5517), 495.
13. Cohen, L.; Walt, D. R., Single-molecule arrays for protein and nucleic acid analysis. *Annu. Rev. Anal. Chem.* **2017**, *10*, 345-363.
14. Barletta, J. M.; Edelman, D. C.; Constantine, N. T., Lowering the detection limits of HIV-1 viral load using real-time immuno-PCR for HIV-1 p24 antigen. *Am. J. Clin. Pathol.* **2004**, *122* (1), 20-27.
15. Peltomaa, R.; Benito-Peña, E.; Moreno-Bondi, M. C., Bioinspired recognition elements for mycotoxin sensors. *Anal. Bioanal. Chem.* **2018**, *410* (3), 747-771.
16. Srinivas, P. R.; Kramer, B. S.; Srivastava, S., Trends in biomarker research for cancer detection. *Lancet Oncol.* **2001**, *2* (11), 698-704.

17. Yu, R.-J.; Ying, Y.-L.; Hu, Y.-X.; Gao, R.; Long, Y.-T., Label-free monitoring of single molecule immunoreaction with a nanopipette. *Anal. Chem.* **2017**, *89* (16), 8203-8206.
18. Mandal, S.; Koirala, D.; Selvam, S.; Ghimire, C.; Mao, H., A Molecular Tuning Fork in Single-Molecule Mechanochemical Sensing. *Angew. Chem.* **2015**, *127* (26), 7717-7721.
19. Woof, J.; Russell, M., Structure and function relationships in IgA. *Mucosal Immunol.* **2011**, *4* (6), 590.
20. Edholm, E.-S.; Bengten, E.; Wilson, M., Insights into the function of IgD. *Dev. Comp. Immunol.* **2011**, *35* (12), 1309-1316.
21. Galli, S. J.; Tsai, M., IgE and mast cells in allergic disease. *Nat. Med.* **2012**, *18* (5), 693.
22. Vidarsson, G.; Dekkers, G.; Rispens, T., IgG subclasses and allotypes: from structure to effector functions. *Front. Immunol.* **2014**, *5*, 520.
23. Berg, J. M.; Tymoczko, J. L.; Stryer, L., *Biochemistry*. New York: WH Freeman, **2012**, Print.
24. Maverakis, E.; Kim, K.; Shimoda, M.; Gershwin, M. E.; Patel, F.; Wilken, R.; Raychaudhuri, S.; Ruhaak, L. R.; Lebrilla, C. B., Glycans in the immune system and The Altered Glycan Theory of Autoimmunity: a critical review. *J. Autoimmun.* **2015**, *57*, 1-13.
25. Wang, W.; Singh, S.; Zeng, D. L.; King, K.; Nema, S., Antibody structure, instability, and formulation. *J. Pharm. Sci.* **2007**, *96* (1), 1-26.
26. Lesk, A. M.; Chothia, C., Evolution of proteins formed by β -sheets: II. The core of the immunoglobulin domains. *J. Mol. Biol.* **1982**, *160* (2), 325-342.
27. Janeway, C. A.; Capra, J. D.; Travers, P.; Walport, M., *Immunobiology: the immune system in health and disease*. New York: Garland Science **1999**, Print.
28. Chang, L. L.; Shepherd, D.; Sun, J.; Tang, X. C.; Pikal, M. J., Effect of sorbitol and residual moisture on the stability of lyophilized antibodies: Implications for the mechanism of protein stabilization in the solid state. *J. Pharm. Sci.* **2005**, *94* (7), 1445-1455.
29. Cleland, J. L.; Lam, X.; Kendrick, B.; Yang, J.; Yang, T. h.; Overcashier, D.; Brooks, D.; Hsu, C.; Carpenter, J. F., A specific molar ratio of stabilizer to protein is required for storage stability of a lyophilized monoclonal antibody. *J. Pharm. Sci.* **2001**, *90* (3), 310-321.
30. Raab, M. S.; Podar, K.; Breitkreutz, I.; Richardson, P. G.; Anderson, K. C., Multiple myeloma. *Lancet* **2009**, *374* (9686), 324-339.
31. Ellington, A. D.; Szostak, J. W., In vitro selection of RNA molecules that bind specific ligands. *Nature* **1990**, *346* (6287), 818.

32. The Nobel Prize in Physiology or Medicine 2009, <https://www.nobelprize.org/prizes/medicine/2009/summary/>. (accessed March 30, 2020).
33. Tuerk, C.; Gold, L., Systematic evolution of ligands by exponential enrichment: RNA ligands to bacteriophage T4 DNA polymerase. *Science* **1990**, *249* (4968), 505-510.
34. Lottspeich, F.; Zorbas, H., Bioanalytik. Heidelberg: Spektrum, **1998**, Print.
35. Stoltenburg, R.; Reinemann, C.; Strehlitz, B., FluMag-SELEX as an advantageous method for DNA aptamer selection. *Anal. Bioanal. Chem.* **2005**, *383* (1), 83-91.
36. Setlem, K.; Mondal, B.; Ramlal, S.; Kingston, J., Immuno affinity SELEX for simple, rapid, and cost-effective aptamer enrichment and identification against aflatoxin B1. *Front. Microbiol.* **2016**, *7*, 1909.
37. Stoltenburg, R.; Reinemann, C.; Strehlitz, B., SELEX—a (r) evolutionary method to generate high-affinity nucleic acid ligands. *Biomol. Eng.* **2007**, *24* (4), 381-403.
38. Rotherham, L. S.; Maserumule, C.; Dheda, K.; Theron, J.; Khati, M., Selection and application of ssDNA aptamers to detect active TB from sputum samples. *Plos One* **2012**, *7* (10), e46862.
39. Harada, K.; Frankel, A. D., Identification of two novel arginine binding DNAs. *EMBO J.* **1995**, *14* (23), 5798-5811.
40. Marshall, K. A.; Ellington, A. D., [14] In vitro selection of RNA aptamers. *Method. Enzymol.* **2000**, *318*, 193-214.
41. Vater, A.; Klusmann, S., Turning mirror-image oligonucleotides into drugs: the evolution of Spiegelmer® therapeutics. *Drug Discov.* **2015**, *20* (1), 147-155.
42. Klußmann, S.; Nolte, A.; Bald, R.; Erdmann, V. A.; Fürste, J. P., Mirror-image RNA that binds D-adenosine. *Nat. Biotechnol.* **1996**, *14* (9), 1112.
43. Park, J. H.; Jee, M. H.; Kwon, O. S.; Keum, S. J.; Jang, S. K., Infectivity of hepatitis C virus correlates with the amount of envelope protein E2: development of a new aptamer-based assay system suitable for measuring the infectious titer of HCV. *Virology* **2013**, *439* (1), 13-22.
44. Shui, B.; Tao, D.; Cheng, J.; Mei, Y.; Jaffrezic-Renault, N.; Guo, Z., A novel electrochemical aptamer-antibody sandwich assay for the detection of tau-381 in human serum. *Analyst* **2018**, *143* (15), 3549-3554.
45. Zhu, H.; Zhang, L.; Liu, Y.; Zhou, Y.; Wang, K.; Xie, X.; Song, L.; Wang, D.; Han, C.; Chen, Q., Aptamer-PEG-modified Fe₃O₄@Mn as a novel T1- and T2-dual-model MRI contrast agent targeting hypoxia-induced cancer stem cells. *Sci. Rep.* **2016**, *6*, 39245.
46. Chakravarty, R.; Goel, S.; Cai, W., Nanobody: the “magic bullet” for molecular imaging? *Theranostics* **2014**, *4* (4), 386.
47. Hofmann, H.-P.; Limmer, S.; Hornung, V.; Sprinzl, M., Ni²⁺-binding RNA motifs with an asymmetric purine-rich internal loop and a GA base pair. *RNA* **1997**, *3* (11), 1289-1300.

48. Sefah, K.; Shangguan, D.; Xiong, X.; O'donoghue, M. B.; Tan, W., Development of DNA aptamers using Cell-SELEX. *Nat. Protoc.* **2010**, *5* (6), 1169.
49. Wylie, D. E.; Lu, D.; Carlson, L. D.; Carlson, R.; Babacan, K. F.; Schuster, S. M.; Wagner, F. W., Monoclonal antibodies specific for mercuric ions. *Proc. Natl. Acad. Sci. U.S.A.* **1992**, *89* (9), 4104-4108.
50. Pagratis, N. C.; Bell, C.; Chang, Y.-F.; Jennings, S.; Fitzwater, T.; Jellinek, D.; Dang, C., Potent 2'-amino-, and 2'-fluoro-2'-deoxyribonucleotide RNA inhibitors of keratinocyte growth factor. *Nat. Biotechnol.* **1997**, *15* (1), 68.
51. Abcam, K_D value: a quantitative measurement of antibody affinity. <https://www.abcam.com/primary-antibodies/kd-value-a-quantitative-measurement-of-antibody-affinity>. (accessed March 30. 2020).
52. Pauling, L., A theory of the structure and process of formation of antibodies. *J. Am. Chem. Soc.* **1940**, *62* (10), 2643-2657.
53. Sherrington, D. C., Preparation, structure and morphology of polymer supports. *Chem. Commun.* **1998**, *21*, 2275-2286.
54. Haupt, K.; Mosbach, K., Molecularly imprinted polymers and their use in biomimetic sensors. *Chem. Rev.* **2000**, *100* (7), 2495-2504.
55. Cormack, P.; Haupt, K.; Mosbach, K., Affinity separation: imprint polymers. In *Encyclopedia of separation science*, Amsterdam: Elsevier, **2000**, 288-296, online.
56. Yan, H.; Row, K. H., Molecularly imprinted monolithic stationary phases for liquid chromatographic separation of tryptophan and N-CBZ-phenylalanine enantiomers. *Biotechnol. Bioproc. E.* **2006**, *11* (4), 357-363.
57. Hosoya, K.; Yoshizako, K.; Shirasu, Y.; Kimata, K.; Araki, T.; Tanaka, N.; Haginaka, J., Molecularly imprinted uniform-size polymer-based stationary phase for high-performance liquid chromatography structural contribution of cross-linked polymer network on specific molecular recognition. *J. Chromatogr. A.* **1996**, *728* (1-2), 139-147.
58. Vorderbruggen, M. A.; Wu, K.; Breneman, C. M., Use of cationic aerosol photopolymerization to form silicone microbeads in the presence of molecular templates. *Chem. Mater.* **1996**, *8* (5), 1106-1111.
59. Vlatakis, G.; Andersson, L. I.; Müller, R.; Mosbach, K., Drug assay using antibody mimics made by molecular imprinting. *Nature* **1993**, *361* (6413), 645-647.
60. Zhang, H., Molecularly imprinted nanoparticles for biomedical applications. *Adv. Mater.* **2020**, *32* (3), 1806328.
61. Shutov, R. V.; Guerreiro, A.; Moczko, E.; de Vargas-Sansalvador, I. P.; Chianella, I.; Whitcombe, M. J.; Piletsky, S. A., Introducing MINA—the molecularly imprinted nanoparticle assay. *Small* **2014**, *10* (6), 1086-1089.
62. Xing, R.; Wen, Y.; Dong, Y.; Wang, Y.; Zhang, Q.; Liu, Z., Dual Molecularly Imprinted Polymer-Based Plasmonic Immunosandwich Assay for the Specific and Sensitive Detection of Protein Biomarkers. *Anal. Chem.* **2019**, *91* (15), 9993-10000.

63. Sellergren, B.; Hall, A. J., Molecularly imprinted polymers. In: *Supramolecular chemistry: from molecules to nanomaterials*, Wiley, **2012**, online.
64. Zhou, T.; Ding, L.; Che, G.; Jiang, W.; Sang, L., Recent advances and trends of molecularly imprinted polymers for specific recognition in aqueous matrix: preparation and application in sample pretreatment. *TRAC Trend. in Anal. Chem.* **2019**, *114*, 11-28.
65. Cui, F.; Zhou, Z.; Zhou, H. S., Molecularly Imprinted Polymers and Surface Imprinted Polymers Based Electrochemical Biosensor for Infectious Diseases. *Sensors*, **2020**, *20* (4), 996.
66. Schuurs, A.; Van Weemen, B., Enzyme-immunoassay. *Clin. Chim. Acta* **1977**, *81* (1), 1-40.
67. Brill, A. S.; Weinryb, I., Reactions of horseradish peroxidase with azide. Evidence for a methionine residue at the active site. *Biochemistry* **1967**, *6* (11), 3528-3535.
68. Kreuzer, M.; O'Sullivan, C.; Guilbault, G., Alkaline phosphatase as a label for immunoassay using amperometric detection with a variety of substrates and an optimal buffer system. *Anal. Chim. Acta.* **1999**, *393* (1-3), 95-102.
69. Sigma Aldrich, Product Information HRP, <https://www.sigmaaldrich.com/content/dam/sigmaaldrich/docs/Sigma/Datasheet/2/p8375dat.pdf>. (accessed March 30. 2020).
70. Adalberto, P. R.; Massabni, A. C.; Carmona, E. C.; GOULART, A. J.; Marques, D. P.; Monti, R., Effect of divalent metal ions on the activity and stability of β -galactosidase isolated from *Kluyveromyces lactis*. *Rev. Ciên. Farm. Básica Apl.* **2010**, *31* (3), 143-150.
71. Tenu, J. P.; Viratell.Om; Garnier, J.; Yon, J., Ph Dependence of Activity of Beta-Galactosidase from *Escherichia-Coli*. *Eur. J. Biochem.* **1971**, *20* (3), 363-370.
72. Chandler, H.; Cox, J.; Healey, K.; MacGregor, A.; Premier, R.; Hurrell, J., An investigation of the use of urease-antibody conjugates in enzyme immunoassays. *J. Immunol. Method.* **1982**, *53* (2), 187-194.
73. Wilchek, M.; Bayer, E. A., [2] Introduction to avidin-biotin technology. In *Method. Enzymol.*, Amsterdam: Elsevier: **1990**; *184*, 5-13, online.
74. Liebherr, R. B.; Hutterer, A.; Mickert, M. J.; Vogl, F. C.; Beutner, A.; Lechner, A.; Hummel, H.; Gorris, H. H., Three-in-one enzyme assay based on single molecule detection in femtoliter arrays. *Anal. Bioanal. Chem.* **2015**, *407* (24), 7443-7452.
75. Liebherr, R. B.; Renner, M.; Gorris, H. H., A Single Molecule Perspective on the Functional Diversity of in Vitro Evolved beta-Glucuronidase. *J. Am. Chem. Soc.* **2014**, *136* (16), 5949-5955.
76. Gorris, H. H.; Blicharz, T. M.; Walt, D. R., Optical-fiber bundles. *FEBS J.* **2007**, *274* (21), 5462-5470.
77. Rissin, D. M.; Kan, C. W.; Campbell, T. G.; Howes, S. C.; Fournier, D. R.; Song, L.; Piech, T.; Patel, P. P.; Chang, L.; Rivnak, A. J.; Ferrell, E. P.; Randall, J. D.;

- Provuncher, G. K.; Walt, D. R.; Duffy, D. C., Single-molecule enzyme-linked immunosorbent assay detects serum proteins at subfemtomolar concentrations. *Nat. Biotechnol.* **2010**, *28* (6), 595-599.
78. Chang, L.; Song, L.; Fournier, D. R.; Kan, C. W.; Patel, P. P.; Ferrell, E. P.; Pink, B. A.; Minnehan, K. A.; Hanlon, D. W.; Duffy, D. C., Simple diffusion-constrained immunoassay for p24 protein with the sensitivity of nucleic acid amplification for detecting acute HIV infection. *J. Virol. Method.* **2013**, *188* (1-2), 153-160.
79. Warren, A. D.; Gaylord, S. T.; Ngan, K. C.; Dumont Milutinovic, M.; Kwong, G. A.; Bhatia, S. N.; Walt, D. R., Disease detection by ultrasensitive quantification of microdosed synthetic urinary biomarkers. *J. Am. Chem. Soc.* **2014**, *136* (39), 13709-13714.
80. Quanterix, Simoa NF-light Advantage Kit, https://www.quanterix.com/sites/default/files/assays/Simoa_NF-Light_Data_Sheet_HD-1_HD-X_Rev05.pdf. (accessed March 30. 2020).
81. Shahim, P.; Gren, M.; Liman, V.; Andreasson, U.; Norgren, N.; Tegner, Y.; Mattsson, N.; Andreasen, N.; Öst, M.; Zetterberg, H., Serum neurofilament light protein predicts clinical outcome in traumatic brain injury. *Sci. Rep.* **2016**, *6*, 36791.
82. Coons, A. H., The demonstration of pneumococcal antigen in tissues by the use of fluorescent antibody. *J. Immunol.* **1942**, *45*, 159.
83. Dandliker, W.; Feigen, G., Quantification of the antigen-antibody reaction by the polarization of fluorescence. *Biochem. Biophys. Res. Commun.* **1961**, *5* (4), 299-304.
84. Smith, J.; Osikowicz, G., Abbott AxSYM random and continuous access immunoassay system for improved workflow in the clinical laboratory. *Clin. Chem.* **1993**, *39* (10), 2063-2069.
85. Siitari, H.; Hemmilä, I.; Soini, E.; Lövgren, T.; Koistinen, V., Detection of hepatitis B surface antigen using time-resolved fluoroimmunoassay. *Nature* **1983**, *301* (5897), 258-260.
86. Bryden, C. C.; Reilley, C. N., Europium luminescence lifetimes and spectra for evaluation of 11 europium complexes as aqueous shift reagents for nuclear magnetic resonance spectrometry. *Anal. Chem.* **1982**, *54* (4), 610-615.
87. Elliott, C. T.; Francis, K. S.; McCaughey, W. J., Investigation of dissociation enhanced lanthanide fluoroimmunoassay as an alternative screening test for veterinary drug residues. *Analyst* **1994**, *119* (12), 2565-2569.
88. Perkin Elmer, DELFIA immunoassays, <https://www.perkinelmer.com/de/lab-products-and-services/application-support-knowledgebase/delfia/delfia-immunoassays.html>. (accessed March 30. 2020).
89. Cowans, N. J.; Stamatopoulou, A.; Hellström, J.; Mäkelä, M. M.; Spencer, K., PAPP-A and free β -hCG stability in first trimester serum using PerkinElmer AutoDELFI[®] and DELFI[®] Xpress systems. *Prenat. Diagn.: Published in Affiliation With the International Society for Prenatal Diagnosis* **2010**, *30* (2), 127-132.

90. Sano, T.; Smith, C. L.; Cantor, C. R., Immuno-PCR: very sensitive antigen detection by means of specific antibody-DNA conjugates. *Science* **1992**, *258* (5079), 120-122.
91. Reinstein, L.; Gluckman, G.; Amols, H., Predicting optical densitometer response as a function of light source characteristics for radiochromic film dosimetry. *Med. Phys.* **1997**, *24* (12), 1935-1942.
92. Fish, K. N., Total internal reflection fluorescence (TIRF) microscopy. *Curr. Protoc. Cytom.* **2009**, *50* (1), 12-18.
93. Weng, R.; Lou, S.; Li, L.; Zhang, Y.; Qiu, J.; Su, X.; Qian, Y.; Walter, N. G., Single-Molecule Kinetic Fingerprinting for the Ultrasensitive Detection of Small Molecules with Aptasensors. *Anal. Chem.* **2018**, *91* (2), 1424-1431.
94. Merck, Single Molecule Counting Erenna Instrument, Software and Kits, <https://www.merckmillipore.com/DE/de/life-science-research/protein-detection-quantification/Immunoassay-Platform-Solutions/single-molecule-counting-immunoassay-technology/SMC-Erenna-Instrument-Software-and-Kits/VS.b.qB.N.UAAAFfn7lc20.J.nav>. (accessed March 30. 2020).
95. Todd, J.; Freese, B.; Lu, A.; Held, D.; Morey, J.; Livingston, R.; Goix, P., Ultrasensitive flow-based immunoassays using single-molecule counting. *Clin. Chem.* **2007**, *53* (11), 1990-1995.
96. Esparza, T. J.; Zhao, H.; Cirrito, J. R.; Cairns, N. J.; Bateman, R. J.; Holtzman, D. M.; Brody, D. L., Amyloid-beta oligomerization in Alzheimer dementia versus high-pathology controls. *Ann. Neurol.* **2013**, *73* (1), 104-119.
97. Wild, E. J.; Boggio, R.; Langbehn, D.; Robertson, N.; Haider, S.; Miller, J. R.; Zetterberg, H.; Leavitt, B. R.; Kuhn, R.; Tabrizi, S. J., Quantification of mutant huntingtin protein in cerebrospinal fluid from Huntington's disease patients. *J. Clin. Invest.* **2015**, *125* (5), 1979-1986.
98. Ries, J.; Schwille, P., Fluorescence correlation spectroscopy. *BioEssays* **2012**, *34* (5), 361-368.
99. Zappa, F.; Tisa, S.; Tosi, A.; Cova, S., Principles and features of single-photon avalanche diode arrays. *Sensor. Actuat. A-Phys.* **2007**, *140* (1), 103-112.
100. Petrov, E.; Schwille, P., State of the art and novel trends in fluorescence correlation spectroscopy. In *Standardization and quality assurance in fluorescence measurements II*, Wiesbaden: Springer: **2008**, 145-197, print.
101. Chatterjee, M.; Nöding, B.; Willemsse, E. A.; Koel-Simmelink, M. J.; van der Flier, W. M.; Schild, D.; Teunissen, C. E., Detection of contactin-2 in cerebrospinal fluid (CSF) of patients with Alzheimer's disease using Fluorescence Correlation Spectroscopy (FCS). *Clin. Biochem.* **2017**, *50* (18), 1061-1066.
102. Miller, A. E.; Hollars, C. W.; Lane, S. M.; Laurence, T. A., Fluorescence cross-correlation spectroscopy as a universal method for protein detection with low false positives. *Anal. Chem.* **2009**, *81* (14), 5614-5622.

103. Farka, Z.; Juřík, T.; Kovář, D.; Trnková, L.; Skládal, P., Nanoparticle-based immunochemical biosensors and assays: recent advances and challenges. *Chem. Rev.* **2017**, *117* (15), 9973-10042.
104. Tkachenko, A. G.; Xie, H.; Liu, Y.; Coleman, D.; Ryan, J.; Glomm, W. R.; Shipton, M. K.; Franzen, S.; Feldheim, D. L., Cellular trajectories of peptide-modified gold particle complexes: comparison of nuclear localization signals and peptide transduction domains. *Bioconjugate Chem.* **2004**, *15* (3), 482-490.
105. Li, X.; Wei, L.; Pan, L.; Yi, Z.; Wang, X.; Ye, Z.; Xiao, L.; Li, H.-W.; Wang, J., Homogeneous immunosorbent assay based on single-particle enumeration using upconversion nanoparticles for the sensitive detection of cancer biomarkers. *Anal. Chem.* **2018**, *90* (7), 4807-4814.
106. Tyagi, H.; Kushwaha, A.; Kumar, A.; Aslam, M., A facile pH controlled citrate-based reduction method for gold nanoparticle synthesis at room temperature. *Nanoscale Res. Lett.* **2016**, *11* (1), 362.
107. Sigma Aldrich, Gold Nanoparticles: Properties and Applications, <https://www.sigmaaldrich.com/technical-documents/articles/materials-science/nanomaterials/gold-nanoparticles.html>. (accessed March 30. 2020).
108. He, H.; Xie, C.; Ren, J., Nonbleaching fluorescence of gold nanoparticles and its applications in cancer cell imaging. *Anal. Chem.* **2008**, *80* (15), 5951-5957.
109. Boyer, D.; Tamarat, P.; Maali, A.; Lounis, B.; Orrit, M., Photothermal imaging of nanometer-sized metal particles among scatterers. *Science* **2002**, *297* (5584), 1160-1163.
110. Barnes, W. L.; Dereux, A.; Ebbesen, T. W., Surface plasmon subwavelength optics. *Nature* **2003**, *424* (6950), 824-830.
111. Sperling, R. A.; Gil, P. R.; Zhang, F.; Zanella, M.; Parak, W. J., Biological applications of gold nanoparticles. *Chem. Soc. Rev.* **2008**, *37* (9), 1896-1908.
112. Kneipp, K.; Kneipp, H.; Itzkan, I.; Dasari, R. R.; Feld, M. S., Ultrasensitive chemical analysis by Raman spectroscopy. *Chem. Rev.* **1999**, *99* (10), 2957-2976.
113. Fu, X.; Wang, Y.; Liu, Y.; Liu, H.; Fu, L.; Wen, J.; Li, J.; Wei, P.; Chen, L., A graphene oxide/gold nanoparticle-based amplification method for SERS immunoassay of cardiac troponin I. *Analyst* **2019**, *144* (5), 1582-1589.
114. Mirkin, C. A.; Letsinger, R. L.; Mucic, R. C.; Storhoff, J. J., A DNA-based method for rationally assembling nanoparticles into macroscopic materials. *Nature* **1996**, *382* (6592), 607-609.
115. de la Rica, R.; Stevens, M. M., Plasmonic ELISA for the ultrasensitive detection of disease biomarkers with the naked eye. *Nat. Nanotechnol.* **2012**, *7*, 821.
116. Nanocrystals in their prime. *Nat. Nanotechnol.* **2014**, *9* (5), 325-325.
117. Ekimov, A. I.; Efros, A. L.; Onushchenko, A. A., Quantum size effect in semiconductor microcrystals. *Solid State Commun.* **1985**, *56* (11), 921-924.

118. Medintz, I. L.; Uyeda, H. T.; Goldman, E. R.; Mattoussi, H., Quantum dot bioconjugates for imaging, labelling and sensing. *Nat. Mater.* **2005**, *4*, 435.
119. Murray, C.; Norris, D. J.; Bawendi, M. G., Synthesis and characterization of nearly monodisperse CdE (E= sulfur, selenium, tellurium) semiconductor nanocrystallites. *J. Am. Chem. Soc.* **1993**, *115* (19), 8706-8715.
120. Merck, Quantum Dots, <https://www.sigmaaldrich.com/technical-documents/articles/materials-science/nanomaterials/quantum-dots.html#ref>. (accessed March 30. 2020).
121. Xu, H.; Sha, M. Y.; Wong, E. Y.; Uphoff, J.; Xu, Y.; Treadway, J. A.; Truong, A.; O'Brien, E.; Asquith, S.; Stubbins, M., Multiplexed SNP genotyping using the Qbead™ system: a quantum dot-encoded microsphere-based assay. *Nucleic Acids Res.* **2003**, *31* (8), e43-e43.
122. Kerman, K.; Endo, T.; Tsukamoto, M.; Chikae, M.; Takamura, Y.; Tamiya, E., Quantum dot-based immunosensor for the detection of prostate-specific antigen using fluorescence microscopy. *Talanta* **2007**, *71* (4), 1494-1499.
123. Goldman, E. R.; Clapp, A. R.; Anderson, G. P.; Uyeda, H. T.; Mauro, J. M.; Medintz, I. L.; Mattoussi, H., Multiplexed toxin analysis using four colors of quantum dot fluororeagents. *Anal. Chem.* **2004**, *76* (3), 684-688.
124. Li, Z.; Zhang, Y.; La, H.; Zhu, R.; El-Banna, G.; Wei, Y.; Han, G., Upconverting NIR photons for bioimaging. *Nanomaterials* **2015**, *5* (4), 2148-2168.
125. Auzel, F., Upconversion and anti-stokes processes with f and d ions in solids. *Chem. Rev.* **2004**, *104* (1), 139-174.
126. Heer, S.; Lehmann, O.; Haase, M.; Gudel, H. U., Blue, green, and red upconversion emission from lanthanide-doped LuPO₄ and YbPO₄ nanocrystals in a transparent colloidal solution. *Angew. Chem. Int. Ed.* **2003**, *42* (27), 3179-3182.
127. Li, Z.; Zhang, Y.; Jiang, S., Multicolor core/shell-structured upconversion fluorescent nanoparticles. *Adv. Mater.* **2008**, *20* (24), 4765-4769.
128. Christian, H.; Lisa, K.; Florian, F.; Bettina, G.; Christian, W.; Ute, R.-G.; Markus, H., NaYF₄:Yb,Er/NaYF₄ Core/Shell Nanocrystals with High Upconversion Luminescence Quantum Yield. *Angew. Chem. Int. Ed.* **2018**, *57* (28), 8765-8769.
129. Arppe, R.; Hyppänen, I.; Perälä, N.; Peltomaa, R.; Kaiser, M.; Würth, C.; Christ, S.; Resch-Genger, U.; Schäferling, M.; Soukka, T., Quenching of the upconversion luminescence of NaYF₄: Yb³⁺, Er³⁺ and NaYF₄: Yb³⁺, Tm³⁺ nanophosphors by water: the role of the sensitizer Yb³⁺ in non-radiative relaxation. *Nanoscale* **2015**, *7* (27), 11746-11757.
130. Chen, X.; Peng, D.; Ju, Q.; Wang, F., Photon upconversion in core-shell nanoparticles. *Chem. Soc. Rev.* **2015**, *44* (6), 1318-1330.
131. Wang, F.; Han, Y.; Lim, C. S.; Lu, Y.; Wang, J.; Xu, J.; Chen, H.; Zhang, C.; Hong, M.; Liu, X., Simultaneous phase and size control of upconversion nanocrystals through lanthanide doping. *Nature* **2010**, *463* (7284), 1061-1065.

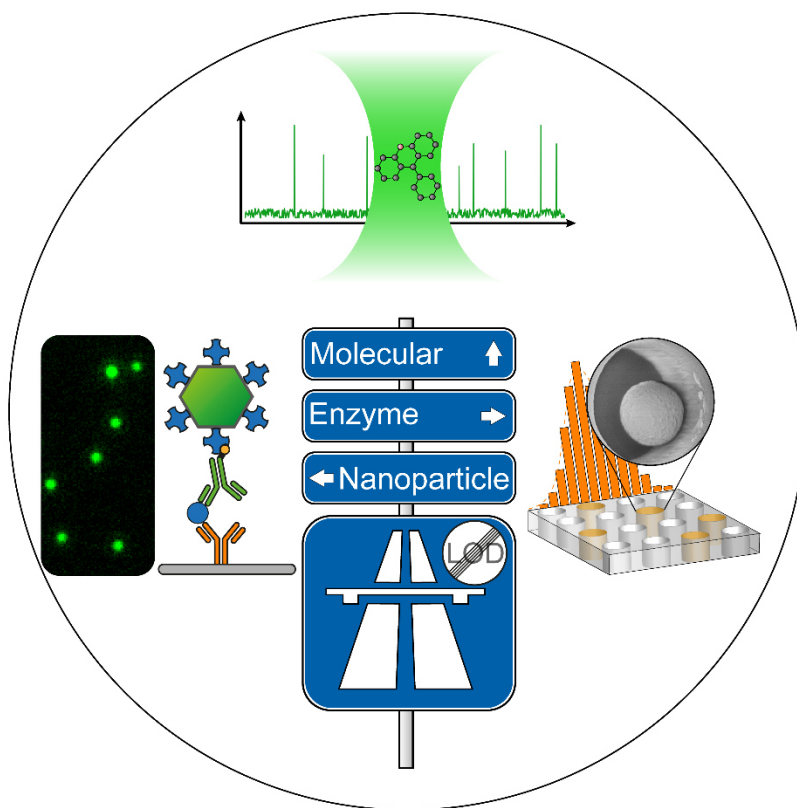
132. Mickert, M. J.; Farka, Z. k.; Kostiv, U.; Hlaváček, A. n.; Horák, D.; Skládal, P.; Gorris, H. H., Measurement of Sub-femtomolar Concentrations of Prostate-Specific Antigen through Single-Molecule Counting with an Upconversion-Linked Immunosorbent Assay. *Anal. Chem.* **2019**, *91* (15), 9435-9441.
133. Farka, Z.; Mickert, M. J.; Hlavacek, A.; Skladal, P.; Gorris, H. H., Single Molecule Upconversion-Linked Immunosorbent Assay with Extended Dynamic Range for the Sensitive Detection of Diagnostic Biomarkers. *Anal. Chem.* **2017**, *89* (21), 11825-11830.
134. Xiong, L.; Yang, T.; Yang, Y.; Xu, C.; Li, F., Long-term in vivo biodistribution imaging and toxicity of polyacrylic acid-coated upconversion nanophosphors. *Biomater.* **2010**, *31* (27), 7078-7085.
135. Wilhelm, S.; Kaiser, M.; Würth, C.; Heiland, J.; Carrillo-Carrion, C.; Muhr, V.; Wolfbeis, O. S.; Parak, W. J.; Resch-Genger, U.; Hirsch, T., Water dispersible upconverting nanoparticles: effects of surface modification on their luminescence and colloidal stability. *Nanoscale* **2015**, *7* (4), 1403-1410.
136. Kostiv, U.; Lobaz, V.; Kucka, J.; Svec, P.; Sedlacek, O.; Hruby, M.; Janouskova, O.; Francova, P.; Kolarova, V.; Sefc, L.; Horak, D., A simple neridronate-based surface coating strategy for upconversion nanoparticles: highly colloidally stable I-125-radiolabeled NaYF₄:Yb³⁺/Er³⁺@PEG nanoparticles for multimodal in vivo tissue imaging. *Nanoscale* **2017**, *9* (43), 16680-16688.
137. Wang, M.; Mi, C.-C.; Wang, W.-X.; Liu, C.-H.; Wu, Y.-F.; Xu, Z.-R.; Mao, C.-B.; Xu, S.-K., Immunolabeling and NIR-excited fluorescent imaging of HeLa cells by using NaYF₄: Yb, Er upconversion nanoparticles. *ACS Nano* **2009**, *3* (6), 1580-1586.
138. Wang, Y.; Bao, L.; Liu, Z.; Pang, D.-W., Aptamer biosensor based on fluorescence resonance energy transfer from upconverting phosphors to carbon nanoparticles for thrombin detection in human plasma. *Anal. Chem.* **2011**, *83* (21), 8130-8137.
139. Hlaváček, A.; Peterek, M.; Farka, Z.; Mickert, M. J.; Prechtel, L.; Knopp, D.; Gorris, H. H., Rapid single-step upconversion-linked immunosorbent assay for diclofenac. *Microchim. Acta* **2017**, *184* (10), 4159-4165.
140. Poon, C.-Y.; Wei, L.; Xu, Y.; Chen, B.; Xiao, L.; Li, H.-W., Quantification of cancer biomarkers in serum using scattering-based quantitative single particle intensity measurement with a dark-field microscope. *Anal. Chem.* **2016**, *88* (17), 8849-8856.
141. Liu, X.; Huang, C.; Dong, X.; Liang, A.; Zhang, Y.; Zhang, Q.; Wang, Q.; Gai, H., Asynchrony of spectral blue-shifts of quantum dot based digital homogeneous immunoassay. *Chem. Commun.* **2018**, *54* (93), 13103-13106.

V. Review Article 1

Advances in Optical Single-Molecule Detection: En Route to Supersensitive Bioaffinity Assays

Zdeněk Farka,* Matthias J. Mickert,* Matěj Pastucha, Zuzana Mikušová, Petr Skládal, Hans H. Gorris

* Zdeněk Farka, and Matthias J. Mickert contributed equally to the review.



This Chapter has been published, text and figures reprinted with permission from Wiley: *Angewandte Chemie International Edition*¹, Copyright 2020.

¹Farka Z., Mickert M. J.,* Pastucha M., Mikušová Z., Skládal P., Gorris H. H., Advances on Optical Single-Molecule Detection: En Route to Supersensitive Bioaffinity Assays, *Angew. Chem. Int. Ed.* **2020**, online, DOI: 10.1002/anie.201913924.

V.1. Abstract

The ability to detect low concentrations of analytes and in particular low-abundance biomarkers is of fundamental importance, e.g., for early-stage disease diagnosis. The prospect of reaching the ultimate limit of detection has driven the development of single-molecule bioaffinity assays. While many review articles have highlighted the opportunities of single-molecule technologies for analytical and diagnostic applications, they are not as widespread in real-world applications as one should expect. This review provides a theoretical background on single-molecule—or better digital—assays to critically assess their potential compared to traditional analog assays. Selected examples from the literature include bioaffinity assays for the detection of biomolecules such as DNA, proteins, and viruses. The structure of the review highlights the versatility of optical single-molecule labeling techniques, including enzymatic amplification, molecular labels and innovative nanomaterials.

V.2. Introduction

The ability to detect individual molecules—at first sight—holds the promise to reach the ultimate sensitivity. Thus, it is not surprising to see a surge in the number and variety of single-molecule approaches. While there have been many review articles on the obvious advantages of single-molecule fluorescence spectroscopy in the field of biophysics,¹ more recent reviews have discussed the potential and limitation of single-molecule applications for analytical chemistry.² Our review is focused on single-molecule bioaffinity assays and does not cover similar techniques for fundamental biophysical or biomolecular research. Furthermore, it was necessary to limit the review to optical single-molecule techniques. Other emerging single-molecule applications of electrochemical³ and force-based techniques⁴ can be found elsewhere. As the labeling technique is the key element for the ability to detect a single analyte target, the review structure follows different types of optical detection labels. We have also included illustrative examples of label-free optical techniques reported for single-molecule assays.⁵

Most bioaffinity techniques rely on antibodies, though aptamers or molecularly imprinted polymers (MIPs)⁶ have also been used to specifically bind and capture an analyte of interest. Antibodies can be generated with high specificity against almost any analyte. Only the affinity ceiling limits their binding constant to approximately 10^{10} M^{-1} ,⁷ which is much lower compared to (strept)avidin-biotin binding (10^{14} M^{-1}).⁸ Since antibodies have a rather large size, cameloid antibodies that consist only of a single binding site have attracted some attention. The advantage of aptamers is the easy large-scale production, whereas MIPs stand out for their high chemical stability. MIPs are especially useful for the detection of small molecules with a rigid

structure. More flexible analytes such as proteins, however, seem less suitable for the specific detection by MIPs.

For detecting the binding event, two approaches can be distinguished: (1) In label-free assays, the binding of the analyte to the detection element results in a signal change that can be directly measured. (2) In the so-called sandwich format, a second affinity reagent, which carries a signal-generating label, binds to the analyte. As a detection label can strongly amplify the signal, this approach is more amenable for implementing single-molecule assays. The first immunoassays used radioactive labels,⁹ but enzyme labels have gradually replaced radionuclides for safety reasons and because each enzyme label generates thousands of measurable product molecules (intrinsic signal amplification step). The enzyme-linked immunosorbent assay (ELISA) is still considered as the gold standard for the quantitative measurement of various analytes ranging from clinical diagnosis to environmental applications not the least because it is relatively easy to use.

Over the last 60 years, the development of immunoassays has been mainly driven by making measurements more sensitive, specific and reproducible. While conventional ELISAs can measure picomolar concentrations of analytes, higher sensitivities are required because few molecules of toxins can be harmful,¹⁰ individual pathogens can initiate an infectious disease,¹¹ and trace amounts of a cancer marker indicate the beginning of a malignant transformation.¹² Additionally, the development of more sensitive immunoassays is essential for the discovery of new potential biomarkers that are not accessible using current diagnostic tests.¹³

A conventional ELISA is performed in a laboratory and requires several washing steps and relatively long incubation times. Thus, the second line of immunoassay development has aimed at a faster throughput using lower sample volumes, and assays that can be performed directly at the site of sample collection (on-site testing), for example, at the bedside for diagnostic tests,¹⁴ or in the field for environmental and food products applications. In diagnostics, such assays are commonly known as point-of-care (POC) tests.¹⁵ Minimally invasive sample collection methods, e.g. from urine or saliva, and no washing steps are preferred to maintain the user-friendliness of POC tests. The most famous antibody-based POC test is the home pregnancy test, a very successful example of a lateral flow assay first described in the 1980s.¹⁶ The wide acceptance and user-friendliness is a precondition for POC methods to become a cornerstone in the predictive, preventive, personalized and participatory medicine, commonly termed P4 medicine.¹⁷

The family of bioaffinity assays, in particular immunoassays, can be subdivided depending on the detection label as shown in **Figure 1**. (1) Enzyme labels represent the central branch and continue to be the most common detection route. (2) Fluorescent molecular labels are in

principal easier to implement because the detection antibody is directly labeled with a fluorescent label and no enzymatic amplification step is necessary. The simplest form, the fluorescence immunoassay (FIA), however, is limited by background fluorescence without the advantage of enzymatic amplification. In addition to the direct intensity-based fluorescence detection, this scheme was adapted for signal amplification (e.g. by Immuno PCR) or to develop homogeneous assays using fluorescence polarization. Nevertheless, the non-zero background of fluorescence remains. A decisive breakthrough was the development of time-resolved (TR) detection by employing lanthanide-based labels that display a long lifetime (microseconds) compared to organic fluorophores (nanoseconds).¹⁸ In a time-gated approach, after luminescence excitation, the signal acquisition is delayed by a few microseconds to let the autofluorescence signal decay, and only the specific signal of the lanthanide is recorded. The TR-FIA is a background-free optical detection method that, however, needs a more sophisticated instrumental setup. The DELFIA (dissociation-enhanced lanthanide fluorescent immunoassay) technology is the most prominent TR-FIA system on the market.¹⁹

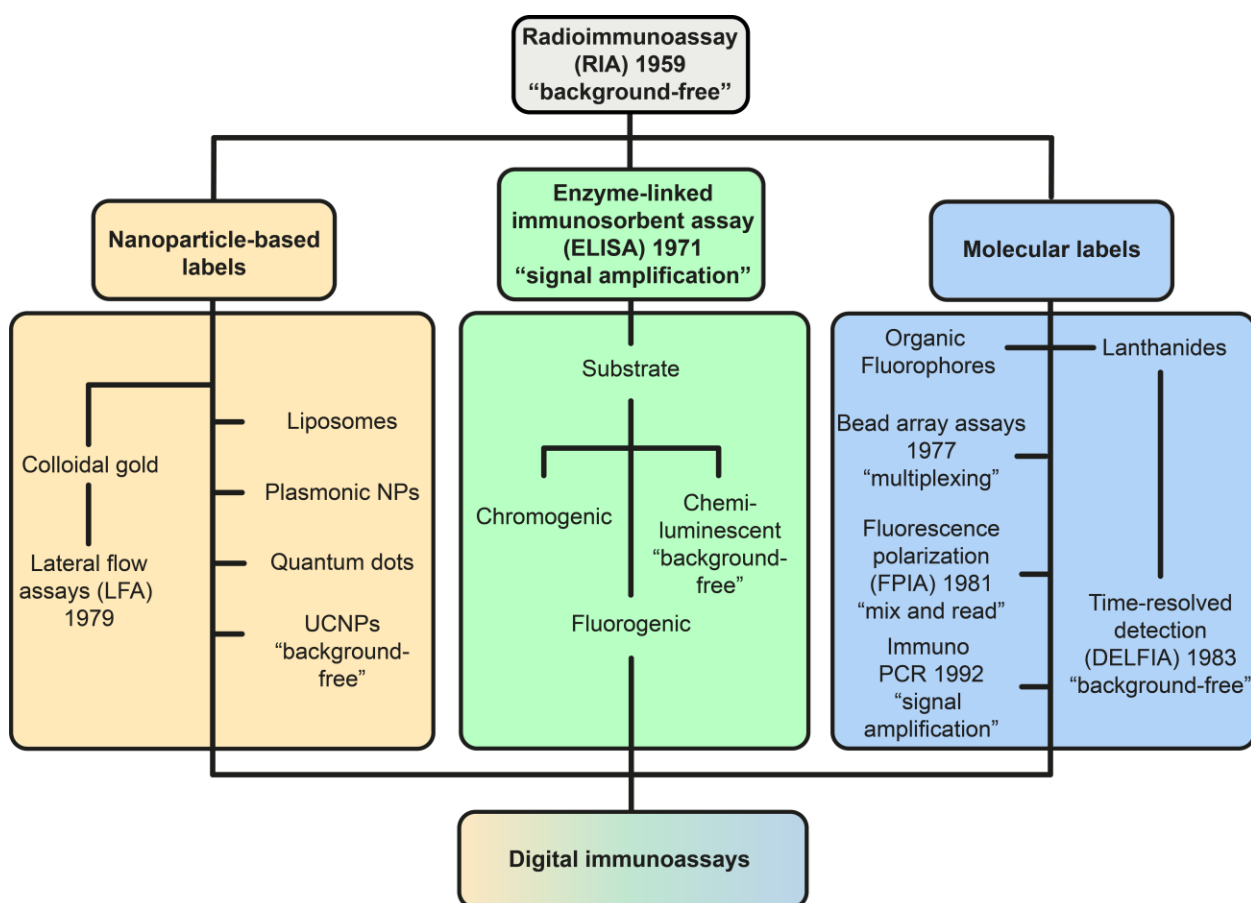


Figure 1: Progress of immunoassay development using optical detection schemes towards single-molecule detection. Radioisotopes were replaced by labels based on enzymes, fluorescent molecules and nanoparticles. By choosing an appropriate readout method, all these labels can be exploited for measurement at the single-molecule level.

Nanoparticles (NP) currently constitute the most rapidly branching labeling strategy for immunoassays.²⁰ Colloidal gold has been used for the readout of lateral flow assays (LFA). Due to their plasmonic properties, gold nanoparticles (Au NPs) strongly absorb and scatter light such that a direct color read-out by eye is possible, and the user is able to make a yes/no decision. In the meantime, the use of NPs in immuno- and other bioaffinity assays has experienced a fast growth as a result of concurrent progress in nanomaterials research. Plasmonic NPs are now in widespread use, but also other NPs and nanocomposites have been designed that enable a convenient optical readout. For example, quantum dots (QDs) are a better alternative for organic fluorophores because they are more photostable and brighter, which is an important feature for single-molecule applications. Photon-upconversion nanoparticles (UCNPs) are another emerging class of labels that can be excited by near-infrared light and emit shorter-wavelength light. The anti-Stokes emission prevents autofluorescence and light scattering and thus allows for an optical readout without background interference.²¹ The background-free detection renders UCNPs an excellent candidate for single-molecule applications.²² Nanocontainers such as liposomes can be filled with large numbers of fluorophores for a strong signal generation. In contrast to enzyme labels that generate the fluorophores *in situ*, the encapsulated fluorophores are released on demand from the nanocontainer to avoid self-quenching inside the confined environment.²³ There are also mixed detection schemes, e.g., in the form of electrochemiluminescence that generates a stronger signal without background.

All three branches shown in **Figure 1** have now blossomed into single-molecule assays as a consequence of innovative assay designs as well as advances in instrumental techniques, detector sensitivities and software capabilities. In simple terms, single-molecule assays can thus be considered as the result of driving conventional assays to the highest sensitivity either by increasing the specific signal to very high levels or by background reduction. Therefore, any standard analytical method can, in principle, reach “single-molecule sensitivity” but background interference such as matrix effects, readout noise or non-specific binding typically prevents it.

It is furthermore essential to understand that the ability to detect a single molecule is not synonymous with the most sensitive analytical assay. For example, some immunoassays from the pre-single-molecule era actually had higher sensitivities than current single-molecule assays.²⁴ If we shift our attention from the detection of a single molecule as the “ultimate” sensitivity to the distinct readout mode, however, it becomes clear that single-molecule detection is a unique and powerful tool for background reduction. Since the signal of a single detection label can be reliably distinguished from the background noise of the instrument and

reagents, the measurement is completely independent of background fluctuations. Thus, the term “digital assay” (as opposed to a conventional “analog assay”) is a much better description of the advantages conferred by single-molecule detection in analytical chemistry. The digital readout, in turn, makes the measurement more robust and thus indirectly leads to lower detection limits.

The signal-to-noise (S/N) ratio determines whether a single molecule can be detected or not. The strength of the specific optical signal depends on the type of label and can be strongly amplified, as discussed in the next chapters. In a digital assay, however, each detectable response is derived from a single analyte molecule, and thus the specific signal strength is ultimately fixed. The only option to assure single-molecule detection is the reduction of the background signal, which decreases with the detection volume. This problem has been extensively discussed for fluorescence spectroscopy, one of the earliest and most important methods for single-molecule detection, but similar considerations also hold for non-fluorescent single-molecule detection methods. Fluorescent molecules are capable of generating a high signal because each fluorophore can emit up to a million photons before it finally photobleaches. Fluorescence excitation, however, also leads to an optical background signal due to autofluorescence and light scattering.²⁵ In order to observe a single fluorescent molecule, it is essential to reduce the detection volume to a femtoliter (fL) volume, commonly by using confocal microscopy, fluorescence correlation spectroscopy (FCS) or total internal reflection microscopy (TIRF).

The requirement for a very small detection volume is associated with two closely related problems that must be addressed in order to achieve higher sensitivity with digital assays. The first problem is analyte sampling. At very low analyte concentrations, there are not enough molecules present in an analyte sample to reach the detection volume by diffusion on a reasonable time scale. For example, it was estimated that it takes on average more than ten minutes for a molecule present in a concentration of 1 fM to reach a detection volume of 10 fL by diffusion.²⁶ Stochastic fluctuations are the second problem.²⁷ At low analyte concentrations, a small observation volume is randomly at one time occupied by a single analyte molecule and, at another time, empty. The so-called Poisson noise (\sqrt{n}/n) depends on the number of counted events (n) and is negligible in conventional analog assays where n is very large. For digital assays, however, it presents a problem because a single detection event of an analyte molecule does not contain enough analytical information. Therefore, it is necessary to make either many parallel measurements on a larger area or many sequential measurements in the same detection volume.

V.3. Enzyme Labels

The enzyme-linked immunosorbent assay (ELISA) has been successfully transformed into single-molecule immunoassays. The production of thousands of fluorescent molecules per enzyme label molecule multiplied by up to a million photons per fluorophore generates a very strong signal that can be detected by simple wide-field fluorescence microscopy. In particular, β -galactosidase from *E. coli* is an excellent enzyme label for single-molecule applications because it is robust and can turn over up to 1000 substrate molecules per second. Based on this strategy, Rotman²⁸ reported the very first single-molecule experiment already in 1961. The enzymatic substrate turnover, however, is a kinetic process and needs time, which leads to product diffusion. Consequently, the signal is not detectable at the same location as the analyte. There are two options to spatially allocate the signal to the analyte.

V.3.1. Assays Based on Product Precipitation

In the easiest case, the enzymatic reaction generates a product that precipitates around the analyte. The group of Suzuki²⁹ designed a digital sandwich immunoassay on beads by using a conjugate of detection antibody and horseradish peroxidase. The enzyme label converted a fluorescence-labeled tyramide substrate to a precipitating fluorescent product, which led to a high local fluorescence signal at the site of analyte binding. It was noted, however, that the detection of the tyramide signal on the beads by flow cytometry was less efficient than that of digital ELISAs in confined environments.

V.3.2. Assays in Confined Environments

Alternatively, the enzyme label converts a substrate to a soluble fluorescent product. In this case, the reaction must be confined in a very small compartment in order to prevent product diffusion.³⁰ The concentration of the reaction product exceeds the detection threshold in small confined volumes. For example, a single molecule of β -galactosidase enclosed in a volume of 50 fL (50 μm^3) can produce a fluorophore concentration of 2 μM in 1 min, which can be easily detected via conventional epifluorescence microscopy.³¹ Enzymatic reactions were confined in water-in-oil emulsion²⁸ or microfluidic droplets, fused silica capillaries,³² virus capsids,³³ lipid vesicles,³⁴ or so-called femtoliter arrays. In particular, femtoliter arrays and water-in-oil microfluidic droplets have found analytical applications.

Femtoliter Arrays

Femtoliter arrays consist of a large number of homogeneous wells fabricated in the surface of optical fiber bundles,³⁵ fused silica slides,³ or polydimethylsiloxane (PDMS)³⁷. The Walt group³⁸ pioneered single-molecule immunoassays based on a fluorogenic enzymatic reaction in femtoliter arrays, which was commercialized by Quanterix. In the so-called Simoa platform

(single molecule arrays, **Figure 2**), magnetic beads with a capture antibody are dispersed in an analyte sample. The bead concentration is typically much higher than the analyte concentration. The beads were magnetically separated and incubated with a biotinylated antibody, followed by the addition of a streptavidin- β -galactosidase conjugate. A high bead-to-analyte ratio ensured resulted in a small fraction of beads labeled with a single enzyme molecule and a large excess of unlabeled beads. The beads were loaded with a fluorogenic substrate onto a femtoliter array and sealed with a gasket or oil film. A highly fluorescent product accumulated only in wells that contained a bead with a bound analyte molecule. The analyte concentration was determined digitally by counting the number of fluorescent wells. Prostate-specific antigen (PSA) and tumor necrosis factor- α were detected with an LOD of 1.5 fg/mL (~ 50 aM) and 2.5 fg/mL (~ 150 aM), respectively. Other clinically relevant analytes included cancer biomarkers,³⁹ urinary biomarkers,⁴⁰ p24 protein of HIV,⁴¹ and the neurofilament light chain protein (NFL), a neuronal injury marker of various neurodegenerative conditions and brain injuries. Traditionally, cerebrospinal fluid needs to be obtained for analysis by lumbar puncture because the concentration of NFL in the blood is too low for a conventional ELISA. Shahim et al.⁴² developed an ultrasensitive immunoassay with an LOD of 0.29 pg/mL, which enabled NFL measurements in the serum of healthy subjects. Olivera et al.⁴³ determined tau protein in blood plasma (LOD of 0.012 pg/mL) to examine the relationship between increased tau protein levels and chronic neurological and psychological symptoms in military personnel after a traumatic brain injury. The ultrasensitive detection of biotoxins such as ricin has also been demonstrated⁴⁴.

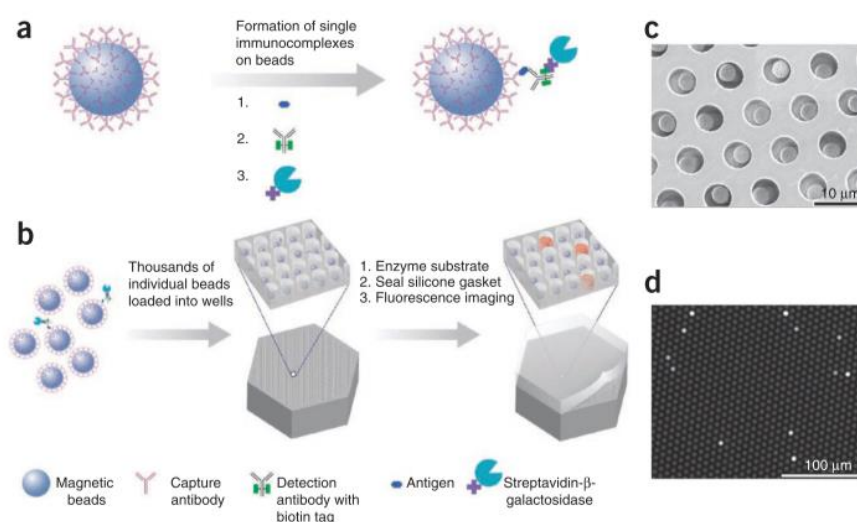


Figure 2: Magnetic bead assisted single-molecule ELISA assay in femtoliter arrays. (a) Many capture antibody-coated magnetic beads are dispersed in the analyte medium. After catching an analyte molecule, a biotinylated antibody forms the sandwich complex and serves as an anchor for a streptavidin-modified β -galactosidase. (b) The beads are loaded—together with a fluorogenic

substrate—onto a femtoliter array and sealed by a PDMS gasket. (c) Scanning electron microscopy shows that only one bead is loaded per femtoliter well. (d) Fluorescence microscopy records the fluorescence increase in wells that contain a bead with a captured analyte molecule. Reprinted with permission from ³⁸. Copyright 2010 Nature America.

The Noji group⁴⁵ developed larger arrays of one million femtoliter wells. Counting a very high number of individual immunocomplexes in the arrays reduced the Poisson noise. The assay was employed for the detection of PSA with an LOD of 60 ag/mL (~2 aM). The authors also showed that the digital assay in femtoliter arrays is amenable to multiplexing by using two different enzyme/substrate labels.⁴⁶ Recently, a competitive femtoliter array format was demonstrated for the detection of small molecules such as cortisol in saliva.⁴⁷ The assay achieved an IC₅₀ down to 0.42 ng/mL, which was 44 times lower than for a conventional ELISA.

Microdroplets

Different ways for the generation of water-in-oil microdroplets have been reviewed earlier.^[30] Water-in-oil droplets divide the reactants and the product into pico- to femtoliter volumes. The oil phase prevents interactions between reagents in the aqueous phase and on solid surfaces. While microdroplets generated by emulsification methods tend to be rather heterogeneous, more homogeneous microdroplets can be generated and handled by microfluidic devices. Microfluidic droplets separate the reactants from the liquid substances, reduce the assay volume, and enable rapid handling, which increases the assay throughput.⁴⁸ Microfluidic droplets have also been used to study single enzyme molecule reactions⁴⁹ and single cells.⁵⁰

Water-in-oil femtoliter droplets generated by a microfluidic device were used to establish a bead-based ELISA (**Figure 3**).⁵¹ A capture antibody on the surface of polystyrene beads immobilized PSA. The presence of PSA was then detected by a biotinylated detection antibody and a streptavidin- β -galactosidase conjugate using fluorescein-di- β -D-galactopyranoside (FDG) as the substrate. The enzyme product fluorescein was recorded by fluorescence microscopy while the beads were identified and counted based on their red autofluorescence. The microdroplet assay achieved an LOD of 46 fM and a linear range of 0.046–4.62 pM.

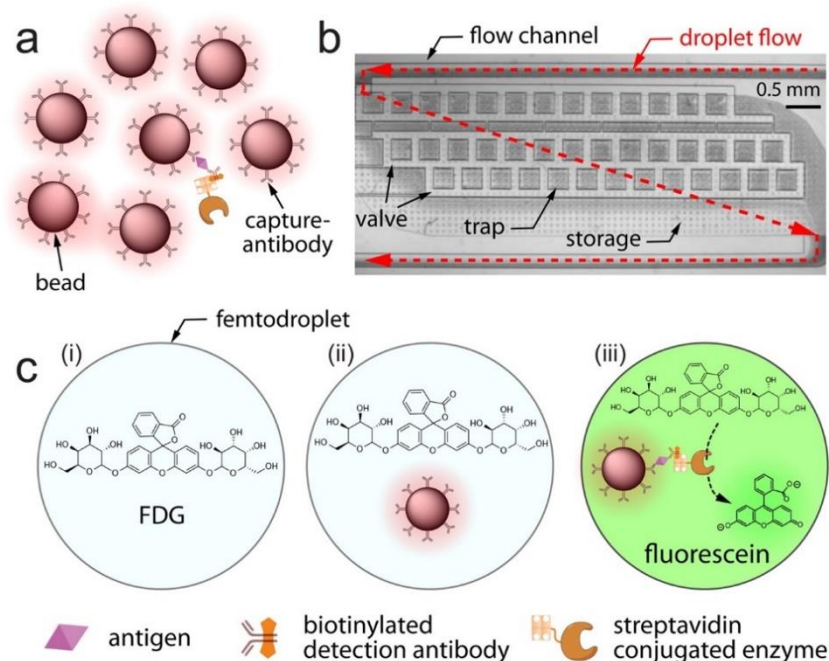


Figure 3: Scheme of single-molecule immunoassay in femtoliter-sized droplets. (a) Antibody-antigen complex formation on beads. (b) Beads with or without immunocomplex are encapsulated in droplets with the substrate and incubated on chip in traps to collect the fluorescent products of single-enzyme labels. (c) Three droplet populations can be distinguished: (i) droplets without bead, (ii) those containing a bead without immunocomplex, and (iii) those containing both a bead and immunocomplex, which exhibit a positive fluorescence signal due to the enzymatic activity of a single β -galactosidase label. Reprinted with permission from ⁵¹. Copyright 2013 American Chemical Society.

Liu et al.⁵² developed another type of enzyme-linked immunoassay on magnetic beads for single-exosome counting in microdroplets (droplet digital ExoELISA). Magnetic beads were equipped with an anti-CD63 antibody to capture exosomes. After sample incubation, a biotinylated detection antibody and a streptavidin- β -galactosidase conjugate were added to the beads. The beads were enclosed in 40 μm droplets (~ 33 fL) containing FDG. The fluorescence increase of fluorescein was detected in each droplet containing a magnetic bead with captured exosome. A bead-to-droplet ratio of 0.3 was employed to ensure that only one magnetic bead was enclosed in a given droplet. The assay achieved an LOD down to 10 enzyme-labeled exosome complexes per microliter ($\sim 10^{-17}$ M).

An indirect bead-based immunoassay in microdroplets was reported for the detection of α -fetal protein (AFP).⁵³ AFP was immobilized on antibody-coated magnetic beads followed by the addition of a biotinylated detection antibody and a streptavidin- β -galactosidase conjugate. After magnetic separation, the excess amount of unbound streptavidin- β -galactosidase was injected into a microfluidic chip to generate microdroplets with FDG. The microdroplets were

collected into a microtiter plate and fluorescent droplets containing free streptavidin- β -galactosidase were counted under a fluorescence microscope. This indirect digital concentration readout reached an LOD in the fM concentration range.

The Di Carlo group⁵⁴ developed a microfluidic digital homogeneous entropy-driven biomolecular assay (dHEBA) for the detection of influenza A. Upon nucleoprotein binding, nucleic acid-labeled antibodies formed a catalytically active complex that drove a hybridization/displacement reaction on a multicomponent nucleic acid substrate and generated many fluorescence-labeled oligonucleotides. The dHEBA format enabled the detection of influenza A nucleoprotein in a concentration of 4 aM in approximately 10 min without the need for a purification step. The dHEBA has the potential to detect single analyte molecules in complex biofluids.

V.4. DNA Labels for PCR Amplification

The polymerase chain reaction (PCR) amplifies DNA—in principle starting from a single template strand—exponentially to very high copy numbers of DNA.⁵⁵ Droplet microfluidics on a microchip enables the rapid isolation of single DNA strands and subsequent PCR amplification in pico- or femtoliter reaction containers.⁵⁶ For example, a digital PCR was performed in rotational chips to detect viral RNA isolated from single HIV viruses.^[57] Wells of different volumes were employed in the chip to enable quantification over a wider dynamic range. The assay achieved an LOD of 40 HIV molecules per mL.

Similar to the digital readout of single enzyme molecule labels, a digital immuno-PCR can be implemented if the PCR reaction is enclosed in microdroplets. The droplet-based digital immuno-PCR (ddIPCR) uses magnetic beads as solid support, DNA as a marker and PCR for signal amplification e.g. for the detection of PSA.⁵⁸ The IPCR is performed in three steps as shown in **Figure 4**. First, the PCR reaction mixture was emulsified to generate tens of thousands of water-in-oil droplets per microchip. Subsequently, the samples underwent thermal amplification cycles and the number of positive droplets was determined by end-point fluorescence detection. In the last step, the number of DNA copies was calculated based on the Poisson distribution. The IPCR can usually enhance the LOD by 100–10 000 fold compared to a standard ELISA. It was noted, however, that the washing steps and the microfluidic droplet system cannot be easily combined. The LOD for PSA was 0.48 ng/mL with a linear range of 0.5–30 ng/mL. Human serum samples correlated well with a reference method based on a commercial automated immunoassay analyzer.

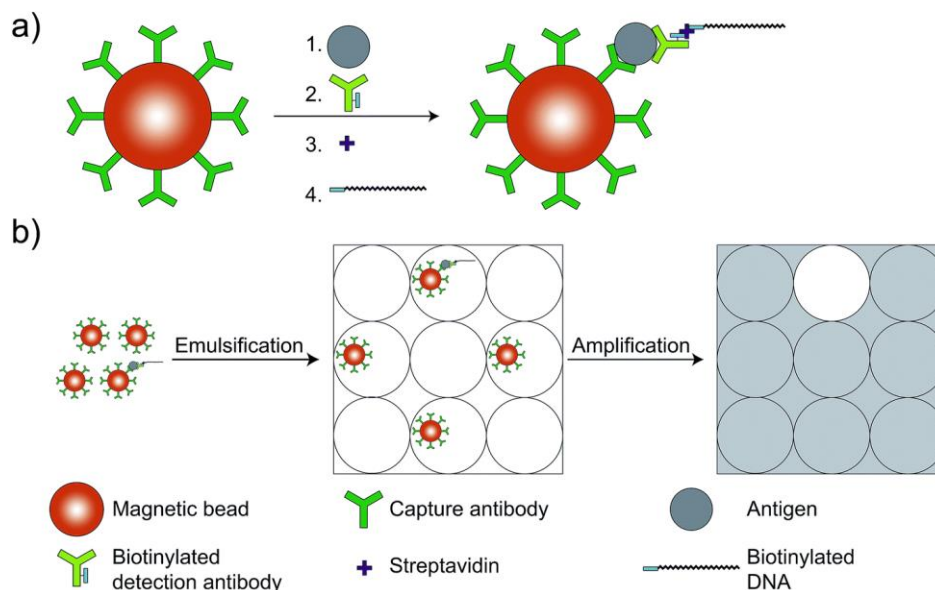


Figure 4: Scheme of immunomagnetic droplet-based digital immuno-PCR (ddIPCR). (a) Antibody-magnetic beads conjugates captured the antigen. A biotinylated antibody, streptavidin, and biotinylated DNA sequence from *Aspergillus fumigatus* are then sequentially ligated. (b) The magnetic beads are resuspended in a reaction mixture and then emulsified. After ddPCR, the numbers of negative and positive droplets are counted. Reprinted with permission from ⁵⁸. Copyright 2018 Royal Society of Chemistry.

The digital PCR was combined with a proximity ligation assay (PLA) to improve the precision of the assay.⁵⁹ Target proteins such as the cytokine IL-6 were immobilized on magnetic beads and detected by two types of DNA-modified antibodies that are capable of forming a pair of PLA probes. If both antibodies bound to the protein, the PLA probes was joined by DNA ligation. The ligated DNA reporter strand was then amplified by rolling circle amplification, and the amplified DNA was detected via fluorescent DNA probes. Because standard rolling circle amplification is not quantitative, the ligated DNA strands were compartmentalized individually by using a microfluidic device, and the protein concentration was determined digitally by counting fluorescent microdroplets.

V.5. Fluorescent Molecular Labels

The detection of molecular labels at the single-molecule level relies on fluorescence spectroscopy and microscopy. Total internal reflection microscopy (TIRF) and confocal microscopy can efficiently generate such a small detection volume that the background signal is reduced, and single fluorescent label molecules can be detected. When crossing a focused laser beam in a confocal microscope set-up, individual fluorophores emit bursts of photons that

are detected.⁶⁰ The residence time depends on the diffusion of the fluorophore through the beam path (with a typical active volume of a few femtoliters) and on photobleaching. Cyanine dyes were proposed for such applications as the excitation within 650–700 nm is well compatible with the spectral window of low light scattering and autofluorescence of biological substances including blood. Even epifluorescence has more recently been reported to enable single fluorophore detection. However, the type of microscopy is not relevant for the assay design as long as it allows for the detection of a single fluorescent molecule. Thus, we have structured this chapter according to different assay formats. Fluorescence counting of single protein analyte molecules immobilized on a surface by capture antibodies seems to be more sensitive compared to correlation techniques in solution.

V.5.1. Detection of Surface-Bound Analytes

Löscher et al.⁶¹ developed a sandwich assay for the detection of single cardiac actin molecules. The scanning system employed a single-photon counting avalanche photodiode together with a CCD camera for imaging under 635-nm laser excitation. A glass surface was coated with a cellulose layer to reduce non-specific binding. Confocal microscopy reduced the optical background by minimizing the detection volume, which enabled the evaluation of photon bursts originating from individual molecules.

A particular kind of bioaffinity assay, the so-called pull-down assay, has been used for the identification of protein-protein interactions. The Ha group⁶² developed a single-molecule pull-down assay (**Figure 5**). A capture antibody was immobilized in a flow chamber coated with polyethylene glycol (PEG) and biotin. Streptavidin was added to the flow chamber, followed by the addition of a biotinylated anti-His antibody, which captured overexpressed His6-tagged yellow fluorescent protein (YFP) from cell extracts. Individual YFP molecules were detected by TIRF microscopy. A stepwise decrease of the fluorescence intensity during single-molecule bleaching experiments enabled the identification of dimeric and trimeric YFP molecules. Individual protein kinase A (PKA) complexes were detected by a two-color single-molecule pull-down assay. In its inactive form, PKA is present as a tetramer which consists of two catalytic and two regulatory subunits. Cyclic adenosine monophosphate (cAMP) activates the enzyme and leads to tetramer dissociation. The investigation of the stoichiometry of individual PKA complexes is essentially not possible using conventional analog detection.

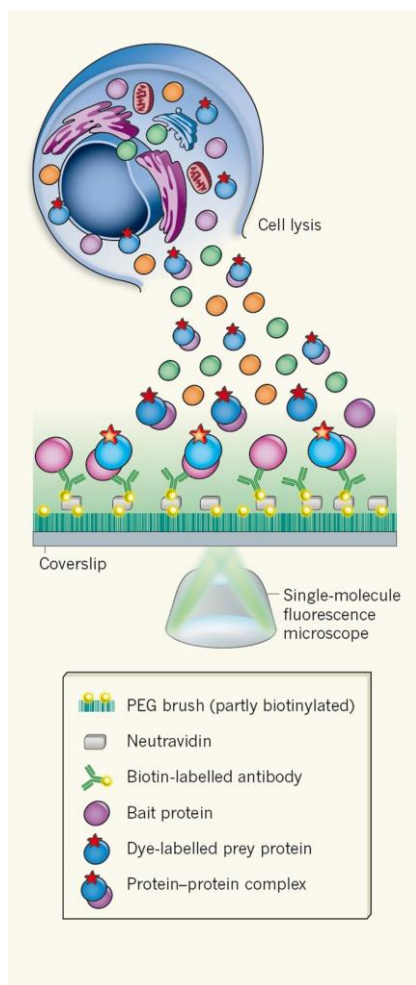


Figure 5: A cell lysate is applied directly onto a coverslip for single-molecule TIRF microscopy. Specific antibodies on the coverslip capture protein complexes. Prey proteins associated with the bait protein are detected via a fluorescent dye fused to the prey. Reprinted with permission from⁶³. Copyright 2011 Macmillan Publishers Limited.

Burgin et al.⁶⁴ developed a single-molecule assay for the detection of enhanced green fluorescent protein (EGFP) and tumor suppressor protein p53. A microfluidic chip was mounted onto a TIRF microscope under 473-nm laser excitation. Two methods for absolute protein quantification were used for the digital readout. In the accumulation method (**Figure 6a**), the analyte was observed over a defined time period, during which the number of fluorescent spots increased until individual EGFP molecules were not distinguishable as diffraction-limited spots anymore. In the detect and bleach method (**Figure 6b**), fluorescent spots were counted, bleached, and after a fixed time interval counted again. Both images were subtracted to identify newly arrived and bleached molecules. Protein p53 was detected in the accumulation method by using a labeled detection antibody.

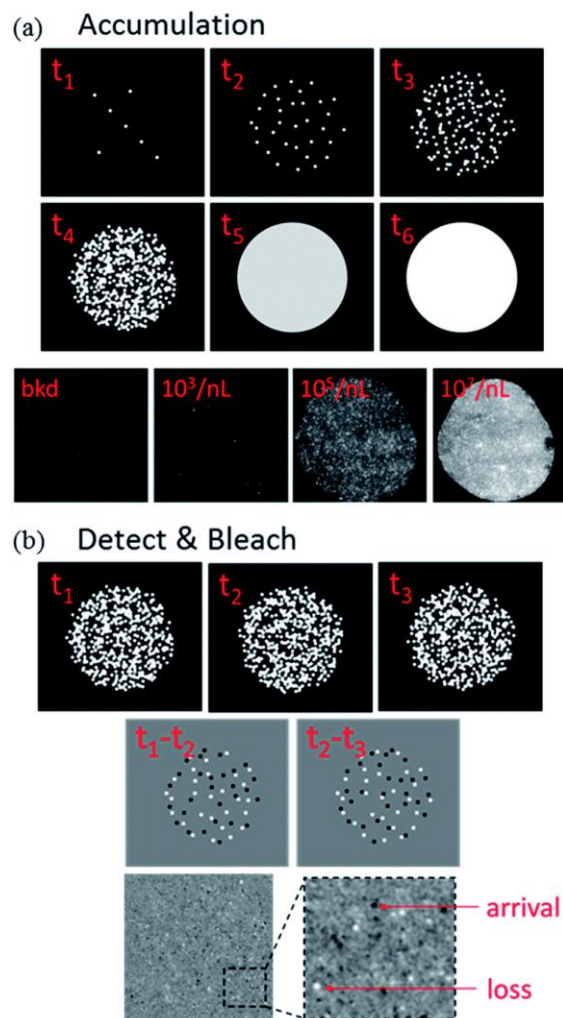


Figure 6: Different approaches for digital protein quantification. (a) For low analyte concentrations, the accumulation method counts the increasing number of fluorescent spots. If the distance between two fluorescent molecules is below the diffraction limit, they appear as one spot and cannot be distinguished anymore. (b) In the detect and bleach method, fluorescent molecules are counted after a certain time interval and subsequently bleached. The bleaching step keeps the average number of fluorophores bound to the surface at a constant level such that higher concentrations can be determined compared to the accumulation method. Reprinted with permission from ⁶⁴. Copyright 2014 Royal Society of Chemistry.

Zhang et al.⁶⁵ developed a digital ATP assay using split aptamers. A coverslip was bound to a glass slide with a 5-mm hole in the center, followed by surface activation with plasma. A mixture of poly(L-lysine)-poly(ethylene glycol)-biotin (PLL-PEG-biotin) and PLL-PEG was added to the activated coverslip. Next, streptavidin was added, and a biotinylated Cy3-3'-labeled split aptamer was bound to streptavidin. The analyte ATP was added together with the other Cy5-3'-labeled aptamer. The coverslip was placed on an epifluorescence microscope, and

the emission of the two dyes was collected simultaneously on the same EM-CCD camera. Diffraction limited spots of a mixed color indicated specific binding, whereas spots with only one color indicated non-specific binding. The assay achieved an LOD of 100 fM and a working range of 1 pM to 5 nM.

Weng et al.⁶⁶ developed an aptasensor for the detection of small molecules. The hairpin-shaped aptamer immobilized on a glass slide changes its conformation to an open state upon analyte binding (**Figure 7**). Fluorescently labeled short ssDNA probes bound preferably (but not exclusively) to the open conformation and the fluorescence trajectories of individual aptamers were monitored by TIRF microscopy. As the binding of the fluorescent probe followed different kinetic patterns depending on the conformation of the aptamer, the kinetic fingerprints were used to distinguish between nonspecific binding and analyte binding. Only spots that showed the signature of specific binding were counted to determine the analyte concentration. The assay achieved LODs of 0.3 pM for adenosine, 0.35 pM for acetamiprid, and 0.72 pM for PCB-77 in spiked chicken meat extract.

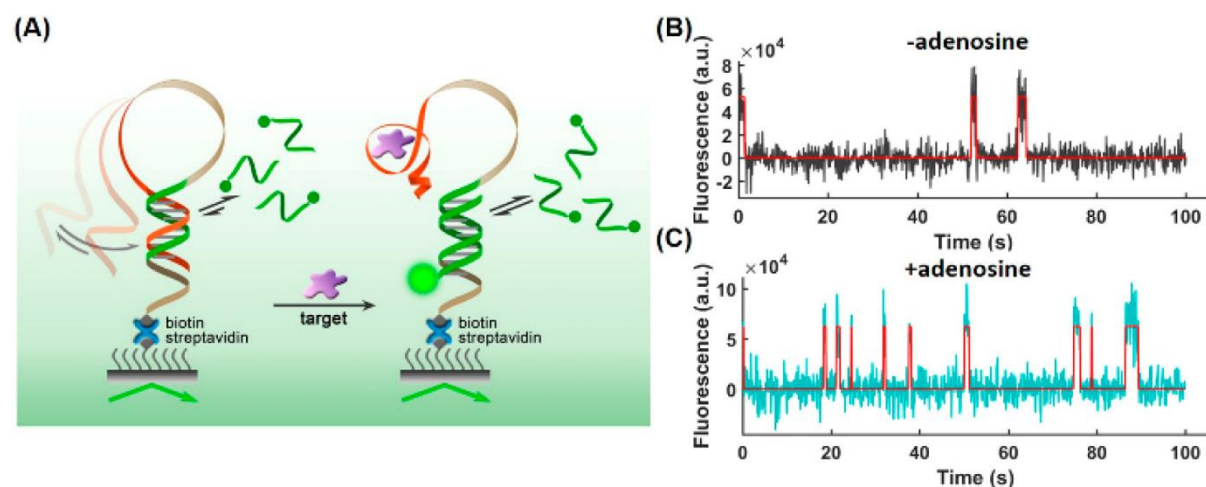


Figure 7: (a) Scheme of a hairpin-shaped aptasensor immobilized on the slide surface. Analyte binding results in a conformational change and binding of a complementary fluorescent ssDNA probe. Single-molecule trajectories (b) without and (c) with 50 pM adenosine are distinguishable. Reprinted with permission from ⁶⁶. Copyright 2019 American Chemical Society.

V.5.2. Laser-Induced Fluorescence Detection Inside a Capillary

The Yeung group pioneered the use of capillary electrophoresis for single-molecule detection.³⁶ In capillary electrophoresis, an electric field drives the sample through the illumination volume, which is small enough to allow for the detection of individual fluorescent molecules. Based on the electrophoretic mobility of individual fluorescently labeled antibodies, fluorescent immunoassays were established.⁶⁷ Antibodies bound to an analyte

molecule have lower electrophoretic mobility and can thus be distinguished from free antibodies using cross-correlation. Individual fluorescence-labeled antibodies were recorded in the capillary by wide-field microscopy using a 20× objective (0.75 NA) and an intensified CCD camera.

Stimulated by the need for reliable and sensitive assays for cardiac troponin, a diagnostic marker of acute myocardial infarction, the Erenna platform was developed. First, a sandwich immunoassay was performed in microtiter plates, and the bound labels were then released and inserted into a capillary electrophoresis device.⁶⁸ As only a single fluorescent molecule passed through the detection volume during the observation interval, individual analyte molecules were counted, and an LOD of 1.7 pg/mL was achieved. In combination with magnetic beads, it was possible to detect troponin I levels of 0.2 pg/mL, which are typically found in healthy individuals (0.3 to 9 pg/mL).⁶⁹ Esparza et al.⁷⁰ used the Erenna assay to study amyloid-beta (A β) aggregation and deposition in Alzheimer's disease. As low as 1.56 pg/mL (0.18 pM) of soluble A β oligomers was detectable above background, and the LOQ was determined to be 6.25 pg/mL (0.72 pM). The method was applied to measure the A β oligomers in human cortical tissue homogenate. Wild et al.⁷¹ detected mutant huntingtin protein (mHTT) in cerebrospinal fluid. The mHTT is a promising biomarker for monitoring Huntington disease progression, but due to its predominantly intracellular localization, the concentration in the cerebrospinal fluid is very low (below pM even in patients with disease in advanced stage) and conventional methods are not sensitive enough to detect it. The Erenna assay provided an LOD of 40 fM and the authors found a significant difference in levels of mHTT in carriers of the genetic mutation in the premanifest stage and in different later stages of the disease.

For the detection of the fertility-related human gonadotropin follicle-stimulating hormone (FSH), the laser beam was shaped into stripes, and 10 “superpixel” zones were evaluated using a CCD camera.⁷² Magnetic beads served as a solid phase for the immunoassay, the LOD for FSH was 34 fM for a few hundreds of fluorescent events counted above the background in 12 s and corresponding to a few zeptomoles of labeled antibodies.

The combination of several excitation lasers (blue 488 nm; green 543 nm; red 635 nm; infrared 730 nm) and four single-photon counting modules allowed for the implementation of multiplexed assays.⁷³ Confocal microsecond-scale alternating-laser excitation (ALEX) single-molecule fluorescence spectroscopy was used to probe the fluorescent acceptor (A) without energy transfer (FRET) and provides also donor (D) excitation-based data for each single molecule. Distinct emission signatures are recovered for interacting species through determining the FRET efficiency E , which relates to the D–A distance, and distance-independent stoichiometry-based ratio S (corresponds to the D–A stoichiometry of the various species). The combination of E and S on 2-dimensional histograms allowed for a virtual sorting

of single molecules. This technique was evaluated by determining 25 DNA sequences, 6 tumor markers, 8 bacterial gene markers and 3 drug resistance determinants.

V.5.3. Fluorescence Correlation Spectroscopy

Fluorescence correlation spectroscopy (FCS) records diffusion at the single-molecule level. Equilibrium concentration fluctuations due to Brownian motion are measured as spikes of fluorescence intensity within a small sampling volume. A concentration in the nanomolar range should be attained for subfemtoliter detection volumes to allow for following individual fluorescence-labeled molecules. Such a small detection volume can be obtained using confocal microscopy or multiphoton microscopy. The sensitivity of FCS depends mainly on the brightness of the fluorescent probe and on the detection volume.⁷⁴ Evaluating fluorescence intensity fluctuations over time by an autocorrelation function yields information on the diffusion rates and the concentration of the fluorescent molecule.⁷⁵ The diffusion time depends on the size and shape of the target molecule, on the viscosity of the solution, and the size of the focused laser beam. The increase of the diffusion time can therefore be used to determine the size of the fluorescently labeled molecule, which can be exploited for following its interactions with other molecules.⁷⁶ FCS has found applications for example in *in vitro* and *in vivo* studies of protein-protein interactions, nucleic acid interactions, enzymatic activities, membrane diffusion.⁷⁷

The detection of fluorescence-labeled molecules at the single molecule level by FCS is applicable for the implementation of homogeneous immunoassays that avoid washing and separation steps as well as non-specific binding to surfaces, which becomes increasingly important at low analyte concentrations.⁷⁵ On the other hand, FCS is prone to background interferences caused by autofluorescence, light scattering, quenching, and potential aggregation of the assay components. The simplest scheme of an FCS immunoassay is based on following the changes of the diffusion rate after the formation of the immunocomplex (**Figure 8**). Chatterjee et al.⁷⁶ employed a sandwich assay for the detection of the neuronal cell adhesion molecule contactin-2 in cerebrospinal fluid. The assay was based on two different anti-contactin antibodies. One antibody was labeled with Alexa Fluor 488 and the other one was unlabeled. The formation of the sandwich immunocomplex of both antibodies with the analyte increased the diffusion rate, which was evaluated from the autocorrelation curve. The authors reached a limit of quantification of 0.2 ng/mL.

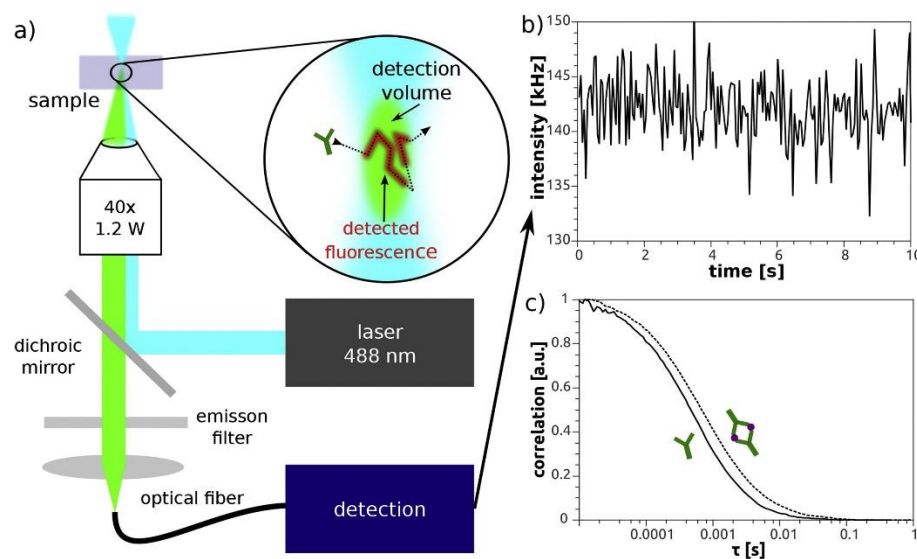


Figure 8: (a) Scheme of FCS setup. A laser is focused to excite fluorescent molecules in a confocal volume. Fluorescence intensity fluctuations due to Brownian motion are measured in solution by an optical fiber-connected photodiode. (b) The emitted photons are collected and plotted as time-dependent intensity changes. (c) The autocorrelation curves show an increase in the diffusion time after formation of the immunocomplex (dotted line) compared to the antibody alone (solid line). Reprinted with permission from ⁷⁶. Copyright 2017 Elsevier.

Changes in the diffusion rates were also recorded by FCS to implement a competitive assay for the detection of the mycotoxin fumonisin B₁ (FB₁).⁷⁸ The analyte FB₁ competed with a tracer consisting of FB₁ and Alexa Fluor 488 for the free binding site of the antibody. The assay provided an LOD of 1 ng/mL.

The sensitivity towards the formation of immunocomplexes with smaller size difference can be enhanced using fluorescence cross-correlation spectroscopy (FCCS). FCCS uses two spectrally different fluorescent probes, which can be simultaneously excited using two separate excitation wavelengths and detected in two different channels. For FCCS, the amplitudes of the cross-correlation curves are calculated to detect the interactions of the fluorescent probes with the analyte. Because two labels are used, the sensitivity and especially the selectivity of FCCS in the quantitative measurement of biomolecules are higher compared to conventional FCS.

The Klenerman group⁷⁹ developed a sandwich assay based on counting of coincidence spikes of the two labeled antibodies. Compared to conventional FCCS, the data evaluation was simplified because only the number of spikes was counted, which corresponds to both labels being present in the confocal volume at the same time. Protein G and herpes simplex virus were detected with an LOD of 50 fM.

Miller et al.⁸⁰ demonstrated a sandwich FCCS-based assay for the detection of human chorionic gonadotropin and the prion protein (**Figure 9**). Two lasers were alternated, and the emissions of different fluorescent labels were measured using separate detectors to eliminate spectral cross-talk and reduce the probability of false positive cross-correlation.⁸¹ The fluorophores were chosen in a way that their emission is separated, reducing the overlap of the emission and the possible energy transfer. To eliminate aggregation effects on the cross-correlation curves, cross-correlations on short time sections were calculated followed by the elimination of the ones with the highest level of fluorescence (top 1% of the intensity distribution). The method provided LODs of 100 pM (human chorionic gonadotropin) and 2 nM (prion protein) with an analysis time of 40 min.

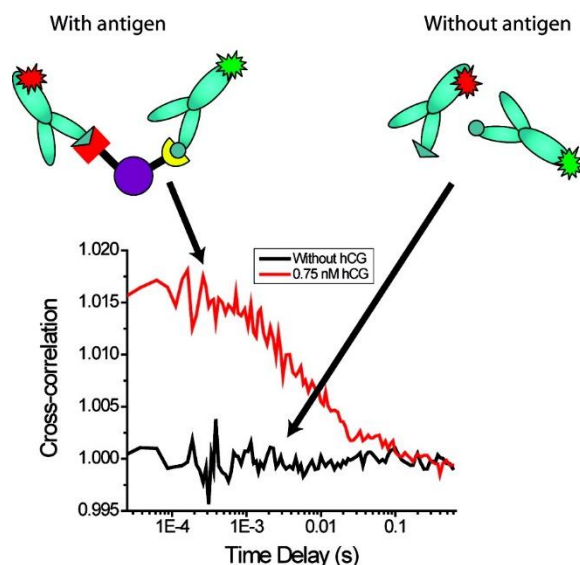


Figure 9: In fluorescence cross-correlation spectroscopy (FCCS), two fluorescence-labeled antibodies bind to the analyte. Black line: cross-correlation of labeled antibodies without analyte (antigen); red line: cross-correlation of labeled antibodies in the presence of the analyte. Reprinted with permission from ⁸⁰. Copyright 2009 American Chemical Society.

V.6. Nanoparticle Labels

In recent years, various kinds of nanomaterials have been introduced as labels for immunoassays in order to enhance the assay performance.^{20a} In particular, NPs with luminescent or plasmonic properties, which allow for a convenient optical readout, are suitable for single-molecule analysis.⁸² Compared to molecular labels, NPs display generally higher signals, which allows for an easier readout. On the other hand, their larger size can be a drawback in terms of steric hindrance of the immunocomplex formation as well as a potentially higher degree of non-specific binding.

V.6.1. Semiconductor Nanoparticles

Quantum dots (QD) are fluorescent semiconductor nanocrystals with dimensions typically between 1 and 10 nm. The photoluminescence properties of QDs can be tuned by changing the nanocrystal size, allowing to reach emission wavelengths in the range of 380 to 2000 nm.⁸³ Compared to conventional fluorophores, QDs provide higher emission intensities, better photostability, wider excitation spectra, and narrower emission bandwidths.⁸⁴ This allows for an easier detection of individual QDs compared to fluorophores.

Detection of Surface-Bound Analytes

Liu et al.⁸⁵ developed a sandwich immunoassay based on QD labels. A capture antibody-coated QD and a detection antibody-coated QD were mixed with the sample, and then immobilized onto a positively charged coverslip. Mixed color spots (yellow) were counted under a fluorescence microscope. Carcinoembryonic antigen (CEA) was detected with an LOD of 6.1 pM. The same group⁸⁶ developed a method that made it possible to build a homogeneous sandwich immunoassay that employs only one label type. Capture and detection antibodies were coated on different QD 655s and formed an immunosandwich with the analyte. The QD emission was monitored through a diffraction grating placed in front of a CMOS camera of the microscope. The grating divided the emission into a zeroth-order spot and a first-order streak. Because of the diffraction limit, it was not possible to distinguish between unbound QDs and the sandwich immunocomplexes. During excitation, the QDs were oxidized, and the first order streak shifted to shorter wavelengths. The oxidation of the QDs started at different times and proceeded at different rates, which caused a splitting of the first order streak into two smaller streaks, if both QDs bound to the same analyte molecule. The number of split streaks was proportional to the amount of analyte molecules. The LODs for CEA and AFP were 6.7 fM and 3.4 fM, respectively.

Detection in Microchannels

A sandwich immunoassay for the detection of viruses was implemented in a microfluidic channel by exciting red and green fluorescent NPs simultaneously by a 488-nm laser⁸⁷. The immunocomplex was detected by monitoring the coincidence of photon bursts in the red and green detection channels. In this way, wild type and mutated respiratory syncytial viruses were quantified in parallel with an LOD of 4×10^6 plaque-forming units (PFU).

Zhang et al.⁸⁸ developed an aptamer-based single QD-FRET assay for the detection of cocaine. They first designed a signal-off assay by assembling a sandwich of a 3' biotinylated oligonucleotide, a cocaine aptamer and a 3' Cy5 labeled oligonucleotide. The sensitivity of the

system was investigated by plotting the Cy5 burst counts against the ratio of Cy5 to 605QD from 0 to 24. It was possible to distinguish a difference between single Cy5 labels. The sandwich complex was dispersed in a diluted cocaine sample to capture the analyte, and then a commercial streptavidin-functionalized 605QD was added to capture the aptamer complex. In the presence of a high amount of cocaine, no FRET signal was observed due to the release of the Cy5 oligo after analyte binding. The signal off assay achieved an LOD of 0.5 μM for cocaine, which is comparable to other electrochemical and enzyme-based assays. The generally low sensitivity was explained by the poor affinity of the aptamer towards cocaine. Additionally, a signal-on assay was designed by forming a sandwich of a 3' biotinylated and 5' Cy5 oligo, the cocaine aptamer and a 3' Iowa black oligo, which quenched the emission of the 605QD/Cy5 FRET. In the presence of cocaine, the quencher containing oligo was released, and the FRET emission between the 605QD and Cy5 was detected. A 488-nm argon laser was focused on the capillary (50 μm inner diameter), and photon bursts of 605QD and Cy5 were detected simultaneously by two avalanche photodiodes (APD).

A high-throughput assay was developed in a very narrow channel (1–2 μm width and height) integrated in a chip system (**Figure 10**).⁸⁹ Semiconducting polymer dots (Pdots) were modified with streptavidin and the binding of biotin-Alexa647 was investigated. Furthermore, Au NPs were added to the solution as an internal standard to compensate for instrumental fluctuations. The platform combined confocal fluorescence detection with narrow channels to allow counting of photon bursts corresponding to individual labeled molecules. The dual laser-based evaluation allowed to count single NPs, but more interestingly, the number of fluorophores per NP was quantified, too. This is a very promising technique for the characterization of different nanoconjugates.

developed by Wohland's group⁹² allowed to overcome this limitation by the use of two probes, which can be excited using the same wavelength, but their emission is separated due to a large difference of the Stokes shifts. This can be conveniently achieved by the use of QDs⁹³ or long Stokes shift fluorescent proteins.⁹⁴ The group of Ren⁹⁵ designed sandwich and competitive assays based on SW-FCCS for the detection of alpha-fetoprotein. In both approaches, QDs (655 nm emission) and Alexa Fluor 488 (520 nm emission) were chosen as the labels. The achieved LODs were 20 pM (sandwich assay) and 180 pM (competitive assay).

V.6.2. Photon-Upconversion Nanoparticles

The optical background of traditional fluorescence readout can be avoided by using photon-upconversion nanoparticles (UCNPs) that emit shorter-wavelength light under near-infrared (NIR) excitation (anti-Stokes emission).⁹⁶ UCNPs are lanthanide-doped nanocrystals and the most efficient UCNPs consist of a hexagonal NaYF₄ host crystal doped with Yb³⁺ and Er³⁺ or Tm³⁺. The anti-Stokes emission strongly reduces autofluorescence and light scattering. Further advantages of UCNPs include a high photostability and multiple and narrow emission bands that can be tuned individually for the multiplexed detection of several analytes in parallel.^[97] For example, the group of Soukka⁹⁸ developed a multiplexed array-in-well assay to determine the immune status against virus infections in human serum samples by the spatial arrangement of several virus antigens on a microtiter plate. Additionally, two types of UCNP labels with different emission colors (Er-doped: green; Tm-doped: blue) were used to distinguish between IgG and IgM antibody classes.

The groups of Fan⁹⁹ and Jin¹⁰⁰ further enhanced the multiplexing capabilities of UCNPs by combining wavelength- and lifetime-based encoding. The combination of several lifetime populations and emission bands laid the foundation for a very high encoding capacity. This approach was used for the detection and differentiation between the DNA of 9 subtypes of human papillomavirus,⁹⁹ but can also be readily adapted for multiplexed antibody-based assays.

Detection of Surface-Immobilized Analytes

We have developed a method for visualizing individual UCNPs (NaYF₄:Yb³⁺,Er³⁺) by conventional epilluminescence microscopy and applied it for the sensitive detection of the cancer marker PSA.^{22a} Individual sandwich immunocomplexes consisting of (1) anti-PSA antibody immobilized on the surface of a microtiter well, (2) PSA, and (3) anti-PSA antibody-UCNP conjugate were counted under an upconversion wide-field microscope equipped with a 980 nm laser excitation source (**Figure 11**). The single-molecule (digital) ULISA provided an LOD of 1.2 pg/mL (42 fM) PSA in 25% blood serum and covered a dynamic range of three

orders of magnitude. The digital readout provided single-particle resolution with almost no instrumental background, which resulted in ten times lower LOD compared to the classical (analog) readout of luminescence intensity. An important advantage of the digital readout is the resistance against NP aggregation. In the analog mode, a large aggregate containing hundreds of luminescent NPs can lead to a very high background signal. By contrast, in the digital mode, each aggregate - independent of its size - only counts as a single binding event and has only a marginal effect on the background signal. Recently, we have prepared a detection label based on a conjugate of PEG-coated UCNP with streptavidin, which allowed to decrease the label concentration and further improved the LOD by a factor of 50 to ~20 fg/mL.^{22b}

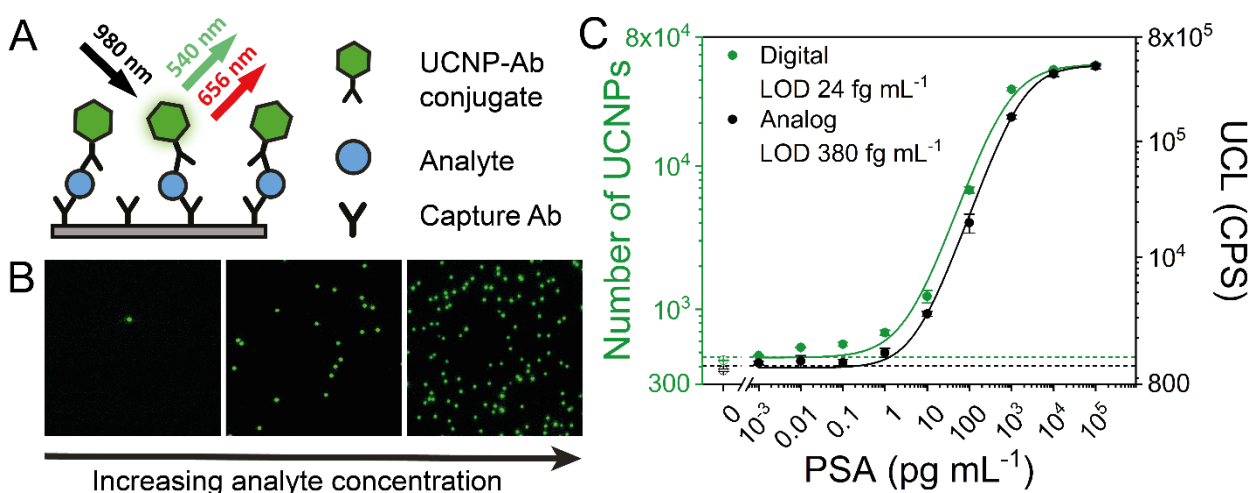


Figure 11: Single-molecule upconversion-linked immunosorbent assay. (A) Scheme of sandwich immunoassay. (B) Wide-field upconversion microscope images of single immunocomplexes carrying a UCNPs label. (C) Calibration curves of the digital (red) and analog ULISA (black). The number of UCNPs is given by the diffraction limited spots in B and the upconversion luminescence (UCL) is recorded by a microtiterplate reader.²²

Li et al.¹⁰¹ designed a digital homogeneous sandwich immunosorbent assay based on UCNP (NaYF₄:Yb³⁺,Er³⁺, 42 nm in diameter) for PSA. The green upconversion-luminescence overlapped strongly with the absorption spectrum of 50 nm Au NPs. By formation of an immunocomplex between UCNP coated with a primary antibody, PSA, and Au NPs coated with another primary antibody, the upconversion luminescence was strongly quenched due to luminescence energy transfer, resulting in a lower ratio of the visible particles in a flow cell and the amount of UCNP that were visible in the negative control. The assay achieved an LOD of 1.0 pM in buffer and 2.3 pM in serum.

Fluorescence Correlation Spectroscopy

If a sample such as blood or plasma is strongly autofluorescent, the FCS/FCCS signal of a label present in sub-nanomolar concentrations is not detectable due to spectral overlap. This effect can either be reduced by using brighter labels or by measuring the cross-correlation of UCNP labels to avoid optical background interference. Lahtinen et al.¹⁰² developed an assay based on upconversion cross-correlation spectroscopy for the detection of thyroid-stimulating hormone (TSH). Green ($\text{NaYF}_4:\text{Yb}^{3+},\text{Er}^{3+}$) and blue ($\text{NaYF}_4:\text{Yb}^{3+},\text{Tm}^{3+}$)-emitting UCNPs were conjugated with anti-TSH antibodies, and the cross-correlation was measured upon binding of the analyte TSH. Compared to small organic fluorophores, NP labels have a higher tendency to form aggregates, bind non-specifically, or induce bridging of more than two NPs. To suppress these effects, large intensity bursts that were attributed to aggregates were removed before calculating the auto- and cross-correlation functions.¹⁰³ However, the smaller bursts were still causing strong variations of the amplitude, which affected the assay sensitivity. The achieved LOD was 15 mIU/L, which is above the range of normal TSH concentrations in serum (0.3–5.0 mIU/L).

V.7. Plasmonic Nanoparticles

Plasmonic NPs have been used in single-molecule immunoassays because they enable a highly sensitive readout based on their light scattering properties or spectral changes upon analyte binding. The most common materials include gold (Au NPs) and silver (Ag NPs). Au NPs are labels that are most frequently used in immunoassays in general, finding applications in lateral flow assays, electrochemistry, colorimetric assays, and plasmonic sensing.¹⁰⁴ Ag NPs are less stable because they can be more easily oxidized, but they display higher extinction coefficients and stronger Raman and fluorescence enhancement.¹⁰⁵ In both cases, the plasmonic properties are strongly dependent on the shape and the size of the NP.¹⁰⁶

Dark-Field Microscopy

Dark-field microscopy is the most common method for the detection of single plasmonic particles. In dark-field microscopy, the illumination light is prevented from entering the objective acceptance cone, whereas the light scattering from immobilized NPs is collected by the objective lens. Background scattering and reflection from interfaces can be further reduced by optimizing the refractive indices.

Poon et al.¹⁰⁷ developed an antibody-based single-particle scattering intensity assay for the detection of various clinical cancer markers such as AFP, CEA and PSA. A gold nanoprobe coated with a capture antibody was immobilized in a flow cell on microscope cover slides.

Then the analyte was added, followed by an Ag NP decorated with the detection antibody. Binding of Au and Ag NPs resulted in a threefold increase of the scattering intensity and a spectrum shift. The LODs for all three analytes were in the range of 1 to 6 pM.

Wu et al.¹⁰⁸ developed a magnetic bead-based sandwich immunoassay for AFP, CEA and PSA using Au NP detection. First, a sandwich immunocomplex was formed by incubating the sample with a biotinylated antibody and a second unlabeled antibody (**Figure 12**). The immunocomplexes were captured on streptavidin-coated magnetic beads. Au NPs coated with a secondary antibody were added, and unbound labels were removed by magnetic separation. After washing, the Au NPs were released from the beads by 8 M urea. The free Au NPs were then immobilized on a cationic coverslip and counted under a dark-field microscope. Zhu et al.¹⁰⁹ developed a similar sandwich immunoassay for PSA using a preconcentration step on magnetic beads.



Figure 12: Assay scheme of Au NP-based detection of PSA with dark-field microscopy readout. Reprinted with permissions from ¹⁰⁸. Copyright 2017 Royal Society of Chemistry.

The Gooding group¹¹⁰ showed the potential use of customer-grade cameras as they appear in smartphones for the high throughput spectral readout of the localized surface plasmon resonance (LSPR) spectra of up to 5000 individual Au NPs (**Figure 13**). Anti-interleukin-6 (IL-6) antibodies were conjugated to Au NPs and spin-coated on a glass slide. A biotinylated anti-IL-6 antibody was attached to a 10-nm streptavidin-modified satellite Au NP and then added to the Au NPs immobilized on glass. The binding of the satellite Au NP resulted in a red shift of the LSPR signal due to plasmon coupling. The spectral shift of single Au NPs before and after the addition of IL-6 was used to calculate the analyte concentration. While the setup was not sensitive enough to detect single binding events, single-molecule sensitivity may be achieved by using bigger satellite particles (20–80 nm).

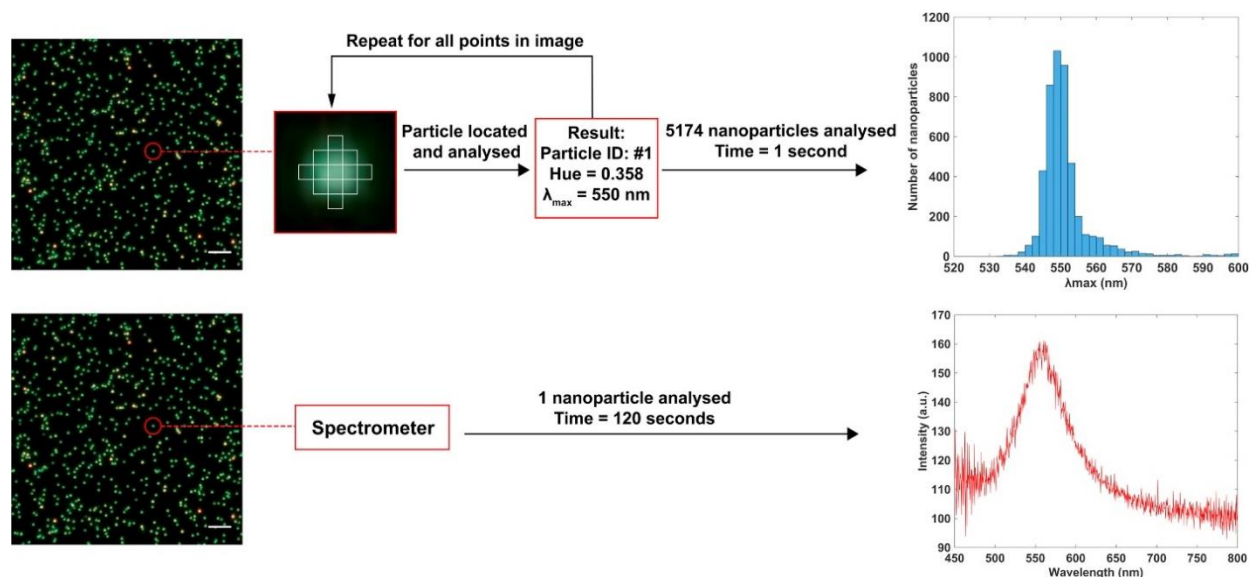


Figure 13: Top: Color analysis using a customer-grade camera. The color of the Au NPs is transformed into a hue value that corresponds to a specific wavelength and arranged into a histogram. Bottom: Color analyses using a spectrometer, each spot has to be processed individually. Reprinted with permission from ¹¹⁰. Copyright 2018 Elsevier.

A method for extracting affinity constants based on statistical fluctuations in equilibrium was proposed by Luthgens and Janshoff.¹¹¹ It is based on a single-molecule readout of an array of isolated sensors, which can accommodate a high amount of simultaneously bound analyte molecules. Aćimović et al.¹¹² employed this principle to follow antibody-antigen binding kinetics on long time scales on the single-molecule level. First, Au nanorods were modified with thiolated PEG followed by binding of an anti-PEG antibody. The signal fluctuations at equilibrium enabled the calculation of kinetic parameters and analyte concentrations.

Yang et al.¹¹³ developed a digital aptamer-based assay for the detection of thrombin. A biotinylated anti-thrombin aptamer was immobilized on commercially available streptavidin-coated magnetic beads. Au NPs coated with a complementary DNA sequence to the aptamer were introduced and bound to the aptamer. In the presence of thrombin, the Au NPs were released, and the beads were magnetically separated. The free Au NPs in the supernatant were either counted individually under a dark-field microscope by dispersing a drop on a coverslip (digital detection) or—at high concentrations—by measuring the absorption resulting from NP aggregation (analog detection). Another aptamer-based thrombin assay was developed by Li et al.¹¹⁴ A glass slide was modified by Au NPs to bind a thrombin-specific aptamer. Thrombin was specifically captured, followed by another anti-thrombin aptamer to form a sandwich complex. After the addition of Au NPs, NP oligomers formed through Au-S binding, which changed the color from green to yellow and red. Individual NPs were detected under a dark-

field microscope, and the thrombin concentration was estimated from the intensity change of the Au NPs. The assay detected thrombin with an LOD of 10 fM.

Chen et al.¹¹⁵ increased the LSPR signal of individual Au NPs by enzymatic amplification. When a single streptavidin horseradish peroxidase conjugate bound to a biotinylated Au NP, the resulting LSPR shift enabled the detection of single molecules. The enzymatic precipitation of 3,3'-diaminobenzidine further increased the colorimetric response by a factor of 50. This method can potentially be developed into a sandwich immunoassay by coating the Au NPs with a capture antibody and conjugating horseradish peroxidase with a detection antibody.

Light Scattering Correlation Spectroscopy

Resonance light scattering correlation spectroscopy (RLSCS) measures the fluctuations of resonance light scattering in small volumes due to the Brownian motion of single NPs. Noble metal NP are excellent labels for RSLCS because of their strong resonance light scattering, which is several orders of magnitude higher than light emission of fluorescent dyes.¹¹⁶ The RSLCS instrumentation is similar to the FCS, but no emission filter is needed. Like FCS, the RLSCS immunoassays are based on the increase of the characteristic diffusion time in the detection volume due to the formation of an immunocomplex. RLSCS was used in a sandwich immunoassay for AFP (LOD 1 pM)¹¹⁷ and in competitive assays for AFP (LOD 100 pM) and 17- β estradiol (LOD 10 pM).¹¹⁸ Similar to FCCS, one of the major limitations of RLSCS is the significant effect of NP label aggregation. Although in both studies the particles were coated by PEG to suppress the NP aggregation, in the presence of a real sample matrix, the assay reproducibility in serum was lower compared to the standard ELISA.

The fluorescence and scattering light cross-correlation spectroscopy (FSCCS) was used by Wang et al.¹¹⁹ in a confocal setup for measuring the scattering of labels based on Au NPs and a fluorescent dye (Alexa Fluor 488) as a probe pair (**Figure 14**). The advantage of FSCCS is the use of a single 488-nm laser as the excitation source for both the Au NP and the fluorescent label. A sandwich immunoassay based on this setup achieved an LOD of 3.1 pM AFP.

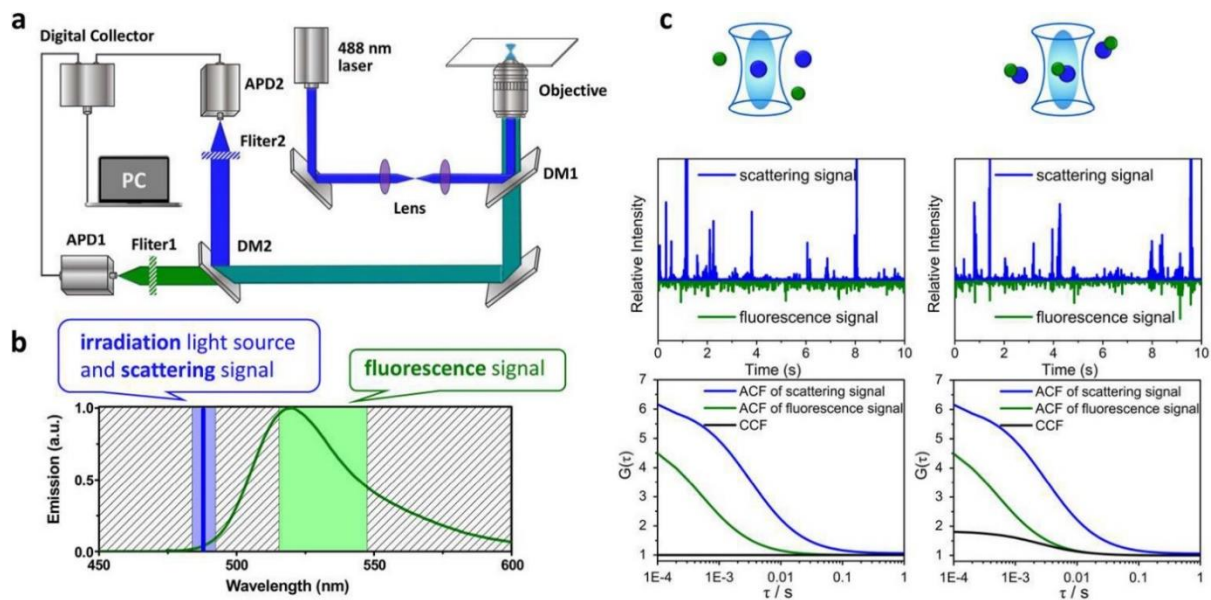


Figure 14: (a) Scheme of fluorescence and scattering light cross-correlation spectroscopy (FSCCS). (b) Spectral separation of excitation and emission wavelengths. (c) Scattering and fluorescence signals and their correlation curves for labeled species diffusing independently (left) or linked (right). ACF: auto-correlation curves; CCF: cross-correlation curves. Reprinted with permission from ¹¹⁹. Copyright 2017 American Chemical Society.

Surface Plasmon Microscopy

The adsorption of individual plasmonic NPs can be followed in real-time using surface plasmon microscopy.¹²⁰ Changes in surface plasmon resonance (SPR) properties affect the reflected light intensity, which is detected by an image sensor.¹²¹ The measurement can be based either on the setup with a high numerical aperture (NA) microscope objective¹²² or on the standard Kretschmann configuration.¹²³ While a high-NA objective provides high resolution, the field of view is typically limited to an area of 0.01 mm². On the other hand, the Kretschmann configuration provides a wider field of view (over 1 mm²), but imperfections in the arrangement of object, lens, and image planes degrade the performance and resolution of the optical system. Surface plasmon resonance (SPR) imaging is typically used for the characterization of homogenous films, where high resolution is not necessary.¹²⁴

The group of Mirsky developed a wide-field approach for the detection and quantification of single NPs¹²¹ and applied it for the analysis of Au and Ag NPs in complex samples such as wine, apple juice and sunscreen (**Figure 15**).¹²⁵ The large imaging area of the wide-field setup increased the probability of detecting single NP adsorption events at low concentrations. The signal strength was mainly determined by the size and refractive index of the NPs, the distance from the plasmonic substrate and the performance of the optical system. The adsorption of a

single NP, however, only led to a small signal change. To enhance the sensitivity, differential images of local temporal and spatial intensity changes were evaluated based on the changes between the two subsequently captured frames. The method provided an LOD of 10^6 NPs/mL (~ 1.6 fM) and a working range of 10^6 – 10^{10} NPs/mL with 1 min measurement time. The sensitivity can be further improved by increasing the analysis time or the sensing surface area.

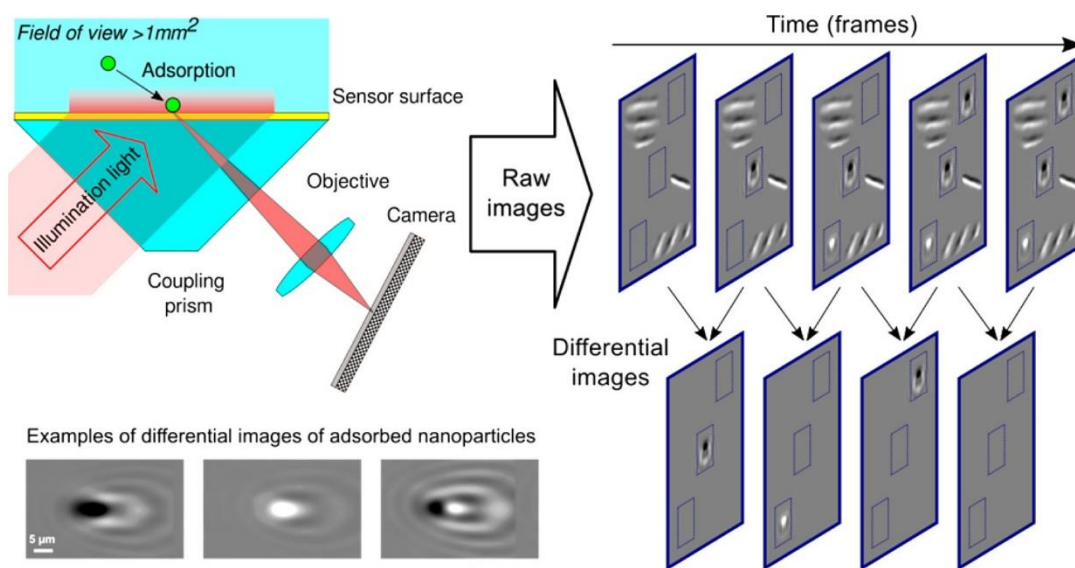


Figure 15: Surface plasmon microscopy for the detection of single NPs adsorbing to the sensor surface. Reprinted from ¹²⁵.

Furthermore, the combination of surface plasmon microscopy with electrochemical analysis allowed to determine the composition of NPs.¹²⁶ This technique was applied to the analysis of Ag and Cu NPs and achieved an LOD of 10^4 NPs/mL. Surface plasmon microscopy was also employed for single-molecule detection of DNA hybridization,¹²⁷ and the application to single-molecule immunoassays would be straightforward.

Detection in Microarrays

Sevenler et al.¹²⁸ used Au nanorods as labels for the detection of hepatitis B virus surface antigen (HBsAg) on a protein microarray. An anti-HBsAg antibody was spotted on an interferometric reflectance imaging sensing (IRIS) substrate and incubated with the antigen followed by the addition of Au nanorods coated with another anti-HBsAg Ab, and the particles were counted in an automated imaging device under illumination by circular polarized light. Light reflected by the IRIS substrate was also polarized, but the light scattered by Au nanorods

was linearly polarized along the longitudinal axis of the NPs and was separated from the reflected light. The assay achieved an LOD of 3.2 pg/mL.

Belushkin et al.¹²⁹ designed a sandwich immunoassay for C-reactive protein (CRP). A gold nanohole array was coated with an anti-CRP capture antibody. The array was immersed in the analyte medium, and the array was washed and immersed in a dispersion of Au NPs that were coated with an anti-CRP antibody. Au NPs in or close the nanoholes could be detected because of a decrease in the extraordinary optical transmission (EOT). EOT is an SPR-based phenomenon which occurs if light passes through a subwavelength-sized regularly shaped metallic film. Particles too far away from nanoholes were not detected. Single Au NPs were counted under a microscope.

V.8. Bead Labels

V.8.1. Fluorescence Microscopy

While it is not possible to make a sharp separation between NPs and beads, here we define beads as labels that are larger than 100 nm in diameter. The larger size, on the one hand, offers an easier way for detection but, on the other hand, impedes the accessibility of the label to the analyte. The Lövgren group¹³⁰ was one of the first to employ a bead label for the detection of single analyte molecules. A europium-doped bead—with a diameter of 107 nm very close to NP size—was detected individually by TRF. A microtiter plate was coated with a monoclonal anti-PSA antibody and biotinylated PSA was added, followed by the streptavidin-coated Eu bead. The analyte binding was measured in the analog mode by time-resolved fluorometry and in the digital mode by counting single bead labels under a time-resolved microscope equipped with a 10× objective and a CCD camera. The assay achieved an LOD of 0.38 pg/mL of biotinylated PSA.

Wu et al.¹³¹ used color-encoded magnetic beads to simultaneously detect single virus particles of three different types of avian influenza (**Figure 16**). Polystyrene beads were coated with γ -Fe₂O₃, followed by QDs with different emission colors (green, yellow, red) and with antibodies against avian influenza. The three bead types, each one specific for a certain avian influenza type, were dispersed in the sample and magnetically separated. The beads were then loaded onto a PDMS microarray that was coated with antibodies for the different virus types. After washing, only beads that captured a virus particle remained in the array. The assay resulted in an LOD of 0.02 pg/mL.

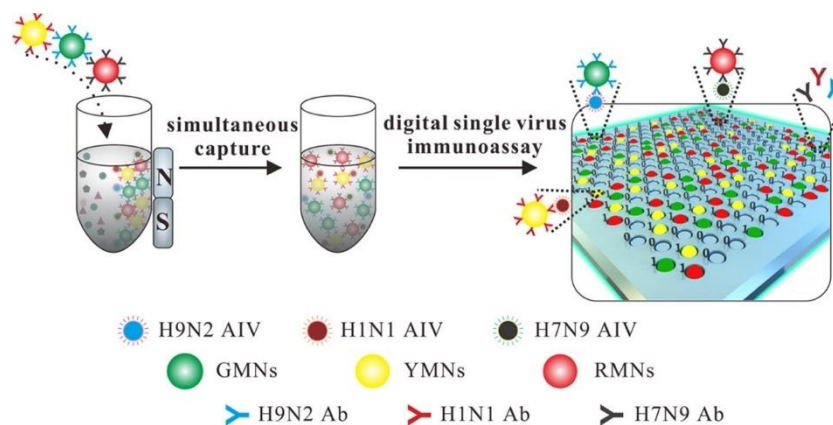


Figure 16: Scheme of the multiplex assay for avian influenza viruses. Color encoded magnetic spheres—each of them coated with a specific anti-avian influenza virus—are dispersed in the analyte medium. After magnetic purification, the particles were loaded onto a PDMS array and digitally counted. Reprinted with permission from ¹³¹. Copyright 2019 American Chemical Society.

Fan et al.¹³² embedded UCNPs of different colors and in different ratios into polymer microbeads to generate codes for the multiplexed detection of DNA. The combination of n intensity levels with m colors resulted in (n^m-1) unique codes. The labels were detected under 980-nm excitation at the single bead level by confocal microscopy. The DNA sequence was identified based on the upconversion encoding signal, while the presence and amount of the target sequence was indicated by conventional fluorescent dyes.

Gite et al.¹³³ developed a sandwich assay consisting of (1) a magnetic particle, (2) an anti-*C. difficile* capture antibody, (3) *C. difficile*, (4) an anti-*C. difficile* detection antibody, and (5) a fluorescent microparticle. A mixture of a visible light absorbing dye-cushion reagent and the density agent iodixanol was dried on the bottom of each microwell (**Figure 17**). The immunoreagents were added, and the magnetic beads were pulled to the bottom of the microplate with a magnet. The dye absorbed all visible light and stayed at the bottom due to the density agent resulting in a strong reduction of the background fluorescence of unbound fluorescent particles. Single fluorescent beads appeared as bright pixels on a digital camera chip.

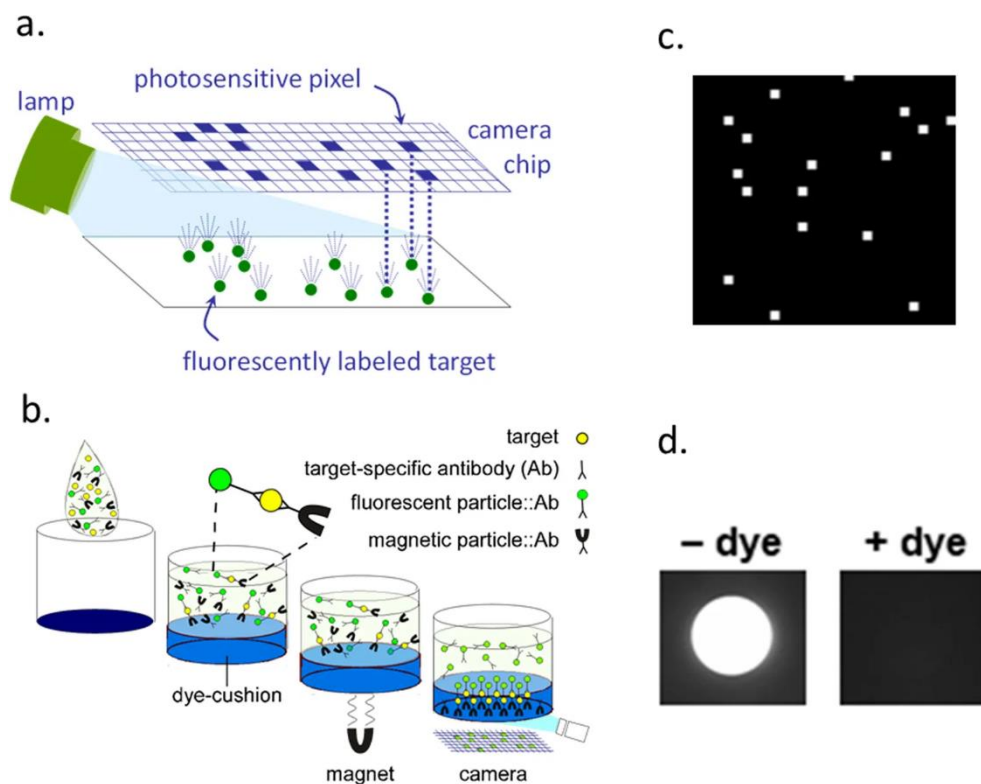


Figure 17: (a) Detection of single fluorescent beads on one or a small group of pixels of a camera chip without the need for microscope magnification. (b) After immunocomplex formation, a magnet immobilizes the magnetic beads at the bottom of a microwell. Only fluorescent beads near the surface are excited because the dye absorbs the excitation light that penetrates deeper into the well. (c) Fluorescent beads appear as bright pixels on the digital camera. (d) A comparison of a well with and without dye shows the efficiency of a dye cushion layer. Reprinted from ¹³³ with the permission of Creative Commons Attribution 4.0 International License.

V.8.2. Bright-Field Microscopy

Tekin et al.¹³⁴ developed a microfluidic-based magnetic bead counting assay for the detection of proteins in serum (**Figure 18**). Magnetic beads (2.8 μm) were modified with a capture antibody to preconcentrate a target protein from fetal bovine serum. The beads were flown over a glass surface patterned with smaller antibody-modified magnetic beads (1 μm). The larger beads were attracted to the surface by a magnetic field, which allowed them to “roll” over multiple smaller beads due to dipolar magnetic forces. An immunocomplex formed when the antigen had a suitable orientation on the bead. The drag force caused by the flow needed to be high enough to release the particles when only dipolar forces were present. The analyte concentration was determined by counting the bound large beads on a conventional optical microscope. The combination of a magnetic preconcentration step and digital counting of

bound magnetic beads in a microfluidic chip afforded an LOD of 60 aM (~ 1 fg/mL) TNF- α , equivalent to ~ 200 molecules in 5 μ L of the sample.

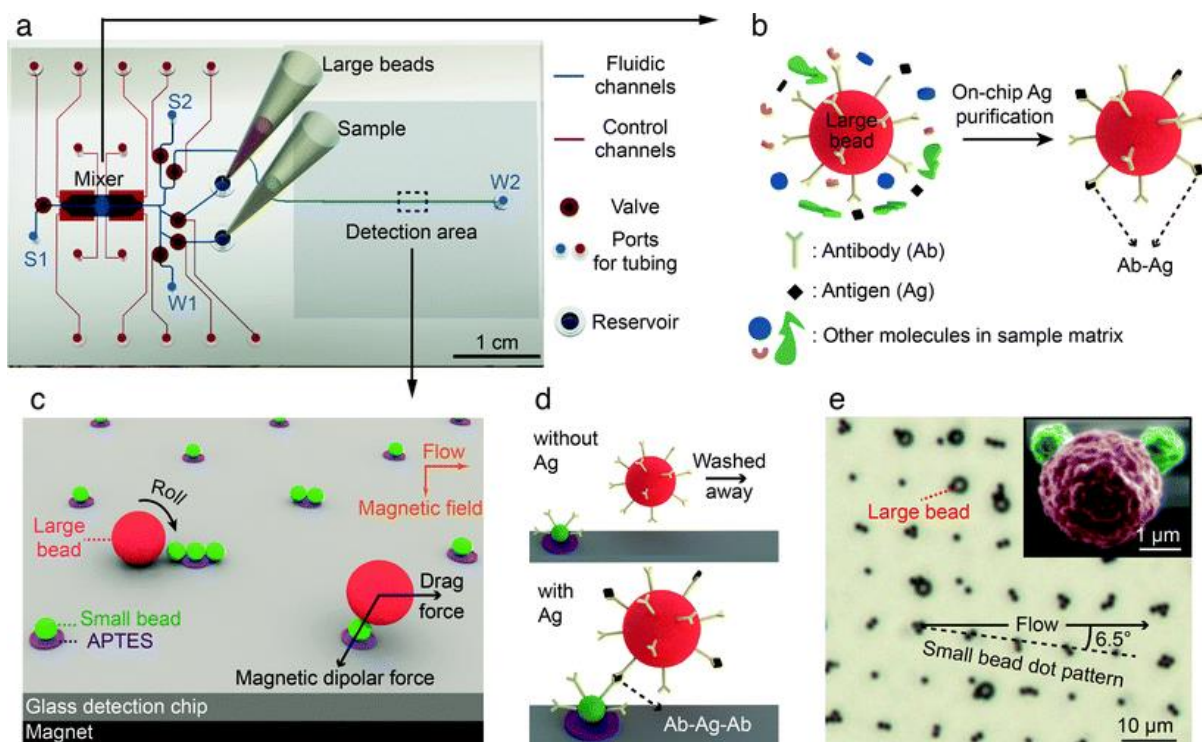


Figure 18: (a) Scheme of microfluidic chip. (b) Large magnetic beads separated the target protein from the matrix. (c) The large beads roll over the patterned smaller beads, magnetically attracted to the surface. (d) A sandwich immunocomplex is formed when the antigen and the large bead have a suitable orientation. (e) Optical micrograph of the captured large beads on the patterned array of small beads. A colored SEM photograph in the inset shows the large bead captured on the small beads. Reprinted with permission from¹³⁴. Copyright 2013 Royal Society of Chemistry.

V.8.3. Dark-Field Microscopy

Tethered particle monitoring is a biophysical technique used to characterize changes in the length of a polymer tethered to a particle on one end and a surface on the other end. The Brownian motion of the particle limited by the tether is usually monitored optically. Schafer et al.¹³⁵ introduced tethered particle monitoring in 1991 to follow the transcription of a DNA template bound to an Au NP by RNA polymerase immobilized on a glass slide. Various modifications of the principle are possible and can be used for monitoring single-molecule binding events in an immunoassay.

Visser et al.¹³⁶ utilized the tethered particle monitoring in an aptamer-based sandwich assay for thrombin. Magnetic beads were modified with an anti-thrombin capture aptamer and the glass surface of a flow chip by a detection aptamer. The beads were tethered to the glass surface by a 40-nm long dsDNA strand. When the analyte was captured between the aptamers, the bead was anchored onto the surface, and its mobility was strongly reduced (**Figure 19**), which was monitored over time by dark-field microscopy. The binding and unbinding events of hundreds of beads were detected simultaneously. The rate of switching between the two states, and especially the lifetime of the unbound state was dependent on the concentration of thrombin in a range of 10–300 nM. As the interaction was reversible and all recognition elements were bound in the flow cell, the system is amenable for continuous biomarker monitoring.

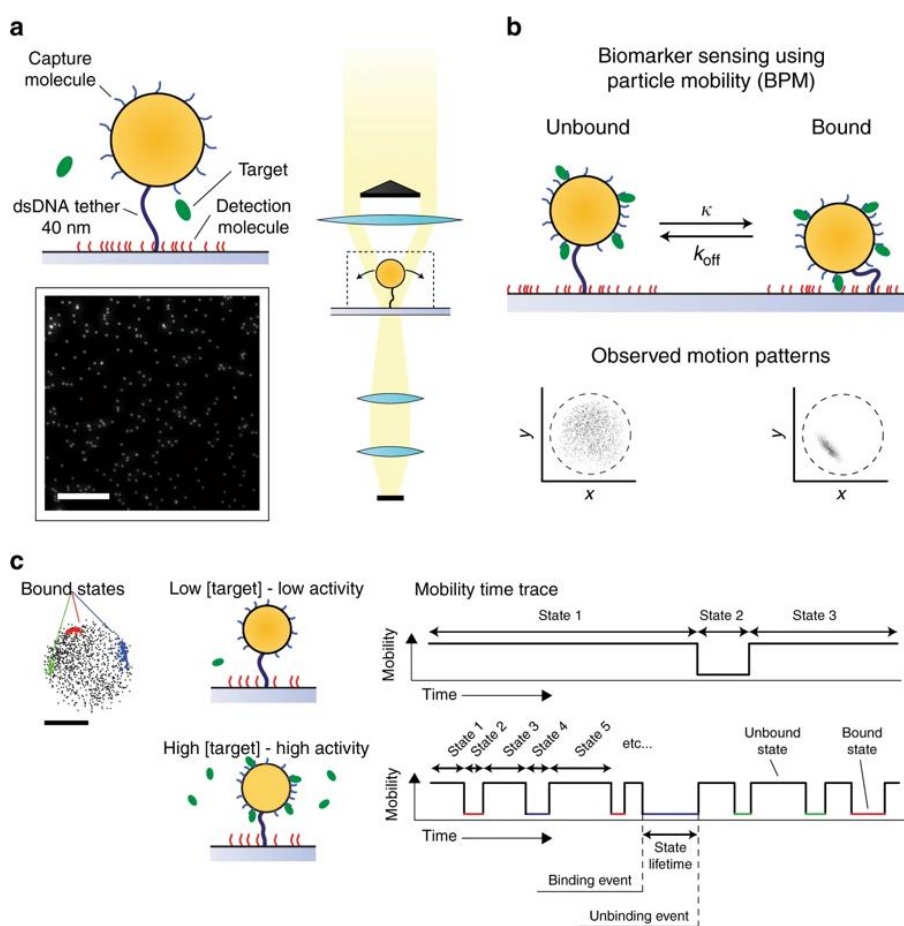


Figure 19: (a) Particles (orange) are modified by capture aptamers (blue) and tethered to the substrate by a 40-nm dsDNA strand (black). The substrate is decorated with detection aptamers (red). The image was recorded by dark-field microscopy (scale bar: 50 μm). (b) After thrombin (green) binding, the particle's movement is restricted, which changes the motion pattern. (c) The particle mobility is continuously analyzed for hundreds of particles in parallel. The mobility time traces of low and high analyte concentration reveal individual binding and unbinding events. Reprinted from ¹³⁶ with the permission of Creative Commons Attribution 4.0 International License.

Silver et al.¹³⁷ developed a sandwich immunoassay for the detection of PSA based on tethered particle monitoring. Magnetic beads (2.8 μm) with immobilized antibody captured PSA from the sample matrix. After magnetic separation, the beads were incubated with the biotinylated detection antibody and introduced into a flow cell. The beads carrying the immunocomplex were captured by a streptavidin-ended DNA tether. This tether allowed the beads to move 12 μm back and forth when the flow direction changed by manual syringe operation. Thus, specifically bound beads were distinguished from nonspecifically bound beads and counted using a low-magnification (10 \times) dark-field microscope. The assay achieved an LOD of 1 pM PSA.

Akama et al.¹³⁸ combined tethered particle monitoring with an immunoassay in femtoliter arrays. In the “digital homogeneous non-enzymatic immunosorbent assay” (HoNon-ELISA), antibody-decorated magnetic particles were used to separate the analyte from the sample matrix. Then, they were magnetically pulled into the microreactors of a femtoliter array chip for the confinement of the antibody-antigen reaction. The antigen was recognized by another antibody immobilized through a PEG linker to the well surface. The sandwich complex tethered the particle to the surface and limited its Brownian motion, which was monitored for thousands of wells in parallel using bright-field or dark-field microscopy and particle tracking analysis. According to the movement patterns, selectively captured particles were discerned from non-specifically bound ones, and individual binding events were counted. The procedure did not require any washing or signal amplification steps and reached an LOD of 0.093 pg/mL PSA.

V.9. Label-Free Detection

Most label-free detection schemes are based on plasmonic effects. While chapter 6.3 describes the use of plasmonic NPs as labels, here we focus on the arrangement of plasmonic nanostructures to generate local hot spots, which are very sensitive to analyte binding.¹³⁹ Localized surface plasmon resonance (LSPR) has been used to follow the changes of local refractive indices near plasmonic NPs. There are various possibilities to link the refractive index changes to the presence of the analyte, as demonstrated by a large number of reports of bulk LSPR-based immunoassays.^{20a, 140} The high sensitivity of LSPR can be exploited to characterize statistical distributions of molecular properties and to follow single-molecule binding events.¹⁴¹ Beuwer et al.¹⁴² used correlated atomic force microscopy (AFM) and optical microscopy to study how the binding location affects the changes of LSPR signals. Au NPs were used as a model analyte and bound to single-crystal Au nanorods using cysteine-cysteine coupling.¹⁴³ In the correlative approach, AFM was used to study the binding locations, and the plasmon shifts were evaluated by single-particle spectroscopy. A broad distribution of LSPR

shifts was observed for similar binding locations, which was attributed to the size-dispersion of the Au NPs. It was found that larger plasmon shifts occur after binding of the Au NPs to the tip of the rod as compared to its sides. Since the probability of binding to various locations of a nanorod is different,¹⁴⁴ the knowledge of the binding location can help not only to determine the level of sensor response but also to evaluate the binding constants. Site-specific functionalization techniques can be used to maximize the sensitivity and reduce the signal distribution.¹⁴⁵ Lee et al.¹⁴⁶ designed plasmon rulers as sensors for the detection of single molecules of matrix metalloproteinase (MMP3). When two noble metal NPs exhibiting LSPR approach each other, their individual surface plasmon resonances couple, which generates a shift in the scattering spectrum and can be detected by dark-field microscopy.

Beuwer et al.¹⁴⁷ used Au nanorods to detect the interaction of biotin and an anti-biotin antibody (**Figure 20**). They functionalized the tips of Au nanorods with thiolated biotin and detected the change in the scattering intensity of individual nanorods. When the plasmon wavelength of a particle was shorter than the 795-nm illumination light, the scattered signal increased upon antibody binding. The intensity change was stepwise and irreversible due to the strong biotin-antibody interaction. The binding constants (k_{on}) were calculated from the mean waiting times and followed a Poisson distribution. The LOD was influenced by the number of binding events in a certain timeframe. As low analyte concentration resulted in long waiting times, a high number of particles had to be observed, which was limited by the field of view of the objective (ca. 50 000 NPs). The high rate of binding events at high analyte concentrations required a fast camera image acquisition. The shorter exposure times were compensated by a higher excitation power, which was limited by photothermal heating of the particles.

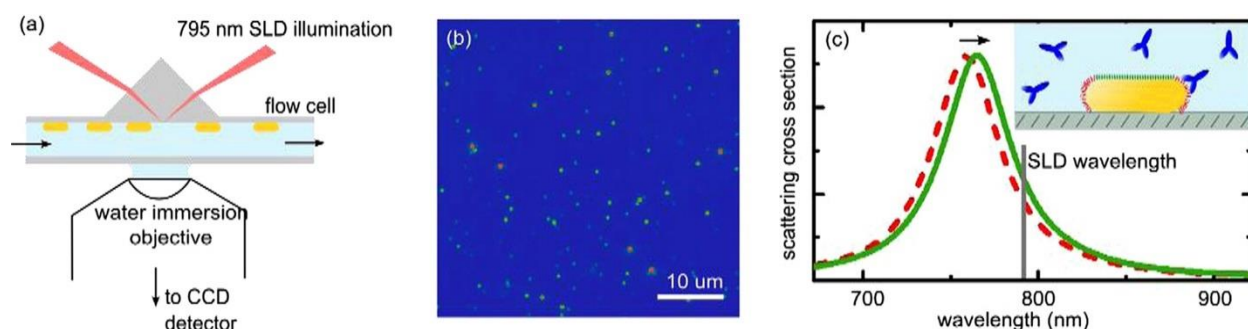


Figure 20: (a) Scheme of dark-field microscope setup with a superluminescent diode (SLD). (b) Image of surface-immobilized gold nanorods shown in pseudocolors. (c) The tips of the gold nanorods are functionalized by receptors (red), while the sides are blocked by tetraethylene glycol (green). Individual antibody binding event result in a red shift of the plasmon resonance. The vertical gray line indicates the SLD center wavelength. Reprinted with permission from ¹⁴⁷. Copyright 2015 American Chemical Society.

Another emerging label-free technique for the detection of single molecules are whispering gallery mode (WGM) microring resonators, which trap light due to multiple total internal

reflections at a curved boundary (**Figure 21**). Analyte binding to the optical ring resonators results in a shift of the resonance wavelength. Arrays of microring resonators were used for the multiplexed detection of five protein biomarkers.¹⁴⁸ Single-molecule sensitivity for protein or DNA has been achieved. More recently, even single ions such as Hg^{2+} and Zn^{2+} have been detected using a gold antenna coupled to a WGM microresonator.¹⁴⁹

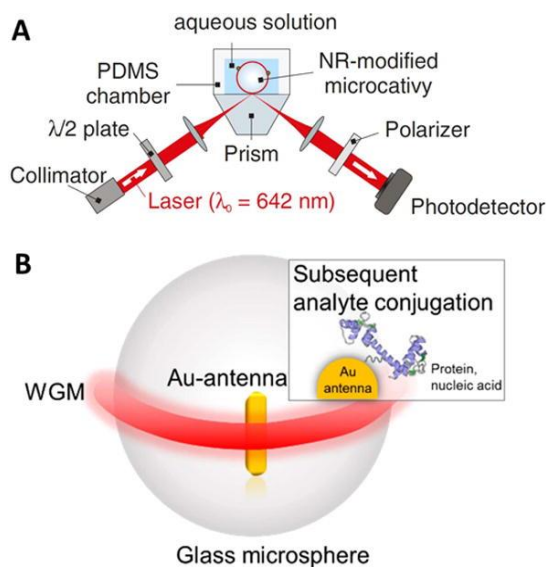


Figure 21: Scheme of optical ring resonators. (A) Instrument setup of coupling a laser into an optical ring resonator. (B) A glass microsphere serves as an optical microcavity to measure physical, chemical and biological entities. Near total internal reflection of light results in an optical resonance (WGM, red). The WGM couples to a gold nanorod where it excites plasmon resonance. Single analyte molecules can be detected if they bind inside plasmonic hot spots. Reprinted with permission from ¹⁵⁰. Copyright 2017 IOP Publishing.

Surface-enhanced (SERS) and tip-enhanced Raman spectroscopy (TERS) also enable the label-free detection of single protein molecules.¹⁵¹ It is, however, difficult to employ these techniques for measuring protein concentrations in routine analytical applications.

V.10. Summary and Outlook

As new and low-abundance disease markers are investigated, there is a growing need for developing more sensitive detection methods. **Tables 1–3** summarize various assay types for the digital readout of analytes that have been discussed in the review.

Table 1: Digital assays for cancer biomarkers. The LODs were converted into molar concentrations wherever applicable.

Analyte	Assay type	Matrix	LOD	Working range	Assay time (min)	Sample volume	Reference
AFP	FCCS with QDs	Buffer	20 pM	20 pM – 5 nM	120	10 μ L	⁹⁵
AFP	Resonance light scattering correlation spectroscopy	Buffer	1 pM	1 pM – 1 nM	50	20 μ L	¹¹⁷
AFP	Fluorescence and scattering light cross correlation spectroscopy	Buffer	3.1 pM	5 – 580 pM	120	10 μ L	¹¹⁹
AFP	Fluorescence aided multiplexed molecule sorting	50% human serum in buffer	100 pM	100 pM – 10 nM	120	n/a	⁷³
AFP	Immunoassay based on spectral blue shifts of QDs	25% plasma in buffer	3.4 fM	10 fM – 100 pM	n/a	n/a	⁸⁶
AFP	Scattering-based quantitative single-particle intensity measurement	Human serum	5.9 pM	0 – 300 pM	n/a	n/a	¹⁰⁷
AFP	Light scattering correlation spectroscopy	Buffer	100 pM	100 pM – 10 nM	120	20 μ L	¹¹⁸
CEA	Counting of spatially overlapping two-color QDs	Plasma in buffer	6.1 pM	10.4 – 666.7 pM	30	n/a	⁸⁵
CEA	Fluorescence aided multiplexed molecule sorting	50% human serum in buffer	14 pM	10 pM – 1 nM	120	n/a	⁷³
CEA	Immunoassay based on spectral blue shifts of QDs	25% plasma in buffer	6.7 fM	10 fM – 100 pM	n/a	n/a	⁸⁶
CEA	Scattering-based quantitative single-particle intensity measurement	Human serum	1.7 pM	0 – 300 pM	n/a	n/a	¹⁰⁷
Exosomes	Droplet microfluidics	n/a	17 aM	10 aM – 1 pM	n/a	n/a	⁵²
PSA	Simoa	25% new born calf	98 fM	100 fM – 500 pM	n/a	n/a	³⁹

		serum in buffer					
PSA	Droplet array	Buffer	2 aM	1 aM – 100 fM	120	n/a	⁴⁵
PSA	Femtoliter microfluidic droplets	Buffer	46 fM	0.046 – 4.62 pM	270	200 μ L	⁵¹
PSA	Droplet-based digital immunoPCR	Buffer	17 pM	17 pM – 1 nM	120	30 μ L	⁵⁸
PSA	Digital ULISA with UCNPs	25% bovine serum in buffer	42 fM	350 fM – 35 pM	150	100 μ L	^{22a}
PSA	Digital ULISA with streptavidin-coated UCNPs	25% bovine serum in buffer	800 aM	3.5 fM – 3.5 pM	210	100 μ L	^{22b}
PSA	Single-UCNP enumeration	Buffer	1 pM	0 – 500 pM	120	n/a	¹⁰¹
PSA	Au NP enumeration with dark-field microscope	Buffer	35 pM	35 – 700 pM	170	95 μ L	¹⁰⁸
PSA	Counting of gold nanorods with dark-field microscopy	Buffer	280 aM	350 aM – 350 fM	195	100 μ L	¹⁰⁹
PSA	Digital HoNon-ELISA	Buffer	3.2 fM	3.2 fM – 3.2 pM	n/a	n/a	¹³⁸
PSA	Tethered-bead immunoassay	Buffer	1 pM	1 – 10 pM	n/a	50 μ L	¹³⁷
PSA	Simoa	25% bovine serum	50 aM	100 aM – 1 pM	360	100 μ L	³⁸
PSA	Fluorescence aided multiplexed molecule sorting	50% human serum in buffer	100 pM	100 pM – 10 nM	120	n/a	⁷³
PSA	Scattering-based quantitative single-particle intensity measurement	Human serum	3.3 pM	0 – 300 pM	n/a	n/a	¹⁰⁷
TNF- α	Simoa	25% bovine serum	150 aM	100 aM – 1 pM	360	100 μ L	³⁸

Table 2: Summary of digital assays for other clinical biomarkers. The LODs were converted into molar concentrations wherever applicable.

Analyte	Assay type	Matrix	LOD	Working range	Assay time	Sample volume	Reference
ATP	Fluorescence colocalization	Buffer	100 fM	1 pM – 5 nM	45	25 μ L	⁶⁵
Contactin-2	FCS	17% CSF in buffer	1.5 pM	n/a	60	10 μ L	⁷⁶
CRP	Microarray based plasmonic biosensor	Buffer	225 fM	n/a	120	100 μ L	¹²⁹
cTnI	Erenna	25% human plasma in buffer	74 fM	n/a	n/a	10 μ L	⁶⁸
cTnI	Erenna bead-based	25% human plasma in buffer	8.7 fM	10 fM – 500 pM	180	100 μ L	⁶⁹
17- β estradiol	Light scattering correlation spectroscopy	Buffer	10 pM	10 pM – 1 nM	120	20 μ L	¹¹⁸
FSH	Single-molecule fluorescence counting	n/a	34 fM	100 fM – 1 nM	n/a	100 μ L	⁷²
hCG	FCCS	Buffer	100 pM	100 pM – 10 nM	40	n/a	⁸⁰
IL-6	Proximity ligation assay	n/a	5 fM	10 fM – 1 nM	n/a	n/a	⁵⁹
IL-6	Counting of Au NPs using dark-field microscopy with digital color analysis	Buffer	4.76 nM	n/a	n/a	n/a	¹¹⁰
Mutant huntingtin	Erenna	30% cerebrospinal fluid in buffer	40 fM	40 fM – 1 nM	n/a	45 μ L	⁷¹
NF-L	Simoa	25% human serum in buffer	4.3 fM	4.2 fM – 26 pM	n/a	152 μ L	⁴²
PrP	FCCS	Buffer	2 nM	n/a	40	n/a	⁸⁰
Synthetic A β dimers	Single-molecule counting fluorescence immunoassay	Buffer	0.18 pM	n/a	o.n. + 90 min	20 μ L	⁷⁰
Tau	Simoa	25% human plasma in buffer	180 – 250 aM	250 aM – 15 pM	n/a	152 μ L	⁴³

Thrombin	Aptamer-based assay using QDs	Buffer	2.6 nM	5 – 500 nM	60	10 μ L	⁹¹
Thrombin	Core-shell based aptasensor using dark-field microscopy	Buffer	2.54 fM	6 – 100 fM	30	n/a	¹¹³
Thrombin	Aptamer sandwich sensor with Au NP oligomers	Buffer	10 fM	20 fM – 20 nM	n/a	n/a	¹¹⁴
Thyroid stimulating hormone	Upconversion cross-correlation spectroscopy	Buffer	15 mIU/L	28.8 – 2880 mIU/L	30	30 μ L	¹⁰²
TNF- α	Magnetic bead surface coverage assay	Serum	60 aM	n/a	20	5 μ L	¹³⁴
Tumor suppressor protein p53	Single-molecule microarray	Buffer	35 fM	100 fM – 100 pM	n/a	0.2 nL	⁶⁴

Table 3: Digital assays for bacteria, viruses, toxins and other contaminants. The LODs were converted into molar concentrations wherever applicable.

Analyte	Assay type	Matrix	LOD	Working range	Assay time	Sample volume	Reference
Acetamiprid	Single-molecule aptasensor	Chicken extract 100 \times diluted in buffer	350 nM	500 fM – 50 pM	n/a	n/a	⁶⁶
Adenosine,	Single-molecule aptasensor	Chicken extract 100 \times diluted in buffer	300 fM,	500 fM – 50 pM	n/a	n/a	⁶⁶
Avian influenza H9N2, H1N1, H7N9	Multiplexed single-virus immunoassay	Buffer	0.02 μ g/mL	n/a	60	n/a	¹³¹
<i>C. difficile</i> toxin B	Digital MultiPath immunoassay	8% pooled stool sample diluted in buffer	170 fM	100 fM – 1 nM	30	100 μ L	¹³³
Cocaine	Single QD-based aptamer nanosensor	Buffer	500 nM	500 nM – 10 μ M	n/a	n/a	⁸⁸

Fumonisin B ₁	FCS	Buffer	1.4 nM	1.4 nM – 35 nM	15	9 μL	⁷⁸
Influenza A nucleoprotein	Microfluidic digital HEBA	Buffer	4 aM	10 aM – 10 pM	10	10 μL	⁵⁴
Hepatitis B surface antigen	Bead-based digital ELISA	Buffer	139 aM	100 aM – 1 pM	210	n/a	²⁹
Hepatitis B virus surface antigen	Digital microarray with interferometric detection of plasmonic nanorods	Buffer	126 fM	100 fM – 100 nM	270	n/a	¹²⁸
Herpes simplex virus	Fluorescence coincidence detection	Buffer	50 fM	100 fM – 100 pM	180	n/a	⁷⁹
HIV p24 capsid	Simoa	Human plasma	117 aM	100 aM – 100 fM	210	100 μL	⁴¹
PCB-77	Single-molecule aptasensor	Chicken extract 100× diluted in buffer	720 nM	500 fM – 50 pM	n/a	n/a	⁶⁶
Respiratory syncytial virus	Counting assay with color-coded NPs	Buffer	20–30 fM	100 fM – 100 pM	100	n/a	⁸⁷
Ricin	Simoa	Buffer	166 aM	100 aM – 100 pM	64	n/a	⁴⁴

Single-molecule immunoassays have gained popularity in clinical research and diagnostics and some platforms have been commercialized. Commercial single-molecule immunoassays offer complete solutions for the detection of a wide range of biomarkers in clinical research, including cytokines, hormones, and signaling proteins. As of September 2019, Merck offered 49 ready-to-use immunoassay kits for the Erenna system,¹⁵² and Quanterix offered 130 kits for the Simoa platform.¹⁵³ Furthermore, custom development services and kits for in-house development of new assays by the customer are available.

Although the detection of individual optical detection labels is relatively easy using state-of-the-art detectors, it is still a challenge to achieve a superior sensitivity of single-molecule assays compared to analog assays. Recently, the advantages of analog and digital detection modes have been compared systematically using the same TIRF platform.¹⁵⁴ The performance of different assays was systematically compared using the same analyte,¹⁵⁵ and three immunoassay platforms were compared for their ability to detect subpicomolar concentrations of the protein biomarker GAD65.¹⁵⁶

Another important challenge is the simplicity and robustness of the assay procedure. Even though single-molecule assays can reach extremely high sensitivity, the need for highly sophisticated instrumentation, well-trained personnel, or long operation times can impede their commercialization. Despite these challenges, single-molecule assays are successfully finding

their way into real-world applications and can replace conventional methods such as the ELISA or electrochemiluminescence assays. The possibility to detect only a few biomarker molecules in a sample opens up many new possibilities for enhanced diagnostics.

V.11. Acknowledgements

Hans H. Gorris acknowledges funding from the German Research Foundation (DFG Heisenberg Program: GO 1968/7-1). This work was further supported by the Ministry of Education, Youth and Sports of the Czech Republic within the program INTER-ACTION (LTAB19011).

V.12. References

- 1 a) S. Weiss, *Science* **1999**, 283, 1676-1683; b) W. E. Moerner, D. P. Fromm, *Rev. Sci. Instrum.* **2003**, 74, 3597-3619; c) C. Joo, H. Balci, Y. Ishitsuka, C. Buranachai, T. Ha, *Annu. Rev. Biochem.* **2008**, 77, 51-76.
- 2 a) L. Cohen, D. R. Walt, *Chem. Rev.* **2019**, 119, 293-321; b) P. Holzmeister, G. P. Acuna, D. Grohmann, P. Tinnefeld, *Chem. Soc. Rev.* **2014**, 43, 1014-1028; c) L. Chang, D. M. Rissin, D. R. Fournier, T. Piech, P. P. Patel, D. H. Wilson, D. C. Duffy, *J. Immunol. Methods* **2012**, 378, 102-115; d) J. J. Gooding, K. Gaus, *Angew. Chem. Int. Ed.* **2016**, 55, 11354-11366; e) Y. F. Wu, R. D. Tilley, J. J. Gooding, *J. Am. Chem. Soc.* **2019**, 141, 1162-1170.
- 3 a) R. J. Yu, Y. L. Ying, Y. X. Hu, R. Gao, Y. T. Long, *Anal. Chem.* **2017**, 89, 8203-8206; b) A. Arima, I. H. Harlisa, T. Yoshida, M. Tsutsui, M. Tanaka, K. Yokota, W. Tonomura, J. Yasuda, M. Taniguchi, T. Washio, M. Okochi, T. Kawai, *J. Am. Chem. Soc.* **2018**, 140, 16834-16841.
- 4 a) U. Wienken, H. E. Gaub, *Biophys. J.* **2013**, 105, 2687-2694; b) S. Mandal, D. Koirala, S. Selvam, C. Ghimire, H. B. Mao, *Angew. Chem. Int. Ed.* **2015**, 54, 7607-7611.
- 5 S. Subramanian, H. Y. Wu, T. Constant, J. Xavier, F. Vollmer, *Adv. Mater.* **2018**, 30, 21.
- 6 I. Surugiu, B. Danielsson, L. Ye, K. Mosbach, K. Haupt, *Anal. Chem.* **2001**, 73, 487-491.
- 7 J. Foote, H. N. Eisen, *Proc. Natl. Acad. Sci. U. S. A.* **1995**, 92, 1254-1256.
- 8 N. M. Green, *Methods Enzymol.* **1990**, 184, 51-67.
- 9 R. S. Yalow, S. A. Berson, *Nature* **1959**, 184 (Suppl 21), 1648-1649.
- 10 R. Peltomaa, E. Benito-Pena, M. C. Moreno-Bondi, *Anal. Bioanal. Chem.* **2018**, 410, 747-771.
- 11 A. Kunze, L. Pei, D. Elsassner, R. Niessner, M. Seidel, *J. Virol. Methods* **2015**, 222, 132-137.
- 12 N. L. Anderson, N. G. Anderson, *Mol. Cell. Proteomics* **2002**, 1, 845-867.
- 13 a) S. M. Hanash, S. J. Pitteri, V. M. Faca, *Nature* **2008**, 452, 571-579; b) N. L. Henry, D. F. Hayes, *Mol. Oncol.* **2012**, 6, 140-146; c) M. J. Aernecke, J. Guo, S. Sonkusale, D. R. Walt, *Anal. Chem.* **2009**, 81, 5281-5290; d) D. R. Walt, *J. Clin. Invest.* **2019**, 129, 3472-3473.
- 14 J. F. Rusling, C. V. Kumar, J. S. Gutkind, V. Patel, *Analyst* **2010**, 135, 2496-2511.
- 15 A. St John, C. P. Price, *Clin. Biochem. Rev.* **2014**, 35, 155-167.
- 16 D. J. Litman, T. M. Hanlon, E. F. Ullman, *Anal. Biochem.* **1980**, 106, 223-229.
- 17 L. Hood, *Annu. Rev. Anal. Chem.* **2008**, 1, 1-43.
- 18 H. Siitari, I. Hemmila, E. Soini, T. Lovgren, V. Koistinen, *Nature* **1983**, 301, 258-260.

- 19 M. Rui, C. S. Hampe, C. Wang, Z. D. Ling, F. K. Gorus, A. Lernmark, D. G. Pipeleers, P. E. M. De Pauw, *J. Immunol. Meth.* **2007**, *319*, 133-143.
- 20 a) Z. Farka, T. Juřík, D. Kovář, L. Trnková, P. Skládal, *Chem. Rev.* **2017**, *117*, 9973-10042; b) M. Pastucha, Z. Farka, K. Lacina, Z. Mikušová, P. Skládal, *Microchim. Acta* **2019**, *186*, 26.
- 21 H. H. Gorris, O. S. Wolfbeis, *Angew. Chem. Int. Ed.* **2013**, *52*, 3584-3600.
- 22 a) Z. Farka, M. J. Mickert, A. Hlaváček, P. Skládal, H. H. Gorris, *Anal. Chem.* **2017**, *89*, 11825-11830; b) M. J. Mickert, Z. Farka, U. Kostiv, A. Hlaváček, D. Horák, P. Skládal, H. H. Gorris, *Anal. Chem.* **2019**, *91*, 9435-9441.
- 23 C. Hofmann, A. Duerkop, A. J. Baeumner, *Angew. Chem. Int. Ed.* **2019**, *58*, 12840-12860.
- 24 a) A. Shalev, A. H. Greenberg, P. J. Mcalpine, *J. Immunol. Methods* **1980**, *38*, 125-139; b) C. C. Harris, R. H. Yolken, H. Krokan, I. C. Hsu, *Proc. Natl. Acad. Sci. U. S. A.* **1979**, *76*, 5336-5339.
- 25 M. Böhmer, J. Enderlein, *ChemPhysChem* **2003**, *4*, 793-808.
- 26 P. Haas, P. Then, A. Wild, W. Grange, S. Zorman, M. Hegner, M. Calame, U. Aebi, J. Flammer, B. Hecht, *Anal. Chem.* **2010**, *82*, 6299-6302.
- 27 C. F. Woolley, M. A. Hayes, P. Mahanti, S. D. Gilman, T. Taylor, *Anal. Bioanal. Chem.* **2015**, *407*, 8605-8615.
- 28 B. Rotman, *Proc. Natl. Acad. Sci. U. S. A.* **1961**, *47*, 1981-1991.
- 29 K. Akama, K. Shirai, S. Suzuki, *Anal. Chem.* **2016**, *88*, 7123-7129.
- 30 H. H. Gorris, D. R. Walt, *Angew. Chem. Int. Ed.* **2010**, *49*, 3880-3895.
- 31 a) R. Liebherr, A. Hutterer, M. Mickert, F. Vogl, A. Beutner, A. Lechner, H. Hummel, H. Gorris, *Anal. Bioanal. Chem.* **2015**, *407*, 7443-7452; b) D. M. Rissin, H. H. Gorris, D. R. Walt, *J. Am. Chem. Soc.* **2008**, *130*, 5349-5353.
- 32 D. B. Craig, E. A. Arriaga, J. C. Y. Wong, H. Lu, N. J. Dovichi, *J. Am. Chem. Soc.* **1996**, *118*, 5245-5253.
- 33 M. Comellas-Aragones, H. Engelkamp, V. I. Claessen, N. A. J. M. Sommerdijk, A. E. Rowan, P. C. M. Christianen, J. C. Maan, B. J. M. Verduin, J. J. L. M. Cornelissen, R. J. M. Nolte, *Nat. Nanotechnol.* **2007**, *2*, 635-639.
- 34 H. M. Piwonski, M. Goomanovsky, D. Bensimon, A. Horovitz, G. Haran, *Proc. Natl. Acad. Sci. U. S. A.* **2012**, *109*, E1437-E1443.
- 35 H. Gorris, T. Blicharz, D. Walt, *FEBS J.* **2007**, *274*, 5462-5470.
- 36 Q. Xue, E. S. Yeung, *Nature* **1995**, *373*, 681-683.
- 37 Y. Rondelez, G. Tresset, K. V. Tabata, H. Arata, H. Fujita, S. Takeuchi, H. Noji, *Nat. Biotechnol.* **2005**, *23*, 361-365.

- 38 D. M. Rissin, C. W. Kan, T. G. Campbell, S. C. Howes, D. R. Fournier, L. Song, T. Piech, P. P. Patel, L. Chang, A. J. Rivnak, E. P. Ferrell, J. D. Randall, G. K. Provuncher, D. R. Walt, D. C. Duffy, *Nat. Biotechnol.* **2010**, *28*, 595-599.
- 39 D. H. Wilson, D. W. Hanlon, G. K. Provuncher, L. Chang, L. N. Song, P. P. Patel, E. P. Ferrell, H. Lepor, A. W. Partin, D. W. Chan, L. J. Sokoll, C. D. Cheli, R. P. Thiel, D. R. Fournier, D. C. Duffy, *Clin. Chem.* **2011**, *57*, 1712-1721.
- 40 A. D. Warren, S. T. Gaylord, K. C. Ngan, M. D. Milutinovic, G. A. Kwong, S. N. Bhatia, D. R. Walt, *J. Am. Chem. Soc.* **2014**, *136*, 13709-13714.
- 41 L. Chang, L. N. Song, D. R. Fournier, C. W. Kan, P. P. Patel, E. P. Ferrell, B. A. Pink, K. A. Minnehan, D. W. Hanlon, D. C. Duffy, D. H. Wilson, *J. Virol. Methods* **2013**, *188*, 153-160.
- 42 P. Shahim, M. Gren, V. Liman, U. Andreasson, N. Norgren, Y. Tegner, N. Mattsson, N. Andreasen, M. Ost, H. Zetterberg, B. Nellgard, K. Blennow, *Sci. Rep.* **2016**, *6*.
- 43 A. Olivera, N. Lejbman, A. Jeromin, L. M. French, H. S. Kim, A. Cashion, V. Mysliwicz, R. Diaz-Arrastia, J. Gill, *JAMA Neurol.* **2015**, *72*, 1109-1116.
- 44 S. T. Gaylord, T. L. Dinh, E. R. Goldman, G. P. Anderson, K. C. Ngan, D. R. Walt, *Anal. Chem.* **2015**, *87*, 6570-6577.
- 45 S. H. Kim, S. Iwai, S. Araki, S. Sakakihara, R. Iino, H. Noji, *Lab Chip* **2012**, *12*, 4986-4991.
- 46 Y. Obayashi, R. Iino, H. Noji, *Analyst* **2015**, *140*, 5065-5073.
- 47 X. Wang, L. Cohen, J. Wang, D. R. Walt, *J. Am. Chem. Soc.* **2018**, *140*, 18132-18139.
- 48 M. T. Guo, A. Rotem, J. A. Heyman, D. A. Weitz, *Lab Chip* **2012**, *12*, 2146-2155.
- 49 H. Song, R. F. Ismagilov, *J. Am. Chem. Soc.* **2003**, *125*, 14613-14619.
- 50 J. J. Agresti, E. Antipov, A. R. Abate, K. Ahn, A. C. Rowat, J. C. Baret, M. Marquez, A. M. Klibanov, A. D. Griffiths, D. A. Weitz, *Proc. Natl. Acad. Sci. U. S. A.* **2010**, *107*, 4004-4009.
- 51 J. U. Shim, R. T. Ranasinghe, C. A. Smith, S. M. Ibrahim, F. Hollfelder, W. T. S. Huck, D. Klenerman, C. Abell, *ACS Nano* **2013**, *7*, 5955-5964.
- 52 C. C. Liu, X. N. Xu, B. Li, B. Situ, W. L. Pan, Y. Hu, T. X. An, S. H. Yao, L. Zheng, *Nano Lett.* **2018**, *18*, 4226-4232.
- 53 S. B. Tian, Z. Zhang, J. Y. Chen, M. Y. Du, Z. Li, H. Yang, X. H. Ji, Z. K. He, *Talanta* **2018**, *186*, 24-28.
- 54 D. Kim, O. B. Garner, A. Ozcan, D. Di Carlo, *ACS Nano* **2016**, *10*, 7467-7475.
- 55 D. Schenk, G. Song, Y. Ke, Z. H. Wang, *PLOS One* **2017**, *12*, 16.
- 56 N. R. Beer, B. J. Hindson, E. K. Wheeler, S. B. Hall, K. A. Rose, I. M. Kennedy, B. W. Colston, *Anal. Chem.* **2007**, *79*, 8471-8475.
- 57 F. Shen, B. Sun, J. E. Kreutz, E. K. Davydova, W. B. Du, P. L. Reddy, L. J. Joseph, R. F. Ismagilov, *J. Am. Chem. Soc.* **2011**, *133*, 17705-17712.

- 58 W. H. Zhou, *Anal. Methods* **2018**, *10*, 3690-3695.
- 59 R. Q. Ke, R. Y. Nong, S. Fredriksson, U. Landegren, M. Nilsson, *Plos One* **2013**, *8*, 5.
- 60 B. Oswald, M. Gruber, M. Bohmer, F. Lehman, M. Probst, O. S. Wolfbeis, *Photochem. Photobiol.* **2001**, *74*, 237-245.
- 61 F. Löscher, S. Böhme, J. Martin, S. Seeger, *Anal. Chem.* **1998**, *70*, 3202-3205.
- 62 A. Jain, R. J. Liu, B. Ramani, E. Arauz, Y. Ishitsuka, K. Raganathan, J. Park, J. Chen, Y. K. Xiang, T. Ha, *Nature* **2011**, *473*, 484-488.
- 63 P. Tinnefeld, *Nature* **2011**, *473*, 461-462.
- 64 E. Burgin, A. Salehi-Reyhani, M. Barclay, A. Brown, J. Kaplinsky, M. Novakova, M. A. A. Neil, O. Ces, K. R. Willison, D. R. Klug, *Analyst* **2014**, *139*, 3235-3244.
- 65 H. D. Zhang, Y. J. Liu, K. Zhang, J. Ji, J. W. Liu, B. H. Liu, *Anal. Chem.* **2018**, *90*, 9315-9321.
- 66 R. Weng, S. T. Lou, L. D. Li, Y. Zhang, J. Qiu, X. Su, Y. Z. Qian, N. G. Walter, *Anal. Chem.* **2019**, *91*, 1424-1431.
- 67 Y. F. Ma, M. R. Shortreed, H. L. Li, W. H. Huang, E. S. Yeung, *Electrophoresis* **2001**, *22*, 421-426.
- 68 A. H. B. Wu, N. Fukushima, R. Puskas, J. Todd, P. Goix, *Clin. Chem.* **2006**, *52*, 2157-2159.
- 69 J. Todd, B. Freese, A. Lu, D. Held, J. Morey, R. Livingston, P. Goix, *Clin. Chem.* **2007**, *53*, 1990-1995.
- 70 T. J. Esparza, H. Z. Zhao, J. R. Cirrito, N. J. Cairns, R. J. Bateman, D. M. Holtzman, D. L. Brody, *Ann. Neurol.* **2013**, *73*, 104-119.
- 71 E. J. Wild, R. Boggio, D. Langbehn, N. Robertson, S. Haider, J. R. C. Miller, H. Zetterberg, B. R. Leavitt, R. Kuhn, S. J. Tabrizi, D. Macdonald, A. Weiss, *J. Clin. Invest.* **2015**, *125*, 1979-1986.
- 72 E. A. Nalefski, C. M. D'Antoni, E. P. Ferrell, J. A. Lloyd, H. Q. Qiu, J. L. Harris, D. H. Whitney, *Clin. Chem.* **2006**, *52*, 2172-2175.
- 73 S. W. Yim, T. Kim, T. A. Laurence, S. Partono, D. S. Kim, Y. Kim, S. M. Weiss, A. M. Reitmair, *Clin. Chem.* **2012**, *58*, 707-716.
- 74 Z. Foldes-Papp, U. Demel, G. P. Tilz, *Proc. Natl. Acad. Sci. U.S.A.* **2001**, *98*, 11509-11514.
- 75 S. Y. Tetin, K. M. Swift, E. D. Matayoshi, *Anal. Biochem.* **2002**, *307*, 84-91.
- 76 M. Chatterjee, B. Noding, E. A. J. Willemse, M. J. A. Koel-Simmelink, W. M. van der Fliere, D. Schild, C. E. Teunissen, *Clin. Biochem.* **2017**, *50*, 1061-1066.
- 77 S. T. Hess, S. H. Huang, A. A. Heikal, W. W. Webb, *Biochemistry* **2002**, *41*, 697-705.
- 78 Y. N. Bian, X. Y. Huang, J. C. Ren, *Anal. Methods* **2016**, *8*, 1333-1338.

- 79 H. T. Li, D. J. Zhou, H. Browne, S. Balasubramanian, D. Klenerman, *Anal. Chem.* **2004**, *76*, 4446-4451.
- 80 A. E. Miller, C. W. Hollars, S. M. Lane, T. A. Laurence, *Anal. Chem.* **2009**, *81*, 5614-5622.
- 81 a) A. N. Kapanidis, N. K. Lee, T. A. Laurence, S. Doose, E. Margeat, S. Weiss, *Proc. Natl. Acad. Sci. U. S. A.* **2004**, *101*, 8936-8941; b) E. Thews, M. Gerken, R. Eckert, J. Zapfel, C. Tietz, J. Wrachtrup, *Biophys. J.* **2005**, *89*, 2069-2076.
- 82 M. Seydack, *Biosens. Bioelectron.* **2005**, *20*, 2454-2469.
- 83 E. Petryayeva, W. R. Algar, I. L. Medintz, *Appl. Spectrosc.* **2013**, *67*, 215-252.
- 84 U. Resch-Genger, M. Grabolle, S. Cavaliere-Jaricot, R. Nitschke, T. Nann, *Nat. Methods* **2008**, *5*, 763-775.
- 85 X. J. Liu, C. H. Huang, C. H. Zong, A. Y. Liang, Z. J. Wu, Y. S. Zhang, Q. Q. Zhang, W. F. Zhao, H. W. Gai, *ACS Sensors* **2018**, *3*, 2644-2650.
- 86 X. J. Liu, C. H. Huang, X. L. Dong, A. Y. Liang, Y. S. Zhang, Q. Q. Zhang, Q. Wang, H. W. Gai, *Chem. Commun.* **2018**, *54*, 13103-13106.
- 87 A. Agrawal, C. Y. Zhang, T. Byassee, R. A. Tripp, S. M. Nie, *Anal. Chem.* **2006**, *78*, 1061-1070.
- 88 C. Y. Zhang, L. W. Johnson, *Anal. Chem.* **2009**, *81*, 3051-3055.
- 89 S. R. Jung, R. Han, W. Sun, Y. F. Jiang, B. S. Fujimoto, J. B. Yu, C. T. Kuo, Y. Rong, X. H. Zhou, D. T. Chiu, *Anal. Chem.* **2018**, *90*, 6089-6095.
- 90 U. Meseth, T. Wohland, R. Rigler, H. Vogel, *Biophys. J.* **1999**, *76*, 1619-1631.
- 91 J. J. Yin, A. D. Zhang, C. Q. Dong, J. C. Ren, *Talanta* **2015**, *144*, 13-19.
- 92 L. C. Hwang, T. Wohland, *ChemPhysChem* **2004**, *5*, 549-551.
- 93 F. Fujii, M. Kinjo, *ChemBioChem* **2007**, *8*, 2199-2203.
- 94 T. Kogure, S. Karasawa, T. Araki, K. Saito, M. Kinjo, A. Miyawaki, *Nat. Biotechnol.* **2006**, *24*, 577-581.
- 95 J. J. Wang, H. Liu, X. Y. Huang, J. C. Ren, *Microchim. Acta* **2016**, *183*, 749-755.
- 96 a) M. Haase, H. Schafer, *Angew. Chem. Int. Ed.* **2011**, *50*, 5808-5829; b) U. Resch-Genger, H. H. Gorris, *Anal. Bioanal. Chem.* **2017**, *409*, 5855-5874; c) H. H. Gorris, U. Resch-Genger, *Anal. Bioanal. Chem.* **2017**, *409*, 5875-5890.
- 97 a) H. H. Gorris, O. S. Wolfbeis, *Angew. Chem. Int. Ed.* **2013**, *52*, 3584-3600; b) Y. Fan, S. F. Wang, F. Zhang, *Angew. Chem. Int. Ed.* **2019**, *58*, 13208-13219.
- 98 V. Kale, H. Pakkila, J. Vainio, A. Ahomaa, N. Sirkka, A. Lyytikainen, S. M. Talha, A. Kutsaya, M. Waris, I. Julkunen, T. Soukka, *Anal. Chem.* **2016**, *88*, 4470-4477.
- 99 L. Zhou, Y. Fan, R. Wang, X. M. Li, L. L. Fan, F. Zhang, *Angew. Chem. Int. Ed.* **2018**, *57*, 12824-12829.

- 100 Y. Q. Lu, J. B. Zhao, R. Zhang, Y. J. Liu, D. M. Liu, E. M. Goldys, X. S. Yang, P. Xi, A. Sunna, J. Lu, Y. Shi, R. C. Leif, Y. J. Huo, J. Shen, J. A. Piper, J. P. Robinson, D. Y. Jin, *Nat. Photonics* **2014**, *8*, 33-37.
- 101 X. Li, L. Wei, L. L. Pan, Z. Y. Yi, X. Wang, Z. J. Ye, L. H. Xiao, H. W. Li, J. F. Wang, *Anal. Chem.* **2018**, *90*, 4807-4814.
- 102 S. Lahtinen, S. Krause, R. Arppe, T. Soukka, T. Vosch, *Chem. Eur. J.* **2018**, *24*, 9229-9233.
- 103 W. Becker, in *Springer Ser. Chem. Phys., Vol. 81*, **2005**, pp. I-387.
- 104 C. Fenzl, T. Hirsch, A. J. Baeumner, *TRAC Trends Anal. Chem.* **2016**, *79*, 306-316.
- 105 R. Nooney, A. Clifford, X. LeGuevel, O. Stranik, C. McDonagh, B. D. MacCraith, *Anal. Bioanal. Chem.* **2010**, *396*, 1127-1134.
- 106 C. J. Murphy, A. M. Gole, J. W. Stone, P. N. Sisco, A. M. Alkilany, E. C. Goldsmith, S. C. Baxter, *Acc. Chem. Res.* **2008**, *41*, 1721-1730.
- 107 C. Y. Poon, L. Wei, Y. L. Xu, B. Chen, L. H. Xiao, H. W. Li, *Anal. Chem.* **2016**, *88*, 8849-8856.
- 108 X. Wu, T. Li, G. Y. Tao, R. Y. Lin, X. J. Pei, F. Liu, N. Li, *Analyst* **2017**, *142*, 4201-4205.
- 109 L. Zhu, G. H. Li, S. Q. Sun, H. Tan, Y. H. He, *RSC Advances* **2017**, *7*, 27595-27602.
- 110 M. Sriram, B. P. Markhali, P. R. Nicovich, D. T. Bennett, P. J. Reece, D. B. Hibbert, R. D. Tilley, K. Gaus, S. R. C. Vivekchand, J. J. Gooding, *Biosens. Bioelectron.* **2018**, *117*, 530-536.
- 111 E. Luthgens, A. Janshoff, *ChemPhysChem* **2005**, *6*, 444-448.
- 112 S. S. Acimovic, H. Sipova-Jungova, G. Emilsson, L. Shao, A. B. Dahlin, M. Kall, T. J. Antosiewicz, *ACS Nano* **2018**, *12*, 9958-9965.
- 113 R. Yang, S. W. Liu, Z. J. Wu, Y. Tan, S. Q. Sun, *Talanta* **2018**, *182*, 348-353.
- 114 J. J. Li, Y. F. Jiao, Q. Y. Liu, Z. B. Chen, *Anal. Chim. Acta* **2018**, *1028*, 66-76.
- 115 S. Chen, M. Svedendahl, R. P. Van Duyne, M. Kall, *Nano Lett.* **2011**, *11*, 1826-1830.
- 116 X. Liu, Q. Dai, L. Austin, J. Coutts, G. Knowles, J. H. Zou, H. Chen, Q. Huo, *J. Am. Chem. Soc.* **2008**, *130*, 2780-2782.
- 117 T. Lan, C. A. Dong, X. Y. Huang, J. C. Ren, *Analyst* **2011**, *136*, 4247-4253.
- 118 T. Lan, C. Q. Dong, X. Y. Huang, J. C. Ren, *Talanta* **2013**, *116*, 501-507.
- 119 J. J. Wang, X. Y. Huang, H. Liu, C. Q. Dong, J. C. Ren, *Anal. Chem.* **2017**, *89*, 5230-5237.
- 120 B. Rothenhausler, W. Knoll, *Nature* **1988**, *332*, 615-617.
- 121 I. Sidorenko, S. Nizamov, R. Hergenroder, A. Zybin, A. Kuzmichev, B. Kiwull, R. Niessner, V. M. Mirsky, *Microchim. Acta* **2016**, *183*, 101-109.
- 122 B. Huang, F. Yu, R. N. Zare, *Anal. Chem.* **2007**, *79*, 2979-2983.

- 123 A. Zybin, Y. A. Kuritsyn, E. L. Gurevich, V. V. Temchura, K. Uberla, K. Niemax, *Plasmonics* **2010**, *5*, 31-35.
- 124 J. Homola, *Chem. Rev.* **2008**, *108*, 462-493.
- 125 S. Nizamov, V. Scherbahn, V. M. Mirsky, *Anal. Chem.* **2016**, *88*, 10206-10214.
- 126 S. Nizamov, O. Kasian, V. M. Mirsky, *Angew. Chem. Int. Ed.* **2016**, *55*, 7247-7251.
- 127 A. R. Halpern, J. B. Wood, Y. Wang, R. M. Corn, *ACS Nano* **2014**, *8*, 1022-1030.
- 128 D. Sevenler, G. G. Daaboul, F. E. Kanik, N. L. Unlu, M. S. Unlu, *ACS Nano* **2018**, *12*, 5880-5887.
- 129 A. Belushkin, F. Yesilkoy, H. Altug, *ACS Nano* **2018**, *12*, 4453-4461.
- 130 H. Harma, T. Soukka, T. Lovgren, *Clin. Chem.* **2001**, *47*, 561-568.
- 131 Z. Wu, T. Zeng, W. J. Guo, Y. Y. Bai, D. W. Pang, Z. L. Zhang, *ACS Appl. Mater. Interfaces* **2019**, *11*, 5762-5770.
- 132 F. Zhang, Q. H. Shi, Y. C. Zhang, Y. F. Shi, K. L. Ding, D. Y. Zhao, G. D. Stucky, *Adv. Mater.* **2011**, *23*, 3775-3739.
- 133 S. Gite, D. Archambault, M. P. Cappillino, D. Cunha, V. Dorich, T. Shatova, A. Tempesta, B. Walsh, J. A. Walsh, A. Williams, J. E. Kirby, J. Bowers, D. Straus, *Sci. Rep.* **2018**, *8*, 8.
- 134 H. C. Tekin, M. Cornaglia, M. A. M. Gijs, *Lab Chip* **2013**, *13*, 1053-1059.
- 135 D. A. Schafer, J. Gelles, M. P. Sheetz, R. Landick, *Nature* **1991**, *352*, 444-448.
- 136 E. W. A. Visser, J. H. Yan, L. J. van Ijzendoorn, M. W. J. Prins, *Nat. Commun.* **2018**, *9*.
- 137 J. Silver, Z. Y. Li, K. Neuman, *Biosens. Bioelectron.* **2015**, *63*, 117-123.
- 138 K. Akama, N. Iwanaga, K. Yamawaki, M. Okuda, K. Jain, H. Ueno, N. Soga, Y. Minagawa, H. Noji, *ACS Nano* **2019**, *13*, 13116-13126.
- 139 A. B. Taylor, P. Zijlstra, *ACS Sensors* **2017**, *2*, 1103-1122.
- 140 B. Sepulveda, P. C. Angelome, L. M. Lechuga, L. M. Liz-Marzan, *Nano Today* **2009**, *4*, 244-251.
- 141 N. J. Halas, S. Lal, W. S. Chang, S. Link, P. Nordlander, *Chem. Rev.* **2011**, *111*, 3913-3961.
- 142 M. A. Beuwer, B. van Hoof, P. Zijlstra, *J. Phys. Chem. C* **2018**, *122*, 4615-4621.
- 143 M. Garai, T. S. Zhang, N. Y. Gao, H. Zhu, Q. H. Xu, *J. Phys. Chem. C* **2016**, *120*, 11621-11630.
- 144 A. Kinkhabwala, Z. F. Yu, S. H. Fan, Y. Avlasevich, K. Mullen, W. E. Moerner, *Nat. Photonics* **2009**, *3*, 654-657.
- 145 P. Zijlstra, P. M. R. Paulo, K. Yu, Q. H. Xu, M. Orrit, *Angew. Chem. Int. Ed.* **2012**, *51*, 8352-8355.

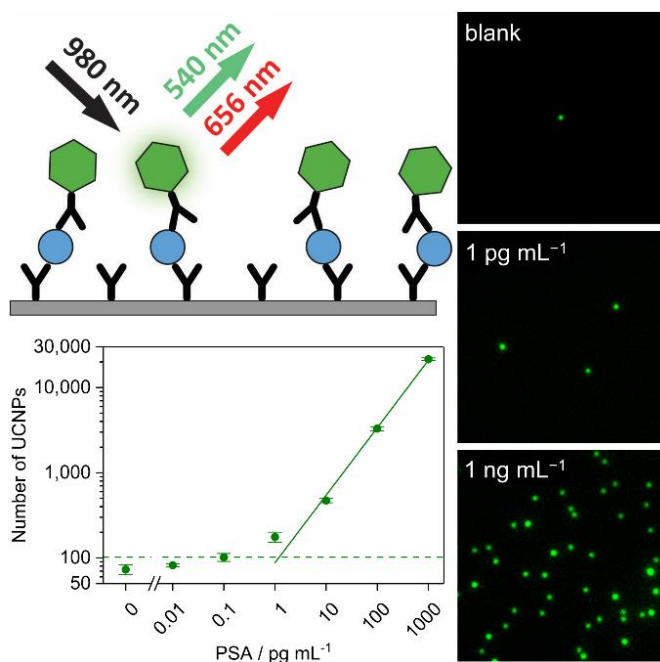
- 146 S. E. Lee, Q. Chen, R. Bhat, S. Petkiewicz, J. M. Smith, V. E. Ferry, A. L. Correia, A. P. Alivisatos, M. J. Bissell, *Nano Lett.* **2015**, *15*, 4564-4570.
- 147 M. A. Beuwer, M. W. J. Prins, P. Zijlstra, *Nano Lett.* **2015**, *15*, 3507-3511.
- 148 A. L. Washburn, M. S. Luchansky, A. L. Bowman, R. C. Bailey, *Anal. Chem.* **2010**, *82*, 69-72.
- 149 M. D. Baaske, F. Vollmer, *Nat. Photonics* **2016**, *10*, 733-739.
- 150 M. F. S. Ferreira, E. Castro-Camus, D. J. Ottaway, J. M. Lopez-Higuera, X. Feng, W. Jin, Y. Jeong, N. Picque, L. M. Tong, B. M. Reinhard, P. M. Pellegrino, A. Mendez, M. Diem, F. Vollmer, Q. M. Quan, *J. Optics* **2017**, *19*, 34.
- 151 A. B. Zrimsek, N. H. Chiang, M. Mattei, S. Zaleski, M. O. McAnally, C. T. Chapman, A. I. Henry, G. C. Schatz, R. P. Van Duyne, *Chem. Rev.* **2017**, *117*, 7583-7613.
- 152 *Single Molecule Counting (SMC) Erenna Instrument, Software and Kits* <http://www.merckmillipore.com/CZ/cs/life-science-research/protein-detection-quantification/Immunoassay-Platform-Solutions/single-molecule-counting-immunoassay-technology/SMC-Erenna-Instrument-Software-and-Kits/VS.b.qB.N.UAAAFfn7lc20.J.nav>, (accessed March 23.2020).
- 153 *Simoa assay kits* <https://www.quanterix.com/products-technology/simoa-assay-kits>, (accessed March 23.2020).
- 154 L. Smith, M. Kohli, A. M. Smith, *J. Am. Chem. Soc.* **2018**, *140*, 13904-13912.
- 155 D. Yeung, S. Ciotti, S. Purushothama, E. Gharakhani, G. Kuesters, B. Schlain, C. Shen, D. Donaldson, A. Mikulskis, *J. Immunol. Meth.* **2016**, *437*, 53-63.
- 156 O. R. Costa, K. Verhaeghen, S. Roels, G. Starige, Z. D. Ling, D. Pipeleers, F. K. Gorus, G. A. Martens, *PLOS One* **2018**, *13*.

VI. Research Article 1

Single Molecule Upconversion-Linked Immunosorbent Assay with Extended Dynamic Range for the Sensitive Detection of Diagnostic Biomarkers

Zdeněk Farka,* Matthias J. Mickert,* Antonín Hlaváček, Petr Skládal, and Hans H. Gorris

*Zdeněk Farka, and Matthias J. Mickert contributed equally to the work.



This Chapter has been published, text and figures reprinted with permission from The American Chemical Society: *Analytical Chemistry*¹, Copyright 2017.

¹Farka, Z., Mickert, M. J., Hlaváček, A., Skládal, P., & Gorris, H. H. Single molecule upconversion-linked immunosorbent assay with extended dynamic range for the sensitive detection of diagnostic biomarkers. *Anal. Chem.*, **2017** 89(21), 11825-11830.

VI.1. Abstract

The ability to detect disease markers at the single molecule level promises the ultimate sensitivity in clinical diagnosis. Fluorescence-based single molecule analysis, however, is limited by matrix interference and can only probe a very small detection volume, which is typically not suitable for real world analytical applications. We have developed a microtiter plate immunoassay for counting single molecules of the cancer marker prostate specific antigen (PSA) using photon-upconversion nanoparticles (UCNPs) as labels that can be detected without background fluorescence. Individual sandwich immunocomplexes consisting of (1) an anti-PSA antibody immobilized to the surface of a microtiter well, (2) PSA, and (3) an anti-PSA antibody-UCNP conjugate were counted under an upconversion wide-field microscope equipped with a 980 nm laser excitation source. The single molecule (digital) Upconversion-Linked Immunosorbent Assay (ULISA) reaches a limit of detection of 1.2 pg mL^{-1} (42 fM) PSA in 25 % blood serum, which is about ten times more sensitive than commercial ELISAs, and covers a dynamic range of three orders of magnitude. This detection scheme has the potential to pave the way for a new generation of digital immunoassays.

VI.2. Introduction

Information on the onset and the progression of diseases is essential to start a therapy as early as possible. Consequently, sensitive diagnostic tests (assays) are required to measure the presence of diagnostic markers with the lowest possible limit of detection (LOD).¹ The development of single molecule immunoassays has recently attracted wide attention^{2,3,4} because the detection and quantification of individual analyte molecules - also termed a digital readout - obviates the need for a (sometimes disputed) classical definition of an LOD and in principle can reach a much higher sensitivity.

A single fluorescent molecule conjugated to an analyte-specific antibody can only be detected in a (sub-)femtoliter volume by using confocal microscopy⁵ or total internal reflection fluorescence microscopy (TIRF)⁶⁻⁷ to minimize the background signal of billions of surrounding molecules. The high microscopic demands and extremely small detection volume are not practicable for analyzing real samples because it takes too long for an analyte molecule present in sub-pM concentrations to diffuse into such a small detection volume.⁸ Mainly two strategies have been developed to make single molecule immunoassays applicable in real analytical assays: First, the analyte can be pre-concentrated on the surface of magnetic microbeads rather than using a planar surface to access a larger probe volume and improve the binding kinetics of surface-bound capture antibody and analyte free in solution. Second, if the

detection antibody is labeled with an enzyme, thousands of fluorescent product molecules can be generated per analyte molecule which yields a much stronger and more robust signal detectable by conventional wide-field microscopy. The enzymatic signal amplification step is in line with an ELISA—the gold standard in immunodiagnostics—but diffusion of the fluorescent product has to be prevented to obtain a high local fluorophore concentration. A local confinement of the fluorescent product has been achieved either by using large arrays of femtoliter-sized wells⁹ to enclose microbeads containing the pre-assembled single enzyme-analyte sandwich complex with a fluorogenic substrate¹⁰ or by using a substrate that is converted to a non-soluble fluorescent product and directly deposits on the surface of the microbeads.¹¹

Photon-upconversion nanoparticles (UCNPs) are lanthanide-doped nanocrystals that can be excited by near-infrared (NIR, 980 nm) light and—depending on the lanthanide dopant composition—emit various colors of short wavelength light. The anti-Stokes emission strongly reduces autofluorescence and light scattering of the surrounding matrix.¹² UCNPs have been used as optical background-free luminescent labels for so-called upconversion-linked immunosorbent assays (ULISAs)¹³ to detect environmental analytes such as diclofenac¹⁴⁻¹⁵ and clinical analytes such as cardiac troponin I¹⁶ or prostate-specific antigen (PSA, $M_w = 28.7$ kDa).¹⁷

PSA is the most important diagnostic marker for prostate cancer, one of the most common cancers in men.¹⁸ PSA levels in serum are in particular important for monitoring the response to therapy and recurrence in patients after radical prostatectomy.¹⁹⁻²⁰ The biochemical recurrence is defined as PSA concentrations rising from <0.1 ng mL⁻¹ to persistently >0.2 ng mL⁻¹, and occurs in up to 40 % after surgery.²¹ Therefore, sensitive assays and high-affinity anti-PSA antibodies are required that allow for the reliable detection of PSA concentrations below 0.1 ng mL⁻¹.

Here, we present a single molecule (digital) ULISA for PSA (**Figure 1**), which is more easily amenable to standard immunoassay protocols compared to single enzyme molecule amplification systems because (1) there is no need to confine the diffusion of the fluorescent product, (2) no pre-concentration step is required, and (3) single analyte molecules can be detected in a conventional 96-well microtiter plate format using wide-field microscopy.²²

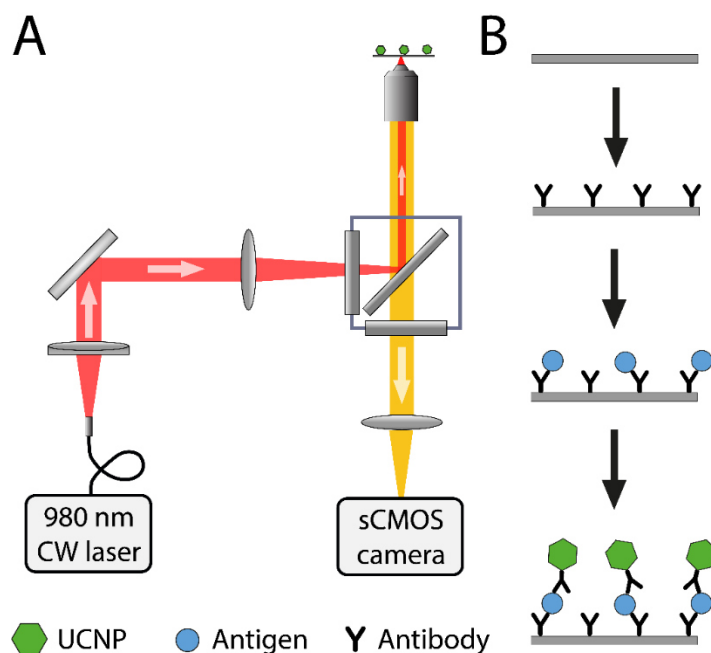


Figure 1: **A)** Scheme of upconversion microscopy. An inverted wide-field epifluorescence microscope is equipped with a fiber-coupled 980 nm continuous-wave laser diode and a sensitive sCMOS camera. **B)** Scheme of sandwich upconversion-linked immunosorbent assay (ULISA) involving (1) immobilization of the anti-PSA capture antibody, (2) binding of the analyte PSA and (3) analyte detection by a UCNPs-antibody conjugate.

VI.3. Experimental Section

Preparation of the UCNPs-Antibody Conjugate

UCNPs (β -NaYF₄:18 mol % Yb³⁺, 2 mol % Er³⁺) of different sizes (**Table S1**) were synthesized by high-temperature co-precipitation²³ and coated with a carboxylated silica layer using reverse microemulsion (**Table S2**).²⁴ The affinity of anti-PSA antibodies was analyzed by surface plasmon resonance (SPR, **Figure S1**). A polyclonal anti-PSA antibody (AF1344, R&D Systems, USA) was conjugated to the surface of UCNPs via EDC/sulfo-NHS activation. The Supporting Information contains experimental details.

Characterization of Nanoparticles

For transmission electron microscopy (TEM, Tecnai F20 FEI, USA), $\sim 4 \mu\text{L}$ of UCNPs were placed onto a 400-mesh copper EM grid coated with a continuous layer of carbon. Size and shape of individual UCNPs were analyzed with the software ImageJ. Dynamic light scattering (DLS) and zeta potential measurements were performed on a Zetasizer Nano ZS (Malvern, UK). For agarose gel electrophoresis,²⁵⁻²⁶ UCNP samples were mixed in a ratio of 10:1 with glycerol (80 % w/w), and $6 \mu\text{L}$ were applied into the pockets of the agarose gel (0.5 % w/v agarose, 45 mM Tris, 45 mM borate, pH 8.6). After electrophoresis (40 min at 100 V), the gel was scanned with a step size of 0.5 mm using a custom-built upconversion scanner (Chameleon, Hidex, Finland) equipped with a continuous 980 nm laser (4 W). The integrated upconversion luminescence intensity of the gel pockets divided by the integrated luminescence over the whole gel lane yielded information on the fraction of aggregated UCNPs. Additionally, the calculation of UCNP mass concentrations is described in the Supporting Information.

Upconversion Epiluminescence Microscopy

A 980 nm continuous wave laser diode (4 W, WSLs-980-004-H-T, Wavespectrum, China) was connected to the motorized illuminator unit (Ti-TIRF-E, Nikon, Japan) of an inverted microscope (Eclipse Ti-E, Nikon) via a multi-mode optical fiber (105 μm fiber core, 0.22 NA, Wavespectrum). A computer was equipped with an analog output module (PCI-6723, National Instruments, USA) to control the laser power (**Figure S2**). The optical filter set included a long-pass excitation filter ($\lambda_{\text{cut-on}} = 830 \text{ nm}$, Schott, Germany), a multiphoton dichroic mirror ($\lambda_{\text{cut-on}} = 875 \text{ nm}$, AHF Analysentechnik, Germany), and a band-pass filter for the green emission of Er-doped UCNPs ($\lambda = 535 \pm 70 \text{ nm}$, $\text{OD}_{980 \text{ nm}} \approx 6$, Chroma, USA). Images were taken with a 100 \times objective (NA = 1.49, CFI HP Apochromat TIRF, Nikon) and a cooled 5.5 megapixel sCMOS camera (Neo, Andor Technology, UK). The maximum laser power of 4 W resulted in a power density of 640 W cm^{-2} in the focal plane. The optimization of the single UCNP detection on glass slides is described in the Supporting Information.

Upconversion-Linked Immunosorbent Assay (ULISA)

A 96-well polystyrene microtiter plate with 190 μm thick bottom foil (high protein binding capacity, μCLEAR , Greiner, Germany) was coated with $0.3 \mu\text{g mL}^{-1}$ of monoclonal anti-PSA antibody (ab403, Abcam, UK) in coating buffer (50 mM $\text{NaHCO}_3/\text{Na}_2\text{CO}_3$, 0.05 % NaN_3 , pH 9.6; 200 μL per well) at 4 $^\circ\text{C}$ overnight. All subsequent steps were carried out at room temperature. After four washing steps with 250 μL of washing buffer (50 mM $\text{NaH}_2\text{PO}_4/\text{Na}_2\text{HPO}_4$, 0.01 % Tween 20, 0.05 % NaN_3 , pH 7.4), the microtiter plate was blocked with 250 μL of 1 % bovine serum albumin (BSA, Sigma-Aldrich) in 50 mM $\text{NaH}_2\text{PO}_4/\text{Na}_2\text{HPO}_4$, 0.05 % NaN_3 , pH 7.4, for 1 h. After four washing steps, serial PSA (ab78528, Abcam) dilutions were prepared either in assay buffer (50 mM Tris, 150 mM NaCl, 0.05 % NaN_3 , 0.5 % bovine gamma globulin (Sigma-Aldrich), 0.2 % BSA, 0.01 % Tween 20, 0.2 % polyvinyl alcohol (M_w : 6000 g mol^{-1}), 1 % glucose and 5 mM EDTA, pH 7.5) or in four-fold diluted bovine serum (Sigma-Aldrich). On each well, 100 μL of the PSA dilution was incubated for 1 h. After four washing steps, the microtiter plate was incubated with 100 μL of the UCNP-antibody conjugate ($10 \mu\text{g mL}^{-1}$ in assay buffer) for 1 h. After four washing steps, the wells were left empty to determine the PSA concentration in each well in two different modes:

Analog Mode

The integrated upconversion luminescence of the UCNP label was detected in the microtiter plate wells by using a custom-built upconversion microplate reader (Chameleon, Hidex). The continuous 980 nm laser (4 W) was focused on the bottom of the microtiter wells resulting in a collimated laser spot size of $\sim 0.8 \text{ mm}$.¹⁴ Each well was scanned 64 times with a raster step size of 0.4 mm and 500 ms signal integration time. The truncated average was calculated for each well after discarding the eight highest and eight lowest luminescence intensities to exclude outliers.

Digital Mode

The number of single UCNP labels in the microtiter plate wells was counted by upconversion epiluminescence microscopy. Adding 100 μL of glycerol to the wells facilitated heat dissipation of the high-power laser beam. Nine images of $166 \times 140 \mu\text{m}^2$ were recorded per well with a step size of 300 μm in a rectangular grid. Single UCNPs were counted automatically using a built-in function of the software NIS Elements (Nikon).

Data Analysis

For each detection mode, the mean and standard deviation were calculated from three replicate wells and two types of regression analyses were applied for the calibration curves. (1) In the four-parameter logistic function

$$Y = \frac{Y_{\max} - Y_{\text{bg}}}{1 + \left(\frac{[\text{PSA}]}{\text{EC}_{50}}\right)^s} + Y_{\text{bg}}$$

[PSA] is the concentration of prostate specific antigen, and Y is either the upconversion luminescence (analog ULISA) or the number of UCNPs (digital ULISA). The equation yields the maximum (Y_{\max}) and background (Y_{bg}) signal, the PSA concentration that reduces ($Y_{\max} - Y_{\text{bg}}$) by 50 % (EC_{50}) and the slope at the inflection point (s).

(2) In the logit-log analysis, a linear regression was applied to the steepest part of the calibration curve and the background level was conventionally defined as the luminescence signal / number of UCNPs detected in the absence of PSA plus three times the standard deviation. The intersection of the regression line and the background level defined the LOD.

VI.4. Results and Discussion

The development of the single molecule ULISA critically depended on the design of a homogeneous and monodisperse UCNP label. The TEM images show a homogeneous size and shape of UCNPs covered by a closed silica shell (**Figure 2**). The shift of the electrophoretic mobility (**Figure 2C**) indicates the successful UCNP-Ab conjugation. Only a small fraction of aggregates (< 10 %) was present in the gel pockets that did not enter the gel matrix. The main fraction of single UCNPs as well as clusters of two and three UCNPs are visible as distinct bands in the gel. The success of the surface modification steps was further confirmed by an increasing hydrodynamic diameter as well as zeta potential measurements (**Figure S4**).

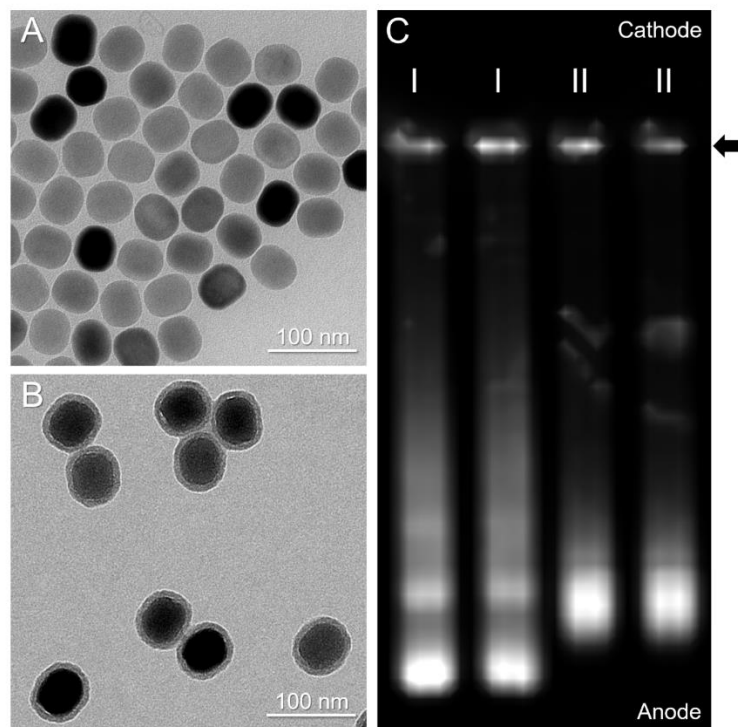


Figure 2: TEM images of **A**) oleic acid-capped UCNPs (diameter 48.2 ± 3.4 nm) and **B**) UCNPs with carboxylated silica shell (thickness 7.1 ± 1.2 nm). **C**) Agarose gel electrophoresis of (I) carboxylated UCNPs and (II) UCNP-antibody conjugates in duplicates (6 % of nanoparticle aggregates in I and 8 % in II). The arrow indicates the starting point of electrophoresis.

Wide-field upconversion microscopy (**Figure 1A**) of single UCNPs was optimized by immobilizing different types of carboxylated UCNPs in a size range of 37 nm to 90 nm on a glass slide modified with cationized bovine serum albumin (cBSA) (**Figure 3**). The carboxylated UCNPs exposing a negative surface potential (**Figure S4**) strongly bind to the cBSA-coated glass slides such that the number of immobilized UCNPs increased linearly with the UCNP concentration (**Figure S5**). Excitation in the upconversion mode ensured a very low background signal that - in absence of UCNPs - only depended on the camera noise (**Figure 3A**). The four types of UCNPs were visible individually (**Figure 3B-E**) as diffraction limited spots of ~ 400 nm in diameter (**Figure 3F**). The brightness of the spots increased so strongly with the size of UCNPs (**Figure 3G**) that the exposure time for the largest UCNPs had to be reduced in order to avoid detector saturation. The histograms in **Figure 3H** follow a single Gaussian distribution, which indicates some heterogeneity in the emission intensity of individual UCNPs - rather than clusters of one, two or more nanoparticles that would result in distinct peaks. Thus, both gel electrophoresis (**Figure 2C**, lines I) and the intensity distribution

confirm that the majority of UCNPs are monodisperse. UCNPs with a size of 48 nm showed highly homogeneous and strong luminescence intensities suitable for all further experiments.

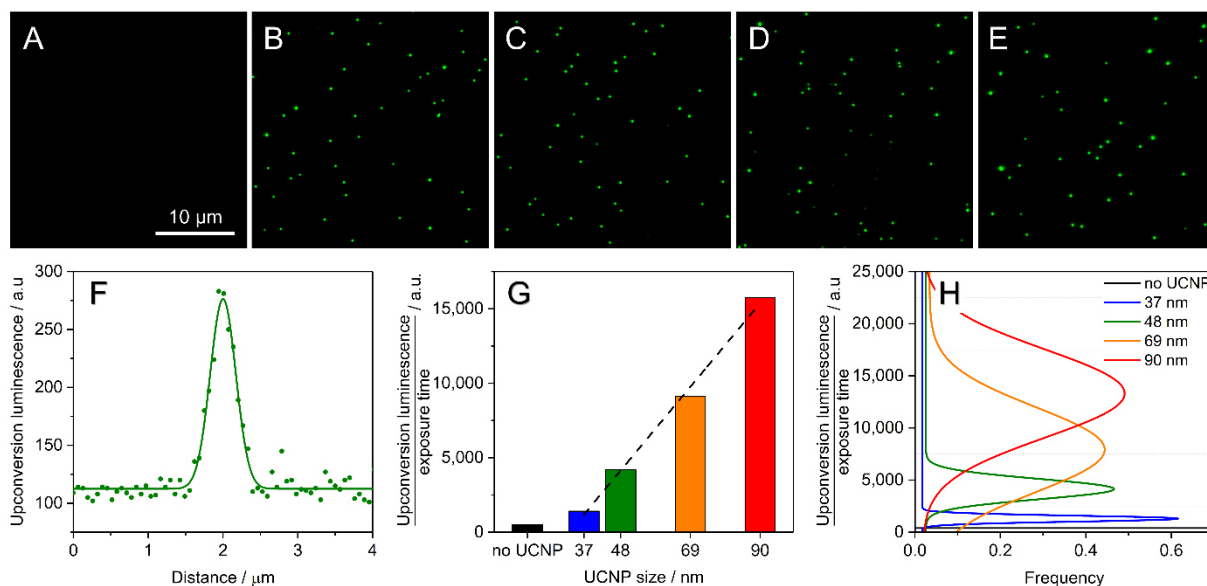


Figure 3: Image sections of individual UCNPs (green spots) bound to cBSA-modified glass slide taken by wide-field microscopy. **A)** no UCNP, 7 s exposure time; **B)** 37 nm, 7 s exposure time; **C)** 48 nm, 5 s exposure time; **D)** 69 nm 4 s exposure time; **E)** 90 nm, 2 s exposure time. **F)** Upconversion luminescence intensity cross-section of a single UCNP (diameter of 48 nm) evaluated from microscope image. **G)** The upconversion luminescence intensities normalized to 1 s exposure time increase with the size of UCNPs. **H)** Gaussian distributions of luminescence intensities with coefficients of variation (CV) of 26 % (37 nm), 28 % (48 nm), 61 % (69 nm) and 37 % (90 nm).

The sandwich immunoassay (**Figure 1B**) was performed on high-binding microtiter plates with a thin foil (190 μm) at the bottom of each well to account for the working distance of the high NA microscope objective. The microtiter plate format allowed for an easier immobilization of the capture antibody and for an improved assay handling and automation compared to glass slides. Serial dilutions of PSA spiked into 25 % serum (diluted in assay buffer) were prepared on the microtiter plate. After binding of the UCNP-antibody conjugate, the microtiter plates were read both by measuring the upconversion luminescence in a microtiter plate reader (analog ULISA) and by counting individual sandwich immunocomplexes as diffraction limited spots under the microscope (digital ULISA, **Figure 4**).

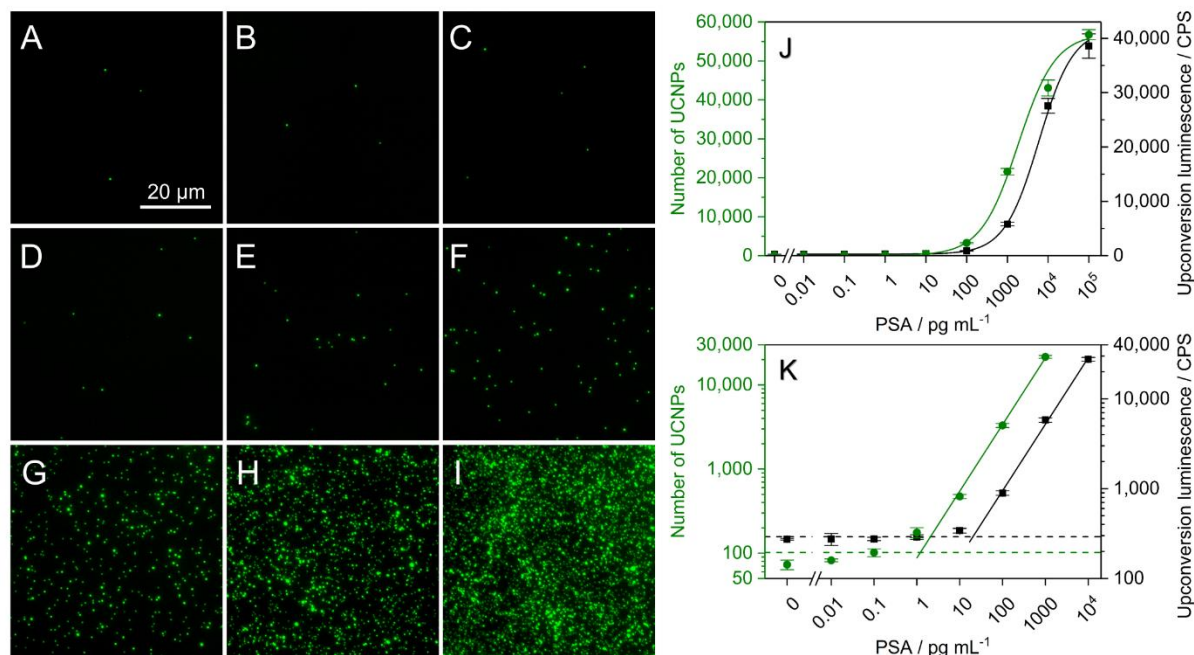


Figure 4: Upconversion microscopy images of serial PSA dilutions in 25 % serum: **A)** no PSA; **B)** 10 fg mL⁻¹; **C)** 100 fg mL⁻¹; **D)** 1 pg mL⁻¹; **E)** 10 pg mL⁻¹; **F)** 100 pg mL⁻¹; **G)** 1 ng mL⁻¹; **H)** 10 ng mL⁻¹; **I)** 100 ng mL⁻¹. PSA is captured on microtiter plate wells and detected by a UCNP-antibody conjugate. A small section (3 600 μm²) of the analyzed area (210 × 263 μm²) is shown. **J)** Calibration based on a 4-parameter logistic regression model shows a test midpoint (EC₅₀) of 1.8 ng mL⁻¹ for the digital readout (green line) and 5.9 ng mL⁻¹ for the analog readout (black line). **K)** Linear regression after logit transformation yields an LOD of 1.2 pg mL⁻¹ in the digital readout and 20.3 pg mL⁻¹ in the analog readout. The hatched lines are the background level defined either as mean number of spots (green) or upconversion luminescence (black) without PSA + 3× standard deviation. Error bars indicate the standard deviation from three replicate wells.

The small number of spots in the absence of PSA (**Figure 4A**) can be attributed to some non-specific binding of the UCNP-antibody conjugate to the microtiter plate surface and defines the LOD of the immunoassay—similar as in a conventional assay. Several advantages of the digital readout over an analog readout, however, should be noted: (1) Non-specific binding of the luminescent reporter and the instrumental background can be assessed separately in each measurement. (2) Counting single immunocomplexes is not affected by variations in the signal intensity of the reporter, e.g. as a result of luminescence heterogeneity or aggregation of UCNP^s.²⁷ By contrast, the size of an aggregate strongly affects the integrated signal in the analog mode even if only very few aggregates are present. To reduce the effect of large aggregates in the analog readout, we raster scanned 64 points on each well with the microtiter plate reader and determined a truncated average for further data evaluation. (3) The number of spots counted on a fraction of the microtiter well area covered by the PSA sample is a direct

measure of the detection efficiency of PSA (Supporting Information), which depends on several factors such as diffusion rates, binding kinetics and steric hindrance due to the nanoparticle size. Here, we have calculated an average detection efficiency of approximately 1 % in the linear detection range of the assay.

For a good precision of the assay, the imaging area must be large enough to minimize the sampling error,²⁸ or—in physical terms—the Poisson noise. While either a 100× or a 60×-microscope objective were suitable for counting single UCNPs, the 100× objective was more sensitive (**Figure S6**). To account for the small field of view of the 100× objective, we acquired consecutive images of nine areas per microtiter plate well. The total imaging area of 0.2 mm² per well was large enough to reduce the Poisson noise below 10 %, and counting of individual immunocomplexes in repeated measurements was highly reproducible (CV < 15 %) (**Table S4**).

Data obtained by single molecule counting (digital ULISA) and by a microtiter plate reader (analog ULISA) were analyzed by a four-parameter regression model commonly used for microtiter plate immunoassays (**Figure 4J**) as well as a logit-log model (**Figure 4K**) to zoom in on low counts of UCNPs and signals close to the background. The digital ULISA achieved an LOD of 1.2 pg mL⁻¹ and a linear working range between 10 pg mL⁻¹ and 1 ng mL⁻¹ of PSA in 25 % serum; this corresponds to the LOD of 4.8 pg mL⁻¹ in the original serum. Higher PSA concentrations were outside the linear range because too many spots with overlapping point-spread functions (**Figures 4H** and **4I**) cannot be resolved individually. Higher PSA concentrations were analyzed by switching from the digital to the analog mode.²⁹ The sensitivity (LOD: 20.3 pg mL⁻¹) and the linear working range (100 pg mL⁻¹ – 10 ng mL⁻¹) of the analog ULISA were comparable to commercial ELISAs for the diagnosis of PSA (**Table S5**). The combination of both detection modes, however, improves the sensitivity by one order of magnitude and extends the linear working range to three orders of magnitude from 10 pg mL⁻¹ to 10 ng mL⁻¹. The analysis of PSA spiked into buffer yielded essentially the same results (**Figure S7** and **Table S3**) and indicates that matrix effects of 25 % serum are negligible.

In the future, the single molecule immunoassay can be improved by (1) optimizing the blocking procedure to reduce non-specific binding, (2) tuning the antibody sandwich combination specifically for single molecule immunoassays³⁰ and/or (3) by reducing the size of the UCNP-antibody reporter. In an earlier report,³¹ fluorescence lifetime imaging of relatively large Eu(III)-doped nanoparticles (107 nm in diameter) did not improve the detection of PSA by counting single immunocomplexes compared to the analog mode. By contrast, we have achieved a 10× higher sensitivity in the digital mode by reducing the label size to 48 nm. It is likely that smaller nanoparticle can further increase the detection efficiency above 1 % by providing better access to the surface-bound PSA. The single molecule ULISA is also

amenable to the multiplexed detection of several analytes in parallel by using UCNPs-antibody combinations that can be excited by 980 nm light but display different emission colors.³²⁻³⁴

VI.5. Conclusions

We have developed a digital sandwich immunoassay using UCNPs as a luminescent label for counting single PSA molecules without background fluorescence. With an LOD of 1.2 pg mL^{-1} and a wide dynamic range of three orders of magnitude, the ULISA is superior to commercial ELISAs for the clinical diagnosis of PSA. While some more sensitive immunoassays have been described in the literature (**Table S5**), none of these are compatible with conventional microtiter plate assay protocols that can be readily adapted for the detection of any other diagnostic markers. Thus, we expect that the ability to detect single analyte molecules reliably and with a relatively simple detection scheme will have a strong impact on the development of future immunoassays.

Zdeněk Farka and Matthias J. Mickert contributed equally to the work.

Acknowledgements

We thank Prof. Yves Mély and Dr. Frederic Przybilla (University of Strasbourg) and Prof. Artur Bednarkiewicz (Polish Academy of Science, Wrocław) for discussing the microscope setup, and Miroslav Peterek for taking TEM images at the CF Cryo-electron Microscopy and Tomography facilities (funded by MEYS CR, LM2015043). We acknowledge financial support from the COST Action CM1403 “The European Upconversion Network: From the Design of Photon-Upconverting Nanomaterials to Biomedical Applications” and the German Academic Exchange Service (DAAD). H.H.G. acknowledges funding from the German Research Foundation (DFG: GO 1968/5-1, Heisenberg Fellowship and GO 1968/6-1), and A.H. funding from the Ministry of Education, Youth and Sports of the Czech Republic (CEITEC 2020, LQ1601, and COST CZ, LD15023) and the Grant Agency of the Czech Republic (P20612G014).

VI.6. References

1. Farka, Z.; Juřík, T.; Kovář, D.; Trnková, L.; Skládal, P., Nanoparticle-based immunochemical biosensors and assays: Recent advances and challenges. *Chem. Rev.* **2017**, *117* (15), 9973-10042.
2. Holzmeister, P.; Acuna, G. P.; Grohmann, D.; Tinnefeld, P., Breaking the concentration limit of optical single-molecule detection. *Chem. Soc. Rev.* **2014**, *43* (4), 1014-1028.
3. Gooding, J. J.; Gaus, K., Single-molecule sensors: Challenges and opportunities for quantitative analysis. *Angew. Chem.-Int. Edit.* **2016**, *55* (38), 11354-11366.
4. Zhang, Y.; Noji, H., Digital bioassays: Theory, applications, and perspectives. *Anal. Chem.* **2017**, *89* (1), 92-101.
5. Löscher, F.; Böhme, S.; Martin, J.; Seeger, S., Counting of single protein molecules at interfaces and application of this technique in early-stage diagnosis. *Anal. Chem.* **1998**, *70* (15), 3202-3205.
6. Tessler, L. A.; Reifenberger, J. G.; Mitra, R. D., Protein quantification in complex mixtures by solid phase single-molecule counting. *Anal. Chem.* **2009**, *81* (17), 7141-7148.
7. Jain, A.; Liu, R. J.; Ramani, B.; Arauz, E.; Ishitsuka, Y.; Rangunathan, K.; Park, J.; Chen, J.; Xiang, Y. K.; Ha, T., Probing cellular protein complexes using single-molecule pull-down. *Nature* **2011**, *473* (7348), 484-489.
8. Schreiber, G.; Haran, G.; Zhou, H. X., Fundamental aspects of protein-protein association kinetics. *Chem. Rev.* **2009**, *109* (3), 839-860.
9. Gorris, H. H.; Walt, D. R., Analytical chemistry on the femtoliter scale. *Angew. Chem.-Int. Edit.* **2010**, *49* (23), 3880-3895.
10. Rissin, D. M.; Kan, C. W.; Campbell, T. G.; Howes, S. C.; Fournier, D. R.; Song, L.; Piech, T.; Patel, P. P.; Chang, L.; Rivnak, A. J.; Ferrell, E. P.; Randall, J. D.; Provuncher, G. K.; Walt, D. R.; Duffy, D. C., Single-molecule enzyme-linked immunosorbent assay detects serum proteins at subfemtomolar concentrations. *Nat. Biotechnol.* **2010**, *28* (6), 595-599.
11. Akama, K.; Shirai, K.; Suzuki, S., Droplet-free digital enzyme-linked immunosorbent assay based on a tyramide signal amplification system. *Anal. Chem.* **2016**, *88* (14), 7123-7129.
12. Haase, M.; Schäfer, H., Upconverting nanoparticles. *Angew. Chem.-Int. Edit.* **2011**, *50* (26), 5808-5829.
13. Gorris, H. H.; Resch-Genger, U., Perspectives and challenges of photon-upconversion nanoparticles - Part II: bioanalytical applications. *Anal. Bioanal. Chem.* **2017**, *409*, 5875-5890.
14. Hlaváček, A.; Farka, Z.; Hübner, M.; Horňáková, V.; Němeček, D.; Niessner, R.; Skládal, P.; Knopp, D.; Gorris, H. H., Competitive upconversion-linked immunosorbent assay for the sensitive detection of diclofenac. *Anal. Chem.* **2016**, *88* (11), 6011-6017.

15. Hlaváček, A.; Peterek, M.; Farka, Z.; Mickert, M. J.; Prechtel, L.; Knopp, D.; Gorris, H. H., Rapid single-step upconversion-linked immunosorbent assay for diclofenac. *Microchim. Acta* **2017**, *184* (10), 4159-4165.
16. Sirkka, N.; Lyytikäinen, A.; Savukoski, T.; Soukka, T., Upconverting nanophosphors as reporters in a highly sensitive heterogeneous immunoassay for cardiac troponin I. *Anal. Chim. Acta* **2016**, *925*, 82-87.
17. Ukonaho, T.; Rantanen, T.; Jämsen, L.; Kuningas, K.; Pääkkilä, H.; Lövgren, T.; Soukka, T., Comparison of infrared-excited up-converting phosphors and europium nanoparticles as labels in a two-site immunoassay. *Anal. Chim. Acta* **2007**, *596* (1), 106-115.
18. Siegel, R. L.; Miller, K. D.; Jemal, A., Cancer Statistics, 2016. *CA-Cancer J. Clin.* **2016**, *66* (1), 7-30.
19. Hayes, J. H.; Barry, M. J., Screening for prostate cancer with the prostate-specific antigen test A review of current evidence. *JAMA-J. Am. Med. Assoc.* **2014**, *311* (11), 1143-1149.
20. Stephan, C.; Ralla, B.; Jung, K., Prostate-specific antigen and other serum and urine markers in prostate cancer. *Biochim. Biophys. Acta-Rev. Cancer* **2014**, *1846* (1), 99-112.
21. Thaxton, C. S.; Elghanian, R.; Thomas, A. D.; Stoeva, S. I.; Lee, J. S.; Smith, N. D.; Schaeffer, A. J.; Klocker, H.; Horninger, W.; Bartsch, G.; Mirkin, C. A., Nanoparticle-based bio-barcode assay redefines "undetectable" PSA and biochemical recurrence after radical prostatectomy. *Proc. Natl. Acad. Sci. USA* **2009**, *106* (44), 18437-18442.
22. Park, Y. I.; Kim, J. H.; Lee, K. T.; Jeon, K. S.; Bin Na, H.; Yu, J. H.; Kim, H. M.; Lee, N.; Choi, S. H.; Baik, S. I.; Kim, H.; Park, S. P.; Park, B. J.; Kim, Y. W.; Lee, S. H.; Yoon, S. Y.; Song, I. C.; Moon, W. K.; Suh, Y. D.; Hyeon, T., Nonblinking and nonbleaching upconverting nanoparticles as an optical imaging nanoprobe and T1 magnetic resonance imaging contrast agent. *Adv. Mater.* **2009**, *21* (44), 4467-4471.
23. Wang, F.; Han, Y.; Lim, C. S.; Lu, Y. H.; Wang, J.; Xu, J.; Chen, H. Y.; Zhang, C.; Hong, M. H.; Liu, X. G., Simultaneous phase and size control of upconversion nanocrystals through lanthanide doping. *Nature* **2010**, *463* (7284), 1061-1065.
24. Sedlmeier, A.; Gorris, H. H., Surface modification and characterization of photon-upconverting nanoparticles for bioanalytical applications. *Chem. Soc. Rev.* **2015**, *44* (6), 1526-1560.
25. Sedlmeier, A.; Hlaváček, A.; Birner, L.; Mickert, M. J.; Muhr, V.; Hirsch, T.; Corstjens, P.; Tanke, H. J.; Soukka, T.; Gorris, H. H., Highly sensitive laser scanning of photon-upconverting nanoparticles on a macroscopic scale. *Anal. Chem.* **2016**, *88* (3), 1835-1841.
26. Hlaváček, A.; Sedlmeier, A.; Skládal, P.; Gorris, H. H., Electrophoretic characterization and purification of silica-coated photon-upconverting nanoparticles and their bioconjugates. *ACS Appl. Mater. Interfaces* **2014**, *6* (9), 6930-6935.
27. Liebherr, R. B.; Hutterer, A.; Mickert, M. J.; Vogl, F. C.; Beutner, A.; Lechner, A.; Hummel, H.; Gorris, H. H., Three-in-one enzyme assay based on single molecule detection in femtoliter arrays. *Anal. Bioanal. Chem.* **2015**, *407* (24), 7443-7452.

28. Crawford, A. C.; Skuratovsky, A.; Porter, M. D., Sampling error: Impact on the quantitative analysis of nanoparticle-based surface-enhanced Raman scattering immunoassays. *Anal. Chem.* **2016**, *88* (12), 6515-6522.
29. Rissin, D. M.; Fournier, D. R.; Piech, T.; Kan, C. W.; Campbell, T. G.; Song, L. A.; Chang, L.; Rivnak, A. J.; Patel, P. P.; Provuncher, G. K.; Ferrell, E. P.; Howes, S. C.; Pink, B. A.; Minnehan, K. A.; Wilson, D. H.; Duffy, D. C., Simultaneous detection of single molecules and singulated ensembles of molecules enables immunoassays with broad dynamic range. *Anal. Chem.* **2011**, *83* (6), 2279-2285.
30. Dinh, T. L.; Ngan, K. C.; Shoemaker, C. B.; Walt, D. R., Using antigen-antibody binding kinetic parameters to understand single-molecule array immunoassay performance. *Anal. Chem.* **2016**, *88* (23), 11335-11339.
31. Härmä, H.; Soukka, T.; Lövgren, T., Europium nanoparticles and time-resolved fluorescence for ultrasensitive detection of prostate-specific antigen. *Clin. Chem.* **2001**, *47* (3), 561-568.
32. Gorris, H. H.; Ali, R.; Saleh, S. M.; Wolfbeis, O. S., Tuning the dual emission of photon-upconverting nanoparticles for ratiometric multiplexed encoding. *Adv. Mater.* **2011**, *23* (14), 1652-1655.
33. Gorris, H. H.; Wolfbeis, O. S., Photon-upconverting nanoparticles for optical encoding and multiplexing of cells, biomolecules, and microspheres. *Angew. Chem.-Int. Edit.* **2013**, *52* (13), 3584-3600.
34. Kale, V.; Pääkilä, H.; Vainio, J.; Ahomaa, A.; Sirkka, N.; Lyytikäinen, A.; Talha, S. M.; Kutsaya, A.; Waris, M.; Julkunen, I.; Soukka, T., Spectrally and spatially multiplexed serological array-in-well assay utilizing two-color upconversion luminescence imaging. *Anal. Chem.* **2016**, *88* (8), 4470-4477.

VI.7. Supporting Information

Characterization of Anti-PSA Antibodies by SPR

The monoclonal anti-PSA antibody (ab403) was obtained from Abcam (UK) and the polyclonal anti-PSA antibody (AF1344) was obtained from R&D Systems (USA). A Biacore 3000 instrument (GE Healthcare, Sweden) was used for surface plasmon resonance (SPR) experiments. For the immobilization of antibody on a carboxymethylated dextran chip (CM5, GE Healthcare, Sweden), the carboxyl groups were first activated by a freshly prepared mixture of EDC (200 mM) and NHS (50 mM) for 5 min followed by binding of antibodies ($10 \mu\text{g mL}^{-1}$, 10 min) in acetate buffer (50 mM, pH 4.5). Free reactive groups were blocked by ethanolamine (1 M, pH 8.5, 5 min). The reference channel was modified by the same procedure without the antibody binding step. HBS-EP (10 mM HEPES, 150 mM sodium chloride, 3 mM EDTA and 0.005 % Tween 20) was used as a running buffer with the flow rate of $5 \mu\text{L min}^{-1}$. Different concentrations of PSA in HBS-EP buffer were injected using the *KINJECT* function with 10 min for both the association and dissociation phase. After each sample application step, the sensor surface was regenerated by 20 mM HCl for 1 min.

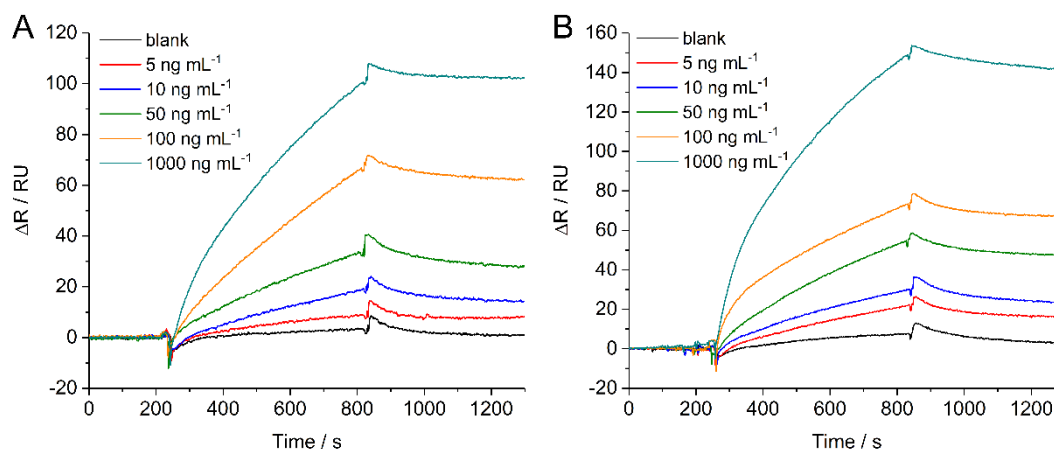


Figure S1: SPR sensorgrams of PSA binding and dissociation to/from the immobilized A) monoclonal antibody ab403 (Abcam) and B) polyclonal antibody AF1344 (R&D). Differential signals ΔR corresponding to the difference between measuring and reference channel are shown.

Measurement of NIR-Power Density

The laser power in the focal plane was measured using a microscope slide thermal power sensor (S175C, ThorLabs, USA) in combination with an USB power and energy meter interface (PM100USB, ThorLabs, USA). The sensor was mounted on the x/y-stage of the microscope and the power was varied by adjusting the input voltage of the laser diode. To

prevent possible damage of the sensor due to the high power densities at the objective, power values for input voltage between 0 and 0.6 V were measured and linear extrapolation was used to evaluate the power for higher input voltages.

To calculate the power density of the laser in the focal plane, the laser diameter was measured. First, the lens of the 100× objective was covered with immersion oil, then a square paper with millimeter scale was placed between a microscopic slide and a coverslip and mounted on the x/y-stage of the microscope. After focusing on the paper, the laser was turned on and an image of the illuminated paper was taken from above using an IR sensitive HD webcam (B525, Logitech, Switzerland). The image was analyzed using ImageJ; the intensity profile of the lasers cross-section was plotted and the scales of the millimeter paper were used to calculate the width of one pixel. The full width at half maximum was evaluated using Gaussian fit.

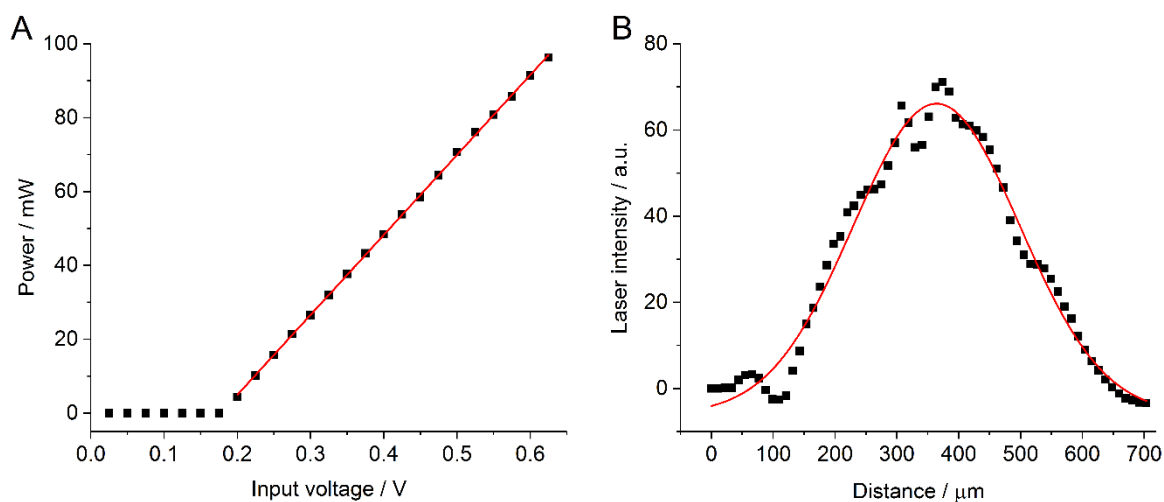


Figure S2: **A)** Laser power calibration. Power values for input voltage between 0 and 0.6 V were measured using a thermal power sensor. According to the linear extrapolation, the maximum input voltage of 2.5 V corresponds to the laser power of 503 ± 17 mW. **B)** Cross-section of the 980 nm CW laser. Full width at half maximum (FWHM) of 317 ± 10 μm was evaluated using a Gaussian fit. The maximum power density of 637 ± 22 W cm^{-2} was evaluated using the maximum laser power and laser diameter.

Synthesis of UCNPs

Materials: $\text{YCl}_3 \times 6 \text{H}_2\text{O}$ (99.99 %), $\text{YbCl}_3 \times 6 \text{H}_2\text{O}$ (99.99 %), $\text{ErCl}_3 \times 6 \text{H}_2\text{O}$ (99.99 %), NH_4F (> 98 %), 1-octadecene (90 %) and oleic acid (90 %) were purchased from Sigma-Aldrich (Germany), and NaOH (p.a.), cyclohexane (p.a.) and methanol (p.a.) from Penta (Czech Republic).

$\beta\text{-NaYF}_4\text{:18 mol \% Yb}^{3+}, 2 \text{ mol \% Er}^{3+}$ UCNPs of different sizes were synthesized by high-temperature co-precipitation.¹ $\text{YCl}_3 \times 6 \text{H}_2\text{O}$, $\text{YbCl}_3 \times 6 \text{H}_2\text{O}$ and $\text{ErCl}_3 \times 6 \text{H}_2\text{O}$ were dissolved in 20 mL of methanol and added to 100 mL three necked round bottom flask containing oleic acid and 1-octadecene. The solution was heated to 160 °C for 30 min under an argon atmosphere and then cooled down to 50 °C. Thereafter, the protective atmosphere was disconnected and the solution of NH_4F and NaOH in 20 mL of methanol was added to the intensively stirred mixture. The argon atmosphere was again connected and the solution was stirred for 30 min. The temperature was carefully increased up to 150 °C avoiding extensive boiling and ensuring evaporation of methanol. Thereafter, the solution was rapidly heated using the rate of 10 °C per minute and afterwards heating was carefully regulated to keep 305 °C (± 3 °C). Finally, the flask was placed on another stirrer and rapidly cooled down to room temperature under air flux. The resulting nanoparticles were precipitated by adding 21 mL of isopropyl alcohol and collected by centrifugation (3,000 g, 10 min). The pellet was redispersed in 20 mL of cyclohexane. Cyclohexane dispersion was precipitated by adding 100 mL of methanol and UCNPs rapidly sedimented without the need for centrifugation. Precipitated waxy UCNPs were finally redispersed in 20 mL of cyclohexane. The size of UCNPs was adjusted by using the specifications listed in **Table S1**.

Table S1: Synthesis of differently sized UCNPs.

Sample	Size (nm)	Reagents	Heating	Yield
UCNP33	37.1 ± 2.3	YCl ₃ × 6 H ₂ O 485.4 mg, 1.6 mmol YbCl ₃ × 6 H ₂ O 139.5 mg, 0.36 mmol ErCl ₃ × 6 H ₂ O 15.3 mg, 0.04 mmol oleic acid 6 mL 1-octadecene 15 mL NH ₄ F 296 mg, 8 mmol NaOH 200 mg, 5 mmol	150 min 305 °C	244 mg 59.7 %
UCNP37	48.2 ± 3.4	YCl ₃ × 6 H ₂ O 534 mg, 1.76 mmol YbCl ₃ × 6 H ₂ O 153.5 mg, 0.395 mmol ErCl ₃ × 6 H ₂ O 16.8 mg, 0.044 mmol oleic acid 6 mL 1-octadecene 15 mL NH ₄ F 326 mg, 8.8 mmol NaOH 220 mg, 5.5 mmol	150 min 305 °C	206 mg 45.7 %
UCNP43	42.5 ± 4.9	YCl ₃ × 6 H ₂ O 776 mg, 2.56 mmol YbCl ₃ × 6 H ₂ O 224 mg, 0.58 mmol ErCl ₃ × 6 H ₂ O 24 mg, 0.063 mmol oleic acid 24 mL 1-octadecene 56 mL NH ₄ F 474 mg, 12.8 mmol NaOH 320 mg, 8.0 mmol <i>In 250 mL flask</i>	90 min 300 °C	360 mg 54.5 %
UCNP64	68.8 ± 3.4	YCl ₃ × 6 H ₂ O 582.5 mg, 1.92 mmol YbCl ₃ × 6 H ₂ O 167.4 mg, 0.43 mmol ErCl ₃ × 6 H ₂ O 18.3 mg, 0.048 mmol oleic acid 6 mL 1-octadecene 15 mL NH ₄ F 356 mg, 9.6 mmol NaOH 240 mg, 6 mmol	150 min 305 °C	270 mg 55 %
UCNP88	89.6 ± 3.6	YCl ₃ × 6 H ₂ O 728 mg, 2.4 mmol YbCl ₃ × 6 H ₂ O 210 mg, 0.54 mmol ErCl ₃ × 6 H ₂ O 23.2 mg, 0.06 mmol oleic acid 6 mL 1-octadecene 15 mL NH ₄ F 444 mg, 12 mmol NaOH 300 mg, 7.5 mmol	150 min 305 °C	263 mg 38.5 %

Preparation of a Carboxylated Silica Shell on UCNPs

UCNPs were silica-coated and carboxylated by a reverse microemulsion method.^{2,3} The protocol was adjusted to account for the different sizes of UCNPs as shown in **Table S2**. UCNPs were diluted in cyclohexane with Igepal CO-520 (Sigma-Aldrich), tetraethyl orthosilicate (99 %, Sigma-Aldrich), and stirred with high intensity for 10 min. The microemulsion was created after adding water solution of ammonium hydroxide 12 % w/v. The resulting mixture was slowly stirred overnight. Another volume of tetraethyl orthosilicate was added and the microemulsion was slowly stirred for 4 hours. Carboxyethylsilanetriol sodium salt (25 % w/v in water, ABCR, Germany) was added and the cloudy emulsion was sonicated for 15 min and further stirred for 60 min. Carboxylated UCNPs were extracted by adding 500 μL of dimethylformamide and five times washed with 2 mL of acetone and three times with 2 mL of water. Carboxylated UCNPs were stored as an aqueous dispersion in a concentration of 10 mg mL^{-1} .

Table S2: Preparation of carboxylated silica shell.

Reagents	UCNP33	UCNP37	UCNP43	UCNP64	UCNP88
UCNP (mg)	10	10	10	10	10
Cyclohexane (μL)	3696	3296	2875	1906	1386
Igepal CO-520 (mg)	291	259	225	150	109
Tetraethyl orthosilicate I (μL)	16	14.3	12.5	8.3	6
Ammonium hydroxide (12 % w/v in water, μL)	17.3	15.4	13.8	17.9	13
Tetraethyl orthosilicate II (μL)	8	7.1	3.1	4.1	3
Carboxyethylsilanetriol sodium salt (25 % w/v in water, μL)	16	14.3	6.3	8.3	6

Conjugation of Carboxylated UCNPs and Antibody

The polyclonal anti-PSA antibody (AF1344) was conjugated to UCNPs according to our previous protocol.³ The carboxylated UCNPs were first activated by 1-ethyl-3-(3-(dimethylamino)propyl) carbodiimide (EDC) and *N*-hydroxysulfosuccinimide (sulfo-NHS). In a typical synthesis, 0.5 mg of carboxylated UCNPs was dispersed in water to obtain a final volume of 200 μL . Then, 50 μL of a mixture containing 0.4 mg of EDC and 1.2 mg of sulfo-NHS in 100 μL of 100 mM sodium 2-(*N*-morpholino)ethanesulfonate (MES) buffer, pH 6.1 was added and mixed for 30 min. A dispersion of 100 μL of activated UCNPs (2 mg mL^{-1}) were mixed with 100 μL of antibody (0.02 mg mL^{-1}) in 100 mM borate buffer, pH 9.0 and incubated for 90 min at room temperature. The nanoconjugates were centrifuged for 10 min at 4,000 g, dispersed in assay buffer and sonicated for 10 min. The conjugates were stored in assay buffer at 4 °C.

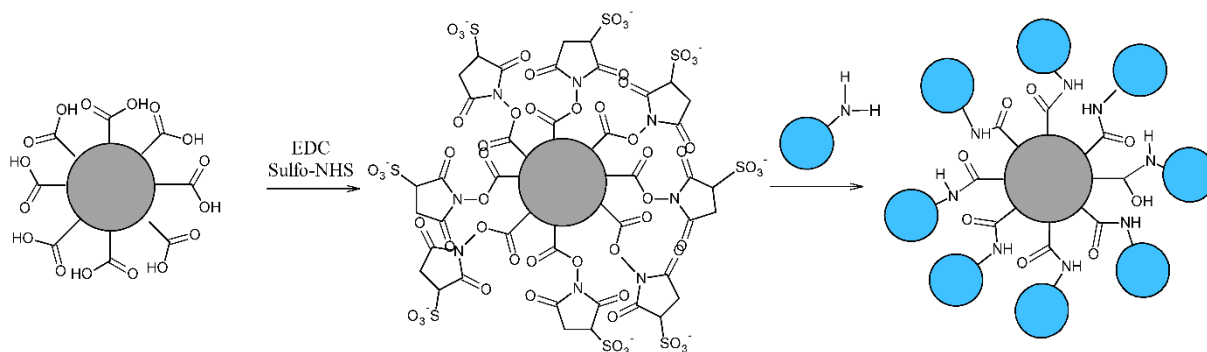


Figure S3: Surface activation of carboxylated UCNPs and conjugation of detection antibody (blue spheres) to activated carboxylated UCNPs.

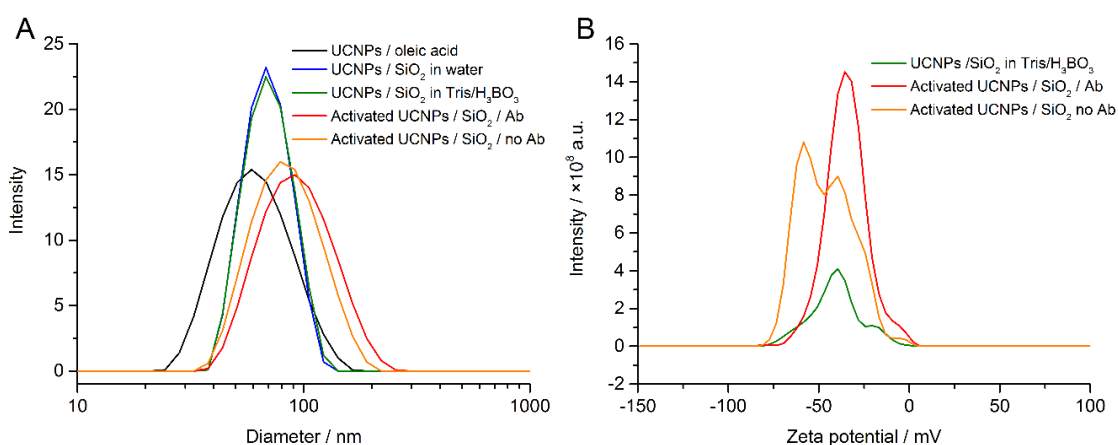


Figure S4: **A)** DLS and **B)** Zeta potentials of UCNPs (48 nm in diameter) during successive steps of antibody conjugation.

Gravimetric Analysis to Determine the Mass Concentration of UCNPs

The volume of 500 μL of oleic acid-capped UCNPs dispersed in cyclohexane (boiling point, bp = 81 $^{\circ}\text{C}$) was loaded into a glass vial. The vial was placed first on a heater to evaporate cyclohexane (bp = 81 $^{\circ}\text{C}$) and then for 3 hours in an oven to evaporate 1-octadecene (bp = 315 $^{\circ}\text{C}$) and oleic acid (bp = 360 $^{\circ}\text{C}$) at 450 $^{\circ}\text{C}$. The mass of the bare (*i.e.* uncapped) UCNPs was used to determine the mass concentration. The same procedure was also utilized for estimating the concentration of the silica-coated UCNPs.

Optimization the Detection of Single UCNPs

UCNPs were adsorbed on glass cover slips modified by cationized BSA (cBSA). The reaction mixture for preparation of cBSA consisting of 0.37 mM BSA, 100 mM ethylenediamine, 100 mM EDC and 500 mM MES was mixed for 2 hours and then dialyzed (150 mL of water, 2 days at 4 °C, water was exchanged 2 times). The cBSA solution was aliquoted and stored at -20 °C.⁴ The glass cover slips were cleaned for 10 min in Piranha solution (3:1 concentrated H₂SO₄ : 30 % H₂O₂) and activated by UV-Ozone cleaner (5 min cycle, 10 min ventilation). The cBSA (0.1 mg mL⁻¹) was adsorbed for 10 min followed by washing with water and drying under nitrogen flow. The carboxylated silica-coated UCNPs were bound for 10 min followed by washing and drying.

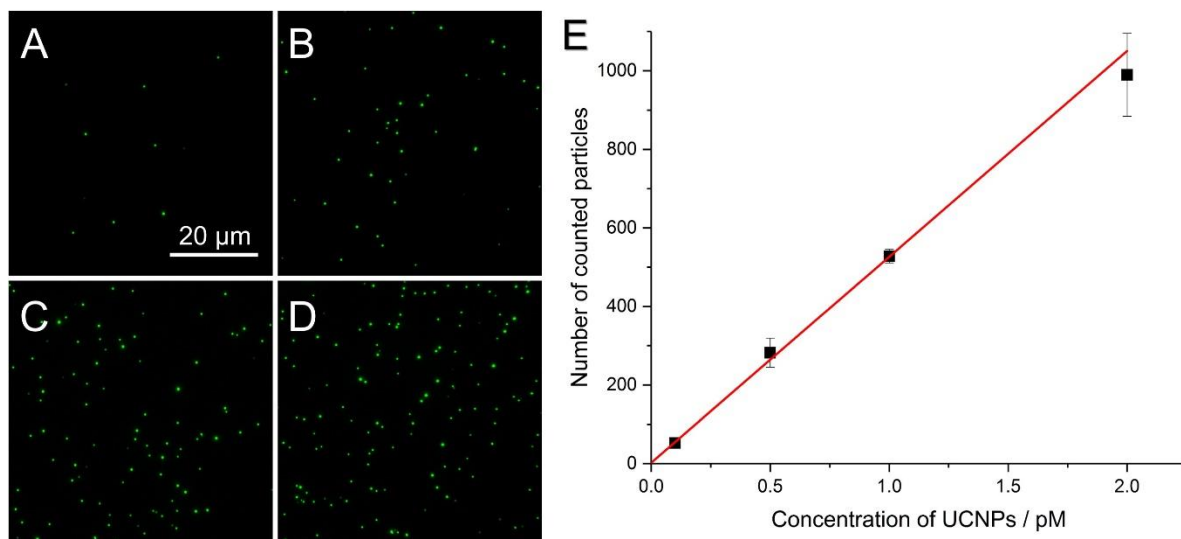


Figure S5: Upconversion microscopy images of UCNPs (diameter 43 nm) bound on cBSA-modified glass cover slips. UCNP concentrations: **A)** 0.1 pM; **B)** 0.5 pM; **C)** 1 pM; **D)** 2 pM. **E)** Calibration graph corresponding to different concentrations of UCNPs counted on cBSA-modified glass slide.

Calculation of Capture Efficiency

Diameter of μ Clear Well: 6.58 mm; sample volume: 100 μ L

(1) Filling height (h):

$$h = \frac{V}{A_W}$$

A_W : area of microplate well

$$h = \frac{V}{r^2 \cdot \pi}$$

r : radius of microplate well

(2) Lateral area (A_L):

$$A_L = \frac{V}{r^2 \cdot \pi} \cdot 2\pi r = \frac{2V}{r}$$

(3) Total area covered by PSA sample (A_T):

$$A_T = \frac{2V}{r} + r^2\pi$$

(4) Number of microscopic (Z) images ($166 \times 140 \mu\text{m}^2$) needed to cover whole surface:

$$Z = \frac{\frac{2V}{r} + r^2\pi}{A_0}$$

A_0 = Observable area

(5) Number of UCNPs (N) on whole surface:

$$N = \frac{\frac{2V}{r} + r^2\pi}{A_0} \cdot n$$

N : Average number of particles per image

(6) Capture efficiency (E):

$$E (\%) = \frac{\frac{2V}{r} + r^2\pi}{A_0} \cdot \frac{n - n_0}{c \cdot V \cdot N_A} \cdot 100$$

N_0 : Average number of non-specifically bound particles

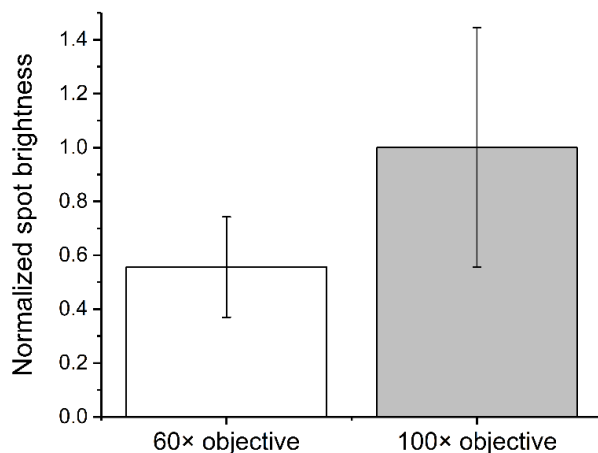


Figure S6: Microscopic detection of individual UCNPs (48 nm in diameter) immobilized on the bottom foil of a microtiter plate well using a 60× objective (NA: 1.40) and a 100× objective (NA: 1.49). The 60× has a 2.8-fold larger field of view but is less sensitive. The error bars show the standard deviation between the brightness of individual diffraction limited spots.

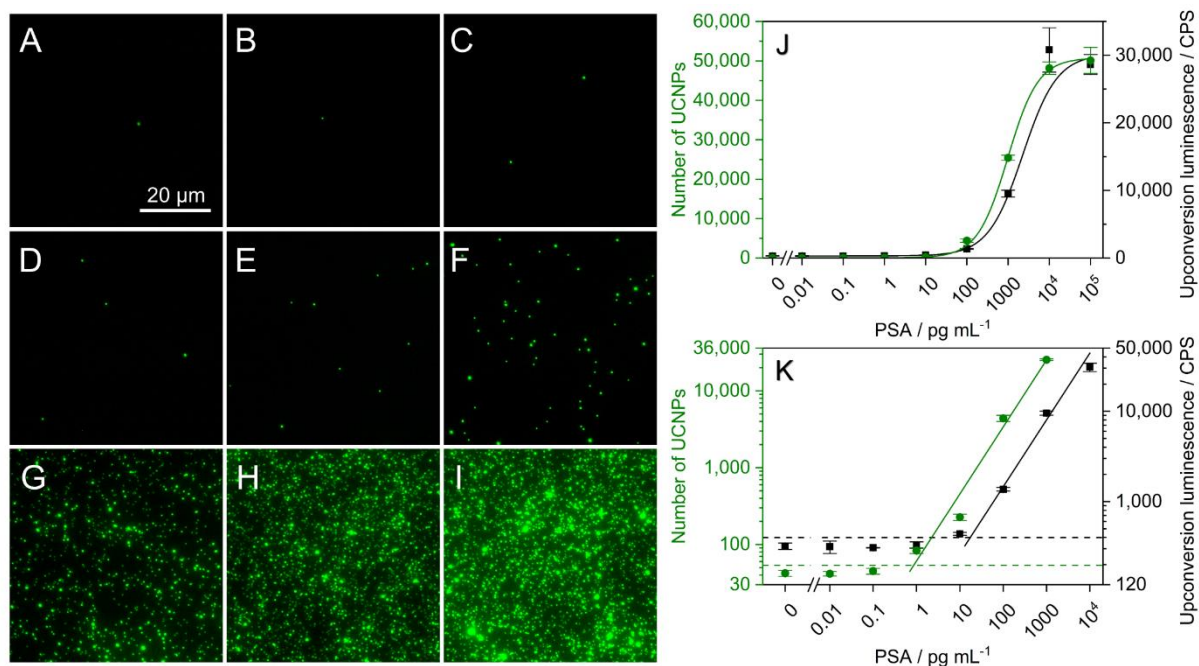


Figure S7: Upconversion microscopy images of serial PSA dilutions in assay buffer: **A)** blank; **B)** 10 fg mL⁻¹; **C)** 100 fg mL⁻¹; **D)** 1 pg mL⁻¹; **E)** 10 pg mL⁻¹; **F)** 100 pg mL⁻¹; **G)** 1 ng mL⁻¹; **H)** 10 ng mL⁻¹; **I)** 100 ng mL⁻¹. **J)** Calibration curve with sigmoidal fit; **K)** Linear regression of the dependency in the double logarithmic plot. LOD of digital ULISA 0.86 pg mL⁻¹, analog ULISA 17.3 pg mL⁻¹.

Table S3: Assay parameters of the PSA detection by digital and analog ULISA.

Method	Sample	EC ₅₀ (ng mL ⁻¹)	LOD (pg mL ⁻¹)
Digital ULISA	buffer	1.0	0.86
	25 % serum	1.8	1.21
Analog ULISA	buffer	2.3	17.28
	25 % serum	5.9	20.34

Table S4: Precision of the digital ULISA. The measurement CV was calculated as the standard deviation of three wells divided by the average number of particles per well. The Poisson noise-associated CV was calculated as \sqrt{n}/n , where n is the number of individual UCNPs counted on an area of 210 263 μm^2 (nine microscope image section combined).

Concentration of PSA	Measurement CV (%)	Poisson noise-associated CV (%)
blank	13.2	5.9
10 fg mL ⁻¹	4.0	5.6
100 fg mL ⁻¹	10.8	5.0
1 pg mL ⁻¹	13.9	4.6
10 pg mL ⁻¹	5.6	3.8
100 pg mL ⁻¹	5.6	2.2
1 ng mL ⁻¹	3.8	0.8
10 ng mL ⁻¹	4.7	0.5
100 ng mL ⁻¹	2.3	0.4

Table S5: Comparison of immunoassay and immunosensing platforms for detecting PSA.

Method	LOD	Working range	Reference
Digital assays			
Digital ULISA	1.2 pg mL ⁻¹ (42 fM)	1 pg mL ⁻¹ – 1 ng mL ⁻¹	This work
Single-molecule ELISA	1.5 fg mL ⁻¹ (52 aM)	1.5 fg mL ⁻¹ – 75 fg mL ⁻¹	⁵
Single-particle time-resolved fluorescence	1.6 pg mL ⁻¹ (50 fM)	1.6 pg mL ⁻¹ – 100 ng mL ⁻¹	⁶
Analog assays			
Analog ULISA	20.3 pg mL ⁻¹ (707 fM)	10 pg mL ⁻¹ – 10 ng mL ⁻¹	This work
Quantum dot-encoded microbeads	1 ng mL ⁻¹ (35 pM)	1 ng mL ⁻¹ – 10 ng mL ⁻¹	⁷
Microbead-based immunoassay	136 pg mL ⁻¹ (4.7 pM)	136 pg mL ⁻¹ – 8 ng mL ⁻¹	⁸
Au NP-based bio-barcode assay	330 fg mL ⁻¹ (11 fM)	330 fg mL ⁻¹ – 33 pg mL ⁻¹	⁹

Electrochemiluminescence immunoarray	50 fg mL ⁻¹ (1.7 fM)	100 fg mL ⁻¹ – 1 ng mL ⁻¹	10
Electrochemiluminescence with conductive nanospheres	40 ag mL ⁻¹ (1.4 aM)	40 ag mL ⁻¹ – 10 fg mL ⁻¹	11
Photoelectrochemistry with rolling circle amplification	320 fg mL ⁻¹ (11 fM)	1 pg mL ⁻¹ – 3 ng mL ⁻¹	12
Au NP-enhanced surface plasmon resonance	290 pg mL ⁻¹ (10 pM)	290 pg mL ⁻¹ – 150 ng mL ⁻¹	13
Localized surface plasmon resonance	100 fg mL ⁻¹ (3.5 fM)	100 fg mL ⁻¹ – 5 ng mL ⁻¹	14
UCNPs as labels in multianalyte microarray	170 pg mL ⁻¹ (5.9 pM)	100 pg mL ⁻¹ – 10 ng mL ⁻¹	15
Plasmon excited quantum dots	100 pg mL ⁻¹ (3.5 pM)	100 pg mL ⁻¹ – 100 ng mL ⁻¹	16
Quantum dot-based FRET immunoassay	0.8 ng mL ⁻¹ (28 pM)	NA	17
Chemiluminescence imaging immunoassay	7 pg mL ⁻¹ (244 fM)	10 pg mL ⁻¹ – 36.7 ng mL ⁻¹	18
Time-resolved fluorescence	1.6 pg mL ⁻¹ (56 fM)	1.6 pg mL ⁻¹ – 100 ng mL ⁻¹	6
Immuno-PCR	4 pg mL ⁻¹ (139 fM)	4 pg mL ⁻¹ – 49 ng mL ⁻¹	19
Commercial ELISAs			
Abcam ab113327	8 pg mL ⁻¹ (278 fM)	10.2 pg mL ⁻¹ – 2.5 ng mL ⁻¹	20
Abcam ab188389	4.9 pg mL ⁻¹ (170 fM)	4.1 pg mL ⁻¹ – 3 ng mL ⁻¹	21
Biorbyt orb339660	0.5 ng mL ⁻¹ (17 pM)	1 ng mL ⁻¹ – 32 ng mL ⁻¹	22
LifeSpan BioSciences LS-F25971	19.1 pg mL ⁻¹ (665 fM)	54.9 pg mL ⁻¹ – 40 ng mL ⁻¹	23
LifeSpan BioSciences LS-F5207	80 pg mL ⁻¹ (2.8 fM)	195 pg mL ⁻¹ – 12.5 ng mL ⁻¹	24
OriGene EA100514	10 pg mL ⁻¹ (348 fM)	312 pg mL ⁻¹ – 20 ng mL ⁻¹	25
R&D systems DKK300	69 pg mL ⁻¹ (2.4 pM)	0.9 ng mL ⁻¹ – 60 ng mL ⁻¹	26
Thermo Fisher Scientific EHKLK3T	8 pg mL ⁻¹ (278 fM)	8 pg mL ⁻¹ – 2 ng mL ⁻¹	27

References

1. Wang, F.; Han, Y.; Lim, C. S.; Lu, Y. H.; Wang, J.; Xu, J.; Chen, H. Y.; Zhang, C.; Hong, M. H.; Liu, X. G., Simultaneous phase and size control of upconversion nanocrystals through lanthanide doping. *Nature* **2010**, *463* (7284), 1061-1065.
2. Hlavacek, A.; Sedlmeier, A.; Skladal, P.; Gorris, H. H., Electrophoretic Characterization and Purification of Silica-Coated Photon-Upconverting Nanoparticles and Their Bioconjugates. *ACS Appl. Mater. Interfaces* **2014**, *6* (9), 6930-6935.
3. Hlaváček, A.; Farka, Z.; Hübner, M.; Hornáková, V.; Němeček, D.; Niessner, R.; Skládál, P.; Knopp, D.; Gorris, H. H., Competitive upconversion-linked immunosorbent assay for the sensitive detection of diclofenac. *Anal. Chem.* **2016**, *88* (11), 6011-6017.
4. Muckerheide, A.; Apple, R. J.; Pesce, A. J.; Michael, J. G., Cationization of protein antigens. 1. Alteration of immunogenic properties. *J. Immunol.* **1987**, *138* (3), 833-837.
5. Rissin, D. M.; Kan, C. W.; Campbell, T. G.; Howes, S. C.; Fournier, D. R.; Song, L.; Piech, T.; Patel, P. P.; Chang, L.; Rivnak, A. J.; Ferrell, E. P.; Randall, J. D.; Provuncher, G. K.; Walt, D. R.; Duffy, D. C., Single-molecule enzyme-linked immunosorbent assay detects serum proteins at subfemtomolar concentrations. *Nat. Biotechnol.* **2010**, *28* (6), 595-599.
6. Härmä, H.; Soukka, T.; Lönnberg, S.; Paukkunen, J.; Tarkkinen, P.; Lövgren, T., Zeptomole detection sensitivity of prostate-specific antigen in a rapid microtitre plate assay using time-resolved fluorescence. *Luminescence* **2000**, *15* (6), 351-355.
7. Han, S. W.; Jang, E.; Koh, W. G., Microfluidic-based multiplex immunoassay system integrated with an array of QD-encoded microbeads. *Sens. Actuators B Chem.* **2015**, *209*, 242-251.
8. Zhu, Q. D.; Trau, D., Gel pad array chip for high throughput and multi-analyte microbead-based immunoassays. *Biosens. Bioelectron.* **2015**, *66*, 370-378.
9. Thaxton, C. S.; Elghanian, R.; Thomas, A. D.; Stoeva, S. I.; Lee, J. S.; Smith, N. D.; Schaeffer, A. J.; Klocker, H.; Horninger, W.; Bartsch, G.; Mirkin, C. A., Nanoparticle-based bio-barcode assay redefines "undetectable" PSA and biochemical recurrence after radical prostatectomy. *Proc. Nat. Acad. Sci. USA* **2009**, *106* (44), 18437-18442.
10. Kadimisetty, K.; Malla, S.; Sardesai, N. P.; Joshi, A. A.; Faria, R. C.; Lee, N. H.; Rusling, J. F., Automated Multiplexed ECL Immunoarrays for Cancer Biomarker Proteins. *Anal. Chem.* **2015**, *87* (8), 4472-4478.
11. Du, S. P.; Guo, Z. Y.; Chen, B. B.; Sha, Y. H.; Jiang, X. H.; Li, X.; Gan, N.; Wang, S., Electrochemiluminescence immunosensor for tumor markers based on biological barcode mode with conductive nanospheres. *Biosens. Bioelectron.* **2014**, *53*, 135-141.

12. Zhuang, J. Y.; Tang, D. Y.; Lai, W. Q.; Xu, M. D.; Tang, D. P., Target-Induced Nano-Enzyme Reactor Mediated Hole-Trapping for High-Throughput Immunoassay Based on a Split-Type Photoelectrochemical Detection Strategy. *Anal. Chem.* **2015**, *87* (18), 9473-9480.
13. Uludag, Y.; Tothill, I. E., Cancer Biomarker Detection in Serum Samples Using Surface Plasmon Resonance and Quartz Crystal Microbalance Sensors with Nanoparticle Signal Amplification. *Anal. Chem.* **2012**, *84* (14), 5898-5904.
14. Sanders, M.; Lin, Y. B.; Wei, J. J.; Bono, T.; Lindquist, R. G., An enhanced LSPR fiber-optic nanoprobe for ultrasensitive detection of protein biomarkers. *Biosens. Bioelectron.* **2014**, *61*, 95-101.
15. Päckilä, H.; Yliharsilä, M.; Lahtinen, S.; Hattara, L.; Salminen, N.; Arppe, R.; Lastusaari, M.; Saviranta, P.; Soukka, T., Quantitative multianalyte microarray immunoassay utilizing upconverting phosphor technology. *Anal. Chem.* **2012**, *84* (20), 8628-8634.
16. Song, H. Y.; Wong, T. I.; Sadovoy, A.; Wu, L.; Bai, P.; Deng, J.; Guo, S. F.; Wang, Y.; Knoll, W. G.; Zhou, X. D., Imprinted gold 2D nanoarray for highly sensitive and convenient PSA detection via plasmon excited quantum dots. *Lab Chip* **2015**, *15* (1), 253-263.
17. Mattered, L.; Bhuckory, S.; Wegner, K. D.; Qiu, X.; Agnese, F.; Lincheneau, C.; Senden, T.; Djurado, D.; Charbonniere, L. J.; Hildebrandt, N.; Reiss, P., Compact quantum dot-antibody conjugates for FRET immunoassays with subnanomolar detection limits. *Nanoscale* **2016**, *8* (21), 11275-11283.
18. Liu, A. R.; Zhao, F.; Zhao, Y. W.; Li, S. G.; Liu, S. Q., A portable chemiluminescence imaging immunoassay for simultaneous detection of different isoforms of prostate specific antigen in serum. *Biosens. Bioelectron.* **2016**, *81*, 97-102.
19. Lind, K.; Kubista, M., Development and evaluation of three real-time immuno-PCR assemblages for quantification of PSA. *J. Immunol. Methods* **2005**, *304* (1-2), 107-116.
20. *Abcam Human PSA ELISA Kit (KLK3) (ab113327)* <http://www.abcam.com/human-psa-elisa-kit-klk3-ab113327.html>, (accessed March 23. 2020).
21. *Abcam Human Free Prostate Specific Antigen ELISA Kit (ab188389)* <http://www.abcam.com/human-free-prostate-specific-antigen-elisa-kit-ab188389.html>, (accessed March 23. 2020).
22. *Biorbyt Human PSA ELISA Kit (orb339660)* <http://www.biorbyt.com/human-psa-elisa-kit-134680>, (accessed March 23. 2020).
23. *LifeSpan BioSciences Human KLK3 / PSA ELISA Kit (CLIA) (LS-F25971)* <https://www.lsbio.com/elisakits/human-klk3-psa-elisa-kit-clia-ls-f25971/25971>, (accessed March 23. 2020).

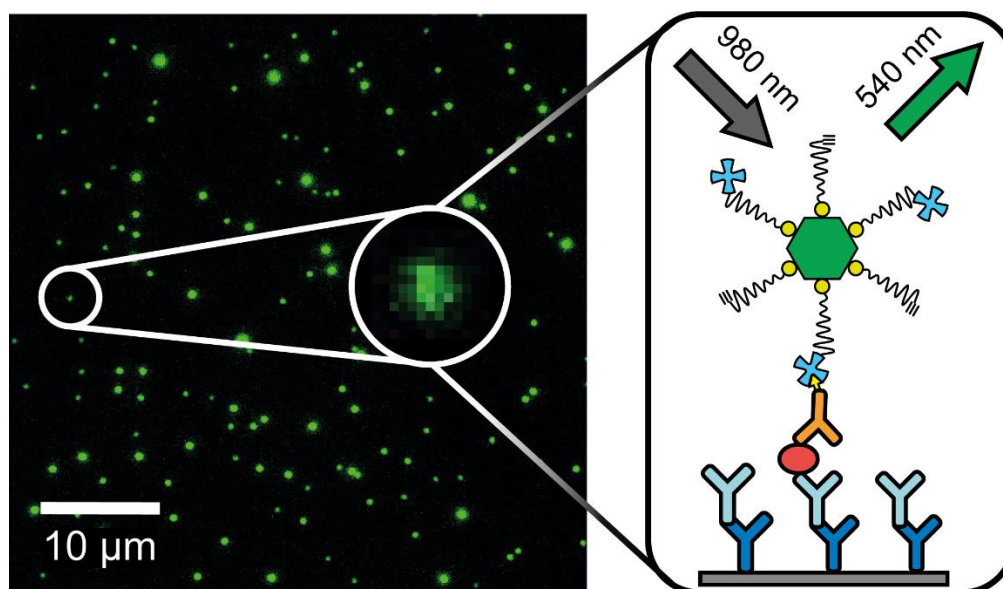
24. *LifeSpan BioSciences Human KLK3 / PSA ELISA Kit (Sandwich ELISA) (LS-F5207)*
<https://www.lsbio.com/elisakits/human-klk3-psa-elisa-kit-sandwich-elisa-ls-f5207/5207>,
(accessed March 23. 2020).
25. *OriGene Human Kallikrein 3 ELISA Kit (EA100514)*
<https://www.origene.com/catalog/assay-kits/elisa-kits/ea100514/human-kallikrein-3-elisa-kit>, (accessed March 23. 2020)
26. *R&D Systems Human Kallikrein 3/PSA Quantikine ELISA Kit (DKK300)*
https://www.rndsystems.com/products/human-kallikrein-3-psa-quantikine-elisa-kit_dkk300, (accessed March 23. 2020).
27. *Thermo Fisher Scientific PSA (Total) Human ELISA Kit (EHK3T)*
<https://www.thermofisher.com/order/catalog/product/EHK3T>, (accessed March 23. 2020).

VII. Research Article 2

Upconversion-Linked Immunosorbent Assay Measures Subfemtomolar Concentrations of Prostate-Specific Antigen through Single-Molecule Counting

Matthias J. Mickert,* Zdeněk Farka,* Uliana Kostiv, Antonín Hlaváček, Daniel Horák, Petr Skládal and Hans H. Gorris

*Matthias J. Mickert and Zdeněk Farka contributed equally to the work.



This Chapter has been published, text and figures reprinted with permission from The American Chemical Society: *Analytical Chemistry*¹, Copyright 2019.

¹Mickert, M. J., Farka, Z., Kostiv, U., Hlaváček, A., Horák, D., Skládal, P., & Gorris, H. H. Measurement of Sub-femtomolar Concentrations of Prostate-Specific Antigen through Single-Molecule Counting with an Upconversion-Linked Immunosorbent Assay. *Anal. Chem.* **2019**, *91*(15), 9435-9441.

VII.1. Abstract

Single-molecule (digital) immunoassays provide the ability to detect much lower protein concentrations than conventional immunoassays. As photon-upconversion nanoparticles (UCNPs) can be detected without optical background interference, they are excellent labels for so-called single-molecule upconversion-linked immunosorbent assays (ULISAs). We have introduced a UCNP label design based on streptavidin-PEG-neridronate and a two-step detection scheme involving a biotinylated antibody that efficiently reduces non-specific binding on microtiter plates. In a microtiter plate immunoassay, individual sandwich immune complexes of the cancer marker prostate specific antigen (PSA) were detected and counted by wide-field epiluminescence microscopy (digital readout). The digital detection is 16× more sensitive than the respective analog readout and thus expands the limit of detection to the subfemtomolar concentration range (LOD: 23 fg mL⁻¹; 800 aM). The single molecule ULISA shows excellent correlation with an electroluminescence reference method. While the analog readout can routinely measure PSA concentrations in human serum samples, very low concentrations have to be monitored after radical prostatectomy. Combining the digital and analog readout covers a dynamic range of more than three orders of magnitude in a single experiment.

VII.2. Introduction

In recent years, the development of immunoassays has been strongly driven by new nanomaterial-based detection labels,¹ such as quantum dots,² europium-based nanoparticles,³ carbon nanotubes,⁴ gold nanoparticles,⁵ silicon nanowires,⁶ nanozymes⁷ and upconversion nanoparticles (UCNPs).⁸ Unlike enzymes, nanomaterials are chemically and physically stable,⁹ and their properties can be tuned by size and/or composition.¹⁰⁻¹¹ In particular, the anti-Stokes emission of UCNPs under NIR excitation (980 nm) prevents autofluorescence, minimizes light scattering, and thus enables the detection of analytes without optical background interference. UCNPs sequentially absorb two or more photons and emit light of shorter wavelengths (NaYF₄:Yb,Er: green/red emission or NaYF₄:Yb,Tm: blue/800 nm emission).¹²⁻¹³ In contrast to organic fluorophores, UCNPs are highly photostable over long periods of time and under high excitation intensities,¹⁴ which is especially important for the design of labels in single-molecule immunoassays.¹⁵ The ability to detect and count single molecules of an analyte of interest (digital readout) opens up the door to reach the ultimate sensitivity in analytical chemistry,¹⁶⁻¹⁸ because the signal-to-background ratio is not affected when analytes have to be measured at ever lower concentrations.¹⁹⁻²²

Prostate cancer is the most frequently diagnosed type of cancer among men and the fifth leading cause of death from cancer worldwide.²³ Epithelial cells of the prostate secrete prostate-specific antigen (PSA) with typical serum concentrations of less than 4 ng mL⁻¹ in healthy men. Higher PSA concentrations are an important indicator of prostate cancer.²⁴⁻²⁶ The removal of the carcinoma by radical prostatectomy leads to a drastic drop of PSA levels,²⁷ which, however, must be monitored repeatedly and with high sensitivity in order to detect cancer recurrence as early as possible.²² Conventional enzyme-linked immunosorbent assays (ELISAs) reach limits of detection (LOD) in the range of 100 pg mL⁻¹ as shown in the Supplemental **Table S1**. We previously developed a single-molecule upconversion-linked immunosorbent assay (ULISA) by using silica-coated UCNPs conjugated to an anti-PSA antibody as a detection label.²⁸ With an LOD of 1.2 pg mL⁻¹, the ULISA was about 10 - 100× more sensitive than conventional ELISAs. Non-specific surface binding and the sterically constrained PSA-capture efficiency of the UCNP-conjugate, however, limited the sensitivity at very low PSA concentrations.

In this work, we have designed a new single-molecule ULISA scheme as shown in **Figure 1**. We replaced the antibody-silica-UCNPs by streptavidin-coated UCNPs linked via poly(ethylene glycol) (SA-PEG-UCNPs) based on the following considerations: First, the hydrophilic PEG renders UCNPs highly water dispersible and resistant against aggregation. Second, steric hindrance and repulsion effects of surface-bound PEG reduce non-specific binding e.g. of serum proteins.²⁹⁻³³ Third, the two-step addition of a biotinylated detection antibody followed by SA-UCNPs allows for using a relatively high concentration of the detection antibody to efficiently label all PSA molecules immobilized on the surface of the microtiter plate. The concentration of the UCNP label (and associated non-specific binding effects), however, can be kept much lower because the extremely high affinity of SA and biotin (10⁻¹⁵ mol L⁻¹) ensures an efficient binding to the detection antibody.³⁴

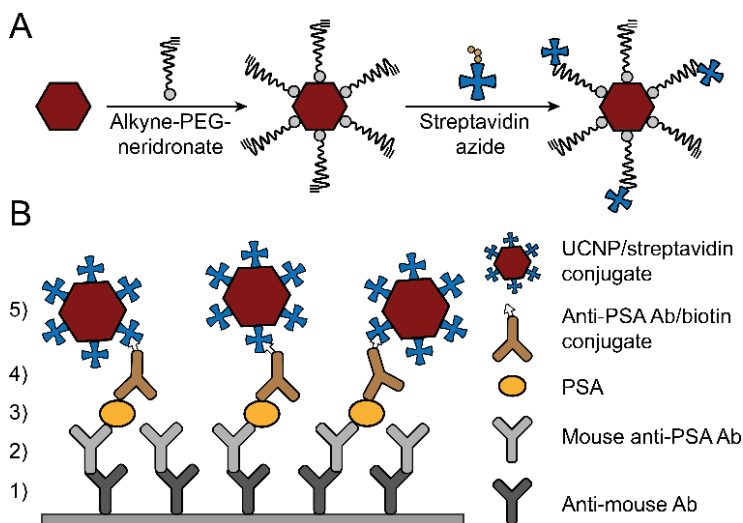


Figure 1: Schematic representation of UCNP conjugation and sandwich ULISA. **A)** Alkyne-PEG-neridronate is bound to the UCNP via coordination of two phosphonate groups of neridronate to surface exposed lanthanide ions. Streptavidin is covalently bound to the PEG via a click reaction between the alkyne group of the PEG and streptavidin azide. **B)** 1) A microtiter well is coated with an anti-mouse antibody. 2) A mouse monoclonal anti-PSA capture antibody binds to the anti-mouse antibody. 3) PSA is captured by the monoclonal anti-PSA antibody. 4) A biotinylated polyclonal anti-PSA antibody forms a sandwich immune complex. 5) SA-coated UCNPs bind to the biotinylated primary antibody. The individual assay steps are shown in **Figure S1**.

VII.3. Materials and Methods

Antibodies were characterized by surface plasmon resonance measurements as described in the **SI (Figure S2)**. Random serum samples and data on PSA levels determined by the Elecsys electroluminescent immunoassay (Roche Diagnostics, Germany) were provided by a hospital in Svitavy, Czech Republic. Streptavidin-coated RD Upcon™ nanoparticles (Erbium-540-SA, 58 nm in diameter) were provided by Kaivogen (Turku, Finland, TEM images shown in **Figure S3**).

Preparation and Characterization of SA-PEG-UCNP Labels

The syntheses of $\text{NaYF}_4:\text{Yb}^{3+},\text{Er}^{3+}$ - and $\text{NaYF}_4:\text{Yb}^{3+},\text{Tm}^{3+}$ -doped UCNPs and of the surface ligand alkyne-PEG-neridronate are described in the **SI**. The surface of UCNPs was modified by mixing an aqueous dispersion of UCNPs (10 mL, 14 mg mL⁻¹) with 28 mg of alkyne-PEG-neridronate ($M_w \sim 5160 \text{ g mol}^{-1}$) and stirring for 24 h at room temperature (RT). The alkyne-PEG-neridronate-functionalized UCNPs were dialyzed (M_w cut-off 100 kDa) against water for 48 h at 4 °C. Streptavidin was attached to the surface ligands via click reaction: A 1-mL dispersion of 7 mg alkyne-PEG-UCNPs in 25 mM Tris/HCl (pH 7.5) was mixed with 25 μL

of streptavidin azide (1 mg mL^{-1} , 7 Bioscience, Germany), $20 \text{ }\mu\text{L}$ of sodium L-ascorbate (20 mg mL^{-1}), and purged with argon for 30 min to remove oxygen. The 1,3-cycloaddition was started by adding $10 \text{ }\mu\text{L}$ of 50 mM CuSO_4 to generate the Cu(I) catalyst *in situ*. The streptavidin-PEG-neridronate-modified nanoparticles (SA-PEG-UCNP, chemical structure shown in **Figure S4**) were sonicated for 10 min and dialyzed (M_w cut-off 100 kDa) against 2 L of 50 mM Tris/HCl (pH 7.5) for 12 h at $4 \text{ }^\circ\text{C}$ (twice exchanged) and stored in the same buffer at $4 \text{ }^\circ\text{C}$.

The morphology of UCNPs was investigated by transmission electron microscopy (TEM; Tecnai G2 Spirit Twin 12, FEI, Czech Republic). TEM images were analyzed by ImageJ (NIH, USA) to determine the size of UCNPs (**Figures S5-S6**). Dynamic light scattering (DLS) was recorded on a Zetasizer Nano ZS instrument (Malvern, UK) (**Figure S7**). The activity of surface-bound streptavidin was tested using a BSA-biotin assay as described in the SI (**Figure S8**).

Upconversion-Linked Immunosorbent Assay (ULISA)

A 96-well microtiter plate (μClear , high binding, Greiner Bio-One) was coated with a polyclonal horse anti-mouse antibody ($3 \text{ }\mu\text{g mL}^{-1}$, $200 \text{ }\mu\text{L}$, Vector Laboratories, USA) in coating buffer (42 mM NaHCO_3 , $8 \text{ mM Na}_2\text{CO}_3$, $0.05\% \text{ NaN}_3$, pH 9.6) at $4 \text{ }^\circ\text{C}$ overnight. The following steps were all performed at RT. The plate was washed four times with $250 \text{ }\mu\text{L}$ of washing buffer ($10.4 \text{ mM NaH}_2\text{PO}_4$, $39.6 \text{ mM Na}_2\text{HPO}_4$, 150 mM NaCl , $0.05\% \text{ NaN}_3$, pH 7.4) and blocked for 1 h with $200 \text{ }\mu\text{L}$ of washing buffer containing $1\% \text{ BSA}$ (Carl Roth, Germany). After four washing steps, the microtiter plate was incubated with $0.3 \text{ }\mu\text{g mL}^{-1}$ of monoclonal mouse anti-PSA antibody (ab403, Abcam, UK) for 1 h in assay buffer (50 mM Tris , 150 mM NaCl , $0.05\% \text{ NaN}_3$, $0.5\% \text{ bovine gamma globulin}$ (Sigma Aldrich), $0.2\% \text{ BSA}$, $0.01\% \text{ Tween 20}$, $0.2\% \text{ poly(vinyl alcohol)}$ ($M_w 6000 \text{ g mol}^{-1}$), $1\% \text{ glucose}$, 5 mM EDTA and 1 mM KF). The microtiter plate was washed four times. For the calibration curve, serial dilutions of a PSA standard (Abcam, ab78528, 0.2 mg mL^{-1}) were prepared in assay buffer containing $25\% \text{ bovine serum}$ (Sigma-Aldrich). For the analysis of real samples, $2.5 \text{ }\mu\text{L}$ of serum was diluted $400\times$ in 1 mL of assay buffer/ $25\% \text{ bovine serum}$. Each sample was added in a volume of $100 \text{ }\mu\text{L}$ to the microtiter wells and incubated for 1 h. The microtiter plate was washed four times and incubated with $100 \text{ }\mu\text{L}$ of $0.25 \text{ }\mu\text{g mL}^{-1}$ biotinylated anti-PSA antibody (BAF1344, R&D Systems, USA) for 1 h. After four washing steps, either $100 \text{ }\mu\text{L}$ of $0.7 \text{ }\mu\text{g mL}^{-1}$ commercial SA-coated UCNPs (Kaivogen) or $100 \text{ }\mu\text{L}$ of $3.5 \text{ }\mu\text{g mL}^{-1}$ SA-PEG-UCNPs were applied to each well and incubated for 1 h. The plate was washed four times and left to air dry before the analog and digital readout.

For the analog readout, a custom-built upconversion microtiter plate reader (Chameleon, Hidex, Finland) scanned each well in a rectangular grid of 8×8 pixels with 1 s exposure time

per pixel and a scanning step size of 0.1 mm.³⁵ The truncated average of the luminescence intensities was calculated excluding the 16 highest and the 16 lowest values. For the digital readout, 100 μ L of glycerol was added to the dry wells to minimize local heating effects during NIR excitation (4 W laser, 640 W cm⁻²). The thin bottom foil (190 μ m) of the microtiter wells compensated for the short working distance of the high numerical aperture objective (NA 1.49). A modified epifluorescence microscope (**SI**) recorded nine wide-field images of 166 \times 140 μ m² per well (total imaging area 0.2 mm²) in a rectangular grid with a step size of 300 μ m and an exposure time of 20 s.²⁸ The software NIS elements (Nikon) automatically identified and counted single UCNP in each image. The total number of UCNP in all nine images was used for the digital data analysis. For both the analog and digital analysis, the average and standard deviation were calculated from three wells and analyzed using a four-parameter logistic function (**SI**).²⁸

VII.4. Results and Discussion

Optimization of the UCNP-Label Design

The sensitivity of the ULISA critically depends on antibodies with a high affinity for the cancer marker as well as the design of well-defined detection labels (SA-UCNP). The high affinity of capture and detection antibodies to PSA was confirmed by surface plasmon resonance (SPR) measurements (**Figure S2**). We optimized the ULISA using PSA from a commercial sample and Er-doped SA-UCNPs. According to the scheme in **Figure 1**, a microtiter plate was coated with an anti-IgG antibody followed by an anti-PSA capture antibody to reduce steric hindrance between the microtiter plate surface and the UCNP label. PSA was serially diluted in assay buffer and then transferred to the microtiter plate. A biotinylated anti-PSA antibody was added followed by an SA-UCNP label. The label concentrations were adjusted individually to achieve the optimal balance between a high labeling efficiency and a low non-specific binding. The upconversion luminescence was detected both by using an upconversion microtiter plate reader (analog mode) and by counting individual immune complexes with a wide-field microscope (digital mode). **Table 1** shows the effects of different labels and readout modes on the immunoassay performance.

Table 1: Influence of the type of UCNP label and the readout mode on the ULISA performance.

Type of UCNP(Er)	SA-PEG-UCNP		Commercial SA-UCNP		Ab-silica-UCNP ²⁸	
Size (nm)	30/35 ^a		58		48 ^a	
Label concentration (pM) ^b	~100		~3		~70	
Readout mode	analog	digital	analog	digital	analog	digital
Non-specific binding ^c	129 ± 7	49 ± 2	45 ± 19	138 ± 13	274 ± 6	73 ± 10
Individual spot brightness	n.a.	70 ± 89	n.a.	39 ± 28	n.a.	69 ± 67
Test midpoint (pg mL ⁻¹)	2100	600	930	430	5900	1800
Working range (pg mL ⁻¹)	1 – 1 000	0.1 – 100	10 – 1 000	1 – 100	100 – 10 000	10 – 1 000
Combined working range	0.1 – 1 000		1 – 1 000		10 – 10 000	
Detection efficiency (%) ^d	n.a.	17	n.a.	3	n.a.	0.5
LOD (pg mL ⁻¹)	0.41	0.023	1.71	0.24	20.3	1.2
LOD (fM)	14	0.8	60	8.4	700	42
Number of PSA molecules ^e	~800 000	~50 000	~3.6×10 ⁶	~500 000	~42×10 ⁶	~2.5×10 ⁶
Sensitivity enhancement ^f	18		7		17	

^a Average diameter/length of 300 UCNP s determined by TEM. ^b Calculation in the SI. ^c Analog readout: UCL (CPS), digital readout: number of luminescent spots in the background images (0.2 mm²). ^d Ratio of background corrected PSA molecules and total number of PSA molecules per well (SI). ^e In a microtiter plate well volume of 100 μL. ^f LOD_{analog}/LOD_{digital}.

The ULISA involving (1) a biotinylated antibody and (2) SA-PEG-UCNPs was 50 times more sensitive compared to our earlier study based on antibody-silica-UCNP conjugates.²⁸ The lower test midpoint further confirms the improved binding kinetics afforded by the two-step label systems. A comparison including SA-PEG-UCNPs (**Figure S9**) and commercial SA-UCNPs (**Figures S10-S11**) shows that the digital readout yields a 7× to 18× lower LOD than the respective analog readout of the same microtiter plate experiment. While the label design is very important to improve the immunoassay performance in general, the digital readout gives a final boost to the assay sensitivity. Additional experiments confirming the long-time stability (> 3 months) of the SA-PEG-UCNPs in suspension and evaluating the effects of label purification by sucrose gradient centrifugation are described and discussed in the SI (**Figures S12-S14**).

We furthermore determined an analog microscope readout by integrating the total spot intensity of each microscope image and compared it to the digital readout of the same image. Since the analog microscope readout was 100-fold less sensitive than the digital readout

(**Figure S15**), the high signal acquisition of the microscope objective (NA 1.49) cannot explain the benefits of the digital readout. The digital readout was rather more sensitive because detecting and counting of individual UCNPs in the confined area of a diffraction-limited spot is independent of the total intensity in the entire imaging area. Especially at low PSA concentrations, the total emission of only few UCNPs distributed over a relatively large area of 0.2 mm^2 is not sufficient to increase the signal above the background.

Determination of PSA in Human Serum Samples

For the analysis of PSA in human serum samples, we prepared SA-PEG-UCNPs doped with Tm because the NIR-emission (800 nm) of Tm-doped UCNPs is brighter than the emission of Er-doped UCNPs and single UCNPs can be counted more easily. **Figure 2** shows microscope images of PSA dilution series in microtiter plates used for single-molecule counting (digital readout). In the background image (no PSA, **Figure 2A**), only 476 luminescent spots were detectable on a total area of 0.2 mm^2 due to non-specific binding of UCNP labels to the microtiter plate surface. As in any conventional immunoassay, low non-specific binding is essential to ensure a low background signal. **Figure 2J** shows the brightness variation of individual luminescent spots that can be attributed to some label aggregation. The following example illustrates the advantage of the digital readout compared to the analog readout: If two types of UCNP labels containing more or less aggregates show the same degree of non-specific binding (e.g. 3 binding events on a given area), the aggregated labels lead to a much higher background signal in the conventional readout scheme (**Figure 2K**, analog signal: 17 UCL) compared to the homogeneous labels (**Figure 2L**, analog signal: 4 UCL). Consequently, the digital readout confers robustness against the effects of label aggregation because each aggregate—independent of its size—only counts as a single binding event.

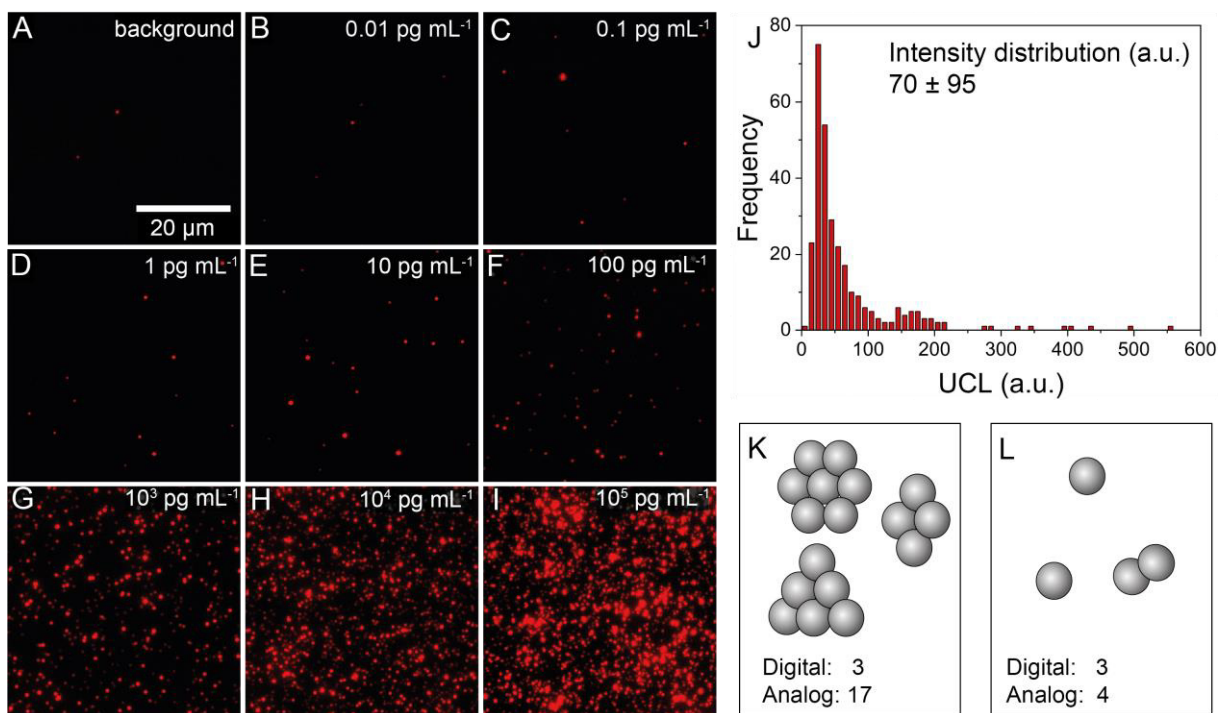


Figure 2: Digital PSA calibration in assay buffer using SA-PEG-UCNP(Tm) labels. **A-I)** Wide-field upconversion microscopy (λ_{ex} : 980 nm, λ_{em} : 800 nm) showing small image sections ($50 \times 50 \mu\text{m}^2$) of serial PSA dilutions. The PSA concentrations are indicated in the panels. **J)** Brightness distribution of 300 luminescent spots recorded at a PSA concentration of 100 pg mL^{-1} . **K)** Small aggregates and **L)** homogeneous nanoparticles affect the background signal of the digital and analog readout in a different way.

In addition to variations between repeated measurements, the precision of the digital immunoassay depends on the sampling error because a limited number of observed binding events is not necessarily representative of all binding events.³⁶ The stochastic nature of discrete binding events is also known as the Poisson noise (\sqrt{n}/n), which depends on the number of counted spots (n). The Poisson noise is highest at low PSA concentration levels and can be reduced by increasing the imaging area. **Table S2** shows a Poisson noise of $< 5\%$ for all PSA concentrations, which is comparable to the variation between repeated measurements. In the upper concentration range, the digital readout is limited if diffraction-limited spots cannot be distinguished individually any more but rather form a continuous layer.

The ULISA calibration curves in **Figure 3A** show that the digital readout reaches a $16\times$ lower LOD of 24 fg mL^{-1} (840 aM) than the respective analog readout of the same microtiter plate experiment. This improvement is similar as the $18\times$ lower LOD achieved by using the digital mode for the readout of Er-doped SA-PEG-UCNP labels (**Table 1**). These experiments also confirm that the advantages of the digital detection are independent of the type of UCNP label. In this context, it should be noted that the dynamic range of the ULISA can be extended by

two orders of magnitude (0.1 pg mL^{-1} - 1 ng mL^{-1}) if the digital readout is used for low PSA concentrations and the analog readout for high PSA concentrations.³⁷

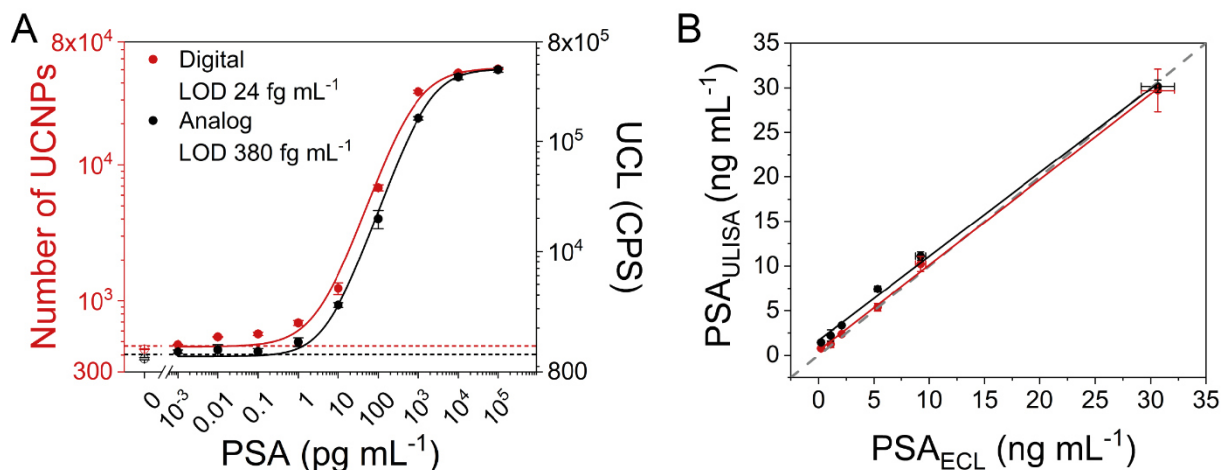


Figure 3: **A)** Calibration curves of the ULISA in the digital (red, LOD: 24 fg mL^{-1}) and analog (black, LOD: 380 fg mL^{-1}) mode. The number of UCNPs(Tm) was determined by microscopy (**Figure 2**) and the upconversion luminescence by a microtiter plate reader. The log scale of the y-axis highlights signals in the lower PSA concentration range. LODs (hatched lines) represent three times the standard deviation of the background (no PSA) above the baseline of the regression curve. **B)** Correlation between the PSA concentrations in human serum samples determined by using the digital (red line) or analog (black line) ULISA and an electrochemiluminescent immunoassay (ECL, digital R^2 : 0.998, analog R^2 : 0.997, **Table S4**). Error bars indicate the standard deviation of three replicate experiments.

Random human serum samples with PSA concentrations determined by an electrochemiluminescent immunoassay were provided by a hospital. Linearity-of-dilution experiments on a serum sample containing 215 pg mL^{-1} of PSA showed recovery rate fluctuations of less than 25% when comparing the analog and digital ULISA with the electrochemiluminescent reference method (**Table S3**). For routine analysis of serum samples, we pre-diluted the human serum samples by a factor of 400 because the serum of healthy individuals contains PSA concentrations of around 4 ng mL^{-1} .²⁴ The results of the analog and the digital readout of the ULISA are in excellent agreement with the values determined by the reference method (**Figure 3B**).

VII.5. Conclusions

In conclusion, the digital ULISA achieves a sub-femtomolar LOD. We used Er³⁺-doped (LOD: 800 aM; 2.3 fg of PSA per well) and Tm³⁺-doped UCNP (LOD: 840 aM; 2.4 fg of PSA per well) and demonstrated that the advantages of the digital readout are independent of the type of label. The indirect labeling system consisting of a biotinylated anti-PSA antibody and SA-UCNPs ensures that the biotinylated antibody without nanoparticle has better access to PSA bound to the surface of the microtiter plate. The extremely strong SA/biotin affinity can then compensate for the sterically constrained access of the SA-UCNP conjugates to the biotinylated antibody on the microtiter plate surface. The digital readout further improves the LOD for two reasons: (1) Individual immune complexes/UCNPs can be distinguished from the local background signal on a very small area, while the whole imaging area contributes to the background signal of the analog readout. (2) The digital readout is largely resistant to label aggregation because each aggregate is detected only as a single binding event. Consequently, the digital detection of PSA always achieved lower LODs than the respective analog detection, and the advantages of the digital mode became more distinctive when the level of non-specific binding was low. Reducing non-specific binding and using smaller UCNP to improve the label binding can even further enhance the ULISA performance. A comparison of various PSA assays described in the literature (**Figure 4**) shows that the digital ULISA can readily outperform commercial analog immunoassays for the detection of PSA. While the digital ELISA based on femtoliter arrays achieves an even lower LOD, the digital ULISA can be operated more easily using standard immunoassay protocols. Analyte binding and detection can be performed at the same site on a standard microtiter plate, whereas other digital immunoassays require a separation step between analyte capture on beads and the detection of the labelled immune complex either in femtoliter arrays²² or in glass capillaries.¹⁹

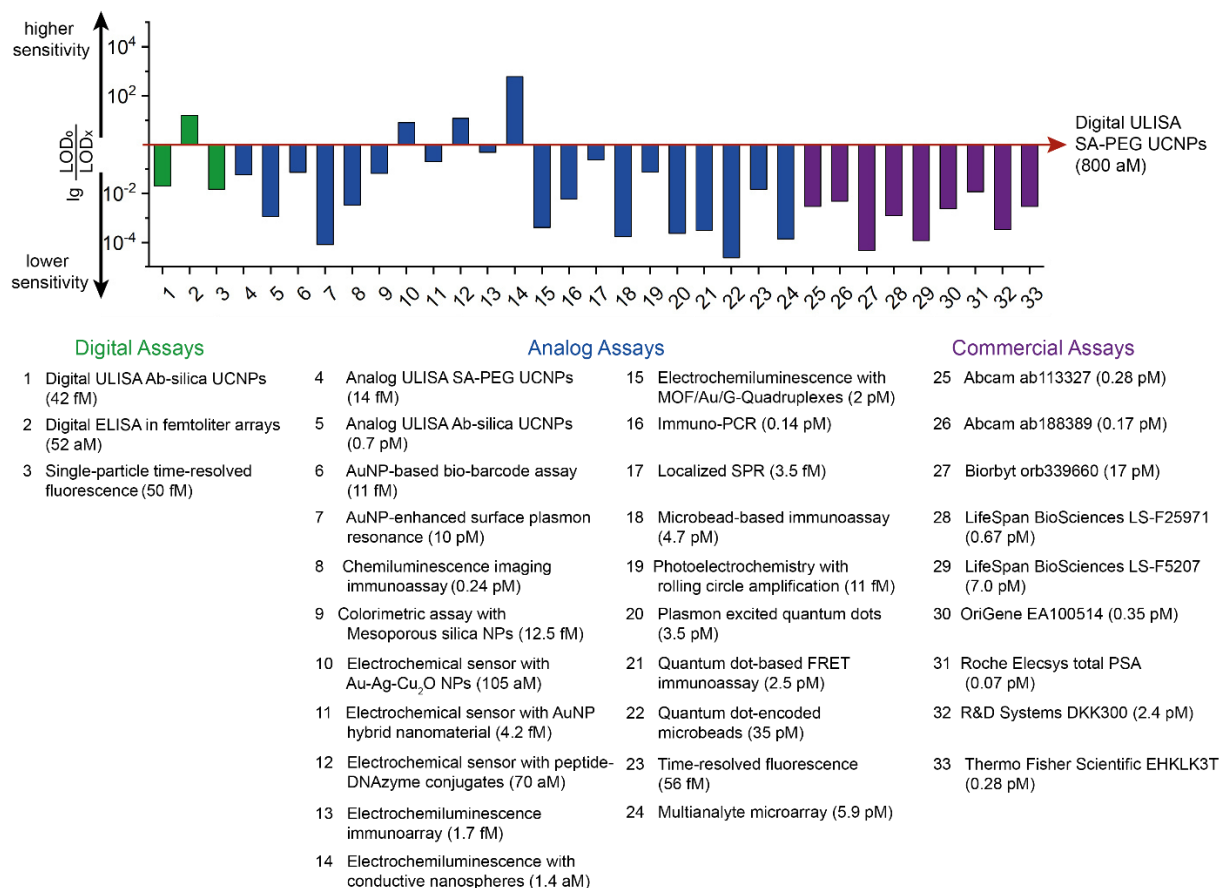


Figure 4: Comparison of the digital ULISA to PSA assays described in the literature. The relative assay performance is indicated as the decadic logarithm of the ratio of LOD_0 (digital ULISA) and LOD_x (other PSA assays). Values above 1 refer to lower LODs, and values below 1 to higher LODs compared to the digital ULISA (red arrow). Green: single-molecule assays (including commercial platforms), blue: non-commercial analog assays, purple: commercial analog assays. References are listed in **Table S1**.

Acknowledgements

We thank Kaivogen (Turku, Finland) for providing streptavidin-coated UCNPs and Dr. Miluše Marečková from the hospital in Svitavy (Czech Republic) for data on PSA serum levels. We further thank Matěj Pastucha (CEITEC, Masaryk University, Brno, Czech Republic) for his help with the SPR measurements and Sandy Franziska Himmelstoß and Dr. Thomas Hirsch (University of Regensburg, Germany) for providing the equipment and their expertise in DLS measurements. We acknowledge financial support from the COST Action CM1403 “The European Upconversion Network: From the Design of Photon-Upconverting Nanomaterials to Biomedical Applications” and the German Academic Exchange Service (DAAD). H.H.G. acknowledges funding from the German Research Foundation (DFG: GO 1968/5-1,

Heisenberg Fellowship and GO 1968/6-1). Z.F. and P.S. acknowledge financial support from the Ministry of Education, Youth and Sports of the Czech Republic under the project CEITEC 2020 (LQ1601). A.H. acknowledges funding from the Czech Science Foundation for project 18-03367Y, and U.K. and D.H. for project 19-00676S.

VII.6. References

1. Farka, Z.; Juřík, T.; Kovář, D.; Trnková, L.; Skládal, P., Nanoparticle-based immunochemical biosensors and assays: recent advances and challenges. *Chem. Rev.* **2017**, *117* (15), 9973-10042.
2. Bhuckory, S.; Mattera, L.; Wegner, K.; Qiu, X.; Wu, Y.-T.; Charbonniere, L.; Reiss, P.; Hildebrandt, N., Direct conjugation of antibodies to the ZnS shell of quantum dots for FRET immunoassays with low picomolar detection limits. *Chem. Commun.* **2016**, *52* (100), 14423-14425.
3. Härmä, H.; Soukka, T.; Lövgren, T., Europium nanoparticles and time-resolved fluorescence for ultrasensitive detection of prostate-specific antigen. *Clin. Chem.* **2001**, *47* (3), 561-568.
4. Yu, X.; Munge, B.; Patel, V.; Jensen, G.; Bhirde, A.; Gong, J. D.; Kim, S. N.; Gillespie, J.; Gutkind, J. S.; Papadimitrakopoulos, F., Carbon nanotube amplification strategies for highly sensitive immunodetection of cancer biomarkers. *J. Am. Chem. Soc.* **2006**, *128* (34), 11199-11205.
5. Grubisha, D. S.; Lipert, R. J.; Park, H.-Y.; Driskell, J.; Porter, M. D., Femtomolar detection of prostate-specific antigen: an immunoassay based on surface-enhanced Raman scattering and immunogold labels. *Anal. Chem.* **2003**, *75* (21), 5936-5943.
6. Cui, Y.; Wei, Q.; Park, H.; Lieber, C. M., Nanowire nanosensors for highly sensitive and selective detection of biological and chemical species. *Science* **2001**, *293* (5533), 1289-1292.
7. Farka, Z.; Čunderlová, V.; Horáčková, V.; Pastucha, M.; Mikušová, Z.; Hlaváček, A.; Skládal, P., Prussian Blue Nanoparticles as a Catalytic Label in a Sandwich Nanozyme-Linked Immunosorbent Assay. *Anal. Chem.* **2018**, *90* (3), 2348-2354.
8. Hlaváček, A.; Peterek, M.; Farka, Z.; Mickert, M. J.; Pechtl, L.; Knopp, D.; Gorris, H. H., Rapid single-step upconversion-linked immunosorbent assay for diclofenac. *Microchim. Acta* **2017**, *184* (10), 4159-4165.
9. Alivisatos, P., The use of nanocrystals in biological detection. *Nat. Biotechnol.* **2004**, *22* (1), 47.
10. Wang, F.; Deng, R.; Wang, J.; Wang, Q.; Han, Y.; Zhu, H.; Chen, X.; Liu, X., Tuning upconversion through energy migration in core-shell nanoparticles. *Nat. Mater.* **2011**, *10*, 968.
11. Medintz, I. L.; Uyeda, H. T.; Goldman, E. R.; Mattoussi, H., Quantum dot bioconjugates for imaging, labelling and sensing. *Nat. Mater.* **2005**, *4*, 435.
12. Haase, M.; Schafer, H., Upconverting Nanoparticles. *Angew. Chem. Int. Ed.* **2011**, *50* (26), 5808-5829.
13. Nam, S. H.; Bae, Y. M.; Park, Y. I.; Kim, J. H.; Kim, H. M.; Choi, J. S.; Lee, K. T.; Hyeon, T.; Suh, Y. D., Long-term real-time tracking of lanthanide ion doped upconverting nanoparticles in living cells. *Angew. Chem. Int. Ed.* **2011**, *123* (27), 6217-6221.

14. Gorris, H. H.; Wolfbeis, O. S., Photon-upconverting nanoparticles for optical encoding and multiplexing of cells, biomolecules, and microspheres. *Angew. Chem. Int. Ed.* **2013**, *52* (13), 3584-3600.
15. Hlaváček, A.; Mickert, M. J.; Soukka, T.; Lahtinen, S.; Tallgren, T.; Pizurova, N.; Król, A.; Gorris, H. H., Large-Scale Purification of Photon-Upconversion Nanoparticles by Gel Electrophoresis for Analog and Digital Bioassays. *Anal. Chem.* **2018**, *91* (2), 1241-1246.
16. Zhang, Y.; Noji, H., Digital bioassays: Theory, applications, and perspectives. *Anal. Chem.* **2016**, *89* (1), 92-101.
17. Holzmeister, P.; Acuna, G. P.; Grohmann, D.; Tinnefeld, P., Breaking the concentration limit of optical single-molecule detection. *Chem. Soc. Rev.* **2014**, *43* (4), 1014-1028.
18. Gooding, J. J.; Gaus, K., Single-Molecule Sensors: Challenges and Opportunities for Quantitative Analysis. *Angew. Chem. Int. Ed.* **2016**, *55* (38), 11354-11366.
19. Todd, J.; Freese, B.; Lu, A.; Held, D.; Morey, J.; Livingston, R.; Goix, P., Ultrasensitive flow-based immunoassays using single-molecule counting. *Clin. Chem.* **2007**, *53* (11), 1990-1995.
20. Wilson, D. H.; Hanlon, D. W.; Provuncher, G. K.; Chang, L.; Song, L.; Patel, P. P.; Ferrell, E. P.; Lepor, H.; Partin, A. W.; Chan, D. W., Fifth-generation digital immunoassay for prostate specific antigen by single molecule array technology. *Clin. Chem.* **2011**, 1712-1721.
21. Liebherr, R. B.; Gorris, H. H., Enzyme molecules in solitary confinement. *Molecules* **2014**, *19* (9), 14417-14445.
22. Rissin, D. M.; Kan, C. W.; Campbell, T. G.; Howes, S. C.; Fournier, D. R.; Song, L.; Piech, T.; Patel, P. P.; Chang, L.; Rivnak, A. J.; Ferrell, E. P.; Randall, J. D.; Provuncher, G. K.; Walt, D. R.; Duffy, D. C., Single-molecule enzyme-linked immunosorbent assay detects serum proteins at subfemtomolar concentrations. *Nat. Biotechnol.* **2010**, *28* (6), 595-599.
23. Torre, L. A.; Bray, F.; Siegel, R. L.; Ferlay, J.; Lortet-Tieulent, J.; Jemal, A., Global cancer statistics, 2012. *CA-Cancer J. Clin.* **2015**, *65* (2), 87-108.
24. Stenman, U.-H.; Leinonen, J.; Zhang, W.-M.; Finne, P., Prostate-specific antigen. *Semin. Cancer Biol.* **1999**, *9* (2), 83-93.
25. Center, M. M.; Jemal, A.; Lortet-Tieulent, J.; Ward, E.; Ferlay, J.; Brawley, O.; Bray, F., International variation in prostate cancer incidence and mortality rates. *Eur. Urol.* **2012**, *61* (6), 1079-1092.
26. Zhang, K.; Lv, S.; Lin, Z.; Li, M.; Tang, D., Bio-bar-code-based photoelectrochemical immunoassay for sensitive detection of prostate-specific antigen using rolling circle amplification and enzymatic biocatalytic precipitation. *Biosens. Bioelectron.* **2018**, *101*, 159-166.
27. Giljohann, D. A.; Mirkin, C. A., Drivers of biodiagnostic development. *Nature* **2009**, *462* (7272), 461-464.

28. Farka, Z.; Mickert, M. J.; Hlavacek, A.; Skladal, P.; Gorris, H. H., Single Molecule Upconversion-Linked Immunosorbent Assay with Extended Dynamic Range for the Sensitive Detection of Diagnostic Biomarkers. *Anal. Chem.* **2017**, *89* (21), 11825-11830.
29. He, Q.; Zhang, J.; Shi, J.; Zhu, Z.; Zhang, L.; Bu, W.; Guo, L.; Chen, Y., The effect of PEGylation of mesoporous silica nanoparticles on nonspecific binding of serum proteins and cellular responses. *Biomater.* **2010**, *31* (6), 1085-1092.
30. Otsuka, H.; Nagasaki, Y.; Kataoka, K., PEGylated nanoparticles for biological and pharmaceutical applications. *Adv. Drug Delivery Rev.* **2012**, *64*, 246-255.
31. Salvati, A.; Pitek, A. S.; Monopoli, M. P.; Prapainop, K.; Bombelli, F. B.; Hristov, D. R.; Kelly, P. M.; Åberg, C.; Mahon, E.; Dawson, K. A., Transferrin-functionalized nanoparticles lose their targeting capabilities when a biomolecule corona adsorbs on the surface. *Nat. Nanotechnol.* **2013**, *8* (2), 137.
32. Liebherr, R. B.; Soukka, T.; Wolfbeis, O. S.; Gorris, H. H., Maleimide activation of photon upconverting nanoparticles for bioconjugation. *Nanotechnology* **2012**, *23* (48), 485103.
33. Shi, Y.; Shi, B.; Dass, A. V. E.; Lu, Y.; Sayyadi, N.; Kautto, L.; Willows, R. D.; Chung, R.; Piper, J.; Nevalainen, H.; Walsh, B.; Jin, D.; Packer, H.; Nicolle, Stable upconversion nanohybrid particles for specific prostate cancer cell immunodetection. *Sci. Rep.* **2016**, *6*, 37533.
34. Weber, P.; Ohlendorf, D.; Wendoloski, J.; Salemme, F., Structural origins of high-affinity biotin binding to streptavidin. *Science* **1989**, *243* (4887), 85-88.
35. Sedlmeier, A.; Hlaváček, A.; Birner, L.; Mickert, M. J.; Muhr, V.; Hirsch, T.; Corstjens, P. L. A. M.; Tanke, H. J.; Soukka, T.; Gorris, H. H., Highly Sensitive Laser Scanning of Photon-Upconverting Nanoparticles on a Macroscopic Scale. *Anal. Chem.* **2016**, *88* (3), 1835-1841.
36. Crawford, A. C.; Skuratovsky, A.; Porter, M. D., Sampling error: Impact on the quantitative analysis of nanoparticle-based surface-enhanced Raman scattering immunoassays. *Anal. Chem.* **2016**, *88* (12), 6515-6522.
37. Rissin, D. M.; Fournier, D. R.; Piech, T.; Kan, C. W.; Campbell, T. G.; Song, L.; Chang, L.; Rivnak, A. J.; Patel, P. P.; Provuncher, G. K., Simultaneous detection of single molecules and singulated ensembles of molecules enables immunoassays with broad dynamic range. *Anal. Chem.* **2011**, *83* (6), 2279-2285.

VII.7.Supporting Information

Table S1: Summary of LODs and working ranges of PSA detection platforms.

Method	LOD	Working range	Reference
Digital assays			
Digital ULISA SA-PEG UCNPs	23 fg mL ⁻¹ (0.80 fM)	70 fg mL ⁻¹ – 1 ng mL ⁻¹	This work
Digital ULISA Ab-silica UCNPs	1.2 pg mL ⁻¹ (42 fM)	1 pg mL ⁻¹ – 1 ng mL ⁻¹	¹
Single-molecule ELISA	1.5 fg mL ⁻¹ (52 aM)	1.5 fg mL ⁻¹ – 75 fg mL ⁻¹	²
Single-particle time-resolved fluorescence	1.6 pg mL ⁻¹ (50 fM)	1.6 pg mL ⁻¹ – 100 ng mL ⁻¹	³
Analog assays			
Analog ULISA SA-PEG UCNPs	0.41 pg mL ⁻¹ (14.3 fM)	1 pg mL ⁻¹ – 10 ng mL ⁻¹	This work
Analog ULISA Ab-silica UCNPs	20.3 pg mL ⁻¹ (707 fM)	10 pg mL ⁻¹ – 10 ng mL ⁻¹	¹
Au NP-based bio-barcode assay	330 fg mL ⁻¹ (11 fM)	330 fg mL ⁻¹ – 33 pg mL ⁻¹	⁴
Au NP-enhanced surface plasmon resonance	290 pg mL ⁻¹ (10 pM)	290 pg mL ⁻¹ – 150 ng mL ⁻¹	⁵
Chemiluminescence imaging immunoassay	7 pg mL ⁻¹ (244 fM)	10 pg mL ⁻¹ – 36.7 ng mL ⁻¹	⁶
Colorimetric assay with mesoporous silica NPs	0.36 pg mL ⁻¹ (12.5 fM)	0.5 pg mL ⁻¹ – 10 pg mL ⁻¹	⁷
Electrochemical sensor with Au@Ag-Cu ₂ O nanoparticles	3 fg mL ⁻¹ (105 aM)	10 fg mL ⁻¹ – 100 ng mL ⁻¹	⁸
Electrochemical sensor with AuNP hybrid nanomaterial	0.12 pg mL ⁻¹ (4.2 fM)	5 pg mL ⁻¹ – 10 ng mL ⁻¹	⁹
Electrochemical sensor with peptide-DNAzyme conjugates	2 fg mL ⁻¹ (70 aM)	5 fg mL ⁻¹ – 20 ng mL ⁻¹	¹⁰
Electrochemiluminescence immunoarray	50 fg mL ⁻¹ (1.7 fM)	100 fg mL ⁻¹ – 1 ng mL ⁻¹	¹¹
Electrochemiluminescence with conductive nanospheres	40 ag mL ⁻¹ (1.4 aM)	40 ag mL ⁻¹ – 10 fg mL ⁻¹	¹²
Electrochemiluminescence with MOF/Au/G-Quadruplexes	58 pg mL ⁻¹ (2.0 pM)	0.5 ng mL ⁻¹ – 500 ng mL ⁻¹	¹³
Immuno-PCR	4 pg mL ⁻¹ (139 fM)	4 pg mL ⁻¹ – 49 ng mL ⁻¹	¹⁴
Localized surface plasmon resonance	100 fg mL ⁻¹ (3.5 fM)	100 fg mL ⁻¹ – 5 ng mL ⁻¹	¹⁵
Microbead-based immunoassay	136 pg mL ⁻¹ (4.7 pM)	136 pg mL ⁻¹ – 8 ng mL ⁻¹	¹⁶

Photoelectrochemistry with rolling circle amplification	320 fg mL ⁻¹ (11 fM)	1 pg mL ⁻¹ – 3 ng mL ⁻¹	17
Plasmon excited quantum dots	100 pg mL ⁻¹ (3.5 pM)	100 pg mL ⁻¹ – 100 ng mL ⁻¹	18
Quantum dot-based FRET immunoassay	80 pg mL ⁻¹ (2.5 pM)	80 pg mL ⁻¹ – 100 ng mL ⁻¹	19
Quantum dot-encoded microbeads	1 ng mL ⁻¹ (35 pM)	1 ng mL ⁻¹ – 10 ng mL ⁻¹	20
Time-resolved fluorescence	1.6 pg mL ⁻¹ (56 fM)	1.6 pg mL ⁻¹ – 100 ng mL ⁻¹	21
UCNPs as labels in multianalyte microarray	170 pg mL ⁻¹ (5.9 pM)	100 pg mL ⁻¹ – 10 ng mL ⁻¹	22
Commercial ELISAs			
Abcam ab113327	8 pg mL ⁻¹ (0.28 pM)	10.2 pg mL ⁻¹ – 2.5 ng mL ⁻¹	23
Abcam ab188389	4.9 pg mL ⁻¹ (170 fM)	4.1 pg mL ⁻¹ – 3 ng mL ⁻¹	24
Biorbyt orb339660	0.5 ng mL ⁻¹ (17 pM)	1 ng mL ⁻¹ – 32 ng mL ⁻¹	25
Roche Elecsys total PSA	2 pg mL ⁻¹ (70 fM)	2 pg mL ⁻¹ – 100 ng mL ⁻¹	26
LifeSpan BioSciences LS-F25971	19.1 pg mL ⁻¹ (665 fM)	54.9 pg mL ⁻¹ – 40 ng mL ⁻¹	27
LifeSpan BioSciences LS-F5207	0.2 ng mL ⁻¹ (7.0 pM)	195 pg mL ⁻¹ – 12.5 ng mL ⁻¹	28
OriGene EA100514	10 pg mL ⁻¹ (348 fM)	312 pg mL ⁻¹ – 20 ng mL ⁻¹	29
R&D Systems DKK300	69 pg mL ⁻¹ (2.4 pM)	0.9 ng mL ⁻¹ – 60 ng mL ⁻¹	30
Thermo Fisher Scientific EHKLK3T	8 pg mL ⁻¹ (0.28 pM)	10 pg mL ⁻¹ – 2.5 ng mL ⁻¹	31

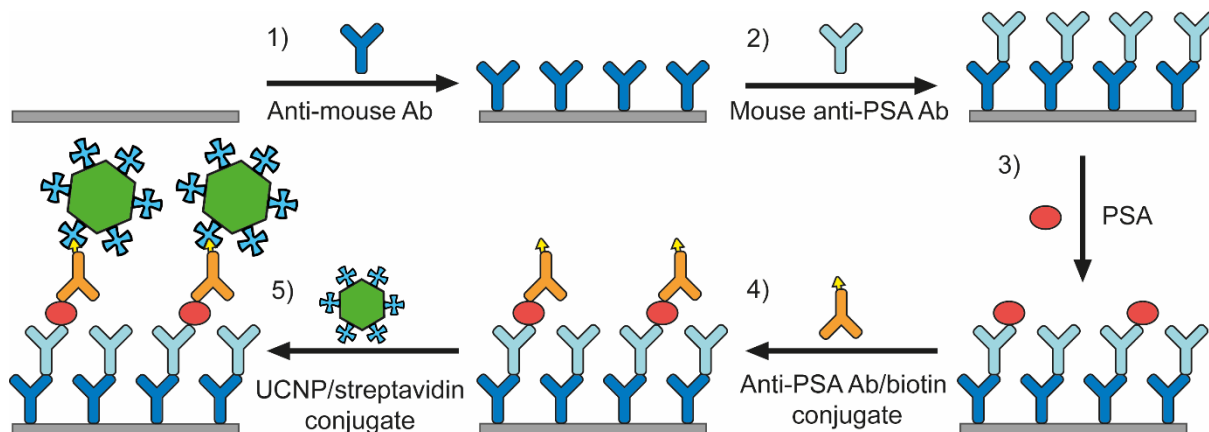


Figure S1: Schematic representation of the sequential steps of the upconversion-linked immunosorbent assay for PSA. **1)** The bottom of a microtiter well is coated with an anti-mouse antibody (dark blue). **2)** A mouse monoclonal anti-PSA capture antibody (light blue) is bound to the anti-mouse antibody. **3)** The monoclonal anti-PSA antibody captures the PSA antigen (red). **4)** A biotinylated polyclonal anti-PSA antibody (orange) forms a sandwich immune complex. **5)** Streptavidin-coated UCNPs (green) bind to the biotinylated detection antibody.

Surface Plasmon Resonance (SPR) Measurements

SPR measurements were performed on an MP-SPR Navi 210A system (BioNavis, Finland) and SPR sensor chips with a 200 nm thick carboxymethylated dextran hydrogel coating (CMD 200 M, BioNavis) for antibody immobilization. First, the surface was activated with mixture of 1-Ethyl-3-(3-dimethylaminopropyl)carbodiimide (EDC, 200 mM) and *N*-Hydroxysuccinimide (NHS, 50 mM) in water (7 min, 20 $\mu\text{L min}^{-1}$). Next, either an anti-mouse antibody (10 min, 20 $\mu\text{L min}^{-1}$, 50 $\mu\text{g mL}^{-1}$, Vector Laboratories, USA) or a monoclonal anti-PSA antibody (10 min, 20 $\mu\text{L min}^{-1}$, 50 $\mu\text{g mL}^{-1}$, ab403, Abcam, UK) in acetate buffer (50 mM, pH 4.5) was immobilized onto the measuring channel of the sensor chip surface. In parallel, BSA (10 min, 20 $\mu\text{L min}^{-1}$, 50 $\mu\text{g mL}^{-1}$) in acetate buffer was immobilized in the reference channel. Remaining reactive sites were then quenched by addition of ethanolamine in water (5 min, 20 $\mu\text{L min}^{-1}$, 1 M, pH 8.5). The surface was blocked by BSA (10 min, 20 $\mu\text{L min}^{-1}$, 1 mg mL^{-1}) in phosphate buffered saline (PBS, 50 mM PO_4^{3-} , 150 mM NaCl, pH 7.4). Sensor chips coated with the anti-PSA antibody were now ready for PSA binding.³² In the case of surfaces with immobilized anti-mouse antibody, a monoclonal mouse anti-PSA antibody (30 min, 6 $\mu\text{L min}^{-1}$, 20 $\mu\text{g mL}^{-1}$, ab403, Abcam) in PBS was added. SPR measurements of the full sandwich immunocomplexes (**Figure S2 A–D**) were based on binding of PSA in PBS (30 min, 6 $\mu\text{L min}^{-1}$, 0.1 $\mu\text{g mL}^{-1}$ /1 $\mu\text{g mL}^{-1}$) followed by the addition of a biotinylated polyclonal anti-PSA antibody in PBS (1 h, 3 $\mu\text{L min}^{-1}$, 2.5 $\mu\text{g mL}^{-1}$, BAF1344, R&D Systems, USA). Two PSA incubations were necessary to account for non-specific adsorption of low PSA concentrations to the tubing during the first addition. Finally, either SA-PEG-UCNPs (30 min,

$6 \mu\text{L min}^{-1}$, $3.5 \mu\text{g mL}^{-1}/175 \mu\text{g mL}^{-1}$, **Figure S2 A/B**) or commercial SA-UCNPs (30 min , $6 \mu\text{L min}^{-1}$, $2.5 \mu\text{g mL}^{-1}$, **Figure S2 C/D**) were added. For PSA kinetic studies (**Figure S2 E/F**) sequential dilutions of PSA in PBS ($20 \mu\text{L min}^{-1}$, $0.1\text{--}1 \mu\text{g mL}^{-1}$) were bound for 10 min followed by 10 min of dissociation period. Due to the high binding capacity of the anti-PSA capture antibody no surface regeneration was necessary prior to the injection of a new PSA dilution.

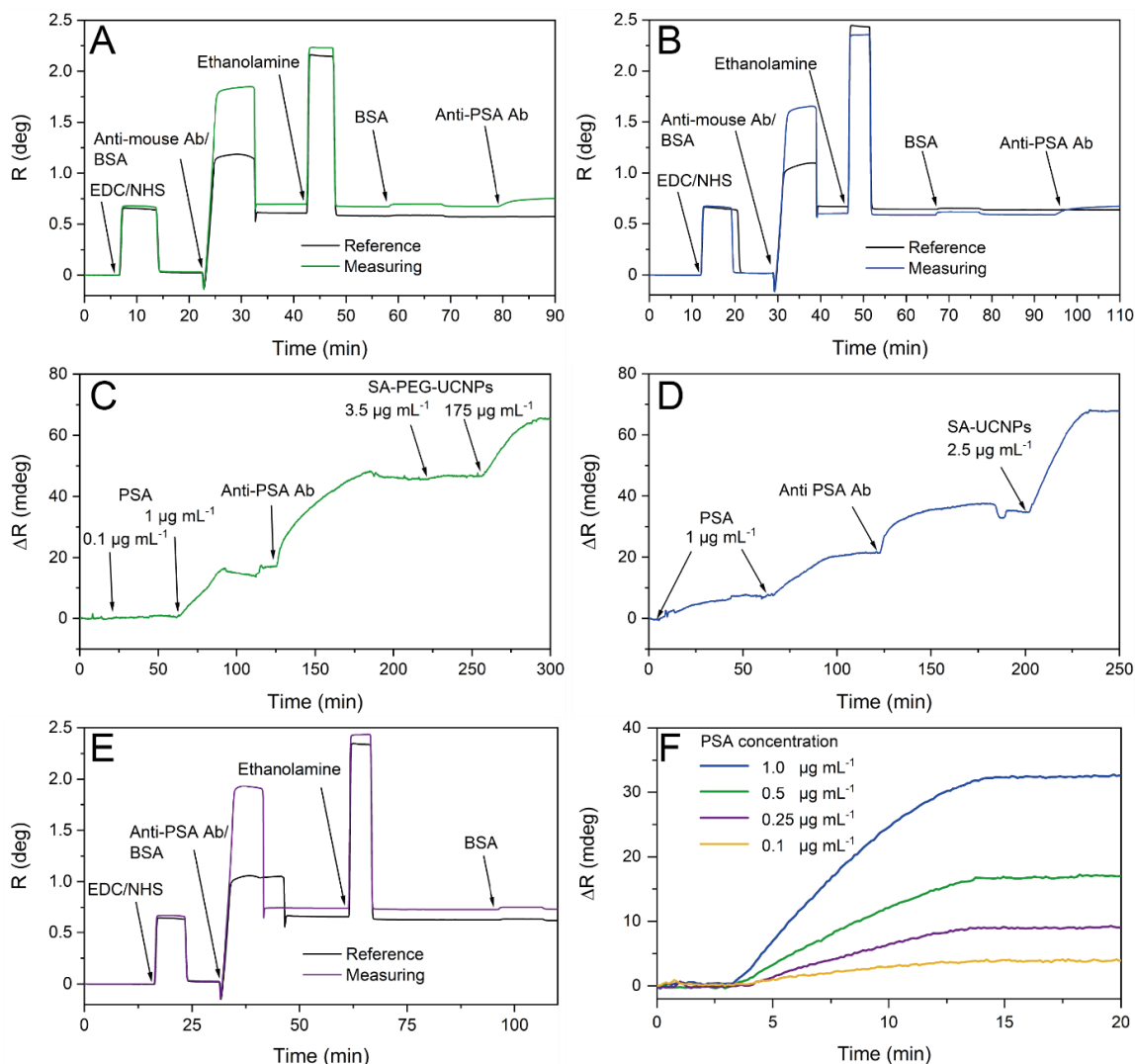


Figure S2: SPR characterization of immunoreagents and bioconjugates used in the upconversion-linked immunosorbent assay (ULISA). **A, B**) Immobilization of an anti-mouse antibody on the sensor chip surface, the green/blue line indicates the changes of the resonance angle in the measuring channel, the black line changes in the reference channel. **C, D**) Changes of resonance angle after subtraction of reference channel during the sequential addition of PSA, biotinylated anti-PSA antibody and either SA-PEG-UCNPs (green line) or commercial SA-UCNPs (blue line). **E**) Immobilization of a monoclonal anti-PSA antibody on the sensor chip surface, the purple line indicates the changes of the resonance angle in the measuring channel, the black line changes in the reference channel. **F**) Changes of

resonance angle after subtraction of the reference during the sequential injection of PSA ($0.1 \mu\text{g mL}^{-1}$, $0.25 \mu\text{g mL}^{-1}$, $0.5 \mu\text{g mL}^{-1}$, $1 \mu\text{g mL}^{-1}$).

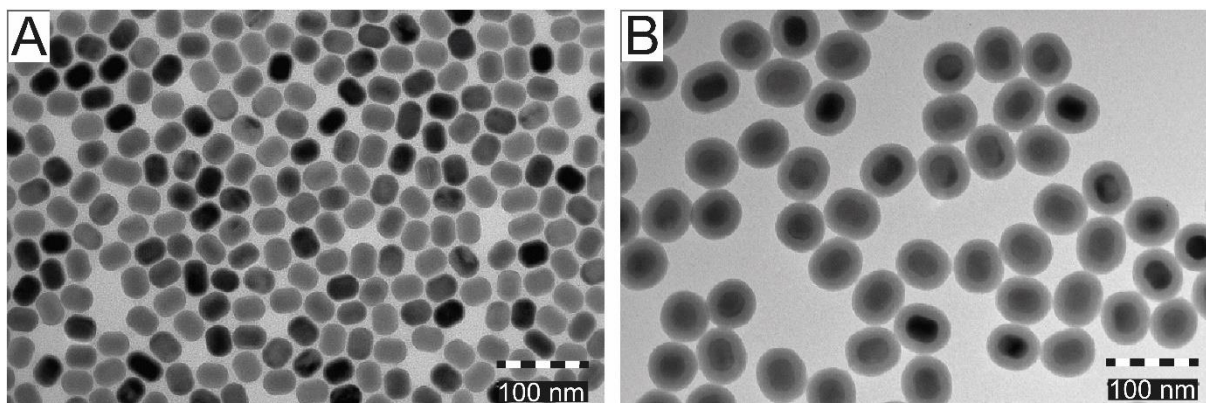


Figure S3: TEM images of Kaivogen RD Upcon™ Erbium-540-SA **A**) before surface coating showing uniform UCNP particles with an average diameter of 45 nm, and **B**) after surface coating revealing homogeneous particles with an average core-diameter of 45 nm and a coating layer of 13 nm thickness.

Synthesis of UCNP Labels

Materials

Anhydrous yttrium(III), ytterbium(III), erbium(III) and thulium(III) chlorides (99%), octadec-1-ene (90%), ammonium hydrogen difluoride, sodium L-ascorbate, copper(II) sulfate, and 2-amino-2-(hydroxymethyl)propane-1,3-diol (Tris) were purchased from Sigma-Aldrich (St. Louis, MO, USA). Alkyne poly(ethylene glycol) succinimidyl ester (alkyne-PEG-NHS; $M_w = 5475$ Da) was from Rapp Polymere (Tuebingen, Germany). Streptavidin azide was purchased from Protein Mods (Madison, WI, USA). Methanol, hexane, acetone, and oleic acid were obtained from Lach-Ner (Neratovice, Czech Republic). Cellulose dialysis membranes (M_w cut-off 3.5, 14 and 100 kDa) were purchased from Spectrum Europe (Breda, Netherlands). All other chemicals were purchased from commercial sources and used without further purification. Buffers and solutions were prepared with ultrapure water obtained by reverse osmosis with UV treatment (Milli-Q Gradient A10 system, Millipore, Germany).

Synthesis of $\text{NaYF}_4:\text{Yb}^{3+}/\text{Er}^{3+}$ and $\text{NaYF}_4:\text{Yb}^{3+}/\text{Tm}^{3+}$ Core Nanoparticles

In a typical synthesis,³³ either YCl_3 (0.78 mmol), YbCl_3 (0.2 mmol) and ErCl_3 (0.02 mmol) for preparation of $\text{NaYF}_4:\text{Yb}^{3+}/\text{Er}^{3+}$ particles, or YCl_3 (0.795 mmol), YbCl_3 (0.2 mmol), and TmCl_3 (0.005 mmol) for the preparation of $\text{NaYF}_4:\text{Yb}^{3+}/\text{Tm}^{3+}$ particles were mixed with oleic acid (6 mL), and octadec-1-ene (15 mL) in a 100 mL three-neck flask. The mixture was heated to 160 °C for 30 min under a gentle Ar flow to form a homogeneous yellowish solution and cooled down to room temperature (RT). NaOH (4 mmol) and $\text{NH}_4\text{F}\cdot\text{HF}$ (2.5 mmol) were

dissolved in methanol (10 mL) and added dropwise to the lanthanide/oleic acid mixture above. The mixture was slowly heated at 120 °C under Ar atmosphere until the methanol evaporated followed by heating to 300 °C for 1.5 h. After cooling to RT, the NaYF₄:Yb³⁺/Er³⁺, or NaYF₄:Yb³⁺/Tm³⁺ nanoparticles were collected by centrifugation (6000 g, 15 min), washed by ethanol, and redispersed in hexane.

Synthesis of Core-Shell Nanoparticles

Core-shell nanoparticles were synthesized as described earlier.³⁴ In a 100 mL three-neck round-bottom flask, YCl₃ (0.8 mmol) and YbCl₃ (0.2 mmol) for Er³⁺-based particles or YCl₃ (1 mmol) for Tm³⁺-based particles were mixed with oleic acid (6 mL) and octadec-1-ene (15 mL) heated at 160 °C for 30 min with stirring under Ar atmosphere. After cooling to RT, core NaYF₄:Yb³⁺/Er³⁺, or core NaYF₄:Yb³⁺/Tm³⁺ nanoparticles (150 mg) were dispersed in hexane and a methanolic solution of NaOH (4 mmol) and NH₄F·HF (2.5 mmol) were added dropwise and the mixture was slowly heated to 120 °C under Ar atmosphere until hexane and methanol evaporated. After heating at 300 °C for 1.5 h, the dispersion was cooled to RT. NaYF₄:Yb³⁺/Er³⁺@NaYF₄:Yb³⁺, or NaYF₄:Yb³⁺/Er³⁺@NaYF₄ nanoparticles were precipitated by acetone (10 mL), washed five times with ethanol, and an ethanol/water mixture, redispersed in 0.01 M HCl, and dialyzed (M_w cut-off 14 kDa) against water for 48 h. The UCNPs were stored as an aqueous dispersion at a concentration of 14 mg mL⁻¹.

Synthesis of Alkyne-PEG-Neridronate

Sodium neridronate was synthesized as described earlier.³⁵⁻³⁶ For the preparation of alkyne-PEG-neridronate, sodium neridronate (0.32 g) was dissolved in PBS (10 mL, pH 7.4) and cooled to 4 °C. Dry alkyne-PEG-NHS (0.5 g) was added and the mixture was stirred for 5 h at 4 °C. The product was dialyzed (M_w cut-off 3.5 kDa) against water for 72 h (water exchanged 9×) and freeze-dried.

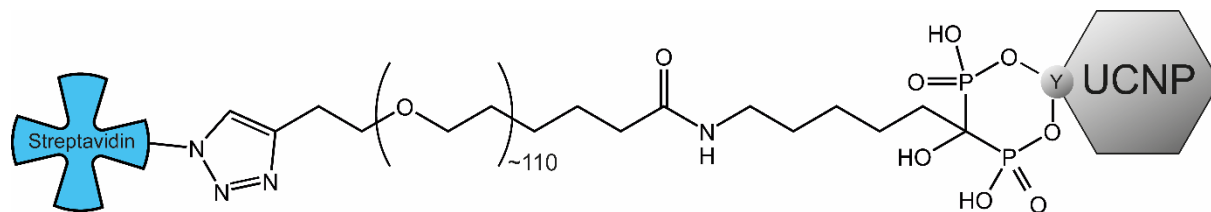


Figure S4: Chemical structure of the streptavidin-PEG-neridronate bound to a UCNP via bisphosphonate groups.

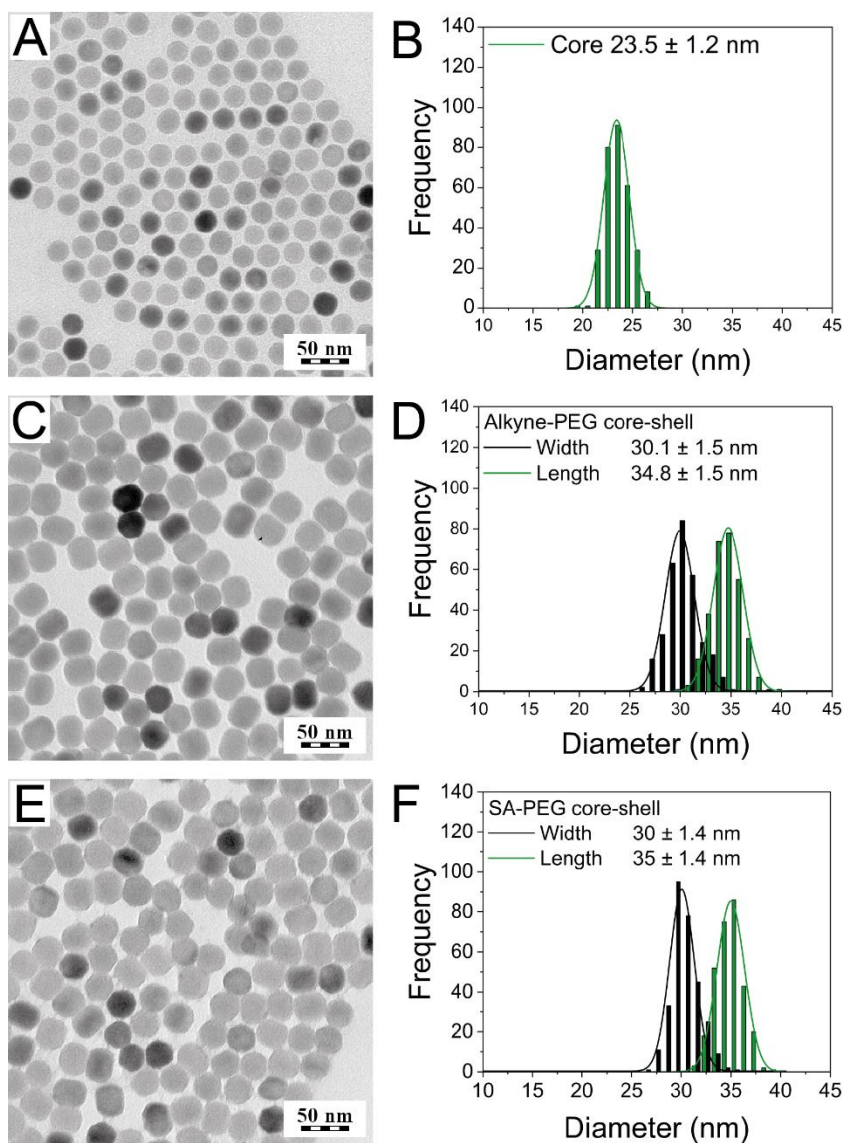


Figure S5: Characterization of Er-doped UCNPs by TEM. **A)** TEM image of UCNP cores. **B)** Gaussian fit of the size distribution of UCNP cores (diameter 23.5 ± 1.2 nm). **C)** TEM image of cylindrical shaped alkyne-PEG core-shell UCNPs. **D)** Gaussian fit of frequency distributions of length (green line, 34.8 ± 1.5 nm) and width (black line, 30.1 ± 1.5 nm) of alkyne-PEG core-shell UCNPs. **E)** TEM image of cylindric SA-PEG core-shell UCNPs. **F)** Gaussian fit of frequency distributions of length (green line, 35.0 ± 1.4 nm) and width (black line, 30.3 ± 1.4 nm) of SA-PEG core-shell UCNPs. In total, 300 UCNPs were analyzed for each size distribution.

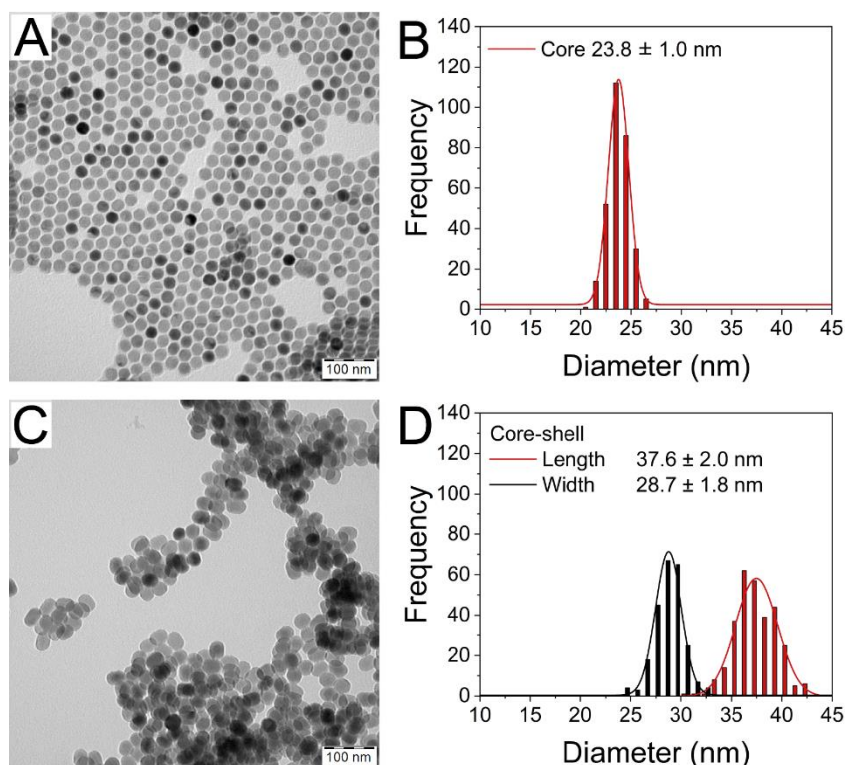


Figure S6: Characterization of Tm-doped UCNP by TEM (A) TEM image of UCNP cores. (B) Gaussian fit of the size distribution of UCNP cores (diameter 23.8 ± 1.0 nm). (C) TEM image of cylindrical shaped core-shell UCNP. (D) Gaussian fit of frequency distributions of length (red line, 37.6 ± 2.0 nm) and width (black line, 28.7 ± 1.8 nm) of core-shell UCNP. In total, 300 UCNP were analyzed for each size distribution.

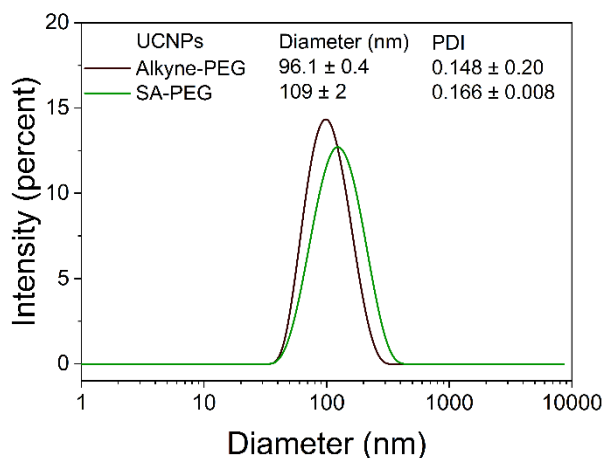


Figure S7: DLS measurements of Er-doped alkyne-PEG-UCNPs and SA-PEG-UCNPs. A hydrodynamic diameter of 96.1 ± 0.4 was found for Alkyne-PEG-UCNPs (black line), for SA-PEG-UCNPs (green line) the diameter was 109 ± 2 nm resulting in an average increase of 12.9 nm. The PDI increased slightly from 0.148 to 0.166. Standard deviations were calculated from three measurements.

BSA-Biotin Binding Assay

A 96-well microtiter plate (μ Clear, high binding, Greiner Bio-One, Austria) was coated with BSA-biotin (0.1; 1; 10 $\mu\text{g mL}^{-1}$, 100 μL , Sigma Aldrich, Germany) in coating buffer (50 mM $\text{NaHCO}_3/\text{Na}_2\text{CO}_3$, 0.05% NaN_3 , pH 9.6, 100 μL) overnight at 4 $^\circ\text{C}$. The plate was washed four times with washing buffer (50 mM $\text{NaH}_2\text{PO}_4/\text{Na}_2\text{HPO}_4$, 0.01% Tween 20, 0.05% NaN_3 , pH 7.4, 250 μL) in a microplate washer (HydroFlex, Tecan, Switzerland) and blocked with blocking buffer (50 mM $\text{NaH}_2\text{PO}_4/\text{Na}_2\text{HPO}_4$, 0.05% NaN_3 , pH 7.4, 1% BSA, 200 μL) for 1 h. After four washings steps the BSA-biotin coated wells and uncoated wells as negative control were incubated with serial dilutions of streptavidin-coated UCNPs (100 μL) for 1 h. At the end of the incubation time the plate was washed four times, dried on air and scanned using the upconversion microtiter plate reader.

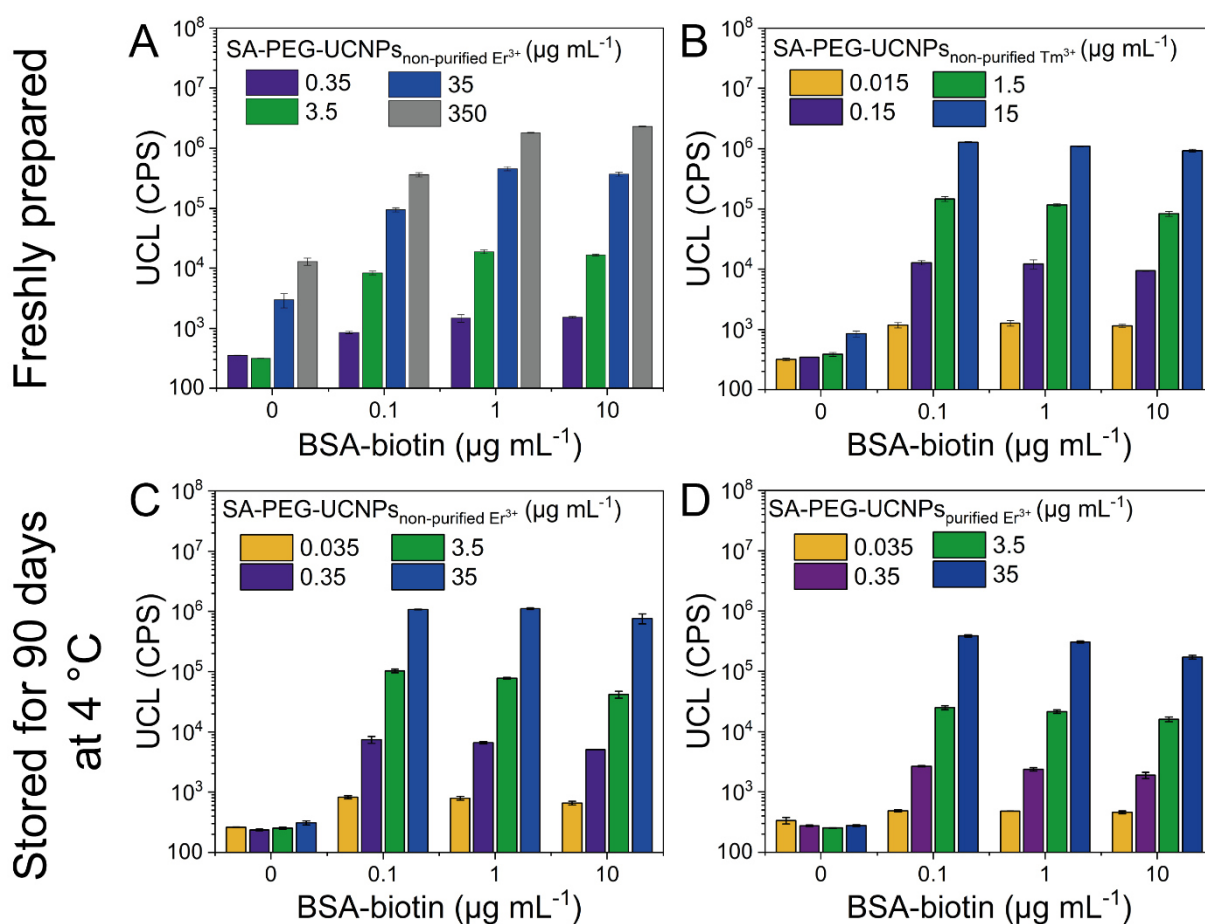


Figure S8: Binding test of SA-PEG-UCNPs. Different BSA-biotin concentrations immobilized on a microtiter plate and incubated with increasing amounts of SA-PEG UCNPs. **A)** Freshly prepared Er³⁺-doped SA-PEG-UCNPs (0.35 $\mu\text{g mL}^{-1}$, 3.5 $\mu\text{g mL}^{-1}$, 35 $\mu\text{g mL}^{-1}$, 350 $\mu\text{g mL}^{-1}$). **B)** Freshly prepared Tm³⁺-doped SA-PEG-UCNPs (0.015 $\mu\text{g mL}^{-1}$, 0.15 $\mu\text{g mL}^{-1}$, 1.5 $\mu\text{g mL}^{-1}$, 15 $\mu\text{g mL}^{-1}$). **C)** 90 days old Er³⁺-doped SA-PEG-UCNPs (0.035 $\mu\text{g mL}^{-1}$, 0.35 $\mu\text{g mL}^{-1}$, 3.5 $\mu\text{g mL}^{-1}$, 35 $\mu\text{g mL}^{-1}$) and **D)** 90 days old Er³⁺-doped SA-PEG-UCNPs that were purified via gradient centrifugation (0.035 $\mu\text{g mL}^{-1}$, 0.35 $\mu\text{g mL}^{-1}$).

mL⁻¹, 3.5 μg mL⁻¹, 35 μg mL⁻¹). Error bars indicate the standard deviation of the UCL of three different wells.

Wide-Field Upconversion Microscopy

For near infrared excitation, a 980 nm continuous wave laser diode (4 W, WSL5-980-004-H-T, Wavespectrum, China) was coupled to a motorized TIRF/Epifluorescence illuminator unit (Ti-TIRF-E, Nikon, Japan) of a conventional epifluorescence microscope (Eclipse Ti-E, Nikon, Japan) via a multimode optical fiber (105 μm fiber core, 0.22 NA, Wavespectrum). The laser was controlled by a computer equipped with an analog output module (PCI-6723, National Instruments, USA). The optical filter cube consisted of a long-pass excitation filter ($\lambda_{\text{cut-on}} = 875$ nm, Schott, Germany), a dichroic mirror suitable for multiphoton applications ($\lambda_{\text{cut-on}} = 830$ nm, AHF Analysentechnik, Germany), and a band-pass filter transparent for the green emission of Er³⁺-doped UCNPs ($\lambda = 535 \pm 70$ nm, OD₉₈₀ ≈ 6, Chroma, USA). For the 800 nm emission of Tm³⁺-doped UCNPs ($\lambda = 809 \pm 81$ nm, AHF Analysentechnik) bandpass filter was used. A 100× objective with a high NA of 1.49 (CFI HP Apochromat TIRF, Nikon) and a 5.5-megapixel vacuum cooled sCMOS camera (Neo, Andor Technology, UK) were used for image acquisition. The whole optical setup resulted in a power density of 640 W cm⁻² in the focal plane.¹

Data Analysis

For the analog as well as the digital readout, mean and standard deviation were calculated for three wells and the LODs were determined by a non-linear regression using a four-parameter logistic fit. The graphs are shown in double logarithmic scale for better visual representation of the low values, however, the original data (linear scale) was fitted. In the four-parameter logistic function:

$$Y = \frac{Y_{\text{max}} - Y_{\text{bg}}}{1 + \left(\frac{[\text{PSA}]}{\text{EC}_{50}}\right)^s} + Y_{\text{bg}}$$

[PSA] is the concentration of prostate specific antigen and Y either the upconversion luminescence (analog readout) or the number of particles counted under the upconversion microscope (digital readout). The parameter Y_{max} marks the highest point of the sigmoidal curve while Y_{bg} is the lowest point corresponding to the background signal. The point where the difference between Y_{max} and Y_{bg} is reduced by 50% is the half maximal effective concentration or EC₅₀ and the slope at the inflection point is indicated as s .

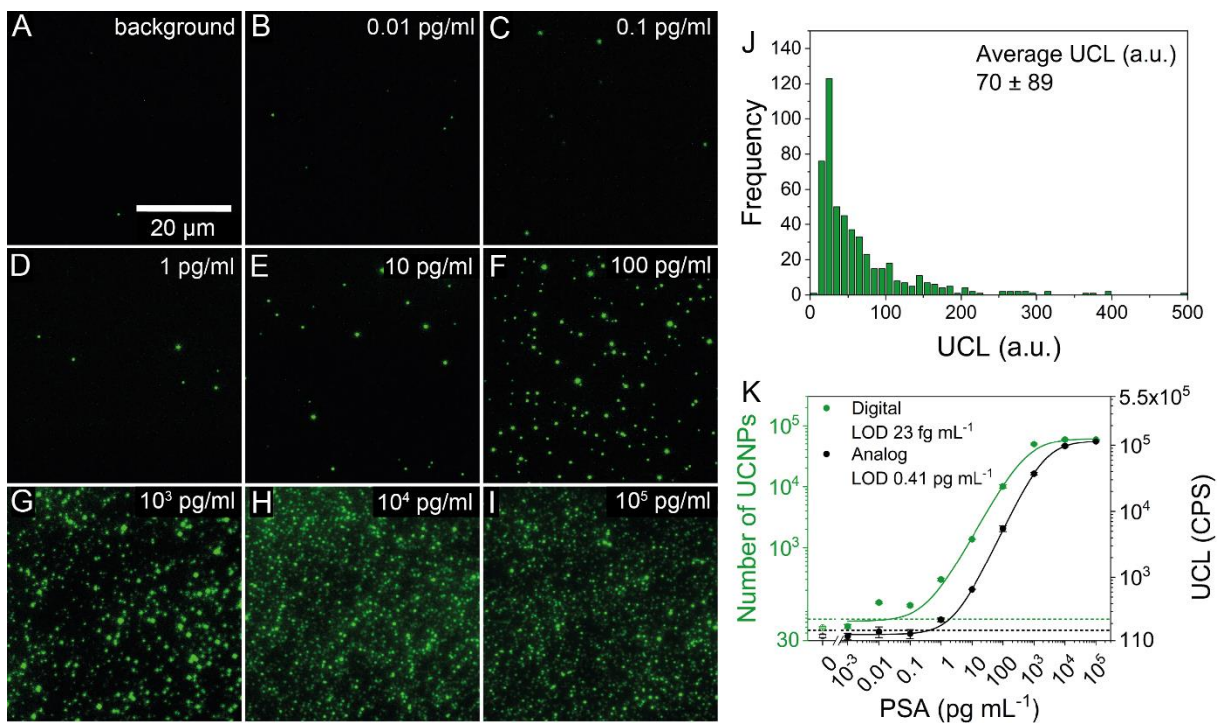


Figure S9: Upconversion microscopy images using Er-doped SA-PEG-UCNPs as a label for the detection of PSA. **A-I)** 50×50 μm² sections of upconversion microscopic images. Images correspond to serial dilutions of PSA as indicated. **J)** The brightness distribution of 500 luminescent spots recorded in panel **F** shows a CV of 130% (SD of spot UCL / average spot UCL). **K)** Calibration curves (analog readout: black; digital readout: green) based on a 4-parameter logistic regression model. The logarithmic scale of the Y-axis visualizes signals at low PSA concentrations. Hatched lines indicate the LOD values and where obtained by adding three times the standard deviation of the background to the baseline values of the regression curve.

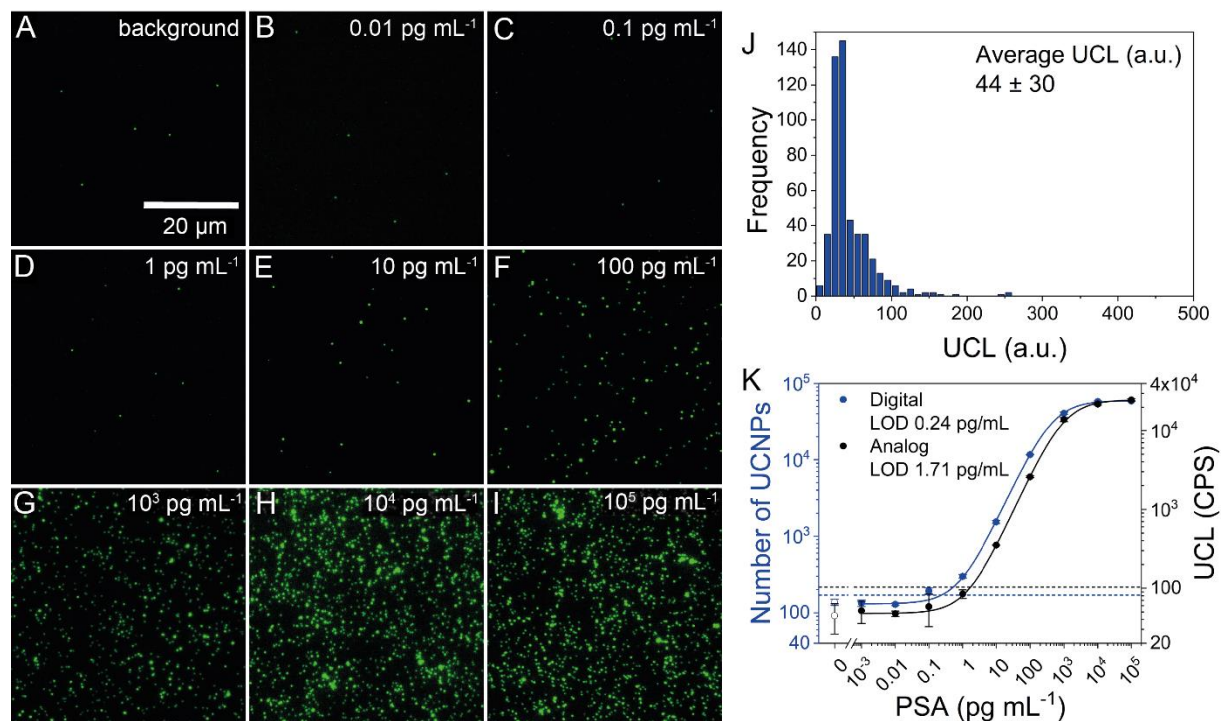


Figure S10: Upconversion microscopy images using commercial Er-doped SA-UCNPs as a label for the detection of PSA. **A-I)** 50×50 μm² sections of upconversion microscopic images. Images correspond to serial dilutions of PSA as indicated. **J)** The brightness distribution of 500 luminescent spots recorded in panel F shows a CV of 70% (SD of spot UCL / average spot UCL). **K)** PSA calibration curves (analog readout: black; digital readout: blue) based on a 4-parameter logistic regression model. The logarithmic scale of the y-axis visualizes signals at low PSA concentrations. Hatched lines correspond to the LOD values and indicate the baseline of the regression curve plus three times the standard deviation of the background.

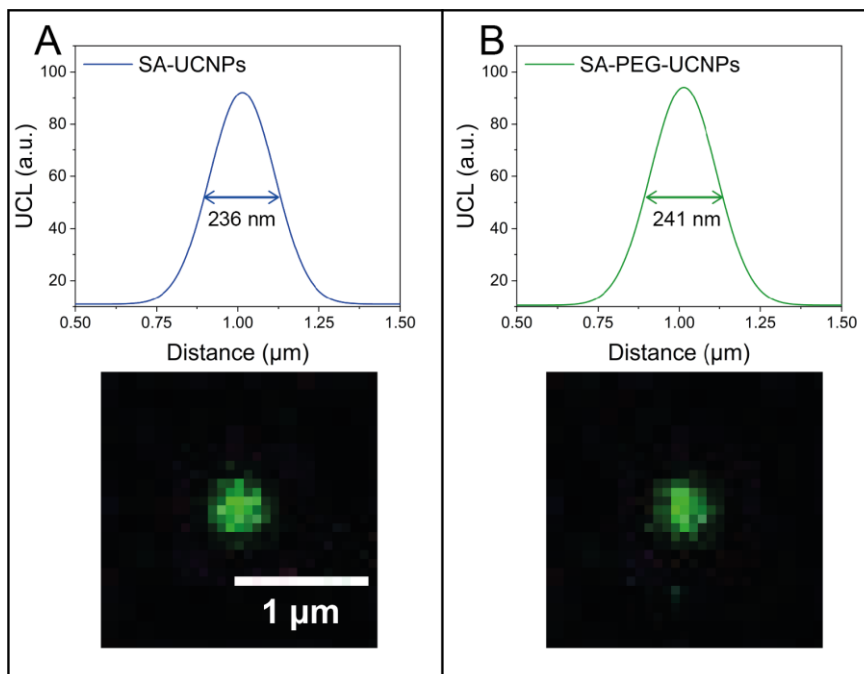


Figure S11: Upconversion luminescence of individual SA-UCNPs recorded under NIR excitation (power density: 640 W cm^{-2} , exposure time: 20 s). Gaussian fit of the intensity cross-section of a single diffraction-limited spot (top) with full width at half maximum (FWHM) and respective microscope images (bottom). **A)** Commercial UCNPs (Kaivogen), and **B)** in-house synthesized SA-PEG-UCNP(Er).

Calculation of Capture Efficiency

Diameter of μ Clear Well: 6.58 mm; sample volume: 100 μL

(1) Filling height (h):

$$h = \frac{V}{A_W}$$

A_W : area of microplate well.

$$h = \frac{V}{r^2 \cdot \pi}$$

r : radius of microplate well.

(2) Lateral area (A_L):

$$A_L = \frac{V}{r^2 \cdot \pi} \cdot 2\pi r$$

$$A_L = \frac{2V}{r}$$

(3) Total area covered by PSA sample (A_T):

$$A_T = \frac{2V}{r} + r^2\pi$$

(4) Number of microscopic images (Z , 166.04 μm *140.09 μm) needed to cover the whole surface:

$$Z = \frac{\frac{2V}{r} + r^2\pi}{A_O}$$

A_O : observable area.

(5) Number of UCNPs (N) on whole surface:

$$N = \frac{\frac{2V}{r} + r^2\pi}{A_O} \cdot n$$

n : average number of particles per image.

(6) Capture efficiency (E):

$$E (\%) = \frac{\frac{2V}{r} + r^2\pi}{A_O} \cdot \frac{n - n_0}{c \cdot V \cdot N_A} \cdot 100$$

n_0 : average number of non-specifically bound particles.

c : theoretical molar PSA concentration.

N_A : Avogadro constant

Nanoparticle Purification by Sucrose Gradient Centrifugation

Three sucrose (for microbiology, Merck, Germany) solutions (10%; 20%; 35% w/v) were prepared in Tris buffer (50 mM Tris, 136 mM NaCl, 0.05% NaN₃, 1 mM KF, pH 7.5). A UCNP dispersion (50 μL , 3.5 mg mL⁻¹) was transferred to a 1.5 mL vial and successively underlayered by 200 μL of (1) 10% sucrose, (2) 20% sucrose, and (3) 35% sucrose. The sample was centrifuged for 30 min at 750 g. The top 250 μL of the dispersion containing the homogeneous fraction of UCNPs was carefully removed, transferred to a new vial and sonicated for 30 s before further experiments. DLS measurements showed that the polydispersity index (PDI) of purified labels as reduced by 35% compared to non-purified labels (**Figure S12B**). The surface functionality was confirmed by immobilizing biotinylated

BSA in a microwell, incubating with purified SA-PEG-UCNPs and comparing the upconversion luminescence to a negative control (**Figure S5D**).

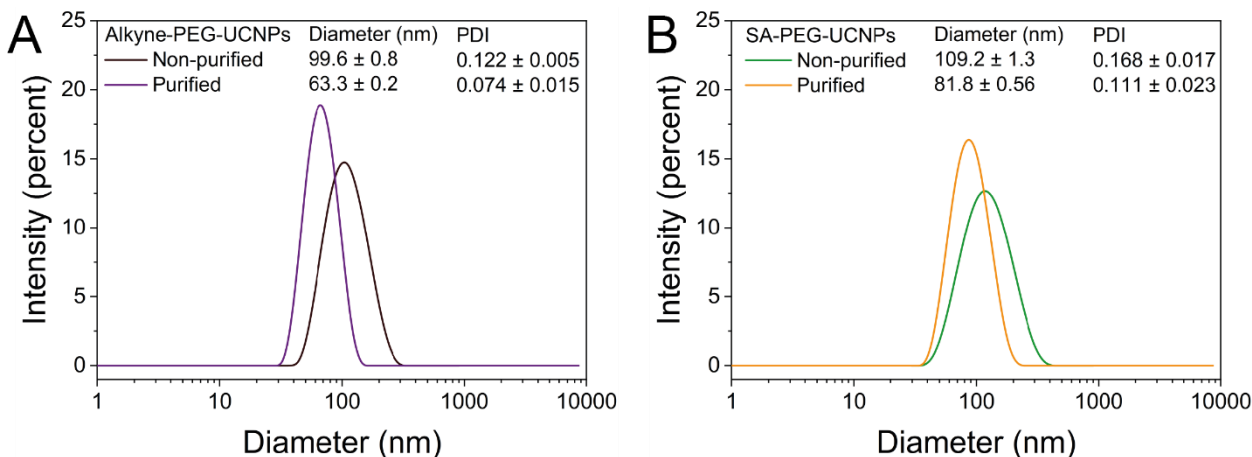


Figure S12: DLS measurements of purified and non-purified Er-doped alkyne-PEG-UCNPs and SA-PEG-UCNPs that were stored for 90 days in 50 mM Tris buffer (pH 7.5; 4 °C). **A**) DLS measurement of Alkyne-PEG-UCNPs before purification (black line, diameter: 99.6 ± 0.8 nm, PDI: 0.122 ± 0.005) and after sucrose gradient centrifugation (30 min at 750 g, purple line, diameter: 63.3 ± 0.2 nm, PDI: 0.074 ± 0.015). **B**) DLS measurement of SA-PEG UCNPs before purification (green line, diameter: 109.2 ± 1.3 nm, PDI: 0.168 ± 0.017) and after sucrose gradient centrifugation (30 min at 750 g, orange line, diameter: 81.8 ± 0.56 nm, PDI: 0.111 ± 0.023).

Influence of Nanoparticle Heterogeneity on the ULISA Performance

The ULISA was performed using either non-purified or purified SA-PEG-UCNPs. Microscope images recorded at a PSA concentration of 100 pg mL^{-1} were used for determining the luminescence heterogeneity among 400 individual diffraction-limited spots. The coefficient of variation (CV) decreased from 130% before purification to 80% after purification. **Figure S14** shows histograms of the luminescence distribution (**A**) before and (**B**) after label purification. The absence of intensity values above 250 a.u. in **Figure S14B** indicates that gradient centrifugation removed larger aggregates efficiently. The difference in the digital and analog LOD conferred by purified labels (**Figure S15**) was only marginal and within the normal variation of the ULISA. Independent of label purification, however, the digital readout was 7–8× more sensitive than the analog readout.

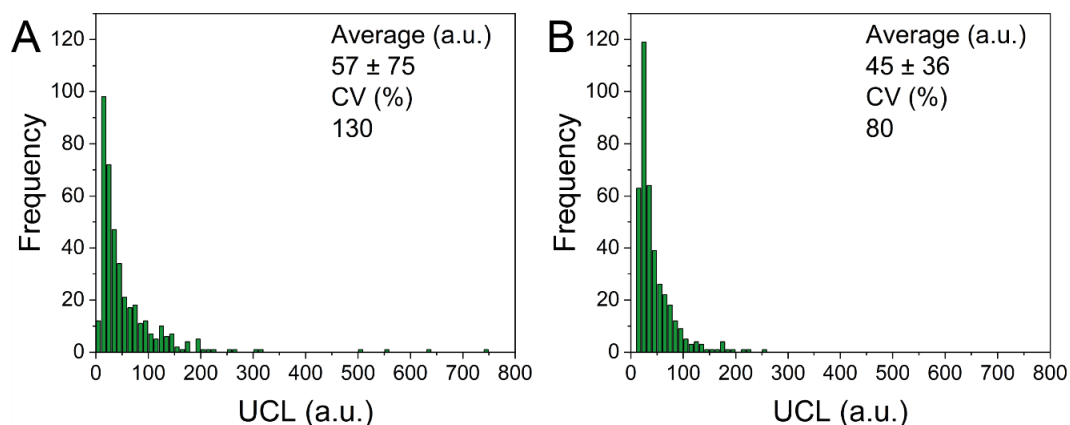


Figure S13: **A)** Intensity distribution of non-purified SA-PEG-UCNPs that were stored over 90 days in Tris buffer (50 mM Tris, pH 7.5). **B)** Intensity distribution of gradient centrifugation-purified SA-PEG-UCNPs. The mean intensity of individual UCNPs bound as part of the sandwich immunocomplex on the bottom of a microtiter plate was determined in the microscope software by placing regions of interest (ROIs) of identical sizes over the luminescent spots. A frequency count of the mean intensities was performed, and the data was arranged in histograms with a bin of 10. For the histogram, the mean intensities of 400 individual UCNPs (randomly selected) were measured and background corrected.

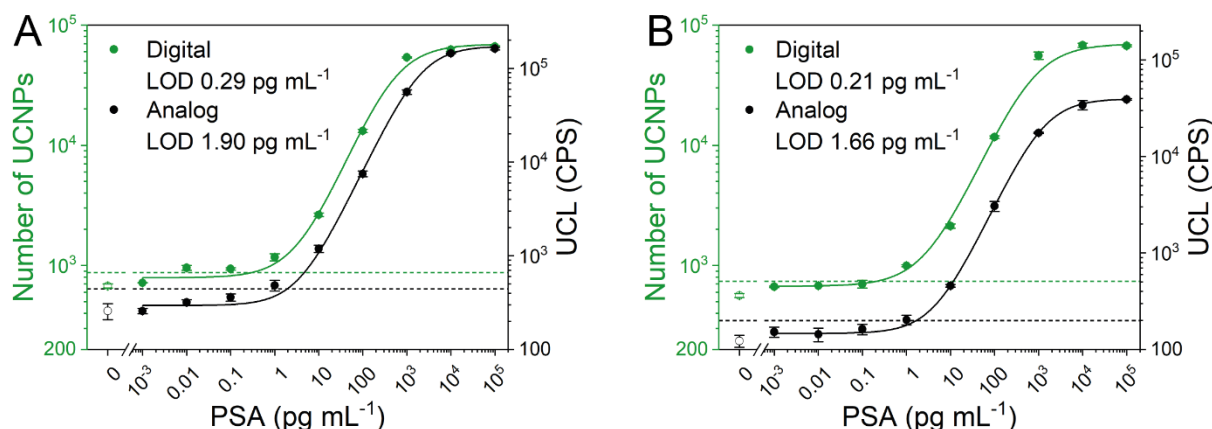


Figure S14: Digital and analog ULISA for PSA using non-purified and purified SA-PEG-UCNPs that were stored over 90 days in Tris buffer (50 mM Tris, pH 7.5). **A)** ULISA using non-purified SA-PEG-UCNPs (LOD digital: 0.29 pg mL⁻¹; LOD analog: 1.90 pg mL⁻¹). **B)** ULISA using SA-PEG-UCNPs that were purified via sucrose gradient centrifugation (LOD digital: 0.21 pg mL⁻¹; LOD analog: 1.66 mg mL⁻¹). The assay was performed in 25% bovine serum diluted with assay buffer. Calibration curves (analog readout: black lines; digital readout: green lines) were based on a 4-parameter logistic regression model. The logarithmic scale of the Y-axis visualizes signals at low PSA concentrations. Hatched lines indicate the LOD values that were obtained by adding three times the standard deviation of the background to the baseline values of the regression curve.

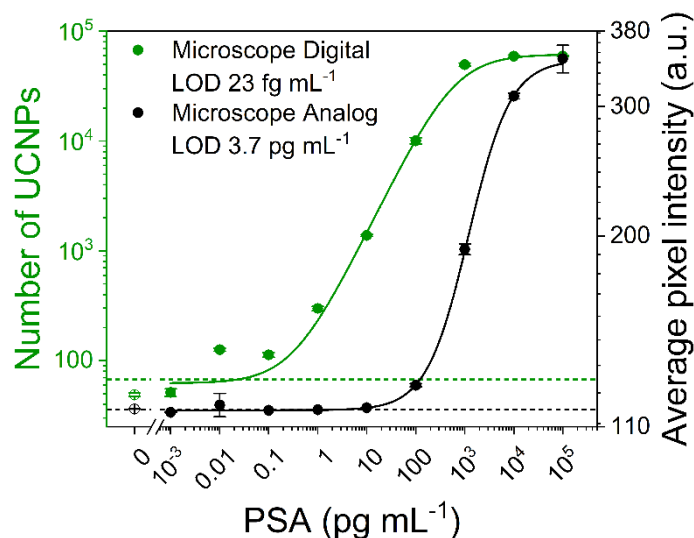


Figure S15: PSA calibration curves (analog readout by averaging the pixel intensities over the whole microscopic image: black; digital readout: green) based on a 4-parameter logistic regression model. The logarithmic scale of the y-axis visualizes signals at low PSA concentrations. Hatched lines correspond to the LOD values (digital: 23 fg mL⁻¹, microscope analog: 3.7 pg mL⁻¹) and indicate the baseline of the regression curve plus three times the standard deviation of the background.

Table S2: Precision of the digital ULISA. The CV was calculated by dividing the standard deviation of three wells by the average number of UCNPs per well. The Poisson noise was calculated by dividing the square root of the average number of UCNPs in an area of 0.2 cm² (9 images of 166 × 140 μm² combined) by the average number of UCNPs in that area (\sqrt{n}/n).

PSA (pg mL ⁻¹)	Average number of UCNPs	Experimental CV (%)	Poisson noise CV (%)
0	441 ± 2	0.4	4.8
0.001	477 ± 3	0.5	4.6
0.01	543 ± 5	0.9	4.3
0.1	570 ± 17	2.9	4.2
1	688 ± 29	4.2	3.8
10	1230 ± 120	9.9	2.8
100	6800 ± 400	5.0	1.2
10 ³	34400 ± 1000	2.8	0.5
10 ⁴	47100 ± 700	1.4	0.5
10 ⁵	50500 ± 500	0.9	0.4

Table S3: Linearity-of-dilution experiments for the determination of PSA concentrations in a human serum sample by using the analog and digital ULISA. The expected PSA concentration was determined by an electrochemiluminescent reference method.

dilution factor (DF)	Analog ULISA			Digital ULISA		
	measured (pg mL ⁻¹) x DF	expected (pg mL ⁻¹)	Recovery (%)	measured (pg mL ⁻¹) x DF	expected (pg mL ⁻¹)	Recovery (%)
2	172.7 ± 19.8	215	80.3 ± 9.2	159.7 ± 11.6	215	74.3 ± 5.4
4	173.7 ± 8.2		80.8 ± 3.8	183.2 ± 31.0		85.2 ± 14.4
6	178.4 ± 18.3		83.0 ± 8.5	166.9 ± 16.0		77.6 ± 7.5
8	186.4 ± 15.2		86.7 ± 7.1	184.0 ± 19.4		85.6 ± 9.0
10	178.8 ± 5.8		83.1 ± 2.7	167.5 ± 7.2		77.9 ± 3.4
15	187.0 ± 18.2		87.0 ± 8.5	190.8 ± 19.4		88.8 ± 9.0
20	246.1 ± 1.2		114.4 ± 0.6	198.9 ± 6.3		92.5 ± 2.9
25	228.1 ± 21.2		106.1 ± 9.9	219.2 ± 10.8		101.9 ± 5.0

Table S4: PSA concentrations of human serum samples determined either by an ECL reference method or after 400× dilution by the digital/analog ULISA.

Sample	ECL ng mL ⁻¹	Analog ULISA		Digital ULISA	
		measured (pg mL ⁻¹)	corr. (400x) (ng mL ⁻¹)	measured (pg mL ⁻¹)	corr. (400x) (ng mL ⁻¹)
1	30.64 ± 1.50	75.44 ± 1.77	30.18 ± 0.71	74.23 ± 6.00	29.69 ± 2.40
2	9.23 ± 0.45	27.79 ± 1.14	11.12 ± 0.46	25.60 ± 2.10	10.24 ± 0.84
3	5.32 ± 0.26	18.58 ± 0.80	7.43 ± 0.32	13.45 ± 1.08	5.38 ± 0.43
4	2.08 ± 0.10	8.39 ± 0.38	3.36 ± 0.15	5.97 ± 0.27	2.39 ± 0.11
5	1.08 ± 0.05	5.56 ± 1.56	2.22 ± 0.63	3.14 ± 0.92	1.26 ± 0.37
6	0.22 ± 0.01	3.65 ± 0.52	1.46 ± 0.20	2.00 ± 0.19	0.80 ± 0.08

References

1. Farka, Z.; Mickert, M. J.; Hlavacek, A.; Skladal, P.; Gorris, H. H., Single Molecule Upconversion-Linked Immunosorbent Assay with Extended Dynamic Range for the Sensitive Detection of Diagnostic Biomarkers. *Anal. Chem.* **2017**, *89* (21), 11825-11830.
2. Rissin, D. M.; Kan, C. W.; Campbell, T. G.; Howes, S. C.; Fournier, D. R.; Song, L.; Piech, T.; Patel, P. P.; Chang, L.; Rivnak, A. J.; Ferrell, E. P.; Randall, J. D.; Provuncher, G. K.; Walt, D. R.; Duffy, D. C., Single-molecule enzyme-linked immunosorbent assay detects serum proteins at subfemtomolar concentrations. *Nat. Biotechnol.* **2010**, *28* (6), 595-599.
3. Härmä, H.; Soukka, T.; Lövgren, T., Europium Nanoparticles and Time-resolved Fluorescence for Ultrasensitive Detection of Prostate-specific Antigen Clin. Chem. **2001**, *47* (3), 561-568.
4. Thaxton, C. S.; Elghanian, R.; Thomas, A. D.; Stoeva, S. I.; Lee, J. S.; Smith, N. D.; Schaeffer, A. J.; Klocker, H.; Horninger, W.; Bartsch, G.; Mirkin, C. A., Nanoparticle-based bio-barcode assay redefines "undetectable" PSA and biochemical recurrence after radical prostatectomy. *Proc. Natl. Acad. Sci. U.S.A.* **2009**, *106* (44), 18437-18442.
5. Uludag, Y.; Tothill, I. E., Cancer biomarker detection in serum samples using surface plasmon resonance and quartz crystal microbalance sensors with nanoparticle signal amplification. *Anal. Chem.* **2012**, *84* (14), 5898-5904.
6. Liu, A.; Zhao, F.; Zhao, Y.; Shangguan, L.; Liu, S., A portable chemiluminescence imaging immunoassay for simultaneous detection of different isoforms of prostate specific antigen in serum. *Biosens. Bioelectron.* **2016**, *81*, 97-102.
7. Shao, F.; Zhang, L.; Jiao, L.; Wang, X.; Miao, L.; Li, H.; Zhou, F., Enzyme-Free Immunosorbent Assay of Prostate Specific Antigen Amplified by Releasing pH Indicator Molecules Entrapped in Mesoporous Silica Nanoparticles. *Anal. Chem.* **2018**, *90* (14), 8673-8679.
8. Yang, Y.; Yan, Q.; Liu, Q.; Li, Y.; Liu, H.; Wang, P.; Chen, L.; Zhang, D.; Li, Y.; Dong, Y., An ultrasensitive sandwich-type electrochemical immunosensor based on the signal amplification strategy of echinoidea-shaped Au@ Ag-Cu₂O nanoparticles for prostate specific antigen detection. *Biosens. Bioelectron.* **2018**, *99*, 450-457.
9. Zhou, X.; Yang, L.; Tan, X.; Zhao, G.; Xie, X.; Du, G., A robust electrochemical immunosensor based on hydroxyl pillar [5] arene@ AuNPs@ g-C₃N₄ hybrid nanomaterial for ultrasensitive detection of prostate specific antigen. *Biosens. Bioelectron.* **2018**, *112*, 31-39.
10. Yu, Q.; Wu, Y.; Liu, Z.; Lei, S.; Li, G.; Ye, B., Novel electrochemical biosensor based on cationic peptide modified hemin/G-quadruples enhanced peroxidase-like activity. *Biosens. Bioelectron.* **2018**, *107*, 178-183.
11. Kadimisetty, K.; Malla, S.; Sardesai, N. P.; Joshi, A. A.; Faria, R. C.; Lee, N. H.; Rusling, J. F., Automated multiplexed ECL immunoarrays for cancer biomarker proteins. *Anal. Chem.* **2015**, *87* (8), 4472-4478.

12. Du, S.; Guo, Z.; Chen, B.; Sha, Y.; Jiang, X.; Li, X.; Gan, N.; Wang, S., Electrochemiluminescence immunosensor for tumor markers based on biological barcode mode with conductive nanospheres. *Biosens. Bioelectron.* **2014**, *53*, 135-141.
13. Shao, K.; Wang, B.; Nie, A.; Ye, S.; Ma, J.; Li, Z.; Lv, Z.; Han, H., Target-triggered signal-on ratiometric electrochemiluminescence sensing of PSA based on MOF/Au/G-quadruplex. *Biosens. Bioelectron.* **2018**, *118*, 160-166.
14. Lind, K.; Kubista, M., Development and evaluation of three real-time immuno-PCR assemblages for quantification of PSA. *J. Immunol. Meth.* **2005**, *304* (1-2), 107-116.
15. Sanders, M.; Lin, Y.; Wei, J.; Bono, T.; Lindquist, R. G., An enhanced LSPR fiber-optic nanoprobe for ultrasensitive detection of protein biomarkers. *Biosens. Bioelectron.* **2014**, *61*, 95-101.
16. Zhu, Q.; Trau, D., Gel pad array chip for high throughput and multi-analyte microbead-based immunoassays. *Biosens. Bioelectron.* **2015**, *66*, 370-378.
17. Zhuang, J.; Tang, D.; Lai, W.; Xu, M.; Tang, D., Target-induced nano-enzyme reactor mediated hole-trapping for high-throughput immunoassay based on a split-type photoelectrochemical detection strategy. *Anal. Chem.* **2015**, *87* (18), 9473-9480.
18. Song, H. Y.; Wong, T. I.; Sadovoy, A.; Wu, L.; Bai, P.; Deng, J.; Guo, S.; Wang, Y.; Knoll, W.; Zhou, X., Imprinted gold 2D nanoarray for highly sensitive and convenient PSA detection via plasmon excited quantum dots. *Lab Chip* **2015**, *15* (1), 253-263.
19. Bhuckory, S.; Mattera, L.; Wegner, K.; Qiu, X.; Wu, Y.-T.; Charbonniere, L.; Reiss, P.; Hildebrandt, N., Direct conjugation of antibodies to the ZnS shell of quantum dots for FRET immunoassays with low picomolar detection limits. *Chem. Commun.* **2016**, *52* (100), 14423-14425.
20. Han, S. W.; Jang, E.; Koh, W.-G., Microfluidic-based multiplex immunoassay system integrated with an array of QD-encoded microbeads. *Sens. Actuators, B* **2015**, *209*, 242-251.
21. Härmä, H.; Soukka, T.; Lönnberg, S.; Paukkunen, J.; Tarkkinen, P.; Lövgren, T., Zeptomole detection sensitivity of prostate-specific antigen in a rapid microtitre plate assay using time-resolved fluorescence. *Luminescence* **2000**, *15* (6), 351-355.
22. Päckilä, H.; Ylihärsilä, M.; Lahtinen, S.; Hattara, L.; Salminen, N.; Arppe, R.; Lastusaari, M.; Saviranta, P.; Soukka, T., Quantitative multianalyte microarray immunoassay utilizing upconverting phosphor technology. *Anal. Chem.* **2012**, *84* (20), 8628-8634.
23. Abcam Human PSA ELISA Kit (KLK3) (ab113327).
<https://www.abcam.com/human-psa-elisa-kit-klk3-ab113327.html>, (accessed March 23, 2020).
24. Abcam Human Free Prostate Specific Antigen ELISA Kit (ab188389).
<https://www.abcam.com/human-free-prostate-specific-antigen-elisa-kit-ab188389.html>, (accessed March 23, 2020).
25. Biorbyt Human PSA ELISA Kit (orb339660).

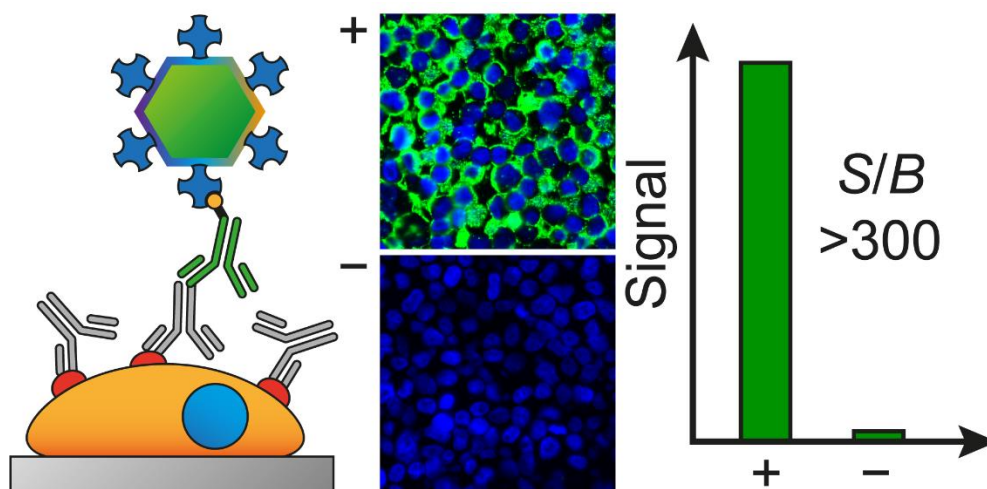
- <http://www.biorbyt.com/human-psa-elisa-kit-134680>, (accessed_March 23. 2020).
26. Roche Elecsys total PSA.
https://www.roche.de/res/content/7854/psa_total_factsheet.pdf, (accessed March 23. 2020).
 27. LifeSpan BioSciences Human KLK3 / PSA ELISA Kit (CLIA) (LS-F25971).
<https://www.lsbio.com/elisakits/human-klk3-psa-elisa-kit-clia-ls-f25971/25971>, (accessed_March 23. 2020).
 28. LifeSpan BioSciences Human KLK3 / PSA ELISA Kit (Sandwich ELISA) (LS-F5207). <https://www.lsbio.com/elisakits/human-klk3-psa-elisa-kit-sandwich-elisa-ls-f5207/5207>, (accessed_March 23. 2020).
 29. OriGene Human Kallikrein 3 ELISA Kit (EA100514).
<https://www.origene.com/catalog/assay-kits/elisa-kits/ea100514/human-kallikrein-3-elisa-kit>, (accessed March 23. 2020).
 30. R&D Systems Human Kallikrein 3/PSA Quantikine ELISA Kit (DKK300).
https://www.rndsystems.com/products/human-kallikrein-3-psa-quantikine-elisa-kit_dkk300 (accessed March 23. 2020).
 31. Thermo Fisher Scientific PSA (Total) Human ELISA Kit (EHK3T).
<https://www.thermofisher.com/elisa/product/PSA-Total-KLK3-Human-ELISA-Kit/EHK3T>, (accessed_March 23. 2020).
 32. Farka, Z.; Jurik, T.; Pastucha, M.; Skladal, P., Enzymatic Precipitation Enhanced Surface Plasmon Resonance Immunosensor for the Detection of Salmonella in Powdered Milk. *Anal. Chem.* **2016**, *88* (23), 11830-11836.
 33. Kostiv, U.; Patsula, V.; Noculak, A.; Podhorodecki, A.; Vetvicka, D.; Pouckova, P.; Sedlakova, Z.; Horak, D., Phthalocyanine-Conjugated Upconversion NaYF₄:Yb³⁺/Er³⁺@SiO₂ Nanospheres for NIR-Triggered Photodynamic Therapy in a Tumor Mouse Model. *ChemMedChem* **2017**, *12* (24), 2066-2073.
 34. Podhorodecki, A.; Krajnik, B.; Golacki, L. W.; Kostiv, U.; Pawlik, G.; Kaczmarek, M.; Horak, D., Percolation limited emission intensity from upconverting NaYF₄: Yb³⁺, Er³⁺ nanocrystals—a single nanocrystal optical study. *Nanoscale* **2018**, *10* (45), 21186-21196.
 35. Kieczkowski, G. R.; Jobson, R. B.; Melillo, D. G.; Reinhold, D. F.; Grenda, V. J.; Shinkai, I., Preparation of (4-Amino-1-Hydroxybutylidene)bisphosphonic Acid Sodium Salt, MK-217 (Alendronate Sodium). An Improved Procedure for the Preparation of 1-Hydroxy-1,1-bisphosphonic Acids. *J. Org. Chem.* **1995**, *60* (25), 8310-8312.
 36. Kostiv, U.; Lobaz, V.; Kucka, J.; Svec, P.; Sedlacek, O.; Hruby, M.; Janouskova, O.; Francova, P.; Kolarova, V.; Sefc, L.; Horak, D., A simple neridronate-based surface coating strategy for upconversion nanoparticles: highly colloiddally stable I-125-radiolabeled NaYF₄:Yb³⁺/Er³⁺@PEG nanoparticles for multimodal in vivo tissue imaging. *Nanoscale* **2017**, *9* (43), 16680-16688.

VIII. Research Article 3

Surface Design of Photon-Upconversion Nanoparticles for High-Contrast Immunocytochemistry

Zdeněk Farka,* Matthias J. Mickert,* Zuzana Mikušová, Antonín Hlaváček, Pavla Bouchalová, Wenshu Xu, Pavel Bouchal, Petr Skládal, and Hans H. Gorris

*Zdeněk Farka and Matthias J. Mickert contributed equally to the work.



This Chapter has been published, text and figures reprinted with permission from The Royal Society of Chemistry: *Nanoscale*¹, Copyright 2020.

¹Farka, Z., Mickert, M. J., Mikušová, Z., Hlaváček A., Bouchalová P., Xu W., Bouchal P., Skládal P., and Gorris H.-H., Surface Design of Photon-Upconversion Nanoparticles for High-Contrast Immunocytochemistry. *Nanoscale*, **2020**, online, DOI: 10.1039/C9NR10568A.

VIII.1. Abstract

Immunohistochemistry (IHC) and immunocytochemistry (ICC) are routinely employed for the microscopic identification and diagnosis of cancerous cells in histological tissues and cell cultures. The maximally attainable contrast of conventional histological staining techniques, however, is low. While the anti-Stokes emission of photon-upconversion nanoparticles (UCNP) can efficiently eliminate optical background interference, excluding non-specific interactions of the label with the histological sample is equally important for specific immunolabeling. To address both requirements, we have designed and characterized several UCNP-based nanoconjugates as labels for the highly specific detection of the cancer biomarker HER2 on various breast cancer cell lines. An optimized streptavidin-PEG-neridronate-UCNP conjugate provided an unsurpassed signal-to-background ratio of 319, which was 50-fold better than conventional fluorescent labeling under the same experimental conditions. In combination, the absence of optical interference and non-specific binding lays the foundation for computer-based data evaluation in digital pathology.

VIII.2. Introduction

Breast cancer is the second most frequent type of cancer worldwide, with approximately 2.1 million new cases reported worldwide every year.¹ The incidence continues to increase despite the implementation of mammography screening, and improvement of adjuvant systemic therapy.² Human epidermal growth factor receptors (HER or ErbB) are membrane receptors that play important roles in biological processes like apoptosis, cell migration, differentiation, and proliferation. In 10–30% of all breast cancer patients, the HER2 receptor is overexpressed on cancer cells, which increases the rate of cell proliferation. The association with rapid cancer growth and poor prognosis render HER2 as an important cancer biomarker.³⁻⁵

IHC enables the detection and localization of antigens in histological tissues, which is routinely employed for the identification and diagnosis of cancerous cells.⁶ Protocols, antibody labeling, and new staining techniques can be optimized by ICC, where target cells are cultivated and prepared similarly as real tissue samples. While the combination of hematoxylin and eosin (H&E) represents the principle chemical counterstaining approach,⁷ antibodies labeled with enzymes,⁸ fluorophores,^{9, 10} or nanoparticles¹¹⁻¹³ are required for the specific detection of cancer biomarkers in IHC and ICC. For example, the antibody–horseradish peroxidase label oxidizes 3,3'-diaminobenzidine (DAB) with hydrogen peroxide, and the brown product precipitating at the target site is visible by light microscopy.^{14, 15}

Typically, pathologists screen images of tissue sections individually by visual inspection, which is a time-demanding procedure. Digital pathology aims at an accurate, automated, and faster screening and diagnosis of tissue slides aided by artificial intelligence¹⁶ to account for a growing population, longer life expectation, as well as the need for personalized medicine. To improve the accuracy and analysis time in clinical diagnosis, it is desirable to have high-quality images with labels that generate a high signal to background ratios and are—in the optimal case—compatible with other staining techniques like the H&E staining.¹⁷

Photon-upconversion nanoparticles (UCNPs), such as NaYF₄:Yb,Er or NaYF₄:Yb,Tm, were used as an alternative labeling strategy in IHC and ICC experiments.¹⁸⁻²⁰ Unlike conventional fluorophores, UCNPs sequentially absorb two or more photons and emit light of shorter wavelengths (anti-Stokes emission), which prevents autofluorescence, minimizes light scattering, and opens the possibility for multiplexing with standard fluorescence but also with counterstaining methods like the H&E staining.²¹ Additionally, UCNPs are not affected by self-quenching and are resistant against photobleaching.^{22,23} Non-specific adsorption of labels to cells and other surfaces, however, strongly influences the practical detection capabilities. Thus, UCNPs with low levels of non-specific binding are urgently needed. We previously used UCNPs coated either with bovine serum albumin (BSA)²⁴ or PEG²⁵ to reduce non-specific binding in microtiter plate-based immunoassays.

In pioneering work, the Tanke group¹⁸ introduced the first upconversion labeling technique for IHC and ICC based on sub-micron-sized ground phosphor powders covered with a silica shell. Other groups²⁶ have since employed silanization,^{19, 20} encapsulation by 5-mercaptopuccinic acid and polyallylamine hydrochloride,²⁷ or polyethylene glycol (PEG)²⁸ to prepare upconversion labels for IHC or ICC. Here, we have designed several well-defined streptavidin-UCNP nanoconjugates for labeling the HER2 receptor on the surface of breast cancer cells (**Figure 1**). We have evaluated the labeling performance of the upconversion labels in terms of non-specific binding and background reduction. A quantitative comparison to fluorescent labels demonstrated that UCNP labels are a highly valuable addition to the existent staining repertoire.

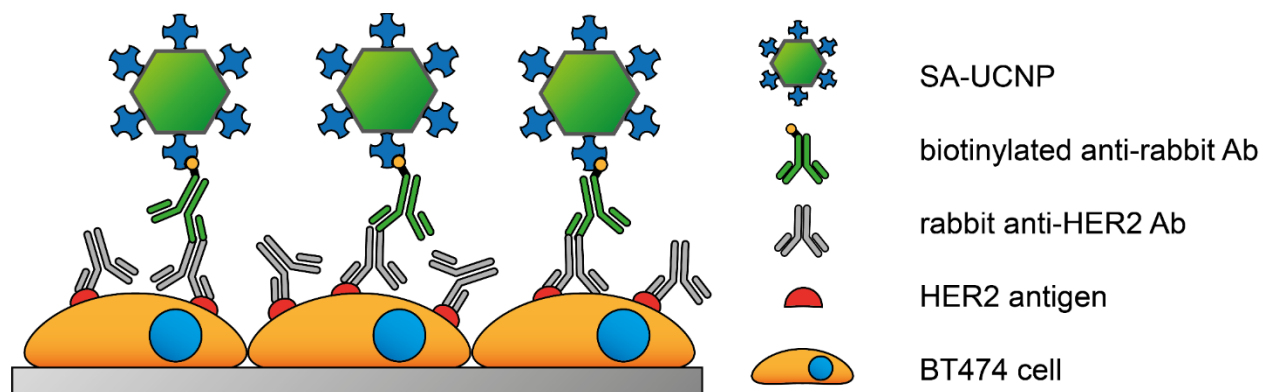


Figure 1: Scheme of the ICC assay. After blocking of the surface (not shown), the primary antibody binds to the HER2 receptor on the surface of the cells, followed by a biotinylated secondary antibody, and the detection UCNP-streptavidin conjugates.

VIII.3. Materials and Methods

Chemicals and Buffers

The list of chemicals is provided in the Supporting Information (SI). Phosphate buffer (PB; 50 mM $\text{NaH}_2\text{PO}_4/\text{Na}_2\text{HPO}_4$, pH 7.4), phosphate-buffered saline (PBS; PB with 150 mM NaCl), Tris buffered saline (TBS; 50 mM Tris, 150 mM NaCl, pH 7.5), TBS-T buffer (TBS with 0.05% Tween 20), antibody dilution buffer (10% SuperBlock in PBS, 0.05% Tween 20, and 0.05% NaN_3 , pH 7.5), SB assay buffer (10% SuperBlock in TBS, 1 mM KF, 0.05% Tween 20, and 0.05% NaN_3 , pH 7.5), BSA/BGG assay buffer (0.2% bovine serum albumin, 0.5% bovine γ -globulin, 50 mM Tris, 150 mM NaCl, 5 mM EDTA, 0.2% PVA, 1% glucose, 0.01% Tween 20, 1 mM KF, and 0.05% NaN_3 , pH 7.5), and epitope retrieval buffer (10 mM Tris, 1 mM EDTA, 0.05% Tween 20, pH 9) were produced in double-distilled water and filtered through a 0.22 μm membrane (Magna Nylon 47 mm; GVS, USA).

Preparation of UCNP-Streptavidin Labels

For the preparation of the Alkyne-PEG-Ner linker, 30 mg of neridronate (Ner; Merck, Germany) was dissolved in 128 μL of 1 M NaOH under sonication, followed by the addition of 398 μL of PB (pH 7.6). Then, 500 μL of 15 mM Alkyne-PEG-NHS (α -N-hydroxysuccinimide- ω -alkyne polyethylene glycol, M_w 3000; Iris Biotech, Germany) in PB (pH 7.6) was added and incubated overnight at 4 °C. The reaction mixture was dialyzed against double-distilled water (1.8 L) in a Float-A-Lyzer G2 dialysis device (MWCO = 500–1000 Da, Fisher Scientific, Germany) at 4 °C for 72 h, double-distilled water was 12 \times changed. The purified, colorless Alkyne-PEG-Ner was lyophilized (Alpha 1-2, Christ, Germany) and stored at 4 °C.²⁹

Oleic acid-capped UCNPs were synthesized by high-temperature co-precipitation, as described in the **SI**.³⁰ UCNPs (10 mg) dispersed in cyclohexane were mixed with an equivalent volume of dimethylformamide (DMF) and approx. 1 mg of NOBF₄ (Merck, Germany) was added per mg of UCNPs. UCNPs were incubated for 20 min at 30 °C under shaking to remove oleic acid from the nanoparticle surface and mediate a phase transfer from cyclohexane to DMF. After discarding the upper cyclohexane phase, chloroform was added in excess to the dispersion in DMF to precipitate the UCNPs. UCNPs were then purified for 5 min by centrifugation (1000 g), redispersed in DMF, precipitated with chloroform and separated for 5 min by centrifugation (1000 g). The UCNP pellet was redispersed in 1 mL of double-distilled water containing 2 mg of the Alkyne-PEG-Ner linker and incubated overnight at 4 °C. The Alkyne-PEG-Ner-UCNP conjugates were dialyzed for 72 h in a Float-A-Lyzer G2 dialysis device (MWCO = 100 kDa, Fisher Scientific) against double-distilled water (1.8 L) containing 1 mM KF at 4°C. The dialysis medium was 9× exchanged.

For the functionalization with streptavidin, Alkyne-PEG-Ner-UCNPs (7 mg in 700 µL water) were diluted with 300 µL of Tris-HCl (75 mM, pH 7.5) and an aqueous solution of L-ascorbic acid sodium salt (20 µL, 20 mg/mL). The mixture was purged with argon for 40 min, then 50 µL streptavidin azide (7 Bioscience, Germany; 1 mg/mL) in 25 mM Tris-HCl (pH 7.5) was added, and the mixture was purged for another 10 min. The click-reaction was started by adding 10 µL CuSO₄ 5 H₂O (25 mM in double-distilled water). After 45 min purging with argon, the suspension was dialyzed in a Float-A-Lyzer G2 dialysis device (MWCO = 100 kDa) against 500 mL TBS containing 1 mM KF and 0.05% NaN₃ at 4 °C for 72 h (dialysis medium 9× exchanged).²⁵ The structure of SA-PEG-Ner-UCNPs is shown in **Figure 2A**. The preparation of SA-PEG-Alen-UCNPs (**Figure 2B**) and SA-BSA-UCNPs (**Figure 2C**) is described in the **SI**.

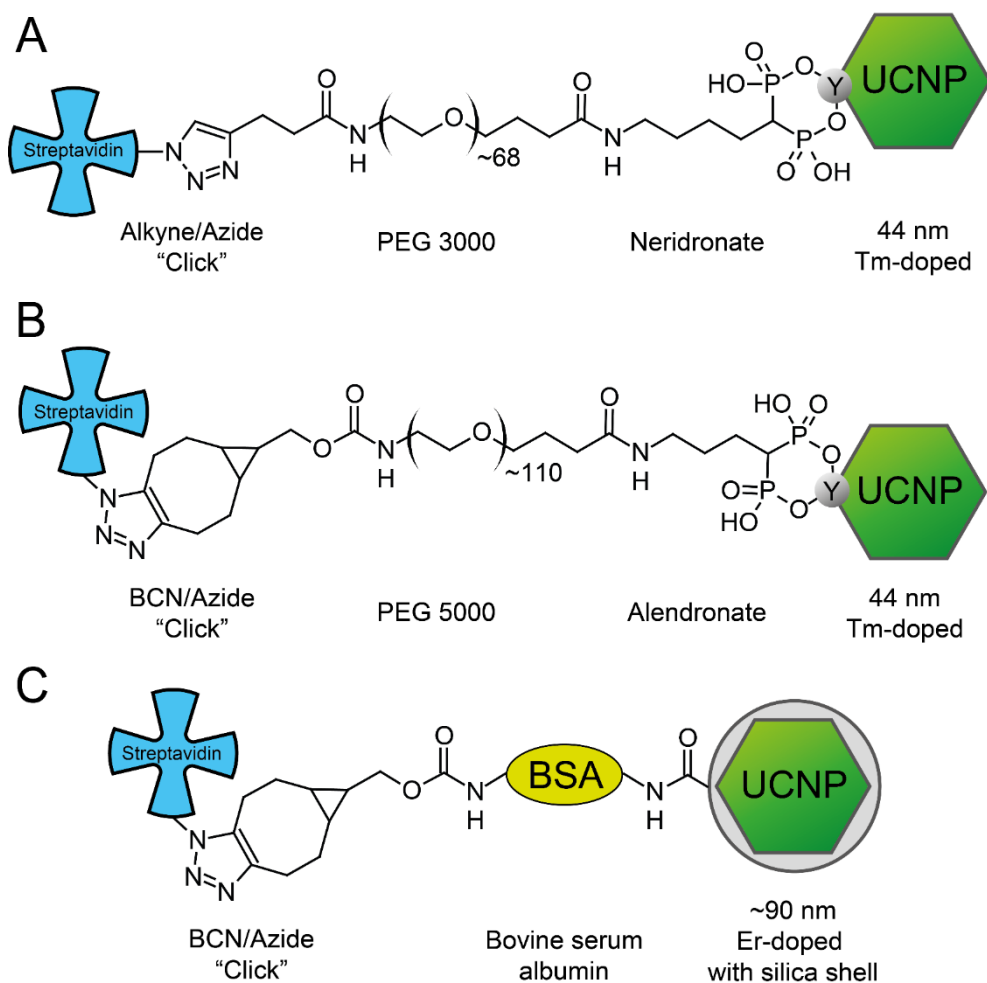


Figure 2: Chemical structures of UCNP-streptavidin labels. **A)** SA-PEG-Ner-UCNP, **B)** SA-PEG-Alen-UCNP, and **C)** SA-BSA-UCNP.

UCNP-conjugates were purified by sucrose gradient centrifugation. Solutions of 10%, 20%, and 35% w/v sucrose were prepared in TBS (containing 1 mM KF, 0.05% NaN₃). A sucrose gradient was formed in a microtube by underlaying successively 50 μ L of the UCNP sample, 10% sucrose (200 μ L), 20% sucrose (200 μ L), and 35% sucrose (200 μ L). After centrifugation (750 g) for 15 min, the top layer (250 μ L) was taken for subsequent experiments. Purified SA-PEG-Ner-UCNPs were stored at 4 °C. KF was included in the storage buffer in order to avoid the dissolution of UCNPs.³¹

Characterization of UCNP Conjugates

The UCNPs and their conjugates were characterized using transmission electron microscopy (TEM), optical spectroscopy, dynamic light scattering (DLS), nanoparticle tracking analysis (NTA), single-particle upconversion microscopy, liquid chromatography coupled with tandem mass spectrometry (LC-MS/MS), and in microtiter plate-based assay as described in the **SI**.

Immunolabeling of Cells

Breast cancer cell lines BT-474 (ATCC HTB-20), MCF-7 (ATCC HTB-22), and MDA-MB-231 (ATCC HTB-26) were cultivated in high-glucose Dulbecco's Modified Eagle's Medium (complete DMEM; Sigma-Aldrich, Germany) supplemented with 10% fetal bovine serum in a humidified atmosphere of 5% CO₂. The cells were trypsinized 24 h before the fixation, centrifuged at 1,000 g for 5 min and resuspended in complete DMEM. An aliquot of 50 µL of the cell suspension was pipetted onto a sterile glass slide (KnittelGlass, Germany) in a cultivation dish and cultivated in drops for 4 h to confine the cells in a small area appropriate for the staining procedure. After 4 h, the cell slides were overlaid with complete DMEM and cultivated for another 20 h. Then the cell slides were washed 3 times with 100 mM phosphate-buffered saline containing 150 mM NaCl (pH 7.2). After removing buffer residues, the slides were submerged into an ice-cold (−20 °C) methanol:acetone (1:1) fixative solution for 6 min. The slides were dried at room temperature and stored at −20 °C.

Formalin-fixed paraffin-embedded (FFPE) cells and cancer tissue were obtained from AMS Biotechnology (UK). BT-474 and MDA-MB-231 cell pellet slides expressing different levels of the HER2 antigen were used for ICC experiments, and slides with breast tumor tissue sections from surgical resection (Infiltrative Ductal Carcinoma, HER2 positive; AMS-8009) for IHC experiments. Human tissue samples were collected in the US under informed consent and in accordance with the ethical standards of the responsible committee (institutional and national) and with the 1964 Helsinki declaration. The slides were first dewaxed using xylene (mixture of isomers; 3× 5 min) and rehydrated in 99% ethanol (2× 5 min), 90% ethanol (2× 5 min), and water (5 min). Afterwards, the heat-induced epitope retrieval was performed by placing the slides in epitope retrieval buffer pre-heated to 60 °C and heating to 80 °C for 20 min in a water bath. The slides were allowed to cool to room temperature for 20 min and then transferred to TBS. After 2 min, the slides were removed from the buffer.

H&E staining was performed according to the manufacturer's instructions (H&E Fast Staining Kit; Carl Roth, Germany). After antigen retrieval, the FFPE slides were incubated in H&E solution 1 for 6 min, rinsed with deionized water for 10 s, followed by differentiation in 0.1 % HCl for 10 s. The slides were rinsed under flowing deionized water for 6 min, incubated in H&E solution 2 for 30 s, and washed under flowing deionized water for 30 s.

For HER2-labeling, cell sections (~0.5 cm in diameter) and tissue sections (~1.5 cm in diameter) were encircled with a PAP pen liquid blocker (Science Services, Germany). After drying of the PAP pen marking, the slides were washed for 1 min in TBS. Either 50- μ L droplets (for ICC experiments) or 150- μ L droplets (for IHC experiments) of the following solutions were applied to the slides at room temperature. After blocking with concentrated SuperBlock containing 0.05% Tween 20 for 60 min and washing 3 times for 5 min with TBS, the slides were incubated with a rabbit anti-HER2 antibody (ab134182, Abcam, UK; 1 μ g/mL in antibody dilution buffer) for 1 h. In a negative control experiment, the slides were incubated in the same dilution buffer without the anti-HER2 antibody. After washing with TBS (3 \times 5 min), biotinylated anti-rabbit antibody was applied (111-065-144, Jackson ImmunoResearch, UK; 2 μ g/mL in antibody dilution buffer, 1 h). Next, the slides were incubated with the purified UCNP conjugate (35 μ g/mL) in SB assay buffer for 1 h. The slides were washed with TBS-T buffer (2 \times 5 min), TBS (5 min), and incubated with DAPI (1 μ g/mL in TBS) for 20 min. Finally, the slides were washed with TBS, a glass cover slip was mounted using 6 μ L of TBS, and the slide was imaged under the upconversion microscope.

A streptavidin-5(6)-carboxyfluorescein conjugate (SA-FAM) was synthesized as described in the SI³² and used as a label for conventional fluorescence microscopy. A solution of 10 μ g/mL SA-FAM in SB assay buffer was employed, with the same staining protocol as described for the UCNP labels.

Microscope Imaging

The H&E staining was recorded under a bright-field transmission microscope (OBE 114; Kern Optics, Germany) equipped with a 40 \times objective (NA 0.65) and an 8.1-megapixel CMOS camera (ODC825; Kern Optics). The ImageJ plugin *Landmark Correspondences* was used to align bright-field images to upconversion luminescence images.

Cells were imaged on a modified inverted wide-field epifluorescence microscope (Eclipse Ti, Nikon, Japan).³³ For UCNP excitation, a 980 nm continuous-wave laser diode (4 W, Wavespectrum, China) was coupled *via* a multi-mode optical fiber (105 μ m fiber core, NA = 0.22, Wavespectrum) into a motorized TIRF illuminator unit (Nikon). The optical filters for UCNP excitation consisted of a long-pass excitation filter with a cut-on at 830 nm (Schott, Germany), a dichroic mirror with a cut-on at 875 nm (AHF Analysentechnik, Germany), and either a green band-pass filter (535 \pm 70 nm) for the emission of Er³⁺-doped UCNP, or a NIR-filter (809 \pm 40 nm) for the emission of Tm³⁺-doped UCNP. A fiber-optical mercury lamp (Intensilight, Nikon) served as an excitation source for fluorescent dyes and optical filter sets (Chroma, USA) were selected for DAPI ($\lambda_{\text{ex}} = 365 \pm 20$ nm, $\lambda_{\text{dichroic}} = 357 \pm 35$ nm, $\lambda_{\text{em}} = 445$

± 30 nm) and carboxyfluorescein ($\lambda_{\text{ex}} = 480 \pm 20$ nm, $\lambda_{\text{dichroic}} = 470 \pm 20$ nm, $\lambda_{\text{em}} = 530 \pm 30$ nm). The emission light was collected with a 40 \times water immersion objective (CFI Apo LWD 40 \times WI Lambda-S, NA = 1.15, Nikon) and recorded on a 5.5-megapixel vacuum-cooled sCMOS camera (Neo 5.5, Andor, UK), which resulted in a field of view of $416 \times 351 \mu\text{m}^2$. The microscope was controlled using NIS Elements 4.5 Advanced Research (Nikon).

Bleaching experiments were performed under continuous excitation over a period of 20 min. Time lapse images were acquired every 30 s using an excitation time of 2s (SA-PEG-Ner-UCNPs) or 200 ms (SA-FAM), respectively. A region of interest of $200 \times 200 \mu\text{m}^2$ was selected and the average intensity was measured for each image. After subtraction of the background signal, the intensities were plotted against time.

Luminescence Scanning

For upconversion scanning, a modified microplate reader (Chameleon, Hidex, Finland) was used.³⁴ Images of the cell pellet slides were acquired by defining several squares that were raster-scanned (18×18 points, $500 \mu\text{m}$ steps) with an exposure time of 500 ms. A microplate reader (Upcon, Labrox, Finland) was used for fluorescence scanning. Carboxyfluorescein was excited at 485 nm, and the emission light was collected at 535 nm. Squares of 18×18 points with a step size of $500 \mu\text{m}$ were scanned with an exposure time of 1 s. The imaging data were analyzed with ImageJ (National Institutes of Health, USA).³⁵ Circular regions of interests (ROIs) of identical size were placed over the area containing the cells followed by averaging the gray values of all pixels included in the ROI. After data evaluation, the images were processed in Origin 2019b (OriginLab, USA). Bilinear interpolation increased the image resolution five-fold.

VIII.4. Results and Discussion

Characterization of UCNP Labels

For efficient immunocytochemistry, it is essential that labels are bright enough for an easy detection without optical background interference and label the cancer biomarker with high specificity but not to the support material or non-target cell materials (non-specific binding). We designed UCNP labels coated with PEG or BSA (**Figure 2**) that are promising candidates for avoiding non-specific binding.^{24, 25}

Tm³⁺-doped UCNPs display strong NIR emission at 801 nm (**Figure S1**) and have a homogeneous size distribution with an average diameter of 44 nm as determined by TEM (**Figures 3A and 3B**). DLS measurements showed that the hydrodynamic diameter increased from 88.7 nm (PDI 0.264) with oleic acid coating to 141.7 nm (PDI 0.234) after the preparation of the SA-PEG-Ner-UCNP conjugate (**Figure S2A**). The presence of streptavidin on the nanoparticle surface was further confirmed by LC-MS/MS (**Table S1**). Sucrose gradient centrifugation removed bigger aggregates, which decreased the average conjugate size to 78.7 nm and improved the particle homogeneity (PDI: 0.187). Nanoparticle tracking analysis (NTA) (**Figure S2B**) showed a main peak at 70.5 nm in both the non-purified and the purified sample, which can be attributed to the non-aggregated conjugate while the decrease in the number of bigger particles (100–250 nm) indicates the successful purification. The dilution of UCNPs during purification was also measured by NTA. A dilution factor of 10.5 ± 3.6 was calculated from three independent purification experiments.

The label homogeneity was further investigated by immobilizing SA-PEG-Ner-UCNPs on a microtiter plate coated with biotinylated BSA (BSA-biotin) and detecting them individually under the upconversion microscope. The non-purified conjugate exhibited a peak of the brightness distribution at 179 a.u. per diffraction-limited spot and a coefficient of variation (CV) of 87% (**Figure 3C**). After purification, the peak brightness slightly decreased to 163 a.u. and the labels were more homogeneous (CV: 66%, **Figure 3D**). The removal of larger aggregates is evident from the absence of peaks above 600 a.u. Detailed microscopy images are shown in **Figure S3**.

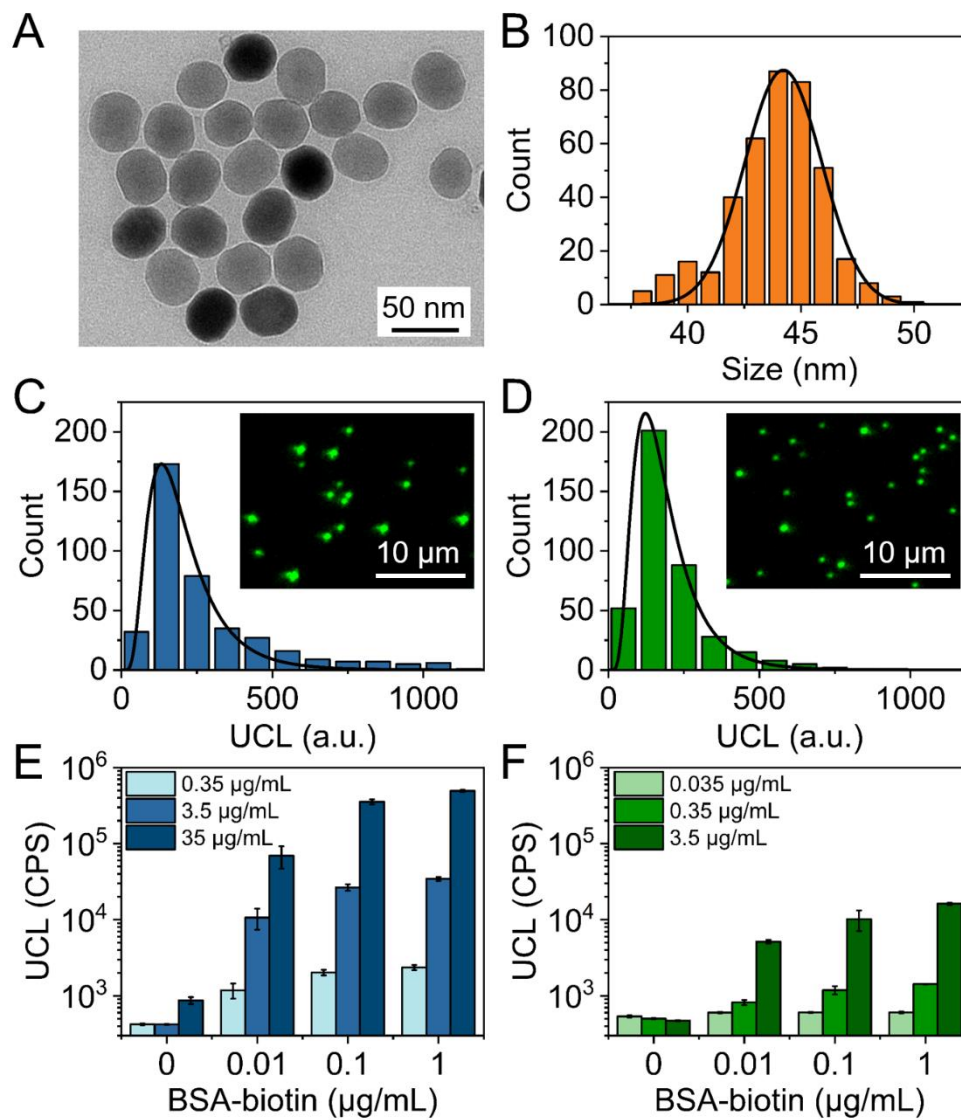


Figure 3: (A) TEM image of oleic acid-capped UCNPs; (B) UCNP size distribution evaluated by TEM (average diameter: 44.2 nm; FWHM 4.0 nm). Brightness distribution of (C) non-purified and (D) purified SA-PEG-Ner-UCNPs; the insets show the upconversion microscopy images. Functional characterization of (E) non-purified and (F) purified conjugate in a BSA-biotin ULISA assay. The error bars correspond to standard deviations of three independent microtiter plate wells.

The BSA-biotin microtiter plate assay was further used for the functional characterization of the different nanoconjugates. Blocking with 10% SuperBlock yielded higher specific signals than BSA blocking, especially at low BSA-biotin coating concentrations. This effect was independent of the UCNP label concentration (**Figure S4**). As the background signal of non-specific binding was in both negligible, 10% SuperBlock was chosen for all further experiments. Both non-purified (**Figure 3E**) and purified (**Figure 3F**) SA-PEG-Ner-UCNPs

(**Figure 2A**) enabled specific binding to BSA-biotin with low levels of non-specific binding. The purification had no significant effect on the signal-to-background ratio (*S/B*), which increased with label concentration from ~6× at 0.35 μg/mL SA-PEG-Ner-UCNP to 566× at 35 μg/mL SA-PEG-Ner-UCNP. Alendronate and a longer PEG (**Figure 2B**) were used to conjugate streptavidin to the surface of UCNPs via copper-free click chemistry (strain-promoted BCN). Compared to the SA-PEG-Ner-UCNP, the alendronate-based conjugate resulted in a 5–10-fold lower *S/B* in the BSA-biotin assay (increasing from 1.1× for 0.07 μg/mL to 12.4 for 7 μg/mL). This can be explained by a lower amount of reactive PEG linker and, therefore, less streptavidin, which leads to a smaller change of the hydrodynamic diameter after conjugation (**Figures S5** and **S6**). SA-BSA-UCNP conjugates (**Figure 2C**) were prepared based on larger Er³⁺-doped UCNPs with a hexagonal prism shape covered by a carboxylated silica layer. Gradient centrifugation had almost no effect on the hydrodynamic diameter, indicating a highly uniform conjugate preparation, and further experiments were performed with the non-purified SA-BSA-UCNP sample. Single-particle microscopy confirmed the highly uniform sample preparation (CV: 43%). In the BSA-biotin microtiter plate assay, the conjugate provided a high *S/B* of ~100× for all label concentrations (**Figure S7**). The results of all three UCNP nanoconjugates are summarized in **Table 1**. The SA-FAM conjugate was also characterized by the BSA-biotin microtiterplate assay (**Figure S8**). Due to the generally higher background of fluorescence, lower *S/B* were observed, however, the general trend of improvement with the increasing label concentration remained (from 5× for 0.4 μg/mL to 10× for 400 μg/mL).

Table 1: Characterization of UCNP labels.

Label	SA-PEG-Ner-UCNP		SA-PEG-Alen-UCNP (Figure S5 and S6)		SA-BSA-UCNP (Figure S7)	
UCNP	NaY _{0.80} Yb _{0.18} Tm _{0.02} F ₄				NaY _{0.895} Yb _{0.100} Er _{0.005} F ₄	
Diameter (TEM / DLS)	44.2 ± 4.0 nm / 88.7 nm (PDI 0.264)				height 80.5 ± 4.7 nm; diameter 105.6 ± 4.3 nm ²⁴ / 126.6 nm (PDI 0.008)	
SA-UCNP- conjugate	Before purification	After purification	Before purification	After purification	Before purification	After purification
∅ _{HD} (DLS)	141.7 nm (PDI 0.234)	78.7 nm (PDI 0.187)	106.2 nm (PDI 0.143)	91.7 nm (PDI 0.201)	142.4 nm (PDI 0.074)	135.0 nm (PDI 0.128)
Single- particle microscopy ^a	179 a.u. CV 87%	163 a.u. CV 66%	186 a.u. CV 99%	193 a.u. CV 70%	126 a.u. CV 43%	n.d.

^a peak of intensity distribution; the exposure times were adjusted to account for the different brightness of Tm³⁺ and Er³⁺-doped UCNP

ICC based on UCNP Labels

The HER2 antigen expressed on the surface of BT-474 cells was labeled with different UCNP conjugates. DAPI (blue emission) served as a counterstain for visualizing the nucleus. **Figure S9** shows microscope images after labeling with the SA-BSA-UCNP conjugate. Due to the relatively large UCNP size (~90 nm), individual labels are visible (*z*-scan experiment is shown in **Figure S10**), but the overall *S/B* was only 2. This may be explained by two effects: (i) the carboxylated silica shell is not completely shielded by the BSA and leads to non-specific binding, and (ii) the BSA can also contribute to the non-specific binding. This finding is in agreement with the testing of the nanoparticle dilution buffer. In both cases, the presence of BSA (either in the buffer or on the nanoparticle surface) led to the increase of the non-specific binding.

In order to avoid the use of serum proteins for ICC staining and reduce the label size, we developed conjugates based on smaller UCNP (44 nm). The oleic acid on the as-synthesized UCNP was replaced by PEG-alendronate *via* a ligand exchange reaction, and streptavidin was subsequently bound by a copper-free click reaction (SA-PEG-Alen-UCNP). The microscope images (**Figure S11**), however, show that this label did not only bind to HER2 on the cell

surface but also stained the nucleus as evident from the overlapping DAPI and upconversion channels. In general, the *S/B* was low (5 at a label concentration of 7 $\mu\text{g/mL}$ and 2 at a label concentration of 35 $\mu\text{g/mL}$).

The third label was also based on 44 nm UCNPs but conjugated to PEG-neridronate and attached to streptavidin *via* copper-mediated click chemistry (SA-PEG-Ner-UCNP). A label concentration of 35 $\mu\text{g/mL}$ improved the *S/B* to 29 compared to a concentration of 7 $\mu\text{g/mL}$ (*S/B* 6) (**Figure S12**). Individual bright spots in the images of the negative control, however, indicated that aggregated labels deposited on the sample and had a negative impact on the *S/B*. Therefore, we removed such aggregates by sucrose gradient centrifugation (**Table 1**). Furthermore, the SA-PEG-Ner-UCNP labeling efficiency strongly depended on the blocking conditions. Both 10% SuperBlock (SB assay buffer) and BSA/BGG assay buffer allowed for a clear distinction between specific labeling of HER2-positive BT-474 cells and respective control experiments without primary antibody (**Figure S13**). The SB assay buffer, however, reduced the non-specific binding much more efficiently, and slightly improved the specific signal, which increased the *S/B* from 23 to 319 (**Figure S13C, F**; with enhanced contrast of the upconversion background image in **Figure S14**). We assume that serum proteins of the BSA/BGG buffer led to a higher degree of non-specific binding in ICC, which is different from the optimal blocking conditions for immunoassays in a microtiter plate format.²⁵

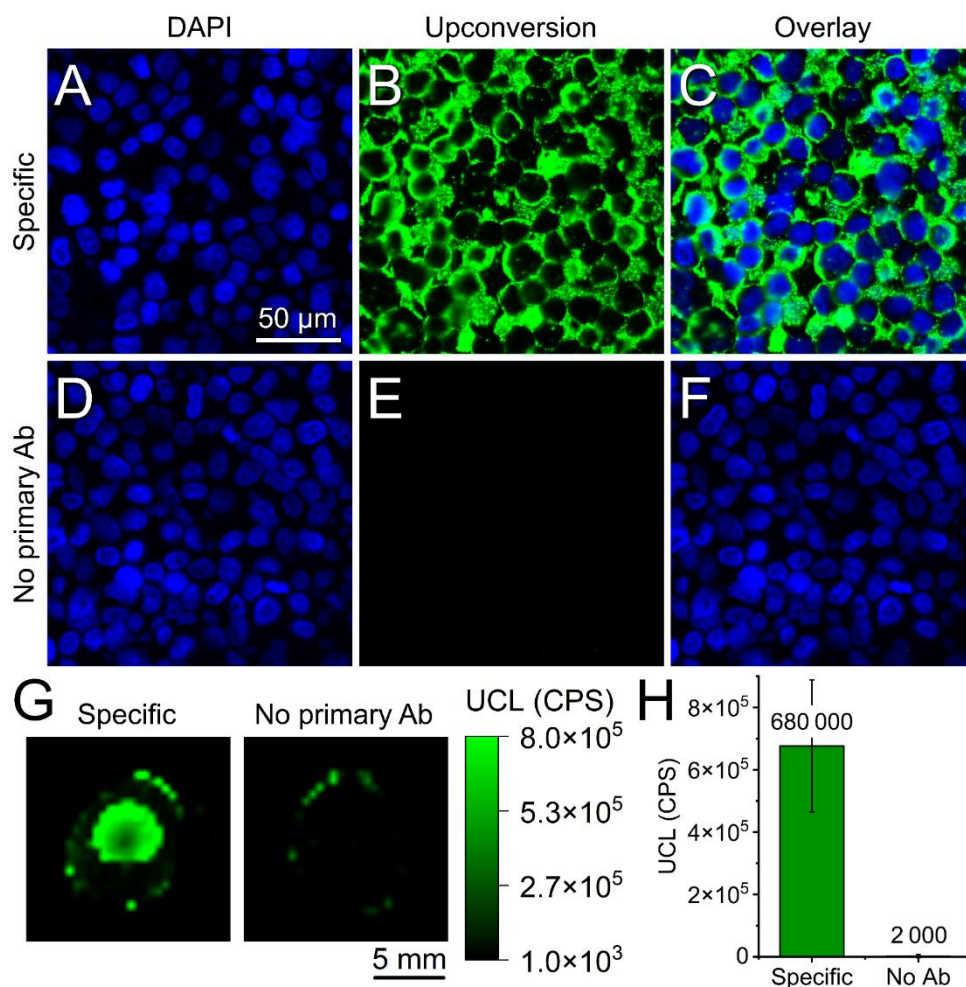


Figure 4: SA-PEG-Ner-UCNP labeling of HER2-positive FFPE BT-474 cells: **A)** DAPI channel, **B)** upconversion channel, **C)** overlay. Negative control (without primary antibody): **D)** DAPI channel, **E)** upconversion channel, **F)** overlay. **G)** Upconversion scan of the cell pellets; **H)** average upconversion intensities. The error bars indicate the standard deviations of intensities in the cell pellet.

Figure 4 shows microscope image sections (full images are shown in **Figure S15**) and upconversion scans of BT-474 cell pellets labeled with purified SA-PEG-Ner-UCNP in an optimal concentration of 35 μg/mL and under optimal blocking conditions. The circle around the cell pellet in **Figure 4G** shows the hydrophobic marking of the PAP pen, which leads to some non-specific label adsorption. The area where the cells were inspected, however, was not affected. Furthermore, there was no overlap between the green (upconversion) and the blue (DAPI) channel, confirming that SA-PEG-Ner-UCNPs did not bind to DNA. The thickness of the cell pellets did not allow for focusing all cells in a single image. Focusing on different *z* positions (± 1.6 μm) in the same cell section (**Figure S16**) confirmed that image blurring was a result of the shallow depth of field but independent of the labels. We then compared the

HER2-positive FFPE cells to HER2-negative FFPE cells under the same experimental conditions using the SA-PEG-Ner-UCNP label. Upconversion scanning resulted in 40× lower specific signals on HER2-negative MDA-MB-231 cells than on HER2-positive BT-474 cells. Essentially no signal was visible, neither in the microscopy images nor in the upconversion scans (**Figure S17**).

We have also demonstrated that upconversion-based HER2-labeling is compatible with H&E staining (**Figure S18**). In ICC experiments, H&E staining of the BT-474 FFPE cells did not interfere with the upconversion signal acquisition, which indicates that both procedures are well compatible and are applicable to IHC experiments where H&E staining is a standard procedure. HER2-positive tumor tissue sections were then labeled with SA-PEG-Ner-UCNPs to show their performance in IHC experiments. There was a 12× difference between images taken with and without primary antibody (**Figure S19**). The lower *S/N* compared to the cultured cell lines can be explained by the more heterogeneous composition of tumor tissues which contain healthy cells as well as various types of tumor cells and thus display different HER2 expression levels.

To confirm that the efficiency of SA-PEG-Ner-UCNP labeling is independent of the cell preparation, we cultivated the BT-474 cell line as well as two HER2-negative cell lines, MDA-MB-231 and MCF-7, in-house (**Figure 5**; individual detection channels shown in **Figure S20**). While HER2-positive BT-474 cells again showed a very high degree of specific labeling, very low upconversion signals were detected on the two HER2-negative cell lines. A slightly higher HER2 expression on MCF-7 cells compared to MDA-MB-231 cells was reported in the literature.³⁶ The average signal intensities of the cultivated cells were three times lower compared to the FFPE cells because of the lower cell density in the detection area. The results of all labeling experiments are summarized in **Table 2**.

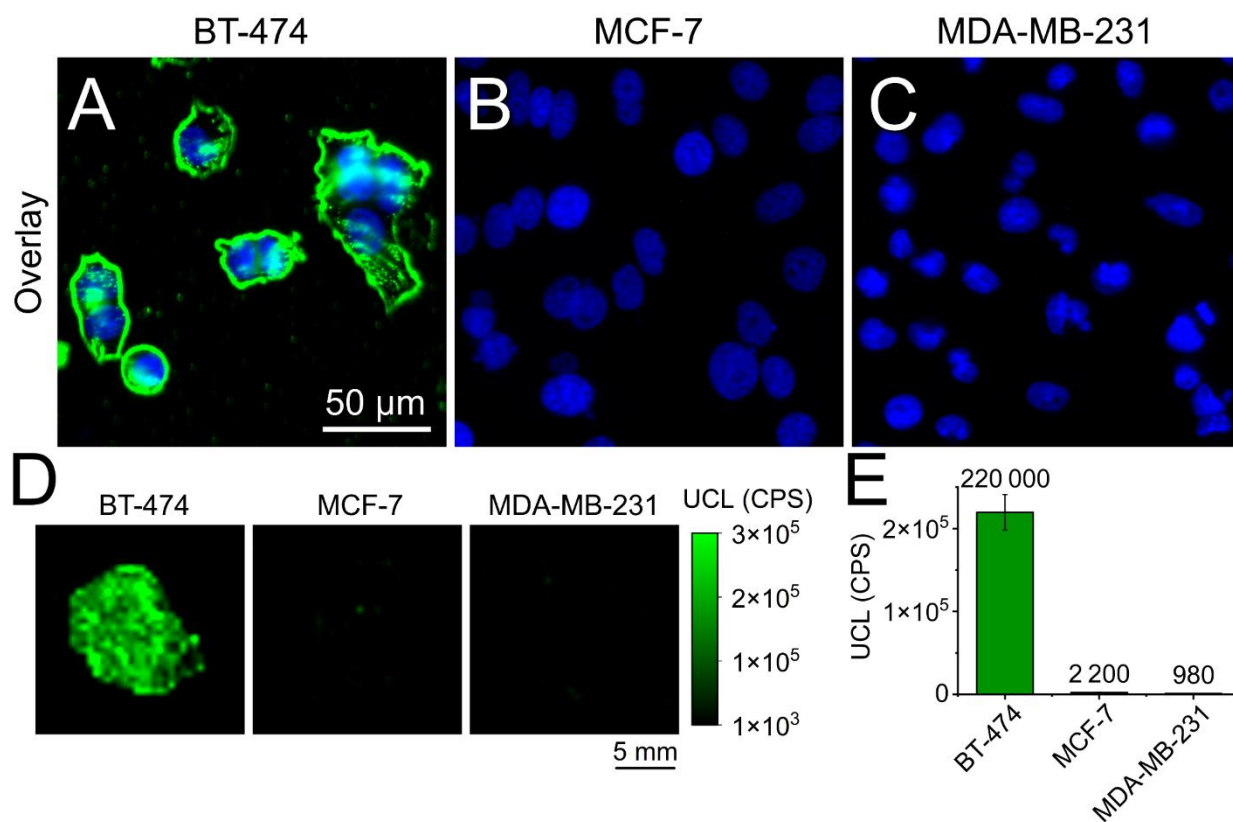


Figure 5: SA-PEG-Ner-UCNP labeling of cultivated breast cancer cell lines. Overlay images (DAPI and upconversion channels) of **A)** BT-474 cells, **B)** MCF-7 cells, and **C)** MDA-MB-231 cells. **D)** Upconversion scan of the cell pellets; **E)** average upconversion intensities. The error bars indicate the standard deviation of three independent cell pellets slides.

Table 2: Summary of histological labeling results.

Cell line	HER2 expression ³⁷	Cell preparation	SA-PEG-Ner-UCNP		SA-FAM	
			UCL ($\times 10^3$ a.u.)	ratio	Fluor. ($\times 10^3$ a.u.)	ratio
BT-474	3+	FFPE	680 ± 210	319 ^a	91 ± 10	6.1 ^a
		FFPE, no Ab	2 ± 5		14.9 ± 1.3	
		Cell culture	220 ± 21	–	25 ± 7	–
MCF-7	0–1+	Cell culture	2.2 ± 0.4	100 ^b	7.8 ± 1.7	3.2 ^b
MDA-MB-231	0–1+	Cell culture	0.98 ± 0.11	223 ^c	6.36 ± 0.12	3.9 ^c

^a Signal to background (*S/B*, no primary antibody)

^b Ratio of HER2 positive BT-474 cell culture to HER2 negative MCF-7 cell culture

^c Ratio of HER2 positive BT-474 cell culture to HER2 negative MDA-MB-231 cell culture

ICC Based on Fluorescent Labels

To compare the UCNP label performance with standard fluorescence labeling, FFPE cells (**Figure 6**) and cell cultures (**Figures S21 and S22**) were labeled with a fluorescent SA-FAM conjugate. Both the specific and the non-specific signal increased at higher concentrations of SA-FAM, and the *S/B* improved from 4 at a label concentration of 1 $\mu\text{g/mL}$ to 6 at 10 $\mu\text{g/mL}$ (**Figure S23**). Fluorescent labeling, however, always resulted in a relatively high background signal (FFPE cells: **Figure 6K** and **Figure S24** shows the fluorescence background of the image with enhanced contrast; cell cultures: **Figure S21E**), which can be explained by cellular autofluorescence, cross-talk between the detection channels and non-specific binding of the SA-FAM conjugate. The bright circles in the fluorescence scan (**Figure 6G–J**) indicate the autofluorescence of the PAP pen marking, but did not affect the analysis of the cell pellet. SA-FAM labeling resulted in a maximum *S/B* of only 6.1. The results of the fluorescence labeling experiments are summarized in **Table 2**. The superior performance of the SA-PEG-Ner-UCNP label (*S/B* 319) is clearly evident from a 50-fold wider dynamic range of upconversion measurements, which enables a much finer distinction between HER2-expression levels on different cancer cell lines. We have also compared the photostability of the SA-PEG-Ner-UCNPs with the SA-FAM (**Figure S25**). The signal of SA-FAM decreased by 59% over a 20-min observation interval. By contrast, the signal of the UCNP labels was stable over the same time period and even increased slightly because the drying sample resulted in a lower quenching effect of the upconversion luminescence by water. Finally, the use of UCNP-based labels avoids the risk of photoconversion of DAPI, which can result in significant interferences for the readout in fluorescein channel.³⁸

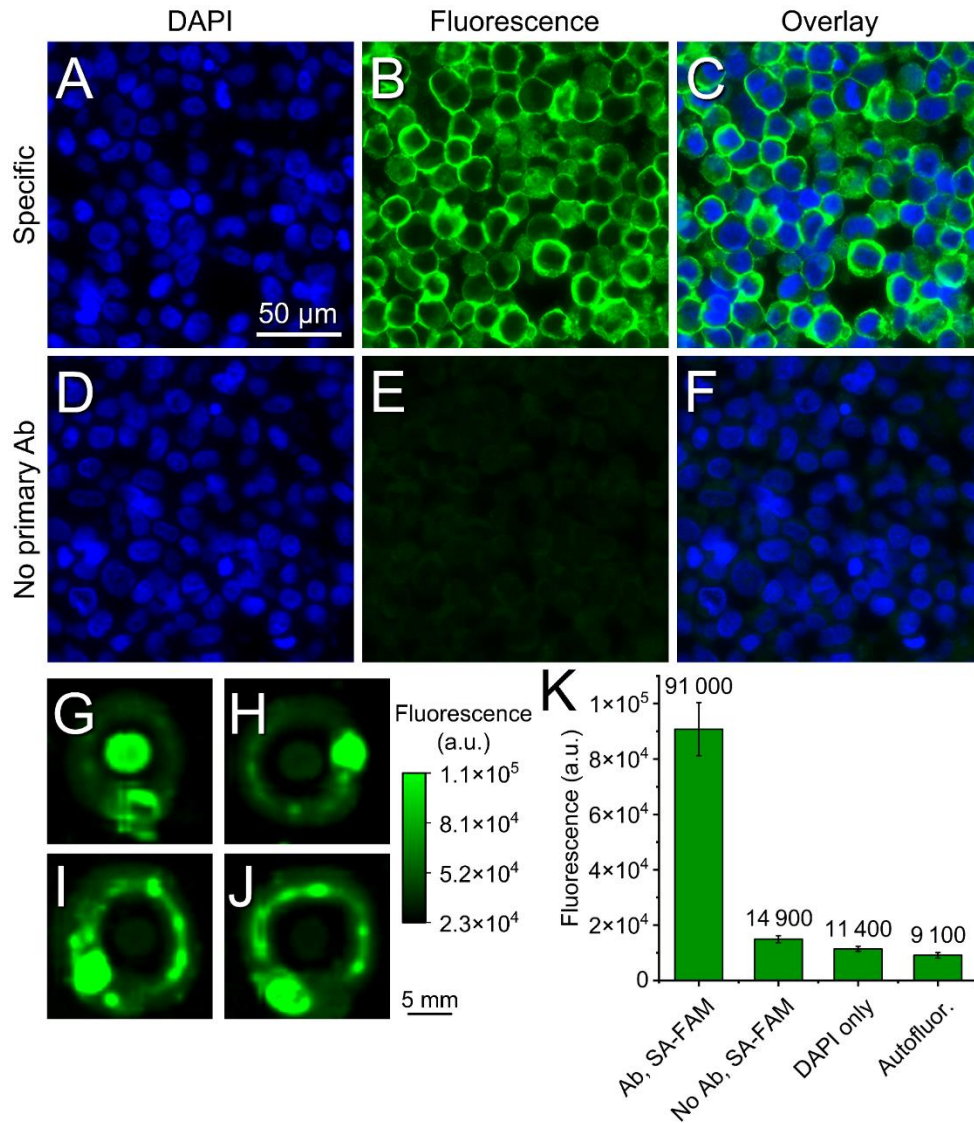


Figure 6: Fluorescence SA-FAM labeling of HER2-positive FFPE BT-474 cells: **A)** DAPI channel, **B)** fluorescein channel, **C)** overlay. Negative control (without primary Ab): **D)** DAPI channel, **E)** fluorescein channel, **F)** overlay. Fluorescence intensity scans of **G)** specific labeling, **H)** negative control (no primary antibody), **I)** incubation with DAPI only, and **J)** autofluorescence. **K)** Average fluorescence intensities measured in the cell pellets. The error bars indicate standard deviations of intensities in the cell pellets.

VIII.5. Conclusions

We have prepared and characterized three types of streptavidin-UCNP conjugates to evaluate their labeling performance in ICC as compared to conventional fluorescence labeling. The design of the nanoparticle surface architecture and blocking conditions were essential for an efficient ICC procedure. PEG-coated UCNP showed lower levels of non-specific binding than BSA-coated labels (SA-BSA-UCNP). Similarly, a blocking buffer composition without serum proteins further reduced the level of non-specific binding. HER2-positive BT-474 cells showed the highest specific signals after labeling with SA-PEG-Ner-UCNPs and extremely low background interference as observed by wide-field upconversion microscopy as well as upconversion scanning (*S/B* 319). By contrast, conventional fluorescence labeling only achieved an *S/B* of 6. Consequently, the optimized SA-PEG-Ner-UCNP labeling protocol resulted in a 50-fold wider dynamic range than fluorescence labeling, which allows for a much finer distinction between HER2-expression levels. The absence of optical background interference under 980 nm excitation in combination with extremely low levels of non-specific binding clearly demonstrate the potential of UCNP as alternative labels in ICC and IHC. The high *S/B* is a great advantage especially for computer-based data evaluation in digital pathology. Without cross-talk between fluorescence channels, UCNP labeling can readily be combined with H&E staining for multiplexed applications.

Conflict of Interest

The company TTP plc received funding from the company Lumito AB for developing an immunochemical labeling protocol based on UCNP.

Acknowledgements

We thank Vít Vykoukal for taking TEM images, Kamil Mikulášek and Zbyněk Zdráhal for LC-MS/MS analysis, Thomas Hirsch for providing the equipment for DLS measurements, Uliana Kostiv for advices regarding the functionalization of UCNP, Wayne Bowen and Verity Jackson from the company TTP for the discussions on ICC and IHC, Simone Rink for sharing experience regarding the ICC workflow, and Julian Brandmeier for the help with the ICC experiments. H.H.G. acknowledges funding from the German Research Foundation (DFG: GO 1968/5-1 and GO 1968/7-1, Heisenberg Program). Z.F., Z.M., and P.S. acknowledge financial support from the Ministry of Education, Youth and Sports of the Czech Republic (MEYS CR) under the projects CEITEC 2020 (LQ1601) and INTER-ACTION (LTAB19011). W.X. acknowledges funding from Lumito AB. This work was further supported by the Czech Science Foundation projects 18-03367Y (to A.H.) and 17-05957S (to P.B.¹, P.B.², and P.S.). CIISB research infrastructure project LM2015043, funded by MEYS CR, is acknowledged for

financial support of the measurements at CF Cryo-electron Microscopy and Tomography, and CF Proteomics.

VIII.6. References

1. F. Bray, J. Ferlay, I. Soerjomataram, R. L. Siegel, L. A. Torre and A. Jemal, *CA-Cancer J. Clin.*, 2018, **68**, 394-424.
2. O. Gluz, C. Liedtke, N. Gottschalk, L. Pusztai, U. Nitz and N. Harbeck, *Ann. Oncol.*, 2009, **20**, 1913-1927.
3. S. Dawood, K. Broglio, A. U. Buzdar, G. N. Hortobagyi and S. H. Giordano, *J. Clin. Oncol.*, 2010, **28**, 92-98.
4. H. A. Burris, H. S. Rugo, S. J. Vukelja, C. L. Vogel, R. A. Borson, S. Limentani, E. Tan-Chiu, I. E. Krop, R. A. Michaelson, S. Girish, L. Amler, M. X. Zheng, Y. W. Chu, B. Klencke and J. A. O'Shaughnessy, *J. Clin. Oncol.*, 2011, **29**, 398-405.
5. S. M. Swain, S. B. Kim, J. Cortes, J. Ro, V. Semiglazov, M. Campone, E. Ciruelos, J. M. Ferrero, A. Schneeweiss, A. Knott, E. Clark, G. Ross, M. C. Benyunes and J. Baselga, *Lancet Oncol.*, 2013, **14**, 461-471.
6. J. S. Ross, E. A. Slodkowska, W. F. Symmans, L. Pusztai, P. M. Ravdin and G. N. Hortobagyi, *Oncologist*, 2009, **14**, 320-368.
7. M. Titford, *Biotech. Histochem.*, 2005, **80**, 73-78.
8. P. K. Nakane and G. B. Pierce, *J. Histochem. Cytochem.*, 1966, **14**, 929-931.
9. A. H. Coons, H. J. Creech, R. N. Jones and E. Berliner, *J. Immunol.*, 1942, **45**, 159-170.
10. E. A. Susaki and H. R. Ueda, *Cell Chem. Biol.*, 2016, **23**, 137-157.
11. M. V. Yezhelyev, X. Gao, Y. Xing, A. Al-Hajj, S. M. Nie and R. M. O'Regan, *Lancet Oncol.*, 2006, **7**, 657-667.
12. J. L. Dong, L. N. Song, J. J. Yin, W. W. He, Y. H. Wu, N. Gu and Y. Zhang, *ACS Appl. Mater. Interfaces*, 2014, **6**, 1959-1970.
13. T. R. Nayak, C. Andreou, A. Oseledchyk, W. D. Marcus, H. C. Wong, J. Massague and M. F. Kircher, *Nanoscale*, 2017, **9**, 1110-1119.
14. E. M. Brey, Z. Lalani, C. Johnston, M. Wong, L. V. McIntire, P. J. Duke and C. W. Patrick, *J. Histochem. Cytochem.*, 2003, **51**, 575-584.
15. L. Fan, Y. Y. Tian, R. Yin, D. D. Lou, X. Z. Zhang, M. Wang, M. Ma, S. H. Luo, S. Y. Li, N. Gu and Y. Zhang, *Nanoscale*, 2016, **8**, 8553-8558.
16. K. Bera, K. A. Schalper, D. L. Rimm, V. Velcheti and A. Madabhushi, *Nat. Rev. Clin. Oncol.*, 2019, **16**, 703-715.
17. J. Griffin and D. Treanor, *Histopathology*, 2017, **70**, 134-145.
18. H. Zijlmans, J. Bonnet, J. Burton, K. Kardos, T. Vail, R. S. Niedbala and H. J. Tanke, *Anal. Biochem.*, 1999, **267**, 30-36.
19. M. Wang, C. C. Mi, W. X. Wang, C. H. Liu, Y. F. Wu, Z. R. Xu, C. B. Mao and S. K. Xu, *ACS Nano*, 2009, **3**, 1580-1586.

20. L. Zhou, R. Wang, C. Yao, X. M. Li, C. L. Wang, X. Y. Zhang, C. J. Xu, A. J. Zeng, D. Y. Zhao and F. Zhang, *Nat. Commun.*, 2015, **6**, 6938.
21. C. Y. Liu, Y. F. Qi, R. R. Qiao, Y. Hou, K. Y. Chan, Z. Q. Li, J. Y. Huang, L. H. Jing, J. Du and M. Y. Gao, *Nanoscale*, 2016, **8**, 12579-12587.
22. S. W. Wu, G. Han, D. J. Milliron, S. Aloni, V. Altoe, D. V. Talapin, B. E. Cohen and P. J. Schuck, *Proc. Natl. Acad. Sci. U.S.A.*, 2009, **106**, 10917-10921.
23. M. Haase and H. Schafer, *Angew. Chem. Int. Ed.*, 2011, **50**, 5808-5829.
24. V. Poláčková, M. Pastucha, Z. Mikušová, M. J. Mickert, A. Hlaváček, H. H. Gorris, P. Skládal and Z. Farka, *Nanoscale*, 2019, **11**, 8343-8351.
25. M. J. Mickert, Z. Farka, U. Kostiv, A. Hlaváček, D. Horák, P. Skládal and H. H. Gorris, *Anal. Chem.*, 2019, **91**, 9435-9441.
26. A. Sedlmeier and H. H. Gorris, *Chem. Soc. Rev.*, 2015, **44**, 1526-1560.
27. Q. Q. Zhan, J. Qian, H. J. Liang, G. Somesfalean, D. Wang, S. L. He, Z. G. Zhang and S. Andersson-Engels, *ACS Nano*, 2011, **5**, 3744-3757.
28. H. He, C. B. Howard, Y. H. Chen, S. H. Wen, G. G. Lin, J. J. Zhou, K. J. Thurecht and D. Y. Jin, *Anal. Chem.*, 2018, **90**, 3024-3029.
29. U. Kostiv, V. Lobaz, J. Kučka, P. Švec, O. Sedláček, M. Hrubý, O. Janoušková, P. Francová, V. Kolářová, L. Šefc and D. Horák, *Nanoscale*, 2017, **9**, 16680-16688.
30. F. Wang, Y. Han, C. S. Lim, Y. H. Lu, J. Wang, J. Xu, H. Y. Chen, C. Zhang, M. H. Hong and X. G. Liu, *Nature*, 2010, **463**, 1061-1065.
31. O. Dukhno, F. Przybilla, V. Muhr, M. Buchner, T. Hirsch and Y. Mely, *Nanoscale*, 2018, **10**, 15904-15910.
32. G. T. Hermanson, *Bioconjugate Techniques (Second Edition)*, Academic Press, New York, 2008.
33. Z. Farka, M. J. Mickert, A. Hlaváček, P. Skládal and H. H. Gorris, *Anal. Chem.*, 2017, **89**, 11825-11830.
34. A. Sedlmeier, A. Hlaváček, L. Birner, M. J. Mickert, V. Muhr, T. Hirsch, P. Corstjens, H. J. Tanke, T. Soukka and H. H. Gorris, *Anal. Chem.*, 2016, **88**, 1835-1841.
35. C. A. Schneider, W. S. Rasband and K. W. Eliceiri, *Nat. Methods*, 2012, **9**, 671-675.
36. H. J. Hathaway, K. S. Butler, N. L. Adolphi, D. M. Lovato, R. Belfon, D. Fegan, T. C. Monson, J. E. Trujillo, T. E. Tessier, H. C. Bryant, D. L. Huber, R. S. Larson and E. R. Flynn, *Breast Cancer Res.*, 2011, **13**, R108.
37. K. Subik, J.-F. Lee, L. Baxter, T. Strzepek, D. Costello, P. Crowley, L. Xing, M.-C. Hung, T. Bonfiglio, D. G. Hicks and P. Tang, *Breast Cancer Basic Clin. Res.*, 2010, **4**, 35-41.
38. M. Jež, T. Bas, M. Veber, A. Košir, T. Dominko, R. Page and P. Rožman, *Histochem. Cell Biol.*, 2013, **139**, 195-204.

VIII.7. Supporting Information

Materials and Methods

Chemicals and Reagents

Alendronate (pharmaceutical grade), neridronate, 5-azidopentanoic acid (APA), (1R,8S,9s)-bicyclo[6.1.0]non-4-yn-9-ylmethyl *N*-succinimidyl carbonate (BCN-NHS), 5(6)-carboxyfluorescein (FAM), 5-carboxyrhodamine *N*-succinimidyl ester (Rh-NHS), nitrosyl tetrafluoroborate (NOBF₄), bovine γ -globulin (BGG), bovine serum albumin (BSA), biotinylated BSA (BSA-biotin), *N*-(3-dimethylaminopropyl)-*N'*-ethylcarbodiimide (EDC), *N*-hydroxysulfosuccinimide sodium salt (sulfo-NHS), copper(II) sulfate pentahydrate, L-ascorbic acid sodium salt, DAPI, Tween 20, and 2-(*N*-morpholino)ethanesulfonic acid (MES) were purchased from Merck (Germany). Dry dimethylformamide (DMF), streptavidin, and SuperBlock TBS (SB) were obtained from Thermo Fisher Scientific (USA). Streptavidin-azide was obtained from 7 Bioscience (Germany). α -*N*-hydroxysuccinimide- ω -alkyne polyethylene glycol (*M*_w 3000, Alkyne-PEG-NHS) was purchased from Iris Biotech (Germany). α -amino- ω -carboxy polyethylene glycol (*M*_w 5000, NH₂-PEG-COOH) was purchased from Rapp Polymere (Germany). Poly(vinyl alcohol) (PVA; 6 kDa) was purchased from Polysciences (USA). All other common chemicals were obtained in the highest quality available from Merck or Carl Roth (Germany). Dialysis buffer consisted of 100 mM H₃BO₃, 80 mM Na₂CO₃, pH 9.4.

Synthesis and Conjugation of UCNPs

Synthesis of UCNPs

YCl₃ · 6 H₂O (728 mg, 2.1 mmol), YbCl₃ · 6 H₂O (209 mg, 0.54 mmol), and TmCl₃ · 6 H₂O (23 mg, 0.06 mmol) were dissolved in methanol (20 mL) and added into a 100-mL three-neck round-bottom flask containing oleic acid (9 g) and 1-octadecene (19.7 g). The solution was heated to 160 °C for 30 min under an N₂ atmosphere and then cooled to 50 °C. Then, the protective atmosphere was disconnected, and the solution of NH₄F (445 mg, 12.0 mmol) and NaOH (300 mg, 7.5 mmol) in methanol (20 mL) was added to the intensively stirred solution. The N₂ atmosphere was reconnected, and the solution was stirred for 30 min. The temperature was carefully increased up to 150 °C, avoiding extensive boiling to ensure the evaporation of methanol. After that, the solution was rapidly heated using the rate of ~10 °C per minute. At 300 °C, the heating was carefully regulated to 305 °C within two or three minutes. The flask was kept under N₂ flow at 305 °C for 150 min. The fluctuation of temperature was \pm 3 °C during this time. Finally, the flask was placed on another stirrer and rapidly cooled to room temperature under air flux. The resulting nanoparticles were precipitated by adding isopropanol (30 mL) and collected by centrifugation (1,000 g, 10 min). The pellet was washed

with methanol (30 mL), centrifuged (1,000 g, 10 min), and dispersed in cyclohexane (20 mL). By adding methanol (100 mL), the nanoparticles precipitated rapidly without the need for centrifugation. The precipitate was dispersed in cyclohexane (30 mL) and slowly centrifuged (50 g, 20 min) to separate coarse particles from the final product.¹

Preparation of SA-PEG-Alen-UCNP Conjugate

NH₂-PEG-COOH ($M_w = 5000$, 32 mg, 3.2 mM) was dissolved in 2 mL PBS (0.1 M, pH 7.4) followed by the addition of BCN-NHS in DMF (40 μ L, 5.54 mg, 475 mM). The reaction mixture was incubated at 4 °C overnight. The resulting BCN-PEG-COOH was dialyzed for 48 h in a Float-A-Lyzer dialysis device (MWCO = 500–1000 Da) against ddH₂O (1.8 L, 6 \times exchanged) at 4 °C and 24 h against MES buffer (100 mM, 0.5 M NaCl, pH 6.0, 200 mL, 3 \times exchanged). The purified BCN-PEG-COOH was activated by the addition of EDC (12 mg, 8 mM) and sNHS (20 mg) for 15 min. Alendronate (5 mg) dissolved in NaOH (1 M, 50 μ L) was added to the activated PEG linker, incubated 4 h at room temperature, and then overnight at 4 °C. The resulting BCN-PEG-Alen was dialyzed 72 h in a Float-A-Lyzer dialysis device (MWCO = 500–1000 Da) against ddH₂O (2 \times exchanged per day). The purified product was stored at 4 °C.²

For the preparation of SA-PEG-Alen-UCNPs, oleic acid capped UCNPs (10 mg) in cyclohexane were mixed with an equivalent amount of DMF, followed by the addition of NOBF₄ (approx. 1 mg per mg UCNPs). UCNPs were incubated for 20 min at 30 °C while shaking. The cyclohexane phase was removed, and the particles precipitated by adding an excess of chloroform. UCNPs were purified by centrifugation (1000 g, 5 min), redispersed in DMF, precipitated with chloroform and separated by centrifugation (1000 g, 5 min). An aqueous solution of BCN-PEG-Alen (750 μ L, 16 mg/mL) was added to the UCNP pellet followed by 1 min sonication and 24 h incubation at room temperature. BCN-PEG-Alen-UCNPs were dialyzed for 48 h against Tris/borate (200 mL, 50 mM Tris, 50 mM borate, pH 8.6, 6 \times exchanged) in a Float-A-Lyzer G2 dialysis device (MWCO = 100 kDa).

For the preparation of SA-PEG-Alen-UCNPs, streptavidin azide (1 mg/mL, 100 μ L) was added to a dispersion of BCN-PEG-Alen-UCNPs (10 mg, 750 μ L) in Tris/borate buffer and the mixture was dialyzed in a Float-A-Lyzer G2 dialysis device (MWCO = 500-1000 Da) overnight against MES (250 mL, 100 mM, pH 4.5, 3 \times exchanged). For purification, the mixture was dialyzed in Float-A-Lyzer G2 (MWCO = 100 kDa) for 48 h at 4 °C against 500 mL of TBS (1 mM KF, 0.05% NaN₃, 6 \times exchanged). The purified SA-PEG-Alen-UCNPs were stored at 4 °C.

Preparation of SA-BSA-UCNP Conjugate

The SA-BSA-UCNP conjugates were prepared according to our previous work.³ In the synthesis, click-reactive BSA-alkyne conjugate was first prepared and bound to carboxylated silica-coated UCNPs,⁴ followed by copper-free click reaction with click-reactive streptavidin-azide.

To prepare the fluorescent click-reactive BSA-alkyne conjugate, 2.92 mg of BCN-NHS was dissolved in 20 μL of DMF and mixed with 1.72 mg of Rh-NHS dissolved in 100 μL of DMF. Afterward, the solution was mixed with 1880 μL of dialysis buffer with 132 mg of BSA for 4 h. The conjugate was dialyzed four times overnight against 500 mL of dialysis buffer.

For the preparation of click-reactive UCNPs, 1 mg of carboxylated UCNPs was centrifuged (1700 *g*, 10 min) and redispersed in 200 μL of 100 mM sodium MES, 30 mM Na_2CO_3 , pH 6.0 with 0.4 mg of EDC and 0.2 mg of sulfo-NHS and the dispersion was sonicated for 10 min. Afterwards, the activated UCNPs were centrifuged (3300 *g*, 1 min) and immediately redispersed in 200 μL of 100 mM sodium MES, 30 mM Na_2CO_3 , pH 6.0 containing 0.5 mg of BSA-alkyne. After 90 min of mixing at room temperature, the UCNP-BSA-alkyne conjugate was centrifuged and redispersed five times in 50 mM Tris with 50 mM H_3BO_3 pH 8.6 (1700 *g*, 15 min, 200 μL of buffer).

To prepare fluorescent click-reactive streptavidin-azide, free carboxyl groups of APA and FAM were first activated using EDC/sulfo-NHS chemistry. The 1.4 mg of APA was dissolved in 100 μL of DMF and mixed with 100 μL of 100 mM sodium MES, pH 6.1 containing 3.8 mg of EDC and 4.3 mg of sulfo-NHS and the solution was shaken for 1 h at room temperature. The 1.5 mg of FAM was dissolved in 100 μL of DMF and mixed with 400 μL of 100 mM sodium MES, pH 6.1 containing 15 mg of EDC and 3.5 mg of sulfo-NHS. After 1 h of reaction, 50 μL of activated FAM and 20 μL of activated APA solutions were mixed together with 5.2 mg of streptavidin dissolved in 60 μL of dialysis buffer. The solution was mixed for 4 h at room temperature, followed by five times overnight dialysis against 500 mL of dialysis buffer.⁵

To perform the copper-free click-conjugation reaction, 1 mg of click-reactive UCNP-BSA-alkyne was centrifuged (1700 *g*, 15 min), and the pellet was redispersed with 2.5 mg of click-reactive streptavidin-azide in 500 μL of dialysis buffer. The solution was dialyzed four times overnight against 250 mL of 100 mM sodium MES, pH 4.5. The change of pH enabled electrostatic attraction of the UCNPs with streptavidin and allowed an efficient click-conjugation. The final SA-BSA-UCNP conjugates were centrifuged (1700 *g*, 15 min), redispersed in 50 mM Tris, 50 mM H_3BO_3 , pH 8.6 to a final concentration of 5 mg/mL and stored at 4 $^\circ\text{C}$.⁶

Characterization of UCNPs and their Conjugates

Transmission Electron Microscopy

A 6 μL droplet of oleic acid-capped UCNPs dispersed in cyclohexane was placed on a 400-mesh copper EM grid coated with a continuous carbon layer and incubated at room temperature for 5 min. Afterwards, the droplet was removed, and the adsorbed particles on dried grids were imaged by transmission electron microscope Tecnai F20 (FEI, Czech Republic). The dimensions of individual particles were analyzed using ImageJ imaging software (National Institutes of Health, USA).⁷

Emission Spectra Measurement

Emission spectra were measured in an Aminco Bowman 2 spectrofluorometer (SLM Aminco, USA) using a 980 nm continuous-wave laser excitation (4 W) that was fiber-coupled into the device in a 90° angle to the detector. A UCNP dispersion (1 mg/mL, 500 μL) in cyclohexane was transferred into a fused silica cuvette, and the high voltage of the detector was adjusted to prevent detector saturation. The emission spectra were measured in 2 nm steps from 300 to 950 nm and a scan rate of 2 nm/s.

Dynamic Light Scattering and Nanoparticle Tracking Analysis

The hydrodynamic diameters of UCNPs and conjugates were determined by DLS using Zetasizer Nano ZS (Malvern, UK). The dispersion of 7 $\mu\text{g/mL}$ of oleic acid capped UCNPs (in cyclohexane) and bioconjugate (in TBS) was used for the characterization.

The concentration of the conjugate and hydrodynamic properties were also studied using NTA. The dispersion of UCNPs in TBS buffer was injected into the measurement cell of the NanoSight NS300 (Malvern, UK), and the tracking was performed at 25 °C as three cycles per 60 s.

Single-Particle Upconversion Microscopy

Single-particle upconversion microscopy was used to evaluate the intensity distribution of the conjugates. No. 1 glass cover slips (1.5 \times 1.5 cm^2) were cleaned by piranha solution (3:1 mixture of concentrated sulfuric acid and 30% hydrogen peroxide; 20 min), washed with deionized water and modified by cationized bovine serum albumin (cBSA; 200 μL , 20 min). After washing with deionized water, the slide was incubated with UCNPs (0.7 $\mu\text{g/mL}$) for 20 min, washed again with deionized water, and dried with nitrogen.⁸

The cover slips were mounted with glycerol and imaged using an upconversion microscope with 40 \times objective. The images were taken with 5 s exposure time, and the mean intensities of the individual UCNPs were determined in the microscope software (NIS elements, Nikon) by

placing regions of interest (ROIs) of identical sizes over the luminescent spots. Mean intensities of 400 randomly selected UCNP were measured and background corrected, frequency count was performed, and the data were arranged in a histogram.

LC-MS/MS Analysis

The successful conjugation of streptavidin to the surface of UCNP was further verified by LC-MS/MS. The samples of conjugate (100 μ L, 3.5 mg/mL) were washed twice by 200 μ L of 50 mM ammonium bicarbonate buffer (AB), followed by resuspending in 15 μ L of AB. The proteins were digested by trypsin (1 μ g) for 2 h at 37 °C. Afterward, the UCNP were removed by centrifugation (14,000 g, 10 min) and the resulting peptides were extracted using acetonitrile (addition of acetonitrile was followed by vortexing of the sample and evaporation of acetonitrile by rotary evaporator to a final volume of 15 μ L).³

The LC-MS/MS analysis was performed using RSLCnano with a Q-TOF detector (Thermo Fisher Scientific, USA). The 65-min LC gradient was used for LC-MS analyses; MS and MS/MS spectra were recorded in a time of flight analyzer (TOF). The MS/MS data were processed using Proteome Discoverer software (version 1.4; Thermo Fisher Scientific, USA). The search engine Mascot (version 2.6; Matrix Science, USA) was used to search the cRAP contaminant database (version 181122; The Global Proteome Machine Organization), which contains 112 protein sequences, including the target sequence of streptavidin (P22629-cRAP). Peptide confidence was assessed based on Mascot expectation value, only peptides with high confidence value ($p < 0.01$) were considered for final data evaluation.

Testing of Conjugate Functionality in BSA-Biotin Assay

A 96-well microtiter plate (μ Clear, high binding, Greiner Bio-One, Austria) was coated with 100 μ L of BSA-biotin in coating buffer (50 mM $\text{NaHCO}_3/\text{Na}_2\text{CO}_3$, 0.05% NaN_3 , pH 9.6) at 4 °C overnight. Afterwards, the plate was washed four times with 250 μ L of washing buffer and blocked for 1 h with 200 μ L of concentrated SuperBlock with 0.05% Tween 20. After four washing steps, 100 μ L of the UCNP conjugate sample was added and incubated for 1 h. Finally, the plate was washed four times and allowed to dry.⁹

The readout was performed using Hidex Chameleon reader. Each well was scanned in a rectangular grid of 8×8 pixels with 1 s exposure time per pixel and a scanning step size of 0.1 mm. The truncated average of the luminescence intensities was calculated, excluding the 16 highest and the 16 lowest values. Averages and standard deviations were calculated from the truncated averages of three independent wells.¹⁰

The immunoassay for the testing of the SA-FAM was performed using the same experimental conditions, except switching the UCNP conjugate for SA-FAM conjugate. The readout was

performed using Labrox reader. Each well was scanned in the grid of 8×8 pixels, with an exposure time of 500 ms and step size 0.1 mm. The data evaluation was performed in the same way as in the case of upconversion scans.

Preparation of Fluorescent Streptavidin

The 1.5 mg of FAM was dissolved in 100 μL of DMF and mixed with 400 μL of 100 mM sodium MES, pH 6.1 containing 15 mg of EDC and 3.5 mg of sulfo-NHS. After 1 h of reaction, 50 μL of activated FAM was mixed with 20 μL of MES buffer and 5.2 mg of streptavidin dissolved in 60 μL of dialysis buffer. The solution was mixed for 4 h at room temperature, followed by five times overnight dialysis against 500 mL of dialysis buffer.^{3,5}

Results and Discussion

Characterization of Labels

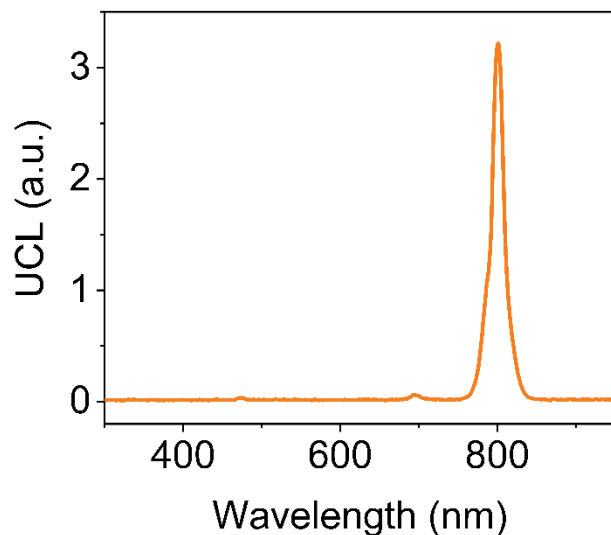


Figure S1: Upconversion luminescence spectrum of Tm^{3+} -doped UCNPs under 980 nm excitation.

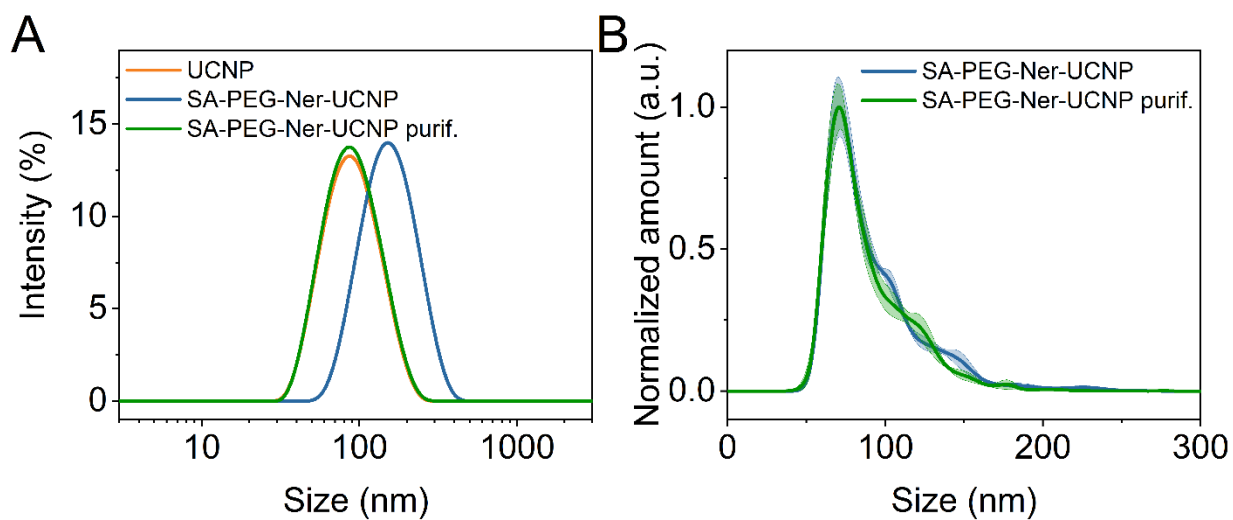


Figure S2: **A)** DLS of oleic acid-capped UCNPs in cyclohexane, SA-PEG-Ner-UCNP conjugate in Tris buffer and purified SA-PEG-Ner-UCNP conjugate in Tris buffer. **B)** NTA of non-purified and purified SA-PEG-Ner-UCNP conjugate.

Table S1: Proteins found in the SA-PEG-Ner-UCNP conjugate by LC-MS/MS.

Protein family	Accession ID	Description	Score	Num. of sequences	emPAI
1	P22629-cRAP	Streptavidin (cRAP) OS= <i>Streptomyces avidinii</i> PE=1 SV=1	4522	6 ^a	1.46
2	P04264-cRAP	Keratin, type II cytoskeletal 1 (cRAP) OS= <i>Homo sapiens</i> GN=KRT1 PE=1 SV=6	1321	19	1.30
3	P35527-cRAP	Keratin, type I cytoskeletal 9 (cRAP) OS= <i>Homo sapiens</i> GN=KRT9 PE=1 SV=3	840	18	1.32
4	iRT-fusion-cRAP	iRT Kit Fusion - real (cRAP)	501	9	4.88
5	P00761-cRAP	Trypsin (cRAP) OS= <i>Sus scrofa</i> PE=1 SV=1	464	4	0.6
6	Q8N1N4-cRAP	Keratin, type II cytoskeletal 78 (cRAP) OS= <i>Homo sapiens</i> GN=KRT78 PE=2 SV=2	76	3	0.17
7	P02662-cRAP-B6E	Alpha-S1-casein (cRAP-B6E) OS= <i>Bos taurus</i> GN=CSN1S1 PE=1 SV=2	54	1	0.12
8	P15252-cRAP	Rubber elongation factor protein (cRAP) OS= <i>Hevea brasiliensis</i> PE=1 SV=2	50	1	0.21
9	P02769-cRAP-B6E	Serum albumin (cRAP-B6E) OS= <i>Bos taurus</i> GN=ALB PE=1 SV=4	37	2	0.09
10	Q5D862-cRAP	Filaggrin-2 (cRAP) OS= <i>Homo sapiens</i> GN=FLG2 PE=1 SV=1	29	1	0.01
11	Q02413-cRAP	Desmoglein-1 (cRAP) OS= <i>Homo sapiens</i> GN=DSG1 PE=1 SV=2	22	1	0.03

^a Protein sequence coverage: 44%.

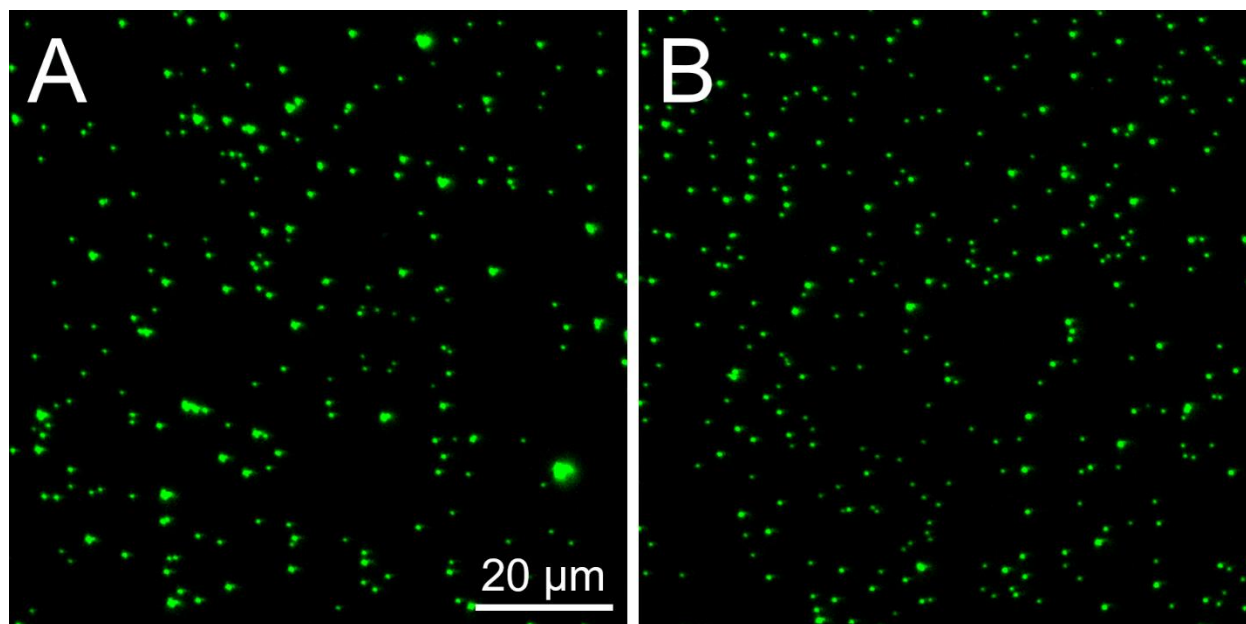


Figure S3: Upconversion microscopy images of **A)** non-purified and **B)** purified SA-PEG-Ner-UCNP conjugates.

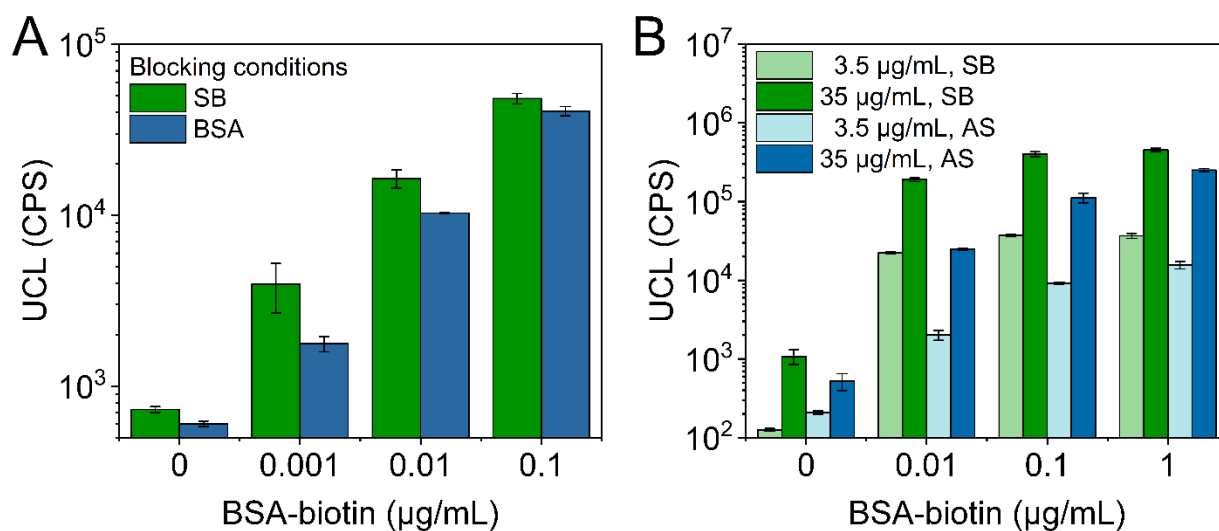


Figure S4: Functional characterization of the SA-PEG-Ner-UCNP conjugate in the BSA-biotin ULISA assay. **A)** Optimization of blocking conditions with UCNP label in concentration of 35 $\mu\text{g/mL}$, SB – 10% SuperBlock in Tris buffer, BSA – 1% BSA in Tris buffer. **B)** Optimization of SA-PEG-Ner-UCNP label dilution and buffer, SB – 10% SuperBlock in Tris, AS – assay buffer. The error bars correspond to the standard deviation of three wells.

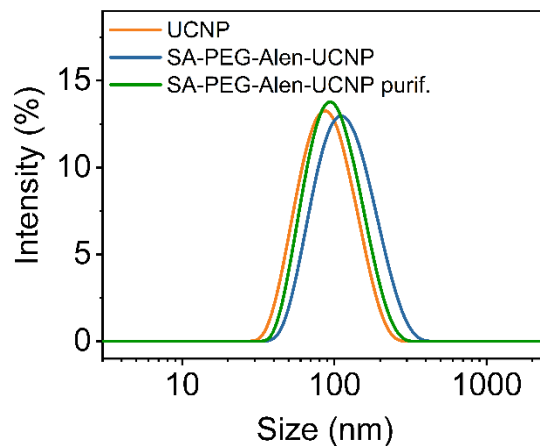


Figure S5: DLS of oleic acid-capped UCNPs in cyclohexane, SA-PEG-Alen-UCNP in Tris buffer, and purified SA-PEG-Alen-UCNP conjugate in Tris buffer.

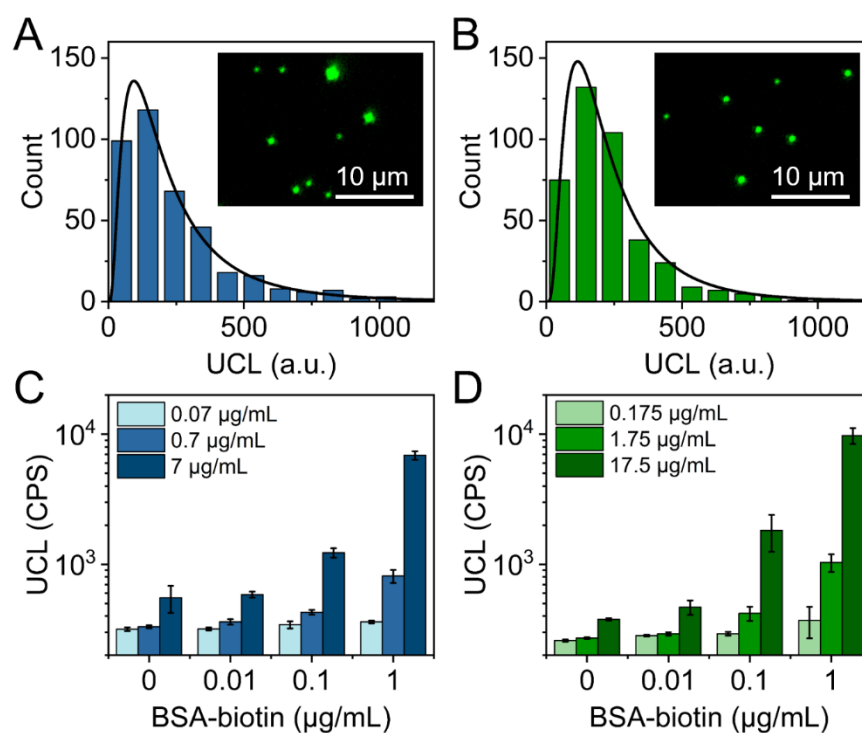


Figure S6: Characterization of the SA-PEG-Alen-UCNP conjugate. Brightness distribution of **A)** non-purified and **B)** purified conjugate. The insets show the upconversion microscopy images. Functional characterization of **C)** non-purified and **D)** purified conjugates in BSA-biotin assay. The error bars correspond to the standard deviation of three wells.

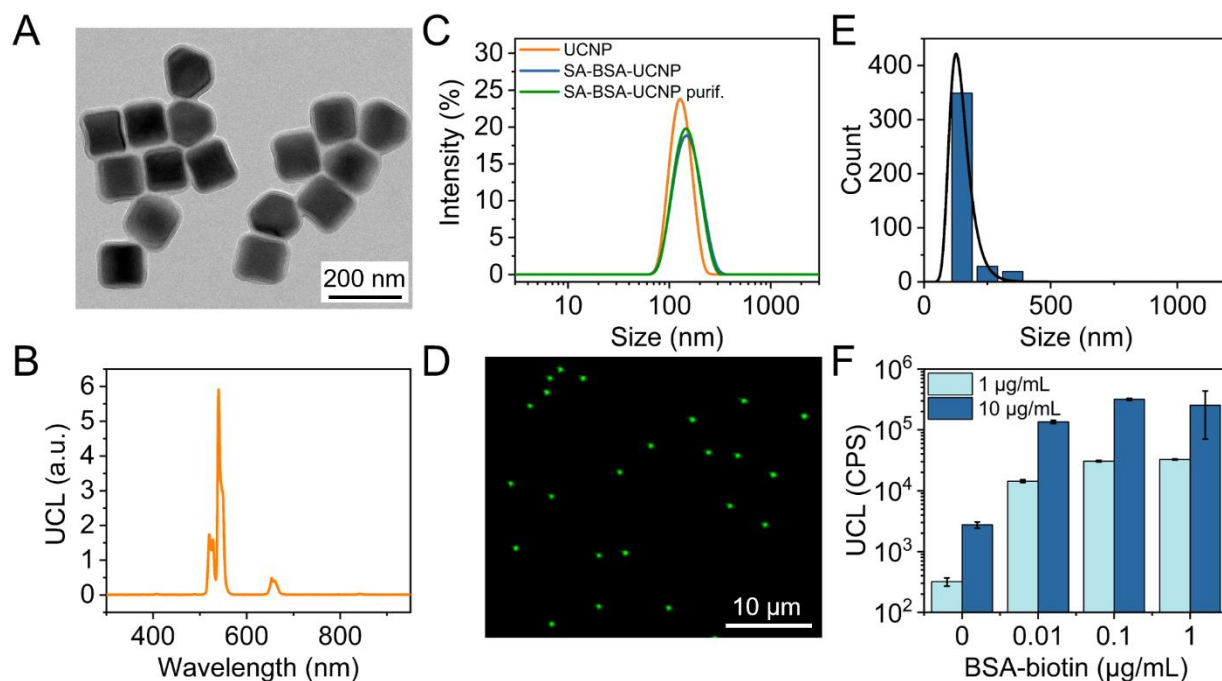


Figure S7: **A)** TEM image of silica-coated Er^{3+} -doped UCNPs; **B)** upconversion luminescence spectrum (980 nm excitation) of silica-coated UCNPs; **C)** DLS of silica-coated UCNPs, SA-BSA-UCNP conjugate, and purified SA-BSA-UCNP conjugate. **D)** Upconversion microscopy image of non-purified SA-BSA-UCNP conjugate, and **E)** brightness intensity distribution. **F)** Functional characterization of SA-BSA-UCNP conjugate in BSA-biotin assay. The error bars correspond to the standard deviation of three wells.

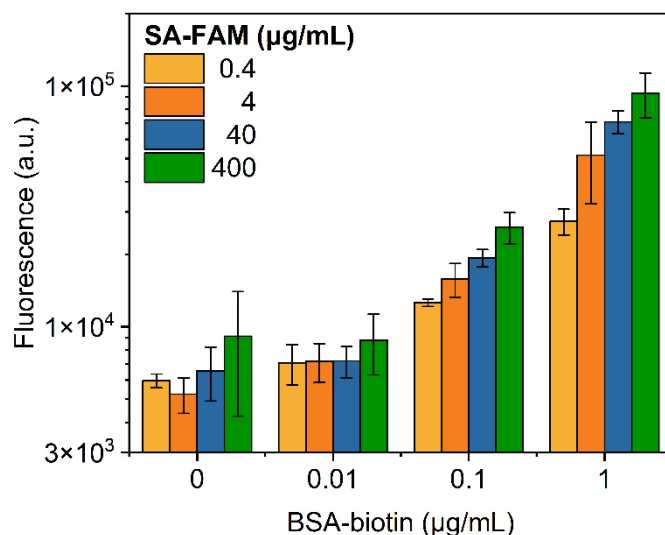


Figure S8: Binding of the streptavidin-carboxyfluorescein (SA-FAM) conjugate to BSA-biotin adsorbed on the surface of microtiter plate. The error bars correspond to the standard deviation of three wells.

ICC based on UCNP Labels

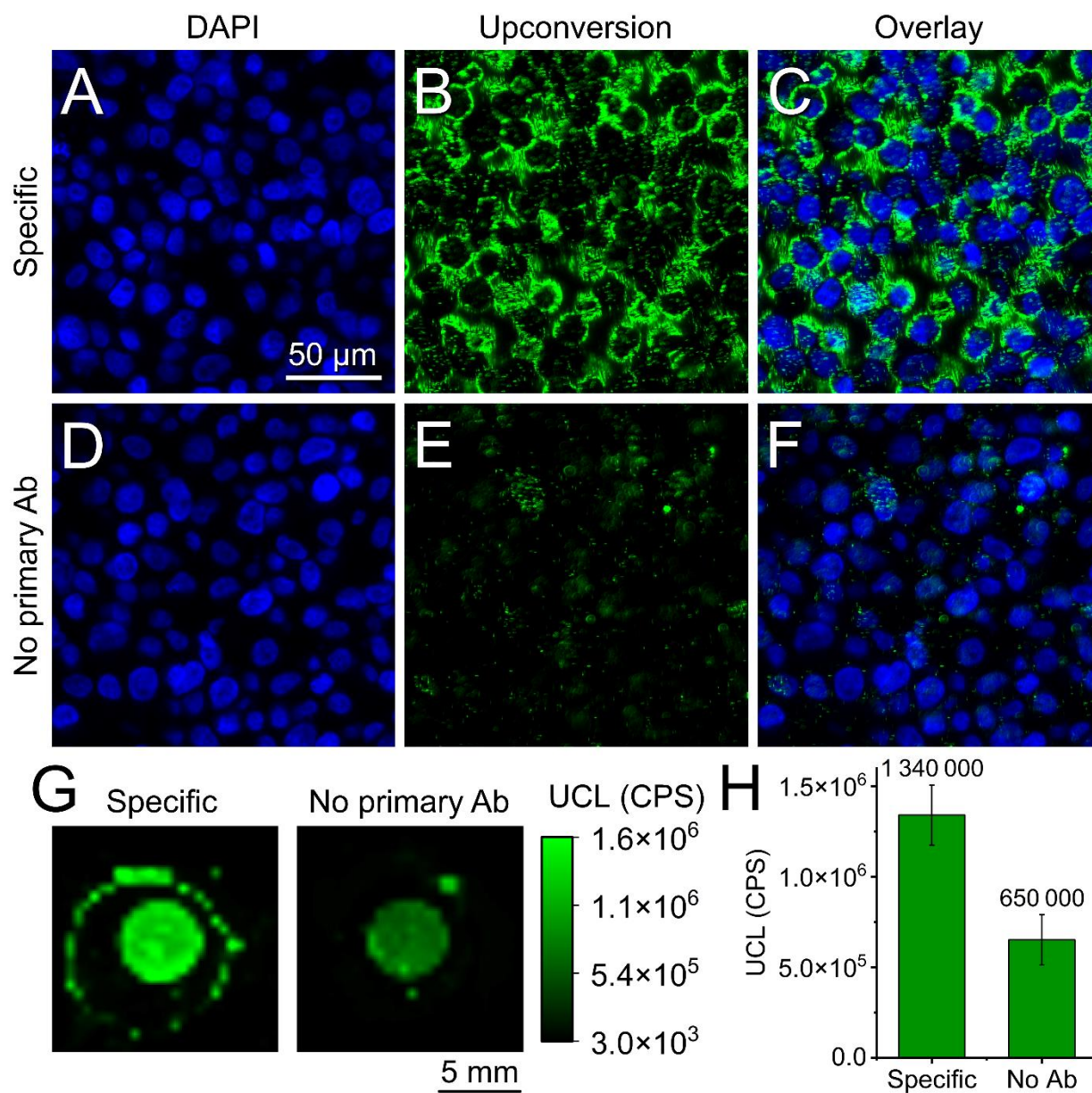


Figure S9: ICC staining of HER2-positive FFPE cells using SA-BSA-UCNP conjugate: **A)** DAPI channel, **B)** upconversion channel, **C)** overlay. Negative control: **D)** DAPI, **E)** upconversion, **F)** overlay. **G)** Upconversion scan of the cell pellets; **H)** average upconversion intensities. The error bars correspond to the standard deviations of intensities in the cell pellet.

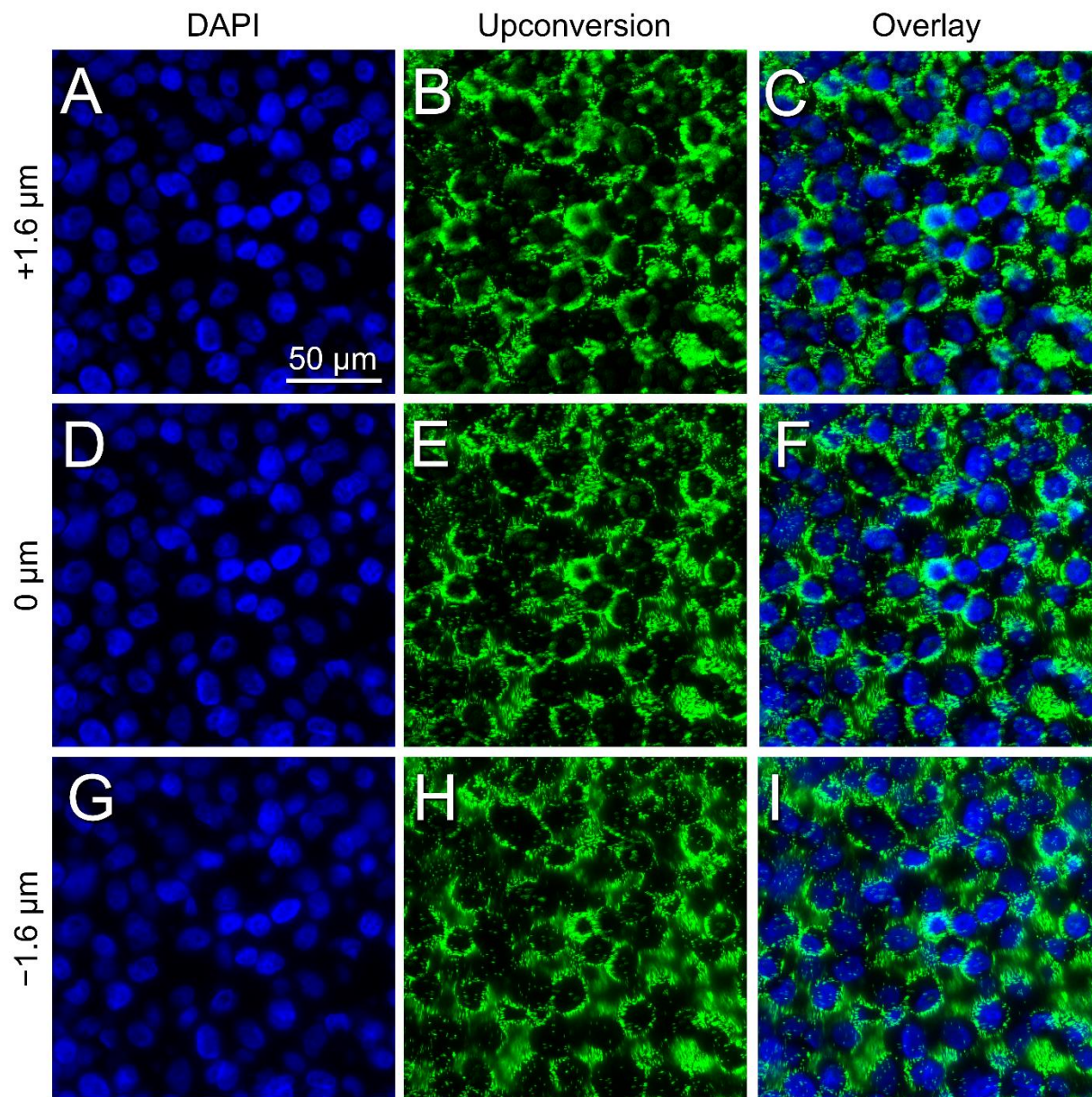


Figure S10: ICC staining of HER2-positive cells measured SA-BSA-UCNP label measured at three focus heights. Focus +1.6 μm: **A)** DAPI, **B)** upconversion, **C)** overlay. Focus 0 μm: **D)** DAPI, **E)** upconversion, **F)** overlay. Focus -1.6 μm: **G)** DAPI, **H)** upconversion, **I)** overlay.

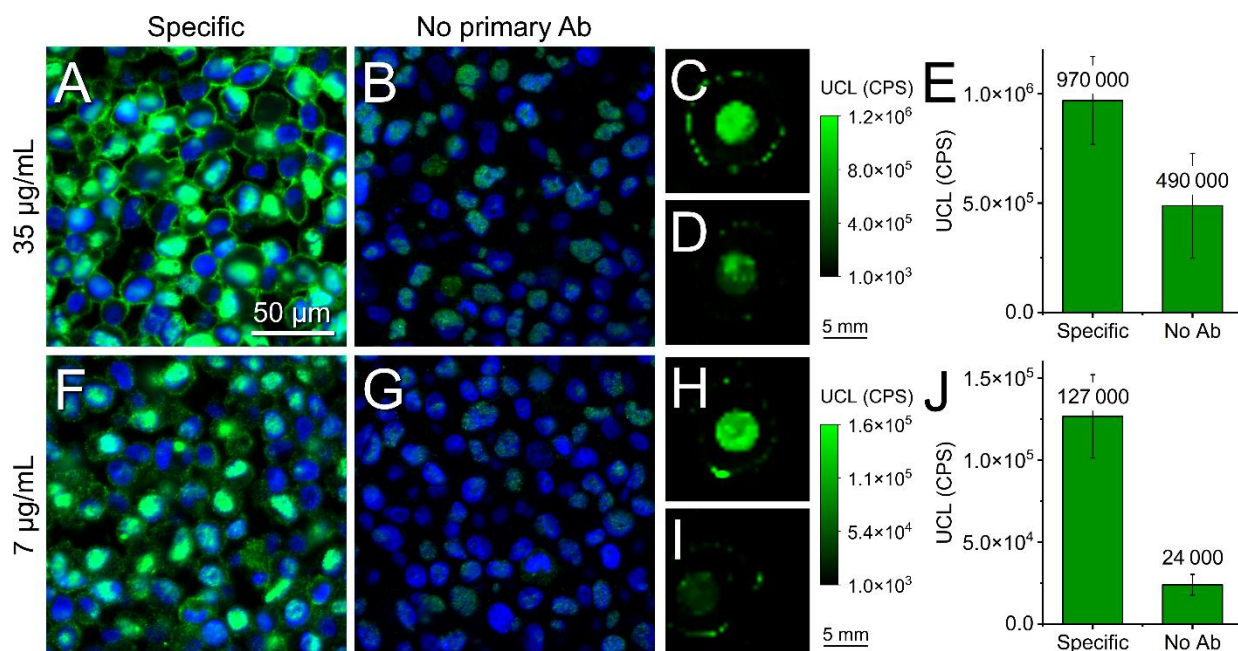


Figure S11: The effect of SA-PEG-Alen-UCNP label concentration on ICC staining of BT-474 cells. Overlay images (DAPI and upconversion channels) of label in the concentration of 35 µg/mL in **A**) specific binding and **B**) negative control. Upconversion scan of the cell pellet for **C**) specific binding and **D**) negative control; **E**) average upconversion intensities. Overlay images of label in the concentration of 7 µg/mL in **F**) specific binding and **G**) negative control. Upconversion scan of the cell pellet for **H**) specific binding and **I**) negative control; **J**) average upconversion intensities. The error bars correspond to the standard deviations of intensities in the cell pellet.

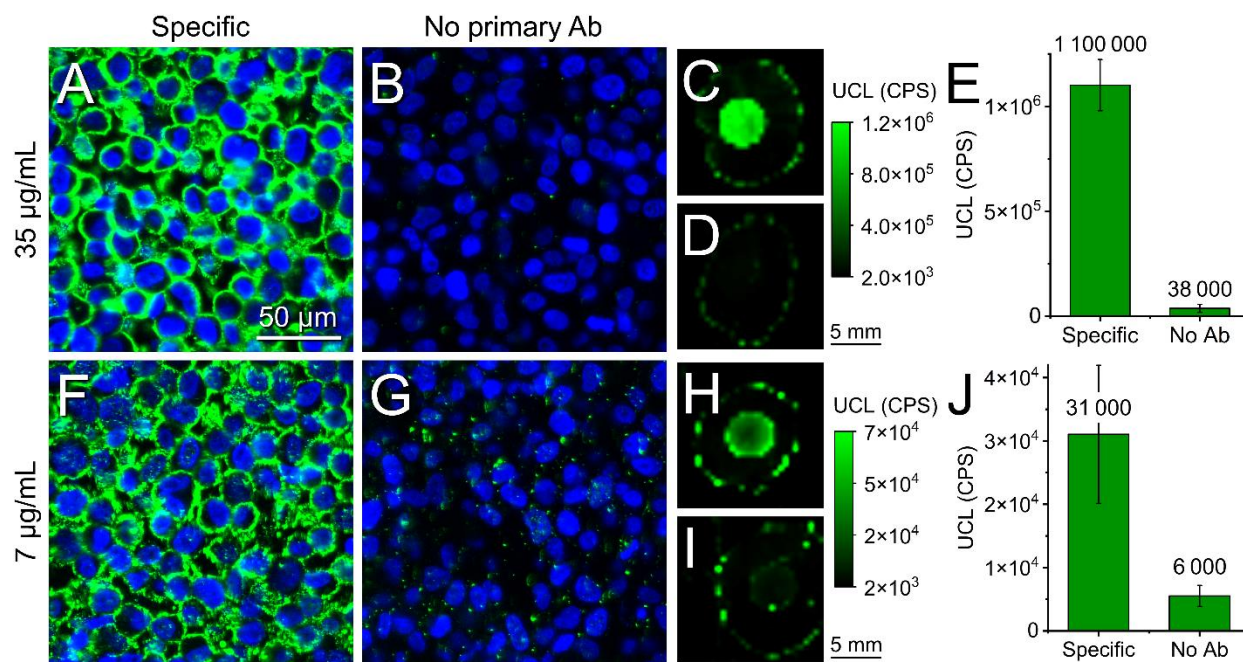


Figure S12: The effect of non-purified SA-PEG-Ner-UCNP label concentration on ICC staining of BT-474 cells. Overlay images (DAPI and upconversion channels) of label in the concentration of 35 µg/mL in **A**) specific binding and **B**) negative control. Upconversion scan of the cell pellet for **(C)** specific binding and **(D)** negative control; **E**) average upconversion intensities. Overlay images of label in the concentration of 7 µg/mL in **F**) specific binding and **G**) negative control. Upconversion scan of the cell pellet for **H**) specific binding and **I**) negative control; **J**) average upconversion intensities. The error bars correspond to the standard deviations of intensities in the cell pellet.

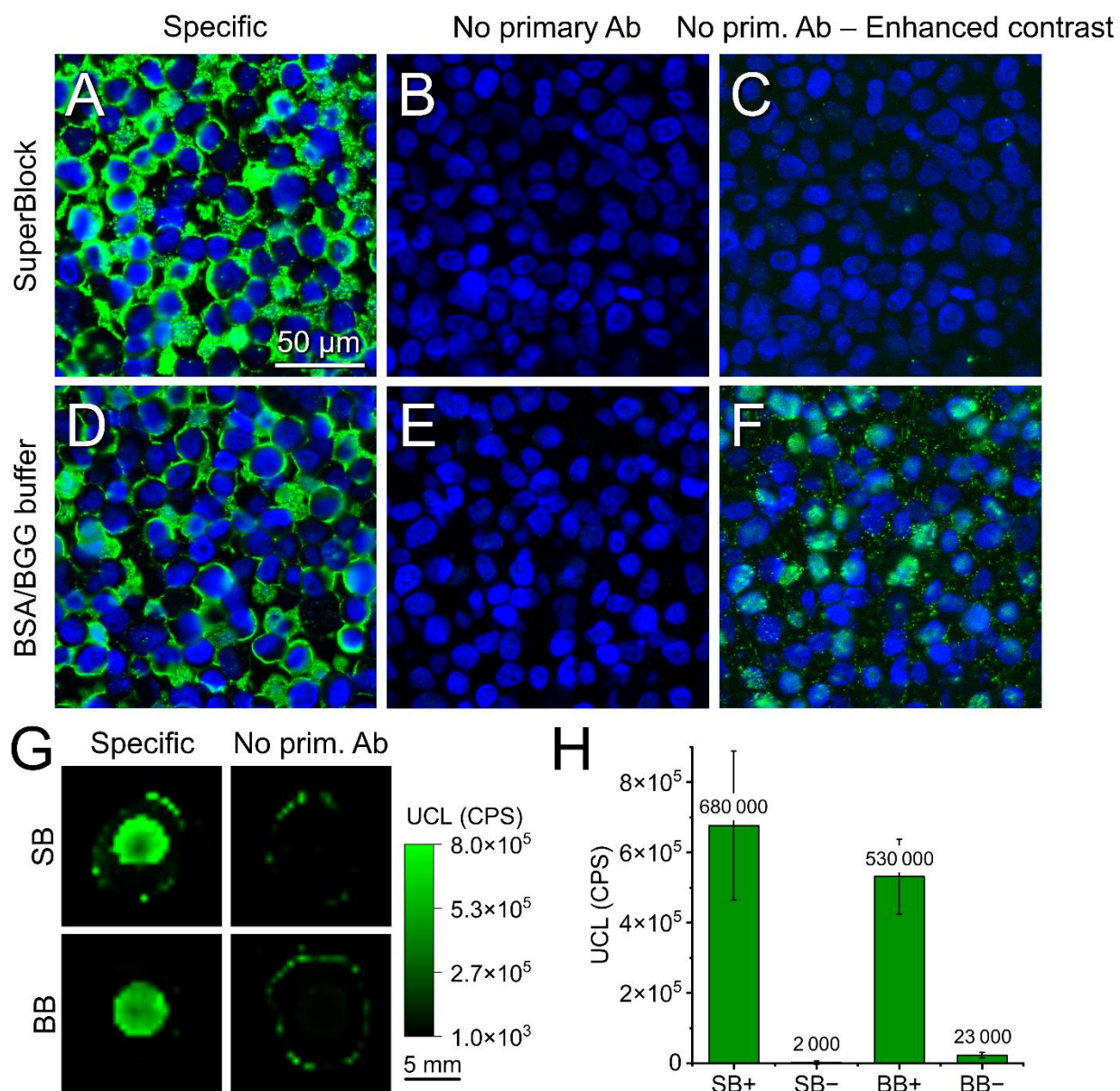


Figure S13: The effect of blocking conditions on ICC staining of BT-474 cells using SA-PEG-Ner-UCNPs. Overlay images (DAPI and upconversion) of cells blocked by SuperBlock: **A)** specific binding, **B)** negative control, **C)** negative control with enhanced contrast; and by BSA/BGG assay buffer: **D)** specific, **E)** negative, **F)** negative with enhanced contrast. **G)** Upconversion scan of the cell pellets, SB – SuperBlock, AS – assay buffer; **H)** average upconversion intensities. The error bars correspond to standard deviations of intensities in cell pellet.

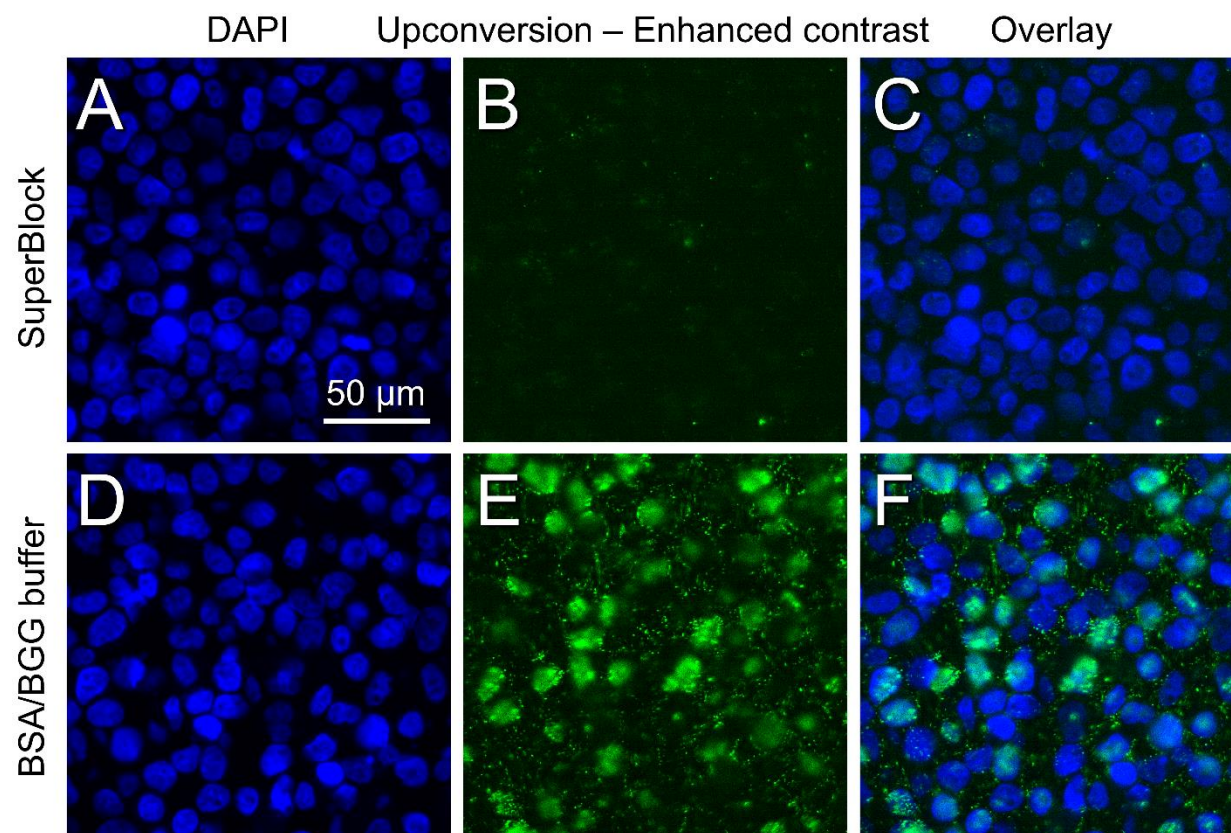


Figure S14: The effect of blocking conditions on the negative control (without primary antibody) in ICC staining of BT-474 cells blocked by SuperBlock: **A)** DAPI channel, **B)** upconversion channel with enhanced contrast, **C)** Overlay; and BSA/BGG buffer **D)** DAPI, **E)** upconversion, **F)** overlay.

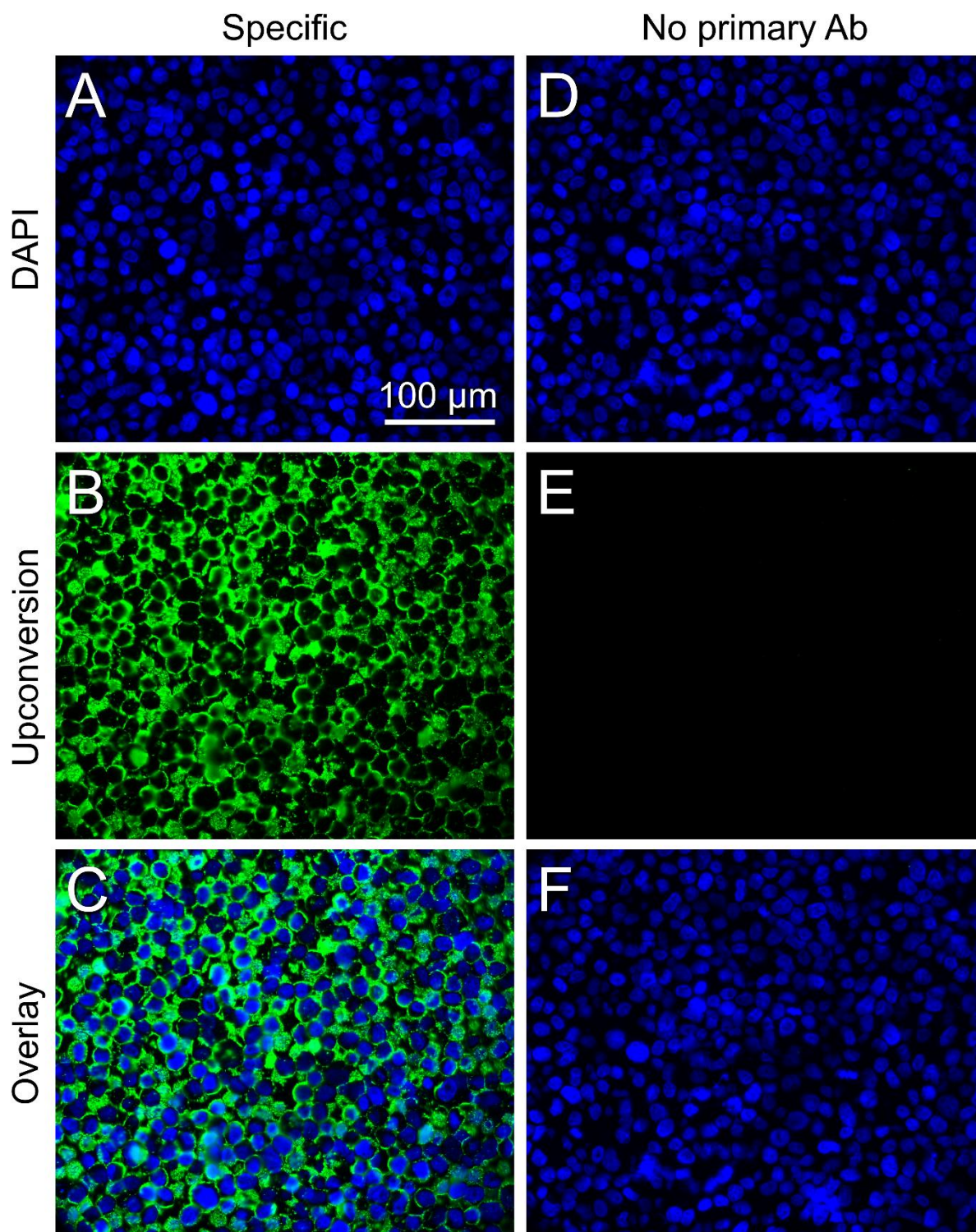


Figure S15: ICC staining of HER2-positive FFPE cells using SA-PEG-Ner-UCNPs: **A)** DAPI channel, **B)** upconversion channel, **C)** overlay. Negative control: **D)** DAPI, **E)** upconversion, **F)** overlay.

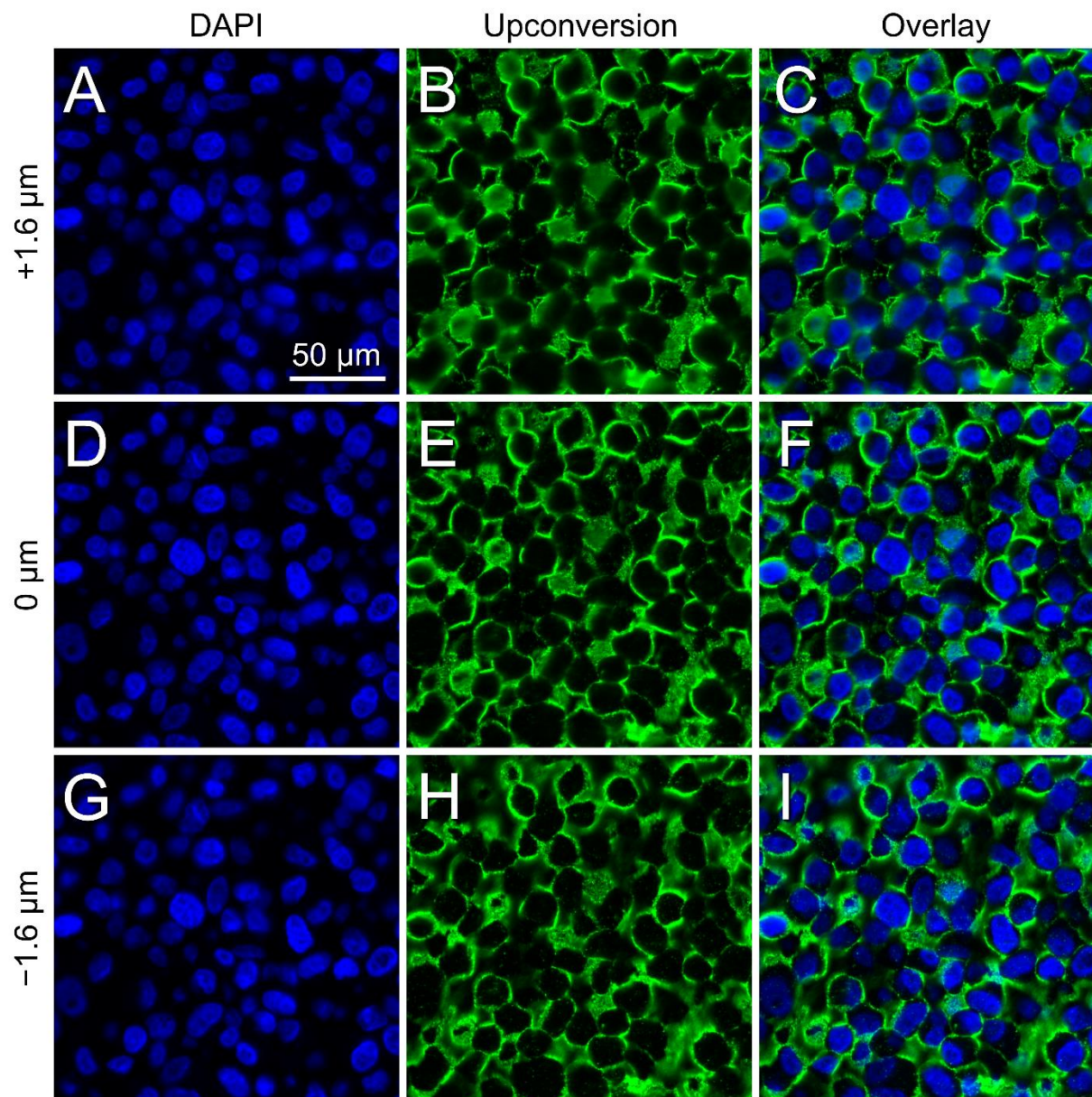


Figure S16: ICC staining of HER2-positive cells measured using SA-PEG-Ner-UCNPs measured at three focus heights. Focus +1.6 μm: **A)** DAPI, **B)** upconversion, **C)** overlay. Focus 0 μm: **D)** DAPI, **E)** upconversion, **F)** overlay. Focus -1.6 μm: **G)** DAPI, **H)** upconversion, **I)** overlay.

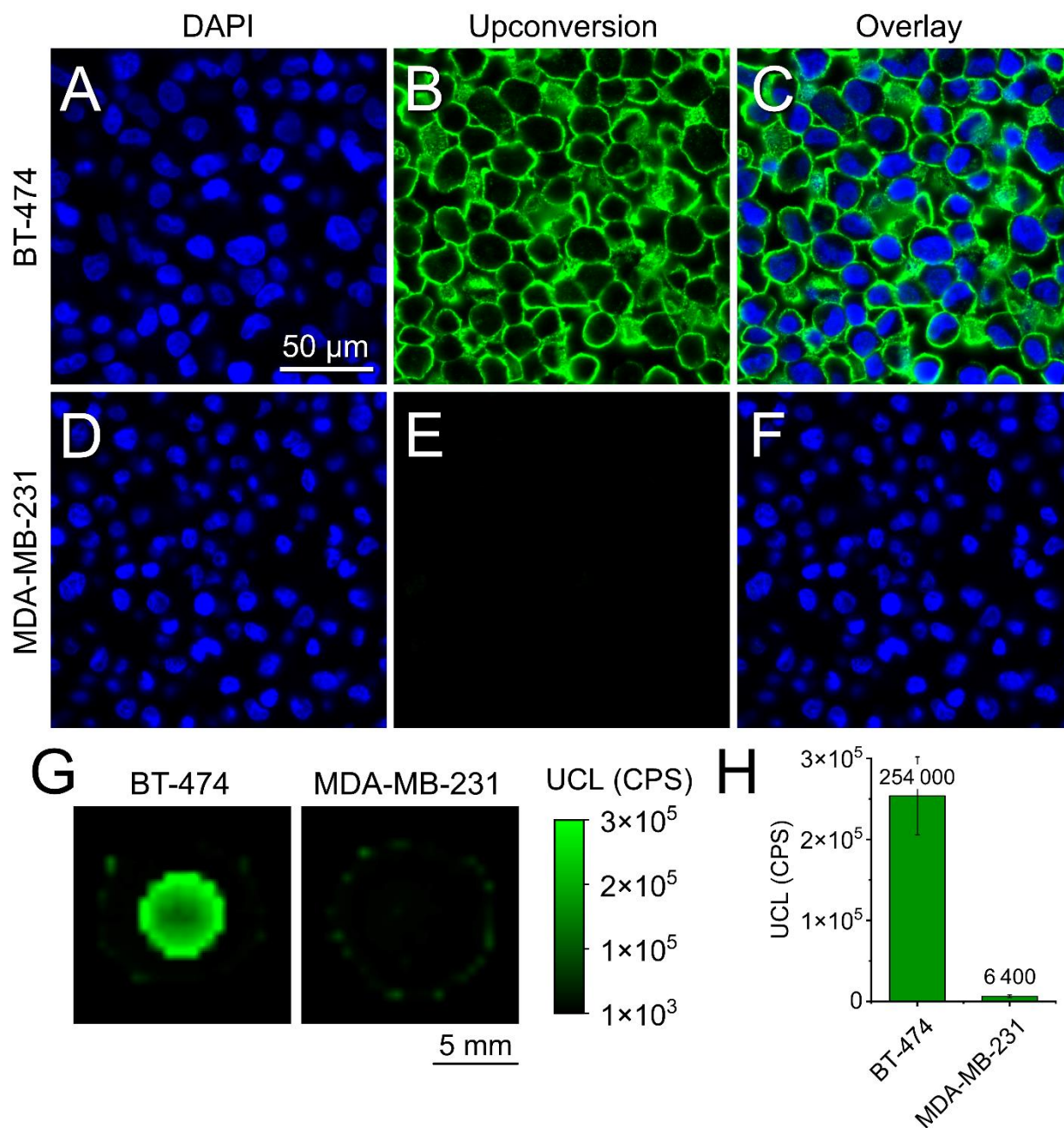


Figure S17: ICC staining of HER2-positive BT-474 cells and HER2-negative MDA-MB-231 cells using SA-PEG-Ner-UCNP label. BT-474 cells: **A)** DAPI channel, **B)** upconversion channel, **C)** overlay. MDA-MB-231 cells: **D)** DAPI channel, **E)** upconversion channel, **F)** overlay. **G)** Upconversion scan of the cell pellets; **H)** average upconversion intensities. The error bars correspond to the standard deviations of three independent cell pellets.

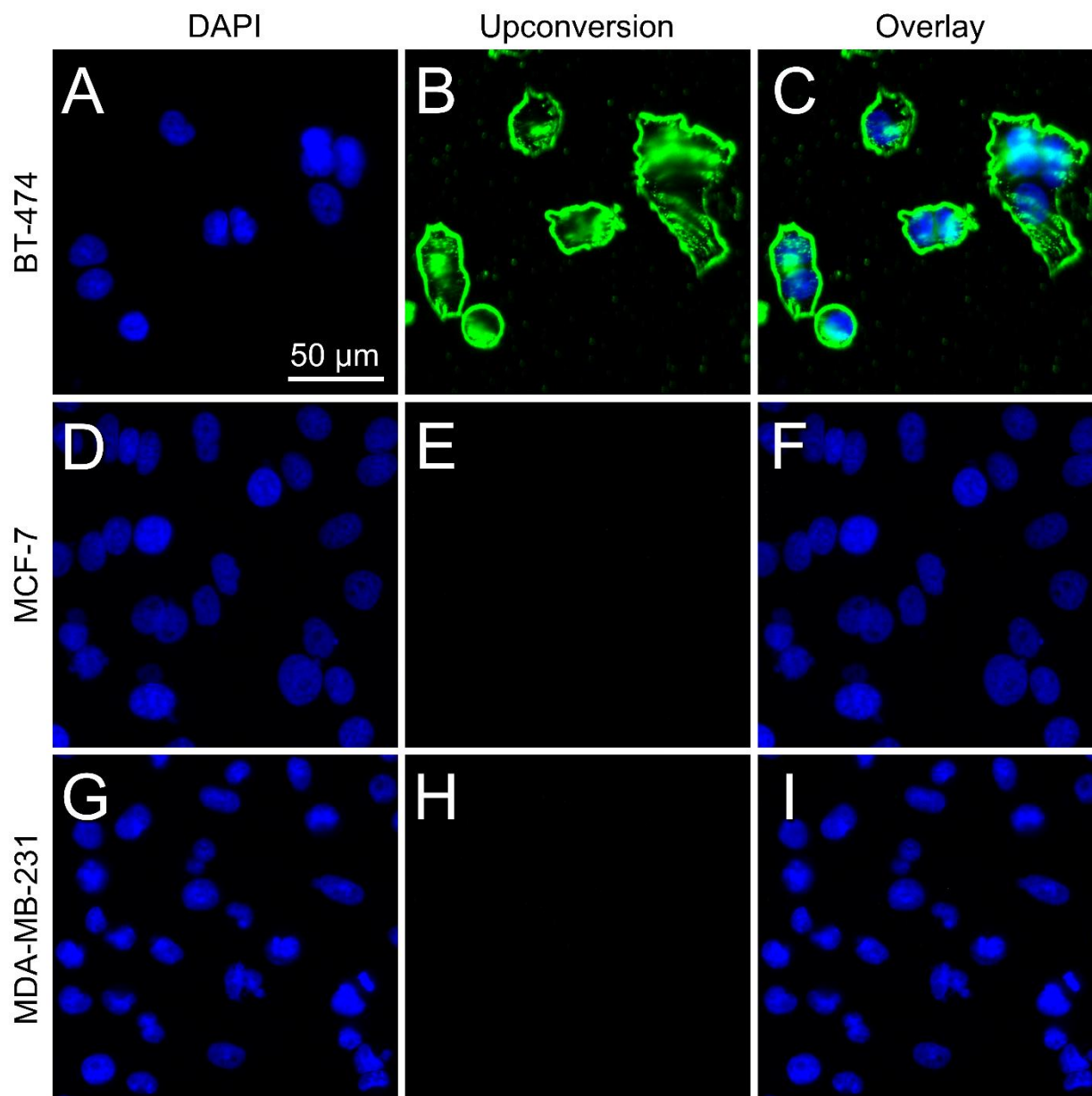


Figure S18: ICC staining of freshly cultivated cells using SA-PEG-Ner-UCNP of BT-474 cells: **A)** DAPI channel, **B)** upconversion channel, **C)** overlay; MCF-7 cells **D)** DAPI, **E)** upconversion, **F)** overlay; MDA-MB-231: **G)** DAPI, **H)** upconversion; **I)** overlay.

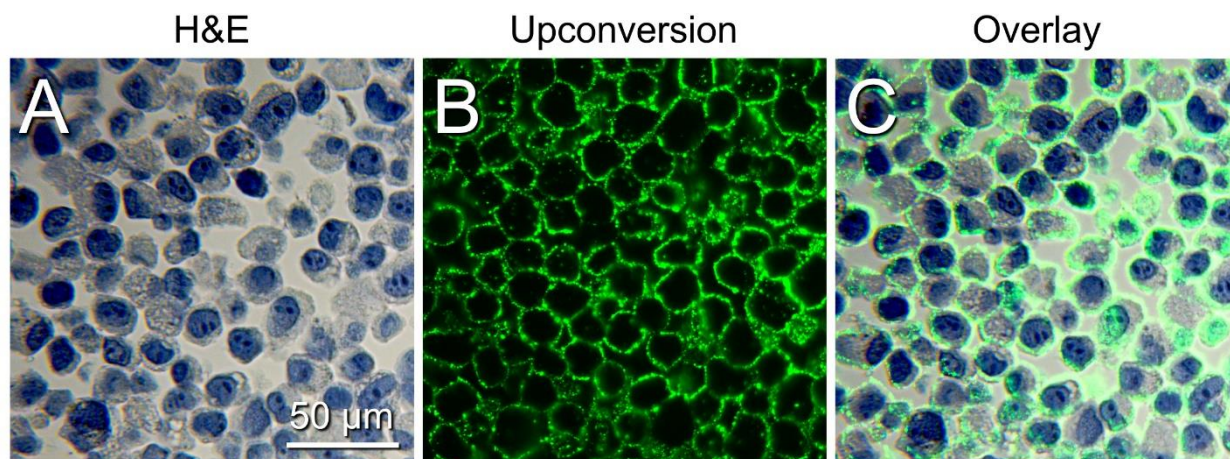


Figure S19: ICC staining of HER2-positive BT-474 cells with H&E counterstain. **A)** Bright-field channel (H&E), **B)** upconversion channel, **C)** overlay.

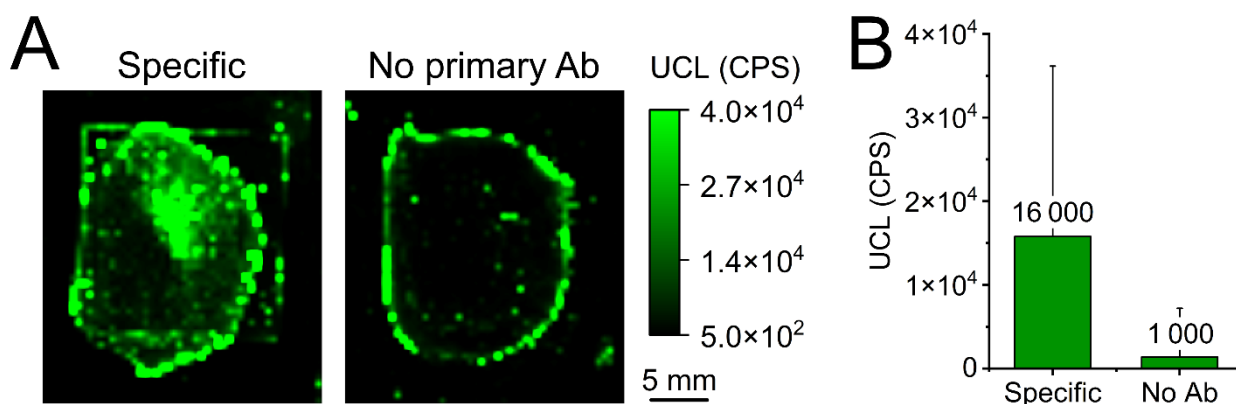


Figure S20: **A)** Upconversion intensity scans of the breast cancer tissue sections labeled with SA-PEG-Ner-UCNPs. **B)** Average upconversion intensities. The error bars indicate the standard deviations of intensities in the cell pellet.

ICC based on Fluorescent Labels

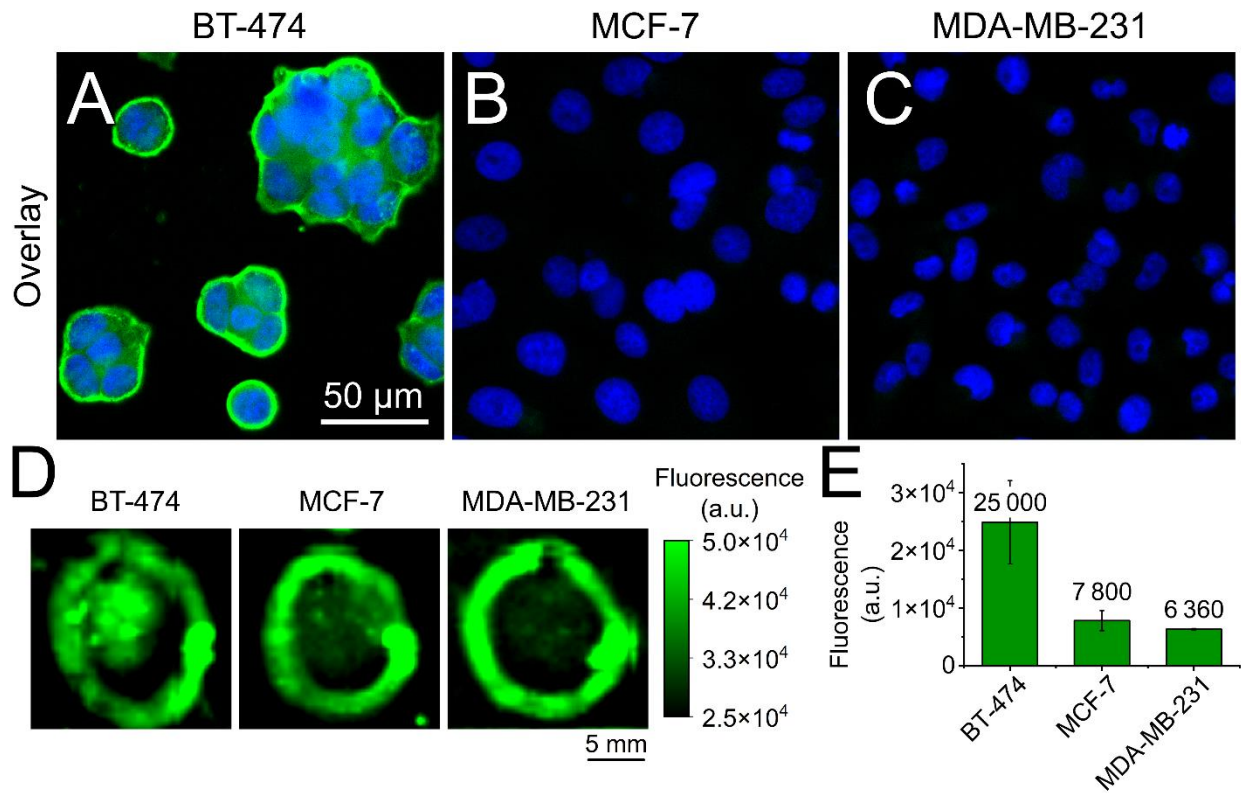


Figure S19: ICC staining of freshly cultivated cells using SA-FAM. Overlay images (DAPI and fluorescence) of cell lines: **A)** BT-474, **B)** MCF-7, **C)** MDA-MB-231. **D)** Fluorescence intensity scan, **E)** average fluorescence intensities measured in the cell pellets. The error bars correspond to the standard deviation of three independent cell pellets.

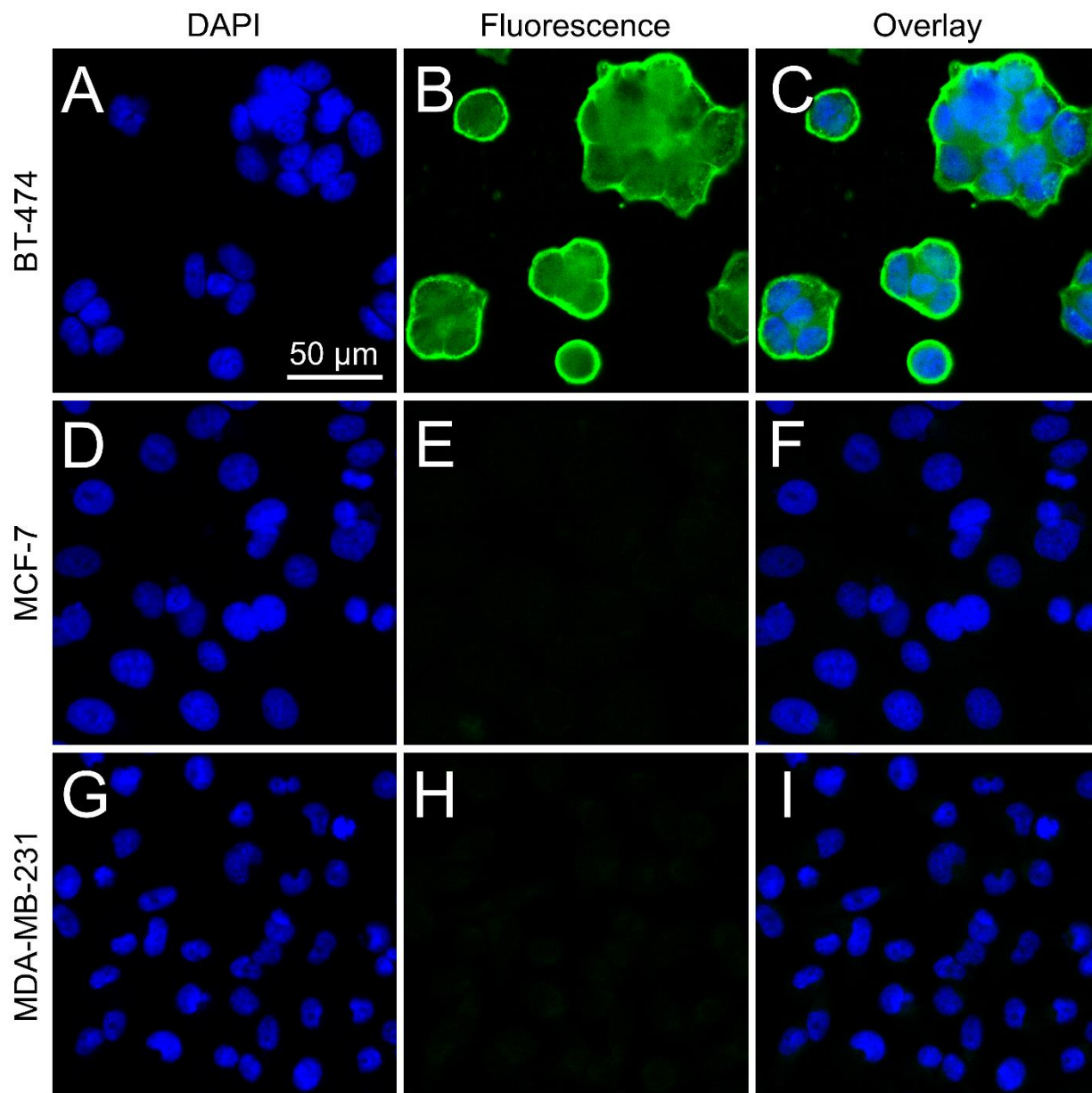


Figure S20: ICC staining of freshly cultivated of BT-474 cells using SA-FAM: **A)** DAPI channel, **B)** fluorescein channel, **C)** overlay; MCF-7 cells **D)** DAPI, **E)** fluorescein, **F)** overlay; MDA-MB-231: **G)** DAPI, **H)** fluorescein; **I)** overlay.

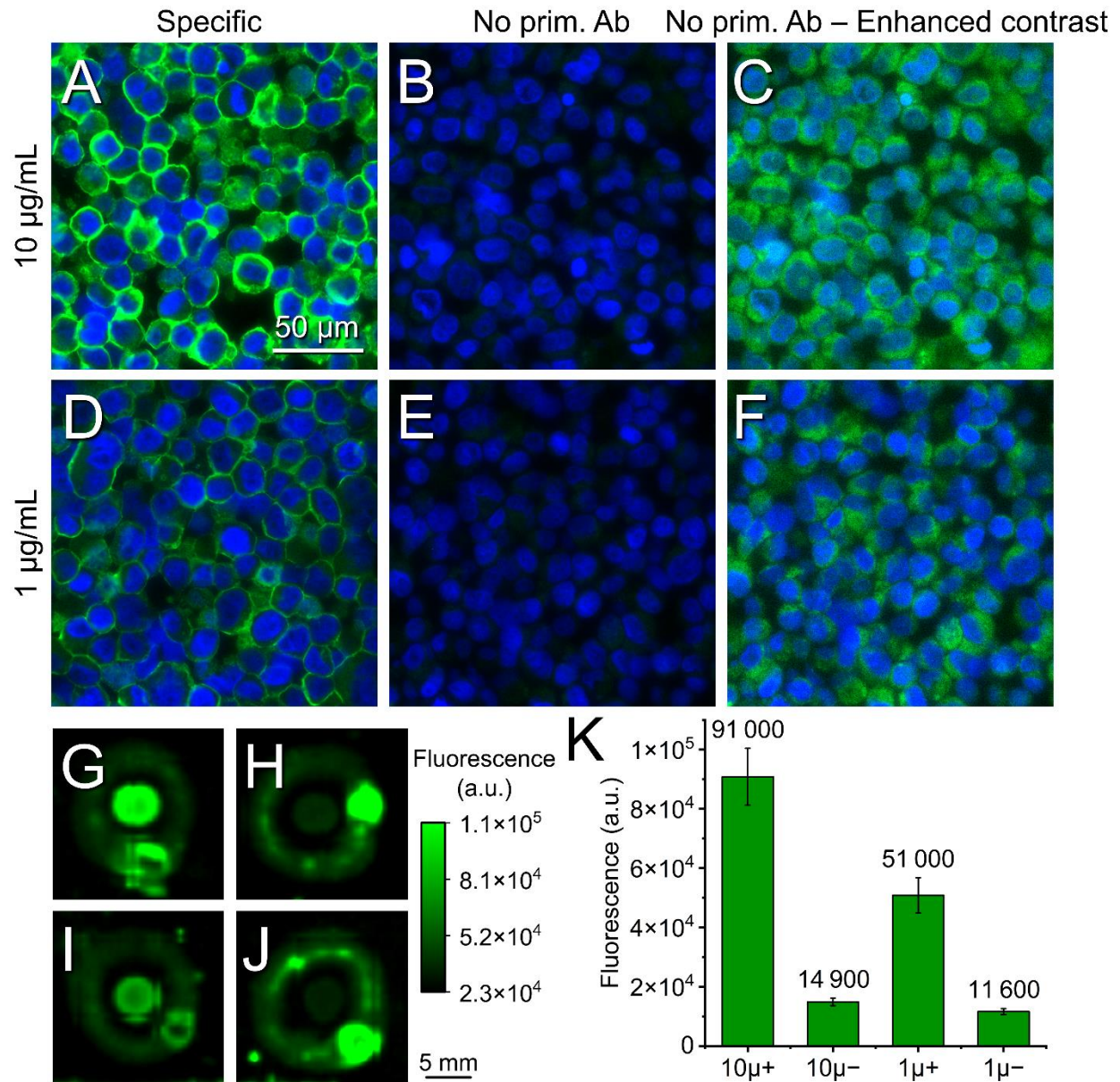


Figure S21: ICC staining of FFPE BT-474 cell pellets using SA-FAM in concentration of 10 µg/mL **A)** specific, **B)** negative control, **C)** negative control with enhanced contrast and 1 µg/mL **D)** specific, **E)** negative control, **F)** negative control. 2D fluorescence intensity scans (fluorescein channel) of: **G)** 10 µg/mL specific, **H)** 10 µg/mL negative; **I)** 1 µg/mL specific; **J)** 10 µg/mL negative. **K)** Average fluorescence intensities measured in the cell pellets. The error bars correspond to standard deviations of intensities in cell pellet.

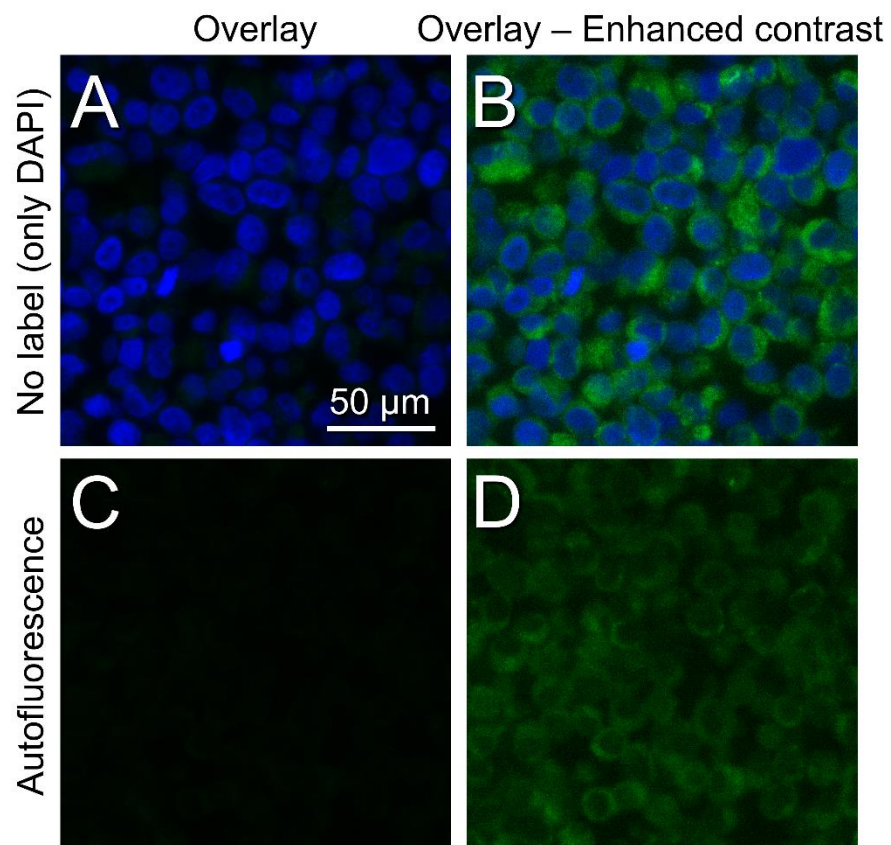


Figure S22: Fluorescence images (overlay signal of DAPI and fluorescein channels) of negative controls in ICC. No detection label, DAPI stained nuclei: **A)** standard contrast settings, **B)** enhanced contrast. No detection label, no DAPI: **C)** standard contrast, **D)** enhanced contrast.

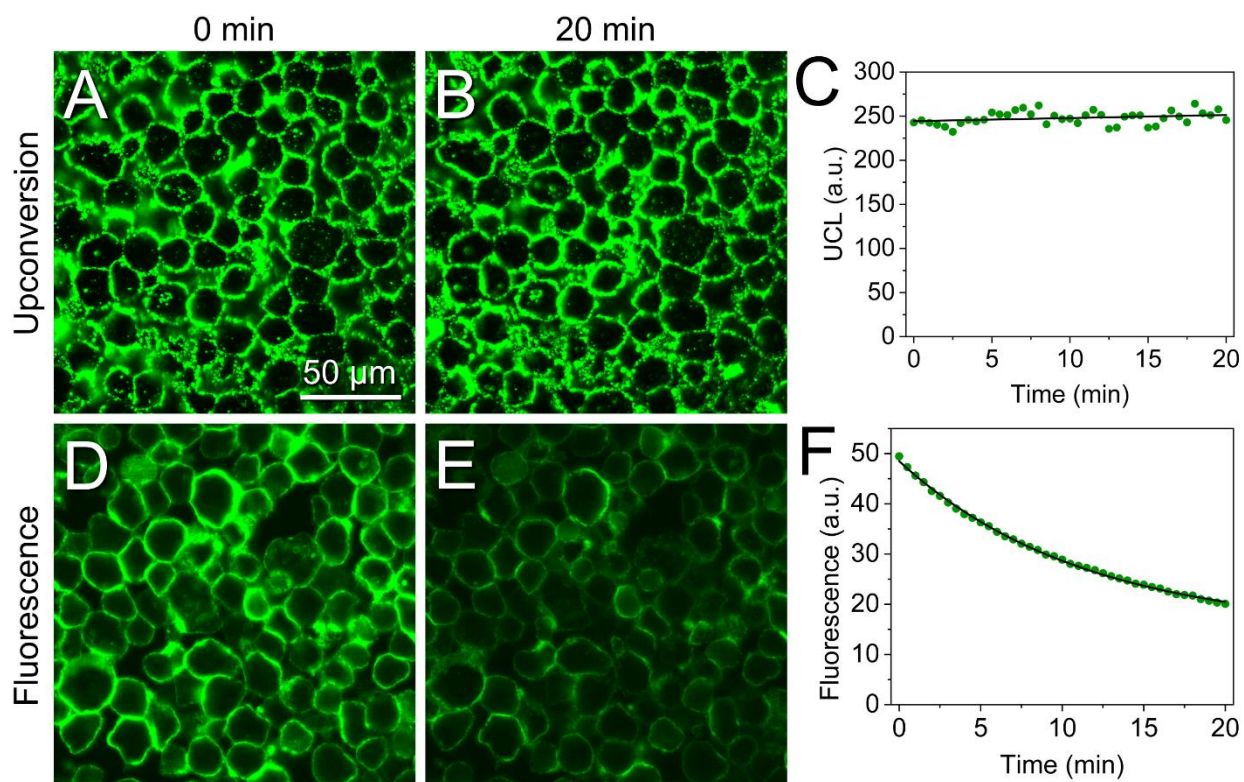


Figure S25: The photostability of ICC staining of the HER2-positive BT-474 FFPE cells. Staining by SA-PEG-Ner-UCNPs after **A)** 0 min, and **B)** 20 min of 980 nm excitation. **C)** Background corrected upconversion signals fitted with linear function. Staining by SA-FAM after **D)** 0 min, and **E)** 20 min of 480 nm excitation. **F)** Background corrected fluorescence signals fitted with exponential function.

References

1. F. Wang, Y. Han, C. S. Lim, Y. H. Lu, J. Wang, J. Xu, H. Y. Chen, C. Zhang, M. H. Hong and X. G. Liu, *Nature*, 2010, **463**, 1061-1065.
2. U. Kostiv, V. Lobaz, J. Kučka, P. Švec, O. Sedláček, M. Hrubý, O. Janoušková, P. Francová, V. Kolářová, L. Šefc and D. Horák, *Nanoscale*, 2017, **9**, 16680-16688.
3. V. Poláchová, M. Pastucha, Z. Mikušová, M. J. Mickert, A. Hlaváček, H. H. Gorris, P. Skládal and Z. Farka, *Nanoscale*, 2019, **11**, 8343-8351.
4. A. Hlaváček, M. Peterek, Z. Farka, M. J. Mickert, L. Prechtel, D. Knopp and H. H. Gorris, *Microchimica Acta*, 2017, **184**, 4159-4165.
5. G. T. Hermanson, *Bioconjugate Techniques (Second Edition)*, Academic Press, New York, 2008.
6. C. R. Becer, R. Hoogenboom and U. S. Schubert, *Angew. Chem. Int. Ed.*, 2009, **48**, 4900-4908.
7. C. A. Schneider, W. S. Rasband and K. W. Eliceiri, *Nat. Methods*, 2012, **9**, 671-675.
8. Z. Farka, M. J. Mickert, A. Hlaváček, P. Skládal and H. H. Gorris, *Anal. Chem.*, 2017, **89**, 11825-11830.
9. M. J. Mickert, Z. Farka, U. Kostiv, A. Hlaváček, D. Horák, P. Skládal and H. H. Gorris, *Anal. Chem.*, 2019, **91**, 9435-9441.
10. A. Sedlmeier, A. Hlaváček, L. Birner, M. J. Mickert, V. Muhr, T. Hirsch, P. Corstjens, H. J. Tanke, T. Soukka and H. H. Gorris, *Anal. Chem.*, 2016, **88**, 1835-1841.

IX. Single-Molecule Enzyme Measurements

Enzymes are biocatalysts that reduce the activation energy of chemical reactions, enabling reactions that would not occur under mild conditions. Conventional enzyme kinetics are measured in bulk solution, meaning that the reaction rates of thousands of enzymes are averaged. As a result, heterogeneities in the reaction rates of individual enzyme molecules remain hidden. In 1961, Boris Rotman developed a technique to measure the activity of single enzyme molecules.¹ In his work, he sprayed a highly diluted enzyme-substrate solution onto a silicone oil leading to the formation of small droplets. Because of the high enzyme dilution, the number of enzyme molecules was lower than the number of droplets resulting in many empty droplets, some that contained a single enzyme molecule, and a neglectable number of droplets held more than a single molecule. Droplets that included at least one enzyme molecule showed an increase in fluorescence over time, which was monitored with a microscope (**Figure 1**). Rotman observed that individual enzyme molecules in droplets of the same size displayed variations in their catalytic activities, which is today known as static heterogeneity in the substrate turnover rates.

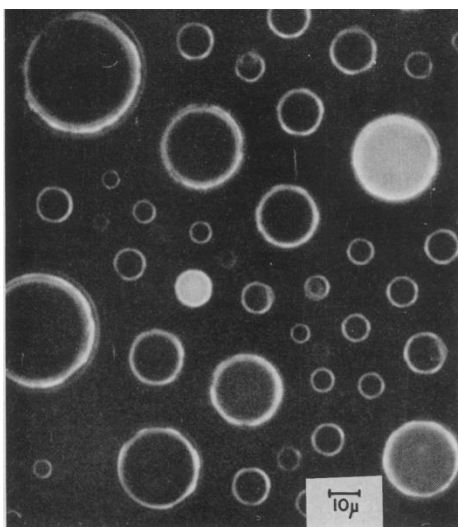


Figure 1: Photo of enzyme-substrate droplets on silicone oil. Droplets that contain at one enzyme molecule show an increasing fluorescence over time. Reprinted with permission from¹. Copyright 1961.

While Rotman's idea of confining individual enzyme molecules in aqueous droplets to restrict the diffusion of the fluorescent product was groundbreaking, it had some problems. First, the droplets varied in size, accounting for that the diameter of each droplet had to be measured to obtain the enzyme activity. Second, the substrate can slightly dissolve in the silicone oil, leading to product diffusion over time. Third, the spraying process might not be optimal for

Single-Molecule Enzyme Measurements

the enzyme stability and could cause denaturation of some enzyme molecules. Consequently, the technique of Rotman was further evolved to account for these problems.

The group of Noji² developed highly homogeneous arrays of micrometer-sized chambers, with a volume of less than 100 fL in PDMS. It was shown that slightly polar molecules do not diffuse through the PDMS, which is essential to prevent leaking of the substrate and its fluorescent product. It was possible to monitor the substrate turnover of individual GAL molecules. The group of David R. Walt developed femtoliter arrays etched into optical fiber bundles with 240,000 individual wells.³ A linear relationship between the enzyme concentration and the number of fluorescent wells could be observed. It was concluded that the technique is of potential use for ultrasensitive bioassays (which turned out to be true, **ChapterIV.6.2**).

Liebherr et al.⁴ fabricated femtoliter arrays in fused silica arrays and observed the reaction rates of a wildtype GUS compared to an *in vitro* partially evolved GUS, aiming to evolve GUS into GAL. They proved that the single-molecule kinetics agreed with the traditional Michaelis-Menten kinetics. By arranging the different substrate turnover rates of individual enzyme molecules into histograms, the activity distributions were obtained. It was found that GUS had the smallest distribution, whereas the evolved GUS and GAL displayed higher variations in their activities. The authors proposed that the broadening in the activity distributions is related to a higher acceptance of substrate molecules, which means that enzyme populations with a small size activity distribution are specialized molecules that catalyze only one reaction. Enzyme populations with broad distributions in their substrate turnover rates can potentially accept different substrate or even catalyze different reactions. From the evolutionary point, this mechanism could have helped primordial cells adapting to new substrates despite a low gene content.

To obtain statistically relevant data for single-molecule enzyme kinetics, many enzyme molecules must be monitored. This can be either achieved by conducting many experiments or by increasing the size (i.e. number of wells) of the fL-array. It is not possible to load each well of the fL-array with a single enzyme molecule, instead a highly diluted enzyme dilution is applied on the array and the enzyme molecules distribute statistically over the array. If the enzyme concentration is too high, all the wells will include an enzyme molecule but many of them will include two or more enzymes, which has to be strictly avoided. A mathematical model to calculate a suitable enzyme concentration is the Poisson distribution:

$$P_{\mu}(x) = \frac{e^{-\mu}\mu^x}{x!}$$

For a single-molecule experiment $P_{\mu}(x)$ is the probability that exactly x enzyme molecules are present in a well if the average number of enzyme molecules per well is μ . If the ratio of enzymes to wells is 1/20, then μ is 0.05. The probability that two enzyme molecules ($x = 2$) are present in one of the wells is 0.1%. The probability that exactly one enzyme molecule is present in a well $P_{0.05}(1)$ is less than 5% (1 enzyme in every 20th well). Consequently, a large array is needed to prevent wells that are occupied with more than one enzyme molecule.

The following chapter describes the use of large fL-arrays consisting of 62,500 wells etched into fused silica to analyze the turnover rates of single GAL and GUS molecules. These are used to calculate the free energy of activation of the enzymatic reactions of single enzyme-molecules. The results obtained were used to adapt the current transition state theory to account for dynamic and static heterogeneities present in enzyme populations.

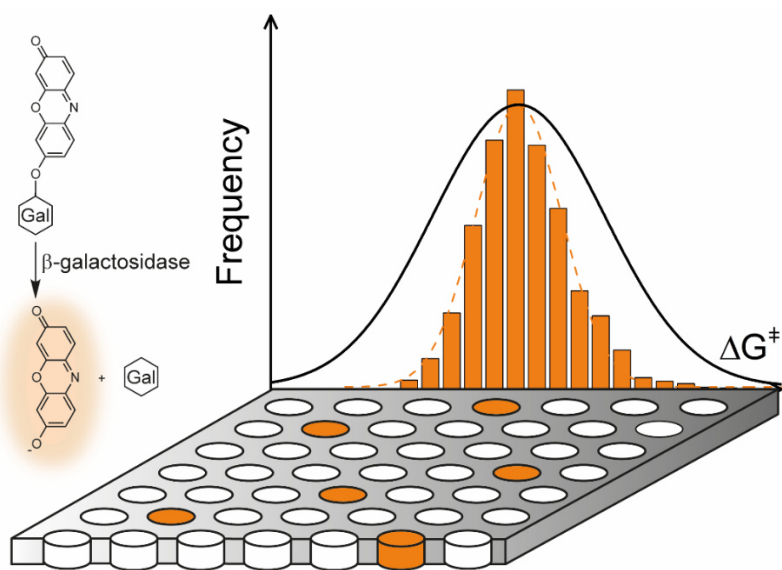
References

1. Rotman, B., Measurement of activity of single molecules of β -D-galactosidase. *Proc. Natl. Acad. Sci. U.S.A.* **1961**, *47* (12), 1981-1991.
2. Rondelez, Y.; Tresset, G.; Tabata, K. V.; Arata, H.; Fujita, H.; Takeuchi, S.; Noji, H., Microfabricated arrays of femtoliter chambers allow single molecule enzymology. *Nat. Biotechnol.* **2005**, *23* (3), 361-365.
3. Rissin, D. M.; Walt, D. R., Digital concentration readout of single enzyme molecules using femtoliter arrays and Poisson statistics. *Nano Lett.* **2006**, *6* (3), 520-523.
4. Liebherr, R. B.; Renner, M.; Gorris, H. H., A Single Molecule Perspective on the Functional Diversity of in Vitro Evolved beta-Glucuronidase. *J. Am. Chem. Soc.* **2014**, *136* (16), 5949-5955.

X. Research Article 4

Transition State Ensembles Navigate the Pathways of Enzyme Catalysis

Matthias J. Mickert and Hans H. Gorrís*



This Chapter has been published, text and figures reprinted with permission from The American Chemical Society: The Journal of Physical Chemistry B¹, Copyright 2018.

¹Mickert, M. J., & Gorrís, H. H. Transition-state ensembles navigate the pathways of enzyme catalysis. *J. Phys. Chem. B*, **2018**, *122*(22), 5809-5819.

X.1. Abstract

Transition state theory (TST) provides an important framework for analyzing and explaining the reaction rates of enzymes. TST, however, needs to account for protein dynamic effects and heterogeneities in enzyme catalysis. We have analyzed the reaction rates of β -galactosidase and β -glucuronidase at the single molecule level by using large arrays of femtoliter-sized chambers. Heterogeneities in individual reaction rates yield information on the intrinsic distribution of the free energy of activation (ΔG^\ddagger) in an enzyme ensemble. The broader distribution of ΔG^\ddagger in β -galactosidase compared to β -glucuronidase is attributed to β -galactosidase's multiple catalytic functions as a hydrolase and a transglycosylase. Based on the catalytic mechanism of β -galactosidase, we show that transition state ensembles do not only contribute to enzyme catalysis but can also channel the catalytic pathway to the formation of different products. We conclude that β -galactosidase is an example of natural evolution, where a new catalytic pathway branches off from an established enzyme function. The functional division of work between enzymatic substates explains why the conformational space represented by the enzyme ensemble is larger than the conformational space that can be sampled by any given enzyme molecule during catalysis.

X.2. Introduction

TST has provided a very fruitful framework for explaining the catalytic power of enzymes: an enzyme binds the transition state much more tightly relative to the substrate to decrease the activation energy. Growing evidence for protein dynamic effects, however, make it necessary to replace the concept of a single well-defined transition state structure by a transition state ensemble.¹ In particular, single molecule studies have revealed catalytically relevant heterogeneities along the reaction coordinate (dynamic heterogeneity) but also among different molecules in an enzyme population (static heterogeneity).² An integrated picture of these two types of heterogeneities in enzyme catalysis, however, is still missing, yet, because: (1) Most single enzyme molecule studies can only observe a single molecule at a time such that it is difficult to obtain statistically relevant information on the enzyme population. (2) Heterogeneities among individual enzyme molecules have been attributed to experimental conditions such as surface immobilization rather than to different enzyme conformers (3). The focus of conventional transition state theory is to explain the catalytic mechanism in a given enzyme molecule. Therefore, differences between enzyme molecules do not fall under the scope of conventional transition state theory.

Previously, we addressed the first and second point by isolating hundreds of individual enzyme molecules without a surface immobilization step in large arrays of homogeneous femtoliter-sized chambers etched into the surface of fused silica slides.³ The individual substrate turnover

of β -D-galactosidase (GAL)⁴⁻⁵ and β -D-glucuronidase (GUS)⁶ has been analyzed in parallel using similar fluorogenic reactions, which created the fluorescent product resorufin and was monitored by wide-field epifluorescence microscopy (**Figure 1**). Both enzymes feature a distinct static heterogeneity of long-lived conformational states that do not interconvert over time, as also observed by others.⁷⁻⁹ In a complementary approach, the Xie group used the same fluorogenic reaction to investigate the waiting time distribution between two subsequent catalytic events of individual GAL molecules (dynamic heterogeneity).¹⁰

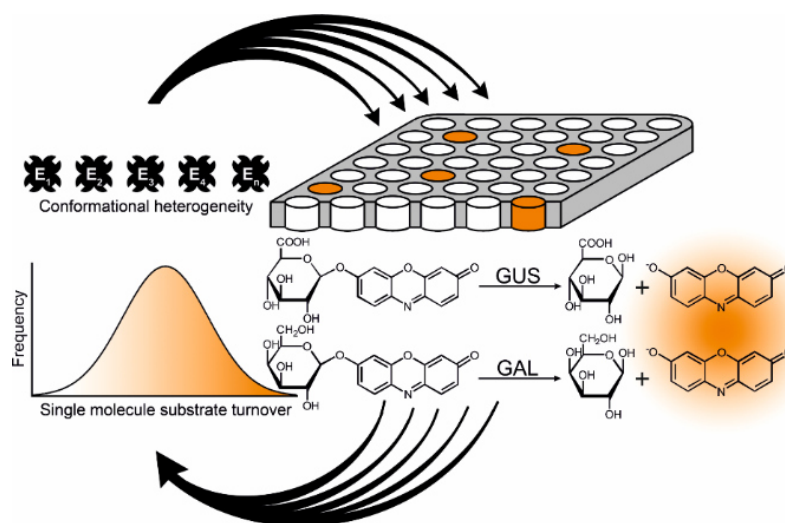


Figure 1: Schematic section of 250x250 (62 500) homogeneous wells each defining a volume of 38 fL on the surface of a fused silica slide (grey). To isolate single enzyme molecules, the femtoliter arrays are filled with 1.8 pM of either GAL or GUS (one enzyme molecule in 20 chambers) together with a large excess of fluorogenic substrate and then tightly sealed (not shown). Only chambers containing a single enzyme molecule hydrolyze the substrate to resorufin (orange), which is recorded by wide-field fluorescence microscopy. The distribution of single molecule substrate turnover rates provides information on the conformational heterogeneity in an enzyme population.

GAL (465 kDa) and GUS (273 kDa) are evolutionary related family 2 glycosyl hydrolases from *Escherichia coli*¹¹ that are frequently used for constructing gene fusion markers.¹² Both enzymes are homotetramers of known crystal structures¹³⁻¹⁴ and comprise four identical catalytic sites located at the interface of two neighboring monomers. They hydrolyze similar glycosidic substrates involving a double displacement reaction mechanism with retention of configuration at the anomeric carbon. GAL is highly specific for D-galactose and GUS for D-glucuronide but either enzyme has low specificity for the second part of the substrate (the leaving group). After substrate binding, the enzyme conformation changes along the reaction coordinate to assist in the formation of the first transition state.¹⁵ The nucleophilic residues Glu-537 in GAL¹⁶ or Glu-504 in GUS¹⁷ form a covalent glycosyl-enzyme intermediate with the anomeric carbon of D-galactose or D-glucuronid, respectively. A second glutamate (Glu-

461 in GAL and Glu-413 in GUS) supports this reaction as a general acid/base catalyst. During the formation of the first transition state the leaving group is released. The reaction coordinate passes through a second transition state to hydrolyze the glycosyl-enzyme (**Figure 2**).

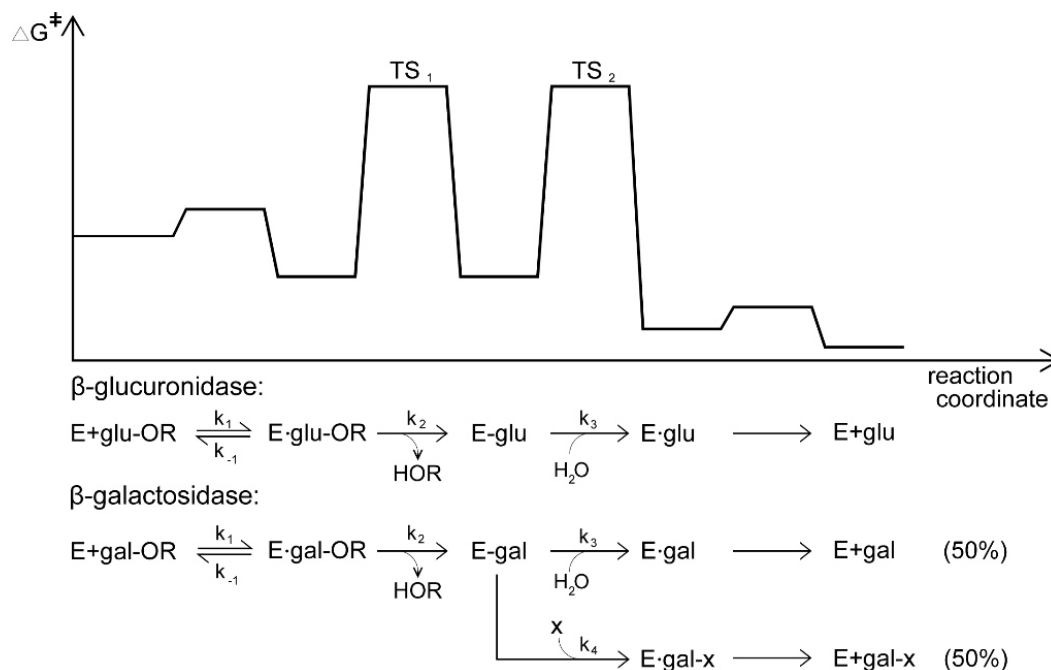


Figure 2: Free energy diagram and catalytic pathways of β -glucuronidase (GUS) or β -galactosidase (GAL), respectively. Both enzymes form two transition states (TS) to complete a catalytic cycle. k_2 leads to the formation of a covalent enzyme-substrate intermediate, which decomposes with k_3 . GAL, however, is also able to perform a transgalactosylation reaction with glucose (x), which leads to the formation of allolactose (k_4). These alternative pathways occur in equal amounts (Adapted from ref. ¹⁸).

Here, we reanalyze our previous work on single molecule reaction rates of GAL⁴ and GUS⁶ to develop a new framework of transition state ensembles that accounts for dynamic and static heterogeneity. The distribution of reaction rates in an enzyme population provides information on the distribution of activation energies, thus characterizing the transition state ensemble. For this aim, GAL and GUS represent excellent model systems because their mode of catalysis is very similar and they have been investigated extensively for many decades on the bulk and more recently on the single molecule level.

X.3. Experimental Section

Buffers, Enzymes and Substrates

All enzyme experiments were conducted in phosphate buffered saline (137 mM NaCl, 10 mM Na₂HPO₄, 2 mM KH₂PO₄, 2.7 mM KCl, pH 7.4) containing either 0.05 mg/mL of bovine serum albumin (BSA, Sigma-Aldrich, www.sigmaaldrich.com), 1 mM of MgCl₂ and 0.005 % of Tween 20 (Sigma-Aldrich) for GAL experiments or 0.05 mg/mL of BSA for GUS experiments. GAL from *E. coli* was purchased from Sigma-Aldrich as a lyophilized powder (Grade VIII) and reconstituted to 2 μM in PBS/MgCl₂. His-tagged GUS from *E. coli* was expressed in *E. coli*, purified by nickel chelate chromatography and its concentration was determined by Bradford assay or absorption spectroscopy as described earlier.⁶ The purity of both enzyme preparations was confirmed by SDS gel electrophoresis. Enzyme aliquots were snap-frozen in liquid nitrogen and stored at -80 °C. Resorufin-β-D-galactopyranoside (Iris Biotechnology, www.iris-biotech.de) served as a substrate for GAL, and resorufin-β-D-glucuronide (Sigma-Aldrich) as a substrate for GUS. Their product resorufin (Thermo Fisher, www.lifetechnologies.com) was used to standardize fluorescent signal intensities. Millimolar stock solutions of these substrates and the product were prepared in DMSO, aliquoted and stored for up to 6 months at -20 °C.

Bulk Enzyme Experiments

Bulk enzyme activities were determined in microtiter plates. An enzyme concentration of 36 pM was employed because a single enzyme molecule in a 38-fL compartment correlates to a bulk concentration of 36 pM without compartmentalization. Substrate saturation curves of both enzymes were recorded by measuring the turnover of various substrate concentrations ($\lambda_{\text{ex}} = 544 \text{ nm}$, $\lambda_{\text{em}} = 575 \text{ nm}$, Fluostar Optima, bMG-Labtech, www.bmg-labtech.com). The fluorescence intensities were calibrated by using resorufin standard solutions.

Single Enzyme Molecule Experiments in Femtoliter Arrays

Arrays of 250 × 250 (62 500) cylindrical wells of 4 μm in diameter and 3 μm depth (38 fL) were formed in the surface of fused silica slides by photolithography and reactive ion etching as described earlier.⁴ When a highly diluted enzyme concentration of 1.8 pM is filled into an array of 38-fL wells, a ratio of 1 enzyme molecule in 20 wells is obtained. The probability $P_{\mu}(x)$ that exactly x enzyme molecules are enclosed in any given well is given by the Poisson distribution (Eq. 1):

$$P_{\mu}(x) = \frac{e^{-\mu} \cdot \mu^x}{x!} \quad \text{Eq. 1}$$

where μ is the average number of enzyme molecules per well ($\mu = 0.05$). Under these conditions, most wells remain empty but the probability of finding more than a single enzyme molecule in a well is negligible ($P_{0.05}(>1) \leq 0.001$).

The femtoliter array was mounted on a custom-built array holder on top of an inverted epifluorescence microscope (Eclipse Ti-E, Nikon, www.nikoninstruments.com).⁴ Just prior to each measurement, enzyme solutions were diluted and mixed with respective fluorogenic substrates to yield a final enzyme concentration of 1.8 pM. Approximately 8 μ l of the solution were dispensed on the femtoliter array, which was tightly sealed by a polydimethylsiloxane (PDMS) gasket under well-defined mechanical pressure. Time lapsed imaging was started within two minutes. Every 30 s, four wide-field images (each covering approximately 5 000 wells) of different sections of the array were taken consecutively using an exposure time of 200 ms. Excitation light from a fiber-optical mercury illuminator (Intensilight, Nikon) was dimmed (ND 4 or ND 8) and filtered for resorufin ($\lambda_{ex} = 577 \pm 10$ nm, $\lambda_{em} = 620 \pm 60$ nm, Chroma Technology, www.chroma.com). Images were recorded with a 20x objective (FI60 Plan Apo, NA 0.75, Nikon) on a cooled sCMOS camera (Andor Technology, www.andor.com).

Analyzing Single Enzyme Molecule Data

Fluorescence time traces of single enzyme molecules were background-corrected by subtracting the fluorescence signals of wells containing no enzyme and calibrated by measuring the fluorescence of resorufin standard solutions in the femtoliter array. The velocity of an individual enzyme molecule (v_i) was calculated from the initial substrate turnover rate over 2 min and follows a modified Michaelis-Menten equation as described earlier:⁹

$$v_i = k_{cat} \frac{[S]}{K_M + [S]} \quad \text{Eq.}$$

2

Steady-state conditions apply for single enzyme molecule experiments assuming a constant probability of finding any given enzyme molecule in the enzyme-substrate complex (ρ_{ES}) rather than a constant concentration of $[ES]$.

Hundreds of v_i were averaged to obtain a representative enzyme ensemble ($\langle v \rangle$) for the regression of single molecule substrate saturation curves:

$$\langle v \rangle = k_{cat} \frac{[S]}{K_M + [S]} \quad \text{Eq.}$$

3

The coefficient of variation (CV %) of a large number (n) of v_i indicates the velocity distribution within an enzyme population:

$$CV = 100 \times \frac{\sqrt{\frac{1}{n-1} \sum_{i=1}^n (v_i - \langle v \rangle)^2}}{\langle v \rangle} \quad \text{Eq.}$$

4

According to transition state theory (TST), the internal states of the reactant (here the substrate S) and the transition state (X^\ddagger) are in a Boltzmann distribution. Hence, there is a local equilibrium between S and X^\ddagger and the rate constant k^{TST} for the formation of product P is given by:

$$k^{\text{TST}} = \kappa \frac{k_B T}{h} e^{-\Delta G^\ddagger / RT} \quad \text{Eq.}$$

5

where k_B is Boltzmann's constant, T is the absolute temperature, h is Planck's constant, ΔG^\ddagger is Gibbs free energy defining the energy barrier between S and X^\ddagger , R is the gas constant and κ is the transmission coefficient. κ can be taken as unity if we assume no re-crossing of the energy barrier between the product P and S . Hence, the reaction rate is directly proportional to the equilibrium concentration of X^\ddagger . In enzymatic reactions, the formation of an enzyme- X^\ddagger complex strongly reduces the free energy of activation (ΔG^\ddagger) and the experimentally observable macroscopic rate constant k_{cat} provides a good estimate for k^{TST} .¹⁹

As GAL and GUS are homotetramers ($n=4$), the contribution of each subunit to the overall enzyme activity is $k_{\text{cat}}^s = k_{\text{cat}}/n$. Consequently, the free energy of activation (ΔG^\ddagger) can be calculated from single molecule experiments for any $[S]$ by inserting Eq. 3 into Eq. 5 and rearranging to ΔG^\ddagger :

$$\Delta G^\ddagger = -\ln \left(\frac{\langle v \rangle K_M + [S]}{n [S]} \frac{h}{k_B T} \right) RT \quad \text{Eq.}$$

6

In analogy, the distribution of ΔG^\ddagger in an enzyme population is calculated for any $[S]$ by inserting Eq. 2 into Eq. 5 and rearranging to ΔG^\ddagger :

$$\Delta G^\ddagger_i = -\ln \left(\frac{v_i K_M + [S]}{n [S]} \frac{h}{k_B T} \right) RT \quad \text{Eq.}$$

7

The single molecule experiments can only access the average activity of all four subunits in a tetramer. Thus, the distribution of ΔG^\ddagger calculated from Eq. 7 (expressed as the standard deviation σ) would only be correct if all four subunits ($n=4$) had the same activity. Considering that each subunit is independent, however, the distribution of ΔG^\ddagger among the subunits is larger than the apparent distribution (**Appendix I**):

$$\sigma_{\text{subunit}} = \sigma_{\text{app}} \sqrt{n} \quad \text{Eq. 8}$$

Determination of Substrate Autohydrolysis Rates

Three 100- μ M solutions of both resorufin- β -D-galactopyranoside and resorufin- β -D-glucuronide were prepared in the respective PBS buffers and stored at room temperature in the dark. Over the course of one month, several 100 μ l samples of the substrate solutions were taken to measure the increase in the fluorescence of the autohydrolysis product resorufin over time ($\lambda_{\text{ex}} = 544$ nm, $\lambda_{\text{em}} = 575$ nm, Fluostar Optima, BMG-Labtech). The samples were compared to a freshly prepared 100 μ M substrate sample (control). The fluorescence intensities were calibrated by using resorufin standard solutions. The calculation of the autohydrolysis rates is described in the **Appendix** and ΔG^\ddagger of the uncatalyzed reaction is given by:

$$\Delta G^\ddagger = -\ln\left(\frac{k_{\text{non}} h}{k_B T}\right) RT \quad \text{Eq.}$$

9

X.4. Results and Discussion

GAL and GUS are very stable and non-glycosylated enzymes that hydrolyze similar resorufin- β -D-glycosides and release the same fluorescent product resorufin, thus establishing very similar biochemical model systems. Analyzing the heterogeneity in the activity of individual enzyme molecules additionally requires homogeneous and reproducible reaction conditions in each chamber of the femtoliter array. We efficiently blocked non-specific surface binding and confirmed that the static heterogeneity in an enzyme population is independent of the type of femtoliter array (fused silica vs. polydimethylsiloxan (PDMS)) as described earlier.⁴

Here, we isolated hundreds of individual enzyme molecules together with their respective fluorogenic substrates in femtoliter chambers etched into the surface of fused silica slides (**Figure 1**). The accumulation of resorufin in enzyme-occupied chambers was recorded by fluorescence microscopy (**Figure 3**) to calculate initial substrate turnover rates over 2 min when substrate depletion and photobleaching were negligible. At the lowest substrate concentration ($[S] = 12.5$ μ M, $\sim 290\,000$ substrate molecules per chamber), both enzymes displayed on average substrate turnover rates of ~ 50 s^{-1} , which was well distinguishable from chambers containing no enzyme.

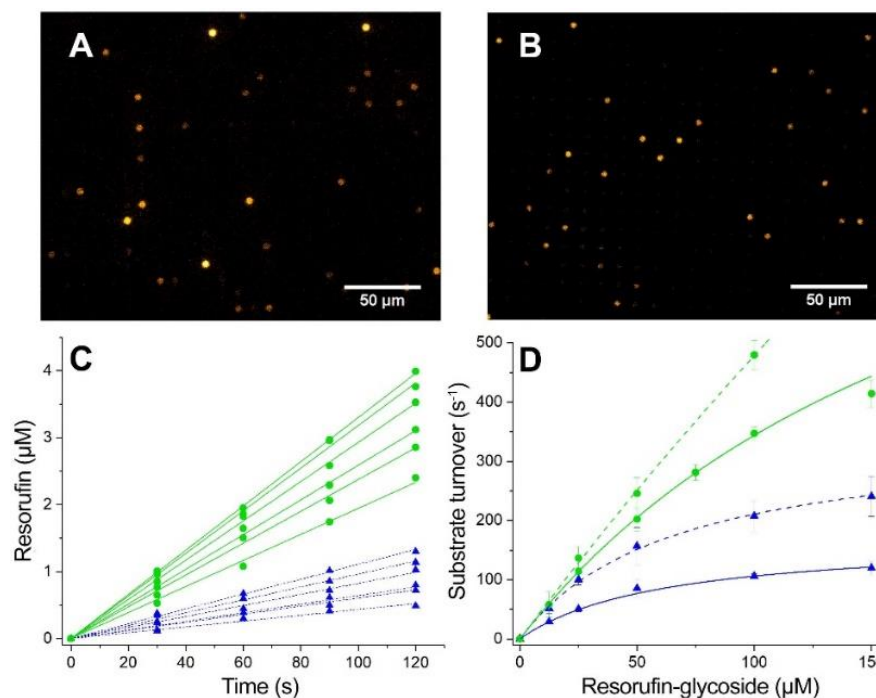


Figure 3: Single molecule enzyme kinetics of GAL and GUS in femtoliter arrays. A concentration of 1.8 pM GAL **A**) or GUS **B**) yields one enzyme molecule in every twentieth femtoliter chamber that hydrolyzes a glycosidic substrate (100 μM). The generation of the fluorescent product resorufin (orange) is shown after 120 s. **C**) Single molecule images of GAL (green circles) and GUS (blue triangles) are recorded every 30 s and six individual time traces are plotted against time. **D**) Single molecule (hatched line) and bulk (solid line) substrate saturation curves of GAL (green circles) and GUS (blue squares). The mean reaction rate and standard deviation of at least three independent experiments are plotted. Error bars indicate the standard deviation between independent measurements.

Bulk and Single Enzyme Molecule Catalysis as Compared to Autohydrolysis

Figure 2D shows substrate saturation curves of GAL and GUS obtained either from a conventional bulk reaction or from an ensemble of individual enzyme molecules ($\langle v \rangle$, Eq. 3). Both enzymes display a similar activity at low $[S]$, but the activity of GAL increases more strongly when $[S]$ is increased. Maximum $[S]$ were chosen according to the limited substrate solubility in aqueous buffer. Compared to GAL's natural substrate lactose ($K_M = 1.35 \text{ mM}$), the hydrolysis of aromatic aglycons such as resorufin is characterized by a lower K_M of 0.05 to 0.5 mM^{20} because the active center of GAL binds aromatic aglycons more tightly than glucose.²¹ As this range of K_M falls into the limit of substrate solubility, we calculated K_M only from GAL bulk experiments that could be performed up to $[S] = 200 \mu\text{M}$. The lower K_M of GUS was accessible from bulk as well as single molecule experiments, which essentially yielded the same results because the calculation of K_M does not depend on the enzyme concentration. By contrast, substrate turnover rates and k_{cat} calculated from bulk reactions are

apparently lower than the respective single enzyme molecule rates because even highly purified enzyme preparations typically contain a fraction of inactive enzyme molecules⁴. Despite differences in K_M and k_{cat} , both enzymes expose a similar catalytic efficiency (k_{cat}/K_M). All kinetic constants derived from the substrate saturation curves are summarized in **Table 1**.

Table 1: Rate constants of uncatalyzed, bulk and single molecule enzyme reactions.

	Substrate (S)	Resorufin- β -D-galactopyranoside	Resorufin- β -D-glucuronide
Non-enzymatic	$t_{1/2}$	10 years	23 years
	k_{non}	$2.2 \pm 0.2 \times 10^{-9} \text{ s}^{-1}$	$1.0 \pm 1.6 \times 10^{-9} \text{ s}^{-1}$
	$\Delta G_{non}^{\ddagger}$	121 kJ/mol	123 kJ/mol
Enzymatic		GAL	GUS
Bulk*	K_M	$235 \pm 24 \mu\text{M}$	$62 \pm 9 \mu\text{M}$
	k_{cat}	$1000 \pm 200 \text{ s}^{-1}$	$170 \pm 20 \text{ s}^{-1}$
	k_{cat}/K_M	$4.3 \times 10^6 \text{ s}^{-1} \text{ M}^{-1}$	$2.8 \times 10^6 \text{ s}^{-1} \text{ M}^{-1}$
Single molecule	K_M	n.d.	$65 \pm 7 \mu\text{M}$
	k_{cat}	n.d.	$350 \pm 20 \text{ s}^{-1}$
	k_{cat}/K_M	$4.7 \times 10^6 \text{ s}^{-1} \text{ M}^{-1} **$	$5.3 \times 10^6 \text{ s}^{-1} \text{ M}^{-1}$
	$\Delta G_{cat}^{\ddagger}$	57.9 kJ/mol	61.4 kJ/mol
Rate enhancement	k_{cat}/k_{non}	4.6×10^{11}	3.5×10^{11}
Catalytic proficiency	$(k_{cat}/K_M)k_{non}$	$2.1 \times 10^{15} \text{ M}^{-1}$	$4.8 \times 10^{15} \text{ M}^{-1}$

*GAL bulk measurements up to $[S] = 200 \mu\text{M}$, ** k_{cat}/K_M determined at $[S] \ll K_M$, (second order rate constant).

Resorufin- β -D-galactopyranoside and resorufin- β -D-glucuronide show slow but distinct autohydrolysis rates (k_{non} , **Supporting Information**) under ambient conditions because aryloxides such as the resorufin anion are less basic ($\text{pK}_a \approx 7$)²² and thus better leaving groups compared to alkoxide anions.²³ Relating the catalytic efficiency to the non-catalyzed reaction yields the catalytic proficiency ($(k_{cat}/K_M)k_{non}$, **Table 1**), which indicates the enzyme's capability to lower the activation energy ΔG^{\ddagger} .²⁴ GAL and GUS have similar catalytic proficiencies within the typical broad range found for enzymes.

Distribution of Reaction Rates in a Population of Individual GAL and GUS Molecules

For analyzing the static heterogeneity in an enzyme population, we assembled individual substrate turnover rates of GAL and GUS as histograms separately for each $[S]$ (**Figure 4**). The peaks of the histograms in the upper panels of **Figure 4A-3E** relate to the data of the substrate saturation curves in **Figure 3D**. Each enzyme displays a distinct distribution of reaction rates, which is independent of $[S]$ as shown by normalizing the histograms (lower panels of **Figure 4A-4E**). In contrast, the static heterogeneity strongly depends on the enzyme:

The reaction rates of GAL are significantly more widely distributed ($CV \approx 42\%$) compared to GUS ($CV \approx 27\%$, **Figure 4F**).

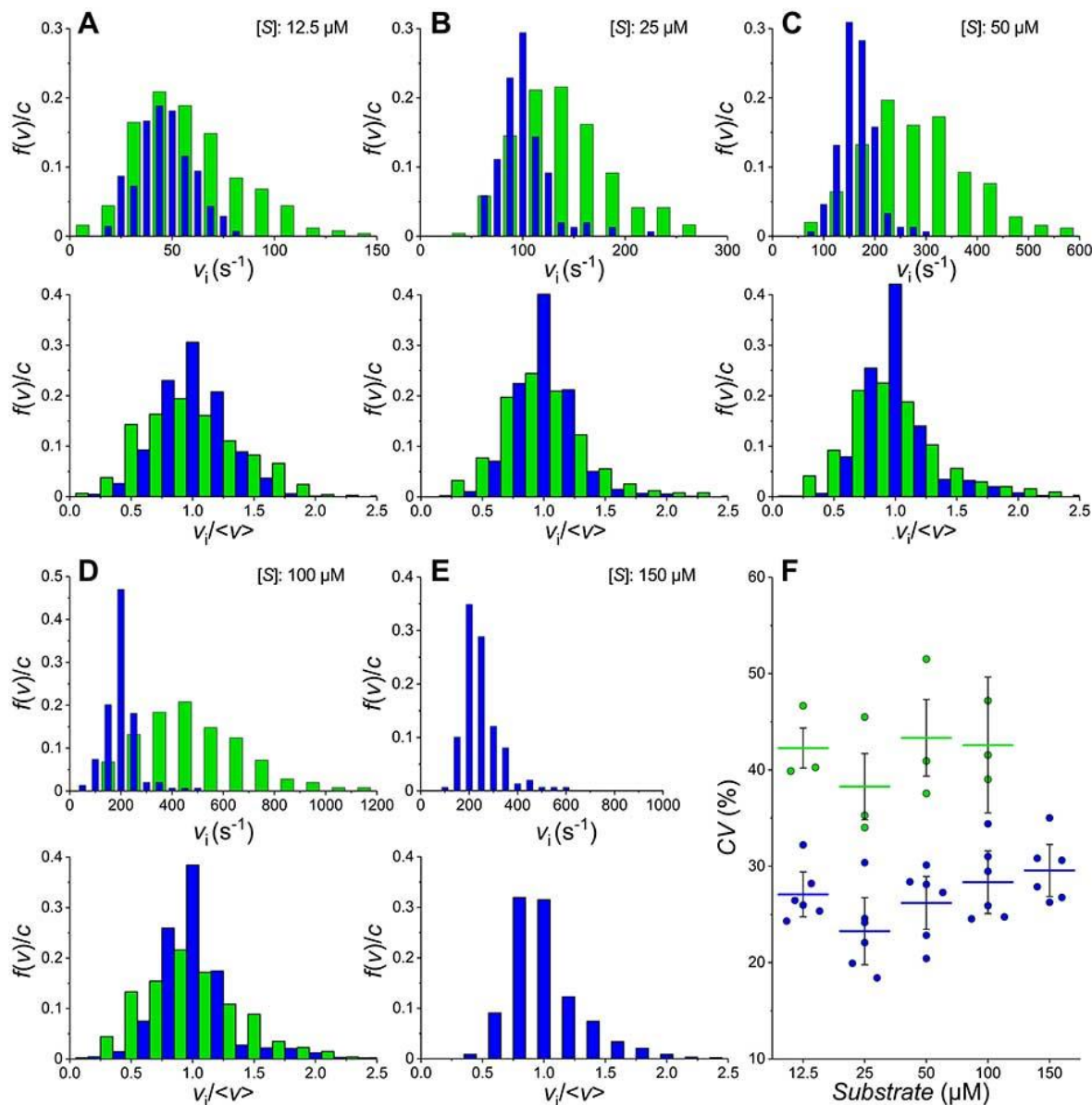


Figure 4: Single molecule substrate turnover distribution of GAL (green) and GUS (blue) in the presence of **A)** 12.5 μM, **B)** 25 μM, **C)** 50 μM, **D)** 100 μM, and **E)** 150 μM substrate. The histograms in the upper panels show several hundred individual substrate turnover rates (v_i) from one representative femtoliter array experiment. The frequency ($f(v)/c$) is the number of enzyme molecules per bin divided by the total count of observed enzyme molecules. The binning times (GAL: 12.5 s⁻¹, GUS: 6.25 s⁻¹ at 12.5 μM) are chosen to scale with the increase of $[S]$. The lower panels show the normalized distribution of reaction rates of at least three independent experiments ($v_i / \langle v \rangle$, bin: 0.2), where $\langle v \rangle$ is the average substrate turnover in each experiment. **F)** Coefficient of variations (CV , Eq. 4) of individual substrate turnover rates in an enzyme population are independent of $[S]$ but significantly different between GAL and GUS (unpaired t tests, $p \leq 0.01$).

The histogram of GAL determined at $[S] = 100 \mu\text{M}$ (**Figure 4D**) is consistent with the broad distribution of reaction rates reported in an earlier study based on femtoliter arrays fabricated in glass-optical fiber bundles.²⁵ In this study, the Walt group demonstrated that single GAL molecules interconvert between different activity states upon heating to 47 °C, but the activity distribution essentially remains the same after each heating step. The Craig group²⁶ investigated individual GAL molecules by using capillary electrophoresis and found that crystallization of GAL does not reduce the activity distribution in an enzyme population. Furthermore, the Yeung group compared the activity of lactate dehydrogenase with the inorganic catalyst Os(VIII) in femtoliter arrays etched into fused silica slides. While the enzyme activity was heterogeneous, the reaction of the inorganic catalyst was homogeneous.²⁷ These complementary single molecule experiments confirm that the distribution of reaction rates is an intrinsic feature of the enzyme rather than a result of the experimental platform or the enzyme preparation.

As an inherent catalytic feature of an enzyme, the distribution of reaction rates can be attributed either to heterogeneity in the formation of the enzyme-substrate complex or to heterogeneity in the catalytic step (k_{cat}) as discussed earlier.⁹ According to **Equation 2**, a heterogeneous rate of enzyme-substrate complex formation would affect the overall enzyme reaction only if $[S] < K_M$ but not under substrate saturation ($[S] \gg K_M$) such that we should expect the distribution of reaction rates to become narrower with increasing $[S]$. The normalized histograms of **Figure 4**, however, clearly show a uniform distribution independent of $[S]$. Consequently, differences in the individual catalytic activity of these enzymes are a result of heterogeneity in k_{cat} . The macroscopic rate constant k_{cat} can be used as an approximation for k^{TST} in order to calculate ΔG^\ddagger (**Equation 5**).

Figure 2 shows that catalysis by GUS and GAL actually involves two subsequent transition states. This distinction is necessary to zoom in from the macroscopic rate constants to individual reaction steps (microscopic rate constants) of the catalytic machinery. While less literature information is available on GUS, the galactosylation (k_2) and degalactosylation step (k_3) of GAL have been investigated in detail using various substrates.^{23, 28} The galactosylation step, which releases the leaving group, is rate-limiting for lactose and other alkyl- β -D-galactopyranosides.²³ In case of aryl- β -D-galactopyranosides, however, k_2 and k_3 are more similar, and k_3 was found to be the rate-limiting step for many substrates with good leaving groups.^{18, 23} As the leaving group has no influence on the mechanism of the degalactosylation step, the macroscopic rate constant k_{cat} of the best GAL substrates can never exceed the limit set by k_3 . The group of Huber determined a k_3 of 1060 s^{-1} for wildtype GAL,²⁹ but slight variations of k_3 due to different reaction conditions should be taken into account. As k_{cat} for

the hydrolysis of resorufin- β -D-galactopyranoside approaches k_3 , we assume k_3 to be the rate-limiting step that determines ΔG^\ddagger .

Transition State Ensemble of Enzyme Catalysis

The distribution of ΔG^\ddagger in an enzyme population can be calculated by applying transition state theory (**Equation 7**) to the distribution of reaction rates (**Figure 4**). The distribution of ΔG^\ddagger is necessarily independent of $[S]$ as confirmed by plotting the histograms separately for each $[S]$ (**Figure 5**).

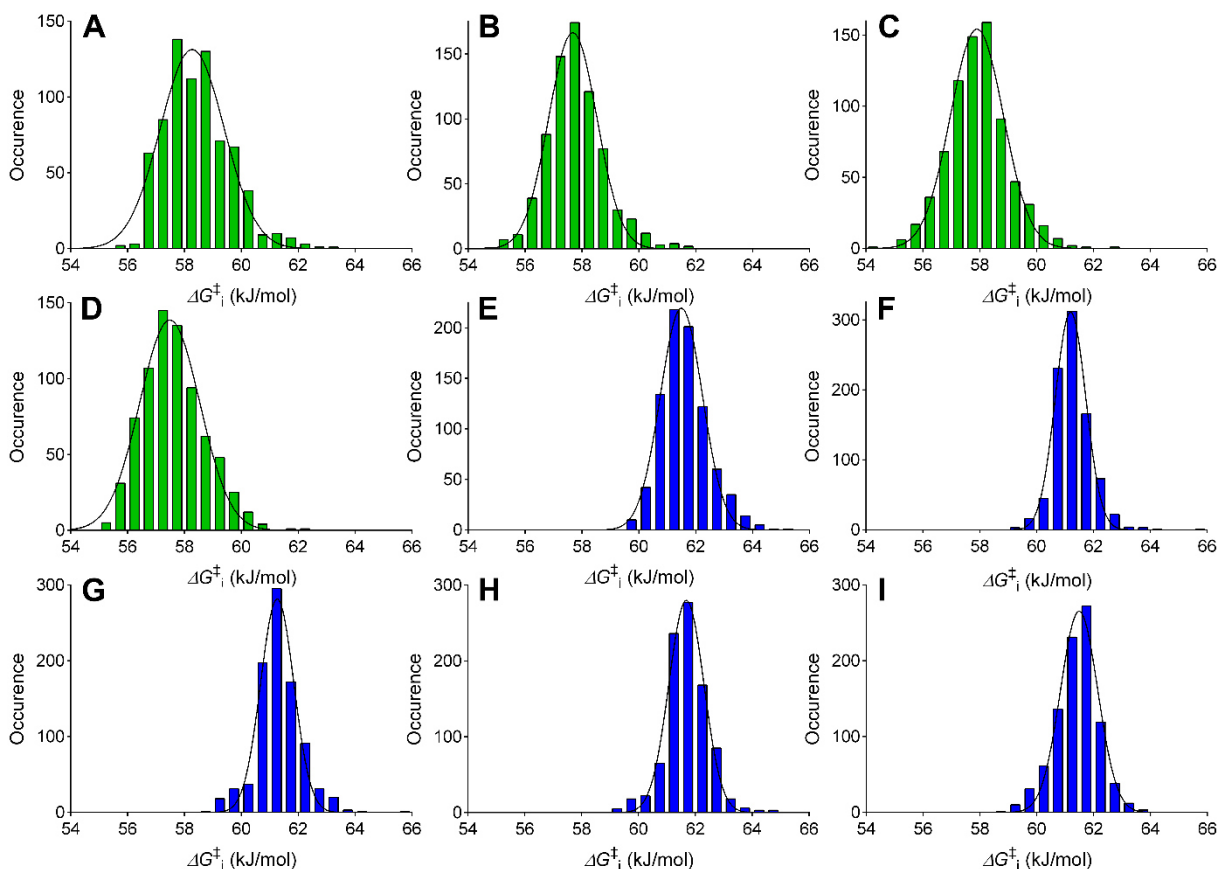


Figure 5: Distribution ΔG^\ddagger in a population of single GAL (A-D, green) and GUS (E-I, blue) molecules determined at various $[S]$ (A, E: 12,5 μM ; B, F: 25 μM ; C, G: 50 μM ; D, H: 100 μM ; I: 150 μM). The occurrence is the number of enzyme molecules per bin (0.5 kJ/mol). ΔG^\ddagger follows a Gaussian distribution.

Thus, we assembled all single molecule rates of GAL and GUS determined at various $[S]$ into a single distribution of ΔG^\ddagger (**Figure 6**). It should be noted that the histograms of ΔG^\ddagger are normally distributed whereas the histograms in **Figure 4** follow a Boltzmann distribution because lowering the activation barrier increases the reaction rate exponentially. In terms of

statistical thermodynamics, the different distributions represent the connection between microscopic states and macroscopic observables of a canonical ensemble.

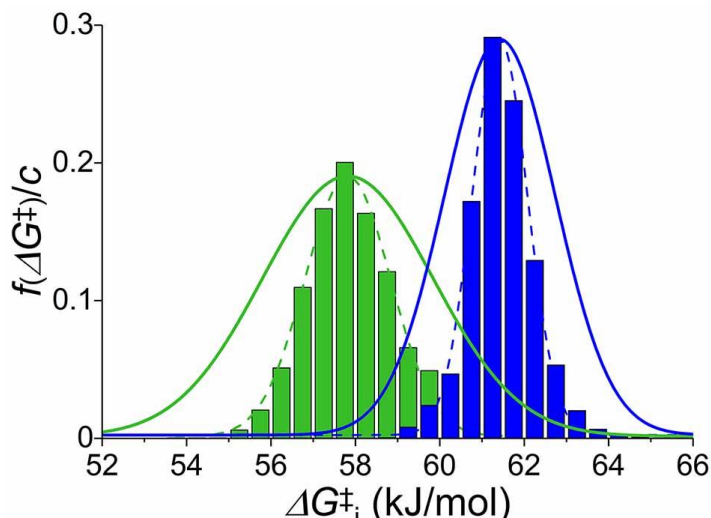


Figure 6: Distribution of the activation energy ΔG^\ddagger in a population of a few thousand single GAL (green) and GUS (blue) molecules determined at various $[S]$. ΔG^\ddagger_i is calculated according to **Equation 7**. The frequency ($f(\Delta G^\ddagger)/c$) is the number of enzyme molecules per bin (0.5 kJ/mol) divided by the total number of enzyme molecules. The histograms follow a Gaussian distribution indicated by the hatched lines, whereas the solid Gaussian curves include the intramolecular heterogeneity of ΔG^\ddagger (**Equation 8**, $n=4$) expressed as mean (μ) \pm standard deviation (σ): GAL= 57.82 ± 2.02 kJ/mol and GUS= 61.42 ± 1.31 kJ/mol.

The combined substrate turnover of all four subunits in a tetrameric enzyme generates the fluorescent product observed in a femtoliter chamber. Thus, the histograms in **Figure 6** are oblivious of the intramolecular heterogeneity in a tetramer as though all four subunits featured equal substrate turnover rates. To account for the additional intramolecular heterogeneity among the four independent subunits we derived **Equation 8**, which shows ΔG^\ddagger to be twice as broadly distributed (solid lines in **Figure 6**) as it appears from the histograms. The averaging effect of the tetramer, however, does not depend on absolute ΔG^\ddagger values and comparing the width of the uncorrected distributions (hatched lines in **Figure 6**) yields relative information on the catalytic heterogeneity of both enzymes. Furthermore, **Equation 8** enables us to compare the distribution of ΔG^\ddagger between enzymes consisting of one (monomer), two (dimer), four (tetramer) or any other number of subunits.

Transition state theory reduces the analysis of all kinetic steps along the reaction coordinate, which are typically not observable experimentally, to the rate-limiting step (k^{TST}) passing through the transition state (X^\ddagger). While classical transition state theory defines X^\ddagger as a single saddle point on the potential energy surface embedded in a homogeneous environment, the dynamic structure of proteins results in a heterogeneous reaction environment consisting of a

broad range of activated enzyme conformations (substates) that amplify the structural variation of the transition state.¹ Such a transition state ensemble defines a hypersurface and allows for many parallel reaction pathways to occur, a view strongly supported by the advent of single molecule studies.³⁰ Consequently, we can distinguish three characteristic cases depending on k^{TST} relative to the rate of conformational interconversion (k^{IC}):³¹

(1) If $k^{\text{TST}} \gg k^{\text{IC}}$, an enzyme ensemble consists of preexisting conformers that do not interconvert on a time scale relevant for the experiment. Consequently, each conformer behaves like an independent enzyme with a distinct rate constant ($k^{\text{TST}}_1, k^{\text{TST}}_2, k^{\text{TST}}_n$). This case is referred to as static heterogeneity as shown in **Figure 6**. (2) If $k^{\text{TST}} \sim k^{\text{IC}}$, interconversion of the conformers occurs on the same time scale as the catalytic reaction and the enzyme can be in a different conformation each time when a new catalytic cycle starts. As each conformer defines a distinct enzyme- X^\ddagger complex, we expect to observe a multi-exponential rate of product formation ($k^{\text{TST}}_1, k^{\text{TST}}_2, k^{\text{TST}}_n$) in a transition state ensemble. While the decay rate of the transition state is not observable in a steady-state bulk experiment, single molecule experiments have revealed different waiting times between subsequent substrate turnover events thus indicating variation in k^{TST} . For example, the Xie group reported variations in the waiting time of GAL in the order of 10^{-3} s to 10 s.¹⁰ The waiting time distribution is independent of $[S]$ ³²⁻³³ for the same reason that we discussed above for the $[S]$ -independent distribution of ΔG^\ddagger . The higher k^{TST} relative to k^{IC} the more coupled are subsequent substrate turnover events, which is manifest as memory effects. The case-2 scenarios are summarized as dynamic heterogeneity. (3) In the last case ($k^{\text{TST}} \ll k^{\text{IC}}$), the conformers are in rapid equilibrium. No heterogeneity in ΔG^\ddagger is observed experimentally because the reaction moves along a single pathway paved by the weighted average conformation.

It is important to note that these three cases are not mutually exclusive but rather reflect different dimensions of what is observable experimentally. In an enzyme, a large number of substates are arranged hierarchically in tiers on the conformational energy landscape.³⁴ Depending on the height of energy barriers separating the substates, conformational interconversions are more or less likely, but occur concurrently at different tiers. Furthermore, the height of the energy barriers between substates is temperature-dependent, such that the three cases are a function of temperature. Substates that interconvert rapidly at ambient temperature become fixed at low temperatures.³⁵ In the opposite direction, individual GAL molecules that display a distinct turnover rate can convert to a new state with a different turnover rate after a short heating pulse to 47 °C.²⁵ Enzymes from thermophilic organisms are only active at high temperatures and thus clearly demonstrate that the right balance between k^{TST} and k^{IC} at each tier is a precondition for the catalytic function of an enzyme. The requirement to maintain this delicate structural balance also provides an explanation why

enzymes—unlike other catalysts—do not follow a typical Arrhenius behavior with increasing temperature.

Figure 7 dissects intramolecular (accessible as dynamic heterogeneity) and intermolecular (accessible as static heterogeneity) variability of conformers in an enzyme population. Each slice represents a single enzyme molecule existing as a distinct subset of conformers. This scheme illustrates that the substrate-enzyme interaction does not involve the entire catalytically potent conformational space. Subsets of conformers that are not accessible through conformational sampling at room temperature are obviously not required to promote catalysis. While frozen in time upon protein folding, all subsets of conformers in an enzyme population are members of the canonical ensemble.

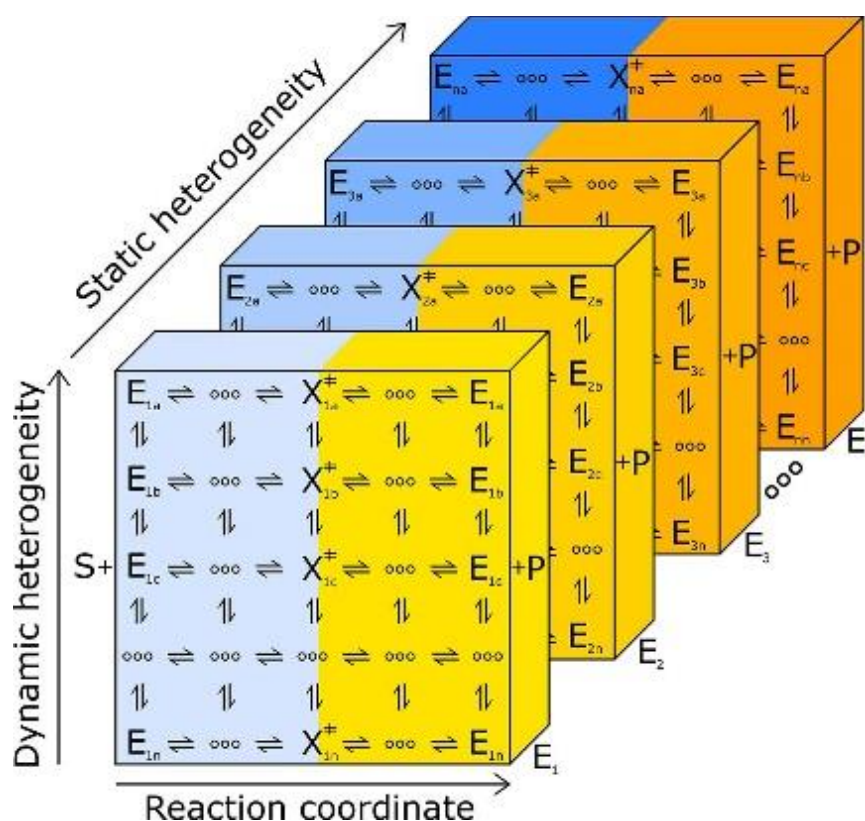


Figure 7: Kinetic scheme of the catalytic network in an enzyme population consisting of a large number of conformers. In a single enzyme molecule, the enzyme-substrate complex forms with an ensemble of interconverting conformers. Each conformer passes through a series of conformational changes along and vertical to the reaction coordinate, which leads to the formation of the transition state ensemble (X_{a}^{\ddagger} , X_{b}^{\ddagger} , X_{n}^{\ddagger}) and promotes barrier crossing from the substrate (blue) to the product region (orange). Thus, many parallel catalytic pathways are possible in each enzyme molecule (dynamic heterogeneity). Different enzyme molecules (E_1 , E_2 , E_3 , E_n) have distinct sets of conformers available for forming the transition state ensemble (static heterogeneity). While the scheme does not show the four subunits of the tetrameric enzymes GUS or GAL, the subunits can mechanistically be considered as independent enzyme molecules (if no allosteric effects are involved) without any implications for the general viability of the scheme.

The fact that there are more catalytically potent conformers than can possibly be used by any given enzyme molecule raises the question about the role of static heterogeneity and the difference between GAL and GUS. In our previous work,⁶ we compared the distribution of reaction rates in wildtype GUS to a mutant GUS containing four amino acid substitutions (T509A/S557P/N566S/K568Q) close to the catalytic center.³⁶ While wildtype GUS is highly specific for β -glucuronides, the mutant catalyzes β -glucuronides, β -galactosides and various related glycosidic substrates. This promiscuous activity - a typical feature of so-called generalists - was found to be associated with a broader distribution of reaction rates and indicated a functional division of work within the enzyme population such that each enzyme molecule with its distinct set of conformers can hydrolyze different types of substrate.⁶ Following this view, here we may attribute part of the static heterogeneity to the catalytic promiscuity regarding the substrate's aglyconic leaving group. This promiscuous activity, however, cannot be the only reason for the much broader distribution of reaction rates in GAL because both enzymes accept a broad range of leaving groups and k_3 (on which the leaving group has no influence) rather than k_2 is the rate limiting step for the hydrolysis of resorufin-galactopyranoside. If we appreciate transition state ensembles as the dividing surface between substrate and product region and consider the general reversibility of enzyme catalysis, we can as well change the perspective to investigate the specificity of product formation.

Biological Relevance of Enzymatic Heterogeneity

The catalytic mechanisms of GUS and GAL are very similar (**Figure 2**) and the formation of the transition state involves larger conformational rearrangements along the reaction coordinate. The most striking catalytic difference is a consequence of their respective mode of gene regulation. While β -glucuronides bind to the *gus* repressor and induce the *gus* operon,^{12, 37} lactose cannot induce the *lac* operon directly. Instead GAL first converts lactose to allolactose, which then binds to the *lac* repressor.³⁸ Consequently, GAL needs to combine three catalytic tasks: (1) the hydrolysis of lactose to galactose and glucose, (2) the transglycosylation of lactose to allolactose and (3) the hydrolysis of allolactose to galactose and glucose. The rates of hydrolysis and transglycosylation are equally high (each 50 %) and independent of $[S]$.³⁹

The need for GAL to induce its own expression has been known as the "lactose paradox".⁴⁰ Similarly, the lactose transporter (permease) - one of the three structural genes under control of the *lac* operon - needs to be present first before lactose can enter the cytoplasm, where it is converted to allolactose and finally induces the *lac* operon. This curiously long feedback loop is not altogether a paradox because even the repressed *lac* operon is occasionally transcribed to low levels of mRNA, which leads to a few copy numbers of GAL and permease per cell.⁴¹ Compared to GUS, however, this type of indirect gene regulation is less efficient because it leads to a long *lag* phase of GAL expression.⁴² There are further inconsistencies with the

current textbook knowledge on the catalytic role of GAL: (1) GAL has an unusual high K_M of 1.35 mM for the hydrolysis of lactose.²⁰ (2) *E. coli*—like other Enterobacteriales—is found in the large intestine of mammals while lactose is degraded in the small intestine, and (3) *E. coli* inhabits the adult mammalian intestine but not the infant intestine. Thus, from an ecological point of view, lactose is only a minor source of food for *E. coli*. By contrast, mammals feeding on plants consume large amounts of galactosyl lipids in chloroplasts that are degraded to galactosyl glycerol in the intestinal tract.⁴³ Boos found that galactosyl-glycerol is an excellent substrate for GAL,⁴⁴ induces the *lac* operon directly to high levels and enters the uninduced cell by a constitutive galactose permease,⁴² thus allowing for a more efficient gene regulation and use of galactosyl glycerol as a food source compared to lactose.

Although galactosyl-glycerol is the primary substrate of GAL its role in the breakdown of lactose is not irrelevant or a fortuitous side reaction as Huber pointed out.¹⁵ After all, each new trait evolution can act on starts as a random mutation. Indeed, GAL contains a specific glucose binding site⁴⁵ and evolutionary alignment studies with GAL from various organisms have shown that glucose binding site contains a specific “allolactose synthesis motif” co-selected with *lac* repressors.¹⁵ Allolactose is a structural mimic of galactosyl glycerol and thus can induce the *lac* operon. The multifunctionality, however, poses a dilemma for the glucose binding site: The formation of allolactose requires a high glucose affinity to hold back glucose for the intramolecular transglycosylation reaction (k_4), while the hydrolytic reaction (k_3) requires a low glucose affinity to empty the catalytic center quickly for the next turnover cycle.¹⁵ From a biochemical view, the glucose binding site is not well defined and glucose is bound in multiple conformations⁴⁶ with a moderate dissociation constant of 17 mM⁴⁵ to keep a balance between these conflicting demands.

A systematic investigation of an active site loop comprising amino acid residues 794-803, which can toggle between an open and closed conformation, yielded a better mechanistic understanding of GAL's multifunctionality. During transition state formation, the loop moves ~1.1 nm to close over the active site. Specific amino acid substitutions can shift the equilibrium between open and closed conformation. For example, if either Gly-794⁴⁷ or Ser-796¹⁸ are replaced by alanine, the closed loop conformation dominates, which improves the galactosylation step (k_2) but decreases the hydrolysis rate (k_3) by a factor of five. Consequently, it was suggested that the loop serves a clasp to fix glucose for the subsequent transglycosylation reaction (k_4).¹⁵

Our results support this hypothesis: The heterogeneity of GAL reflects the variability of the equilibrium constant between open and closed loop conformation. Roughly, two subpopulations of the ensemble can be distinguished, one where the open conformation dominates ($k_3 > k_4$) and another where the closed conformation dominates ($k_3 < k_4$). The

specialized enzyme subsets channel one catalytic pathway towards hydrolysis and the other pathway towards the production of allolactose. We do not have to assume a strict separation of these two subsets, there can be a rather continuous range of intermediate equilibrium constants.

The wider heterogeneity of GAL can be explained by an incomplete adaption to lactose as a relatively new food source for *E. coli*, e.g. resulting from the widespread use of milk in the diet of human adults starting 5 000 - 10 000 years ago.⁴⁸ Broadening the catalytic spectrum of GAL by a few point mutations in the amino acid sequence as a first step of adaption seems to be easier to implement than evolving a new repressor. As the *lac* operon is under negative control, a new repressor released by lactose would be useless unless it is also released by galactosyl glycerol. The most efficient way of gene regulation of the *lac* operon by lactose would probably require gene duplication.

X.5. Conclusions

We have developed a framework of transition state ensembles integrating dynamic and static heterogeneity. The distribution of activation energies (ΔG^\ddagger) in an enzyme population is a fundamental parameter for understanding enzyme substrate interactions. The distribution of ΔG^\ddagger in GAL was much broader compared to GUS and indicates that there are more catalytically potent conformations in an enzyme population than can be accessed by any given enzyme molecule. We conclude that transition state ensembles do not only contribute to enzyme catalysis but can also channel the catalytic pathway to the formation of different products. Distinct conformational subsets in an enzyme population enable GAL to act simultaneously as a hydrolase and a transglycosylase.

This observation of a functional division of work is in line with our previous work on *in vitro* evolved GUS.⁶ As an example of natural evolution, we see a new trait branching off from an established catalytic function.⁴⁹ We may even speculate that the new catalytic function of GAL allowing for the breakdown of lactose is the bacterial equivalent to the lifelong production of human lactase in European-derived populations.⁴⁸ Both enzymes may have evolved as an adaption to the increased nutrition from milk, the only dietary source of lactose.

X.6. Appendices

Calculation of the Standard Deviation of ΔG^\ddagger in a Multimeric Enzyme (Equation 8)⁵⁰⁻⁵¹

If a multimeric enzyme consists of n independent catalytic subunits, each enzyme molecule represents a random sample of X_1, X_2, \dots, X_n (*i.e.* $\Delta G^\ddagger_1, \Delta G^\ddagger_2, \dots, \Delta G^\ddagger_n$) of size n taken from a larger population (*i.e.* the transition state ensemble) with mean μ and variance σ^2 .

1) Expected Value (E) of Sample Mean \bar{X} :

$$E(\bar{X}) = E\left[\sum_{i=1}^n \frac{1}{n} X_i\right] = \frac{1}{n} [E(X_1) + E(X_2) + \dots + E(X_n)]$$

Because X_i are identically distributed and thus have the same mean, $E(X_i)$ can be replaced by μ :

$$E(\bar{X}) = \frac{1}{n} [\mu + \mu + \dots + \mu] = \frac{1}{n} [n\mu] = \mu$$

which shows that the mean of the sample mean \bar{X} is the same as the mean of individual X_i .

2) Variance (Var) of Sample Mean \bar{X} :

$$Var(\bar{X}) = E[(\bar{X} - \mu)^2] = E\left[\left(\sum_{i=1}^n \frac{1}{n} X_i - \sum_{i=1}^n \frac{1}{n} \mu_i\right)^2\right] = E\left[\left(\sum_{i=1}^n \frac{1}{n} (X_i - \mu_i)\right)^2\right]$$

$$\text{And: } Var(\bar{X}) = \frac{1}{n^2} E[(X_1 - \mu_1)^2] + \frac{1}{n^2} E[(X_2 - \mu_2)^2] + \dots + \frac{1}{n^2} E[(X_n - \mu_n)^2]$$

Because X_i are identically distributed and thus have the same variance σ^2 , $E[(X_i - \mu_i)^2]$ can be replaced by σ^2 :

$$Var(\bar{X}) = \frac{1}{n^2} [\sigma^2 + \sigma^2 + \dots + \sigma^2] = \frac{1}{n^2} [n\sigma^2] = \frac{\sigma^2}{n}$$

The variance of the sample mean decreases with increasing sample size n .

Thus, we can calculate the decrease of the standard deviation of ΔG^\ddagger when observing a multimeric enzyme in a femtoliter chamber: \bar{X} is the mean substrate turnover of the 4 subunits (denoted as ‘‘apparent’’) and X_i is the substrate turnover of each subunit.

$$\sigma_{app}^2 = \frac{\sigma_{subunit}^2}{n}$$

$$\text{And: } \sigma_{subunit} = \sigma_{app} \sqrt{n}$$

Calculation of Substrate Autohydrolysis Rates

The average fluorescence intensity of three freshly prepared control samples (I_0) was subtracted from the average of 3 to 4 autohydrolysis samples (I_t) and divided by the slope (m) of the calibration curve to calculate the amount of hydrolyzed resorufin ($[P]_t$):

$$[P]_t = \frac{\bar{I}_t - \bar{I}_0}{m}$$

Integration of the differential representation of a first order reaction yields the reaction rate coefficient (k_{non}) of the non-catalyzed reaction (autohydrolysis):

$$k_{non} = \frac{-\ln\left(1 - \frac{[P]_t}{[S]_0}\right)}{t}$$

where $[S]_0$ is the initial substrate concentration (100 μM , at $t=0$) and t the incubation time of the substrate. The half-life of the substrate in solution is $t_{1/2} = \ln 2/k_{non}$.

Acknowledgments

We thank Prof. Reinhard Sterner and his group (University of Regensburg) for enzyme expression, Prof. Ichiro Matsumura (Emory University, Atlanta, USA) for providing GUS plasmids, Dr. Raphaela Liebherr (University of Regensburg) for experimental support and Daniel Gahler (University of Regensburg) for discussions. We acknowledge the fabrication of femtoliter arrays by Albert Hutterer, Prof. Helmut Hummel, Prof. Alfred Lechner (Regensburg University of Applied Sciences, Germany). We further acknowledge financial support from the German Research Foundation (DFG grants GO 1968/3-1 and GO 1968/5-1, Heisenberg Fellowship).

X.7. References

1. Ma, B. Y.; Kumar, S.; Tsai, C. J.; Hu, Z. J.; Nussinov, R., Transition-state ensemble in enzyme catalysis: Possibility, reality, or necessity? *J. Theor. Biol.* **2000**, *203* (4), 383-397.
2. Gorris, H. H.; Walt, D. R., Analytical chemistry on the femtoliter scale. *Angew Chem Int Ed* **2010**, *49* (23), 3880-3895.
3. Liebherr, R. B.; Gorris, H. H., Enzyme molecules in solitary confinement. *Molecules* **2014**, *19* (9), 14417-14445.
4. Liebherr, R. B.; Hutterer, A.; Mickert, M. J.; Vogl, F. C.; Beutner, A.; Lechner, A.; Hummel, H.; Gorris, H. H., Three-in-one enzyme assay based on single molecule detection in femtoliter arrays. *Anal Bioanal Chem* **2015**, *407* (24), 7443-7452.
5. Gorris, H. H.; Rissin, D. M.; Walt, D. R., Stochastic inhibitor release and binding from single-enzyme molecules. *Proc Natl Acad Sci U S A* **2007**, *104* (45), 17680-17685.
6. Liebherr, R. B.; Renner, M.; Gorris, H. H., A single molecule perspective on the functional diversity of in vitro evolved beta-glucuronidase. *J Am Chem Soc* **2014**, *136* (16), 5949-5955.
7. Rondelez, Y.; Tresset, G.; Tabata, K. V.; Arata, H.; Fujita, H.; Takeuchi, S.; Noji, H., Microfabricated arrays of femtoliter chambers allow single molecule enzymology. *Nat Biotechnol* **2005**, *23* (3), 361-365.
8. Craig, D. B., Single enzyme molecule assay with time resolution using capillary electrophoresis. *Rev Anal Chem* **2013**, *32* (2), 103-112.
9. Rissin, D. M.; Gorris, H. H.; Walt, D. R., Distinct and long-lived activity states of single enzyme molecules. *J Am Chem Soc* **2008**, *130* (15), 5349-5353.
10. English, B. P.; Min, W.; van Oijen, A. M.; Lee, K. T.; Luo, G.; Sun, H.; Cherayil, B. J.; Kou, S. C.; Xie, X. S., Ever-fluctuating single enzyme molecules: Michaelis-Menten equation revisited. *Nat Chem Biol* **2006**, *2* (2), 87-94.
11. Henrissat, B., A classification of glycosyl hydrolases based on amino-acid-sequence similarities. *Biochem J* **1991**, *280*, 309-316.
12. Jefferson, R. A.; Burgess, S. M.; Hirsh, D., Beta-glucuronidase from Escherichia coli as a gene-fusion marker. *Proc Natl Acad Sci U S A* **1986**, *83* (22), 8447-8451.
13. Jacobson, R. H.; Zhang, X. J.; DuBose, R. F.; Matthews, B. W., Three-dimensional structure of beta-galactosidase from E. coli. *Nature* **1994**, *369* (6483), 761-766.
14. Wallace, B. D.; Wang, H. W.; Lane, K. T.; Scott, J. E.; Orans, J.; Koo, J. S.; Venkatesh, M.; Jobin, C.; Yeh, L. A.; Mani, S.; Redinbo, M. R., Alleviating cancer drug toxicity by inhibiting a bacterial enzyme. *Science* **2010**, *330* (6005), 831-835.
15. Wheatley, R. W.; Lo, S.; Jancewicz, L. J.; Dugdale, M. L.; Huber, R. E., Structural explanation for allolactose (lac operon inducer) synthesis by lacZ β -galactosidase and the evolutionary relationship between allolactose synthesis and the lac repressor. *J. Biol. Chem.* **2013**, *288* (18), 12993-13005.

16. Gebler, J. C.; Aebersold, R.; Withers, S. G., Glu-537, not Glu-461, is the nucleophile in the active site of (lac Z) beta-galactosidase from *Escherichia coli*. *J Biol Chem* **1992**, 267 (16), 11126-30.
17. Islam, M. R.; Tomatsu, S.; Shah, G. N.; Grubb, J. H.; Jain, S.; Sly, W. S., Active site residues of human beta-glucuronidase - Evidence for Glu(540) as the nucleophile and Glu(451) as the acid-base residue. *J Biol Chem* **1999**, 274 (33), 23451-23455.
18. Jancewicz, L. J.; Wheatley, R. W.; Sutendra, G.; Lee, M.; Fraser, M. E.; Huber, R. E., Ser-796 of beta-galactosidase (*Escherichia coli*) plays a key role in maintaining a balance between the opened and closed conformations of the catalytically important active site loop. *Arch. Biochem. Biophys.* **2012**, 517 (2), 111-122.
19. Pu, J.; Gao, J.; Truhlar, D. G., Multidimensional tunneling, recrossing, and the transmission coefficient for enzymatic reactions. *Chem Rev* **2006**, 106 (8), 3140-69.
20. Huber, R. E.; Gaunt, M. T., Importance of hydroxyls at positions 3, 4 and 6 for binding to the "galactose" site of beta-galactosidase (*Escherichia coli*). *Arch Biochem Biophys* **1983**, 220 (1), 263-271.
21. van der Groen, G.; Wouters, J.; Yde, M.; De Bruyne, C. K., Effects of alcohols on beta-galactosidase-catalyzed hydrolysis of alkyl-beta-D-galactopyranosides. *Eur J Biochem* **1973**, 38 (1), 122-129.
22. Towne, V.; Will, M.; Oswald, B.; Zhao, Q. J., Complexities in horseradish peroxidase-catalyzed oxidation of dihydroxyphenoxazine derivatives: appropriate ranges for pH values and hydrogen peroxide concentrations in quantitative analysis. *Anal Biochem* **2004**, 334 (2), 290-296.
23. Richard, J. P.; Westerfeld, J. G.; Lin, S., Structure-reactivity relationships for beta-galactosidase (*Escherichia coli*, lac Z). 1. Bronsted parameters for cleavage of alkyl beta-D-galactopyranosides. *Biochemistry* **1995**, 34 (37), 11703-11712.
24. Radzicka, A.; Wolfenden, R., A proficient enzyme. *Science* **1995**, 267 (5194), 90-93.
25. Rojek, M. J.; Walt, D. R., Observing single enzyme molecules interconvert between activity states upon heating. *PLoS ONE* **2014**, 9 (1), 1-7.
26. Shoemaker, G. K.; Juers, D. H.; Coombs, J. M. L.; Matthews, B. W.; Craig, D. B., Crystallization of beta-galactosidase does not reduce the range of activity of individual molecules. *Biochemistry* **2003**, 42 (6), 1707-1710.
27. Tan, W. H.; Yeung, E. S., Monitoring the reactions of single enzyme molecules and single metal ions. *Anal Chem* **1997**, 69 (20), 4242-4248.
28. Sinnott, M. L.; Souchard, I. J., Mechanism of action of beta-galactosidase - Effect of aglycone nature and alpha-deuterium substitution on hydrolysis of aryl galactosides. *Biochem J* **1973**, 133 (1), 89-98.
29. Kappelhoff, J. C.; Liu, S. Y. J.; Dugdale, M. L.; Dymianiw, D. L.; Linton, L. R.; Huber, R. E., Practical considerations when using temperature to obtain rate constants and activation thermodynamics of enzymes with two catalytic steps: Native and N460T-beta-galactosidase (*E. coli*) as examples. *Protein J.* **2009**, 28 (2), 96-103.

30. Antikainen, N. M.; Smiley, R. D.; Benkovic, S. J.; Hammes, G. G., Conformation coupled enzyme catalysis: Single-molecule and transient kinetics investigation of dihydrofolate reductase. *Biochemistry* **2005**, *44* (51), 16835-16843.
31. Demchenko, A. P., Does biocatalysis involve inhomogeneous kinetics. *FEBS Letters* **1992**, *310* (3), 211-215.
32. Min, W.; Gopich, I. V.; English, B. P.; Kou, S. C.; Xie, X. S.; Szabo, A., When does the Michaelis-Menten equation hold for fluctuating enzymes? *J Phys Chem B* **2006**, *110* (41), 20093-20097.
33. Velonia, K.; Flomenbom, O.; Loos, D.; Masuo, S.; Cotlet, M.; Engelborghs, Y.; Hofkens, J.; Rowan, A. E.; Klafter, J.; Nolte, R. J. M.; de Schryver, F. C., Single-enzyme kinetics of CALB-catalyzed hydrolysis. *Angew Chem Int Ed* **2005**, *44* (4), 560-564.
34. Frauenfelder, H.; Sligar, S. G.; Wolynes, P. G., The energy landscapes and motions of proteins. *Science* **1991**, *254* (5038), 1598-1603.
35. Ansari, A.; Berendzen, J.; Bowne, S. F.; Frauenfelder, H.; Iben, I. E. T.; Sauke, T. B.; Shyamsunder, E.; Young, R. D., Protein states and protein quakes. *P Natl Acad Sci USA* **1985**, *82* (15), 5000-5004.
36. Matsumura, I.; Ellington, A. D., In vitro evolution of beta-glucuronidase into a beta-galactosidase proceeds through non-specific intermediates. *J Mol Biol* **2001**, *305* (2), 331-339.
37. Novel, G.; Didier-Fichet, M. L.; Stoeber, F., Inducibility of beta-glucuronidase in wild-type and hexuronate-negative mutants of *Escherichia coli* K-12. *J Bacteriol* **1974**, *120* (1), 89-95.
38. Juers, D. H.; Matthews, B. W.; Huber, R. E., LacZ beta-galactosidase: Structure and function of an enzyme of historical and molecular biological importance. *Protein Sci* **2012**, *21* (12), 1792-1807.
39. Huber, R. E.; Kurz, G.; Wallenfels, K., A quantitation of the factors which affect the hydrolase and transgalactosylase activities of beta-galactosidase (*E. coli*) on lactose. *Biochemistry* **1976**, *15* (9), 1994-2001.
40. Egel, R., The lac operon: an irrelevant paradox? *Trends Genet* **1988**, *4* (2), 31-31.
41. Cai, L.; Friedman, N.; Xie, X. S., Stochastic protein expression in individual cells at the single molecule level. *Nature* **2006**, *440* (7082), 358-362.
42. Boos, W.; Wallenfels, K., Untersuchungen zur Induktion der Lac-Enzyme. 2 Die Permeation von Galaktosylglycerin in *Escherichia coli* *European J. Biochem.* **1968**, *3* (3), 360-363.
43. Sastry, P. S., Glycosyl glycerides. *Adv Lipid Res* **1974**, *12* (0), 251-310.
44. Silhavy, T. J.; Boos, W., Convenient synthesis of (2R)-glyceryl-beta-D-galactopyranoside - substrate for beta-galactosidase, lactose repressor, galactose-binding protein, and beta-methylgalactoside transport system. *J Biol Chem* **1973**, *248* (18), 6571-6574.

45. Huber, R. E.; Gaunt, M. T.; Hurlburt, K. L., Binding and reactivity at the "glucose site" of galactosyl-beta-galactosidase (*Escherichia coli*). *Archives of Biochemistry and Biophysics* **1984**, *234* (1), 151-160.
46. Juers, D. H.; Heightman, T. D.; Vasella, A.; McCarter, J. D.; Mackenzie, L.; Withers, S. G.; Matthews, B. W., A structural view of the action of *Escherichia coli* (lacZ) beta-galactosidase. *Biochemistry* **2001**, *40* (49), 14781-14794.
47. Juers, D. H.; Hakda, S.; Matthews, B. W.; Huber, R. E., Structural basis for the altered activity of Gly794 variants of *Escherichia coli* beta-galactosidase. *Biochemistry* **2003**, *42* (46), 13505-13511.
48. Bersaglieri, T.; Sabeti, P. C.; Patterson, N.; Vanderploeg, T.; Schaffner, S. F.; Drake, J. A.; Rhodes, M.; Reich, D. E.; Hirschhorn, J. N., Genetic signatures of strong recent positive selection at the lactase gene. *Am. J. Hum. Genet.* **2004**, *74* (6), 1111-1120.
49. Khersonsky, O.; Tawfik, D. S., Enzyme promiscuity: A mechanistic and evolutionary perspective. *Annu Rev Biochem* **2010**, *79*, 471-505.
50. Zehna, P. W., *Probability Distributions and Statistics*. Allyn and Bacon: Boston, **1970**.
51. Penn State, Mean and Variance of Sample Mean, <https://onlinecourses.science.psu.edu/stat414/node/167> (accessed March 31. 2020).

X.8. Supporting Information

Calculating the Half-Life of Substrate Autohydrolysis

Calibration

For quantification of hydrolysed substrate, a resorufin calibration curve was created. A resorufin stock solution (1 mM in DMSO) was diluted to 10 μM in assay buffer. 100, 200, 300, 400 and 500 nM dilutions were prepared by diluting the 10 μM resorufin solution with assay buffer. 100 μl of each resorufin dilution and a blank (assay buffer only) were pipetted in triplicates into a black microplate (Greiner Microlon, 96 well, non-binding) and the emission of resorufin was measured ($\lambda_{\text{ex}}=544$ nm, $\lambda_{\text{em}}=570$ nm) in a microplate reader (FluoStar Optima, BMG). The average intensity of three measurements was calculated and the blank value subtracted from each intensity. A linear regression analysis with a fixed intercept at zero was performed in the graphical analysis software Origin 2017.

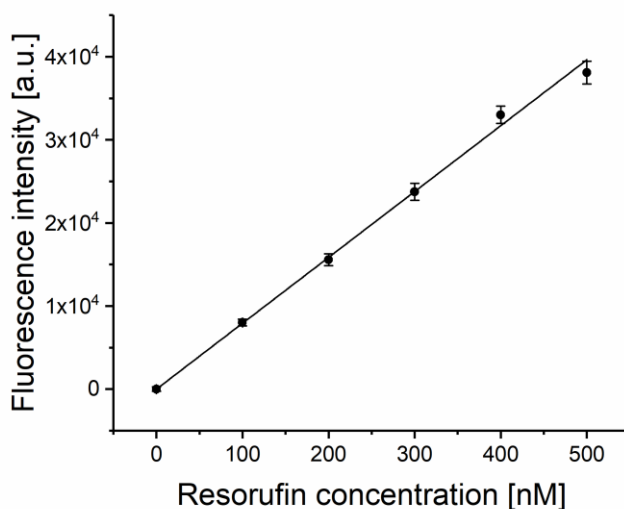


Figure S1: Resorufin calibration curve. The fluorescence intensities of 0, 100, 200, 300, 400 and 500 nM resorufin concentrations were measured and plotted against the respective resorufin concentrations. The error bars indicate the standard deviation of three measurements.

Substrate

Four 100 μM resorufin- β -D-galactopyranoside dilutions were obtained by diluting a 20 mM stock solution (in DMSO) with assay buffer. Analogously four 100 μM resorufin- β -D-glucuronide were obtained by diluting a 3 mM stock solution with assay buffer. Both substrate dilutions were stored for the length of the experiment at room temperature, under exclusion of

light. At certain time intervals the resorufin intensity was measured in 100 μl of each dilution and compared to a freshly prepared 100 μM substrate solution (control).

Calculations

First the average fluorescence intensity of three freshly prepared control measurements (I_0) was calculated and subtracted from the average of 3 to 4 substrate measurements (I_t) (**Equation 1**).

$$\bar{I}_t - \bar{I}_0 = I_{hydrolysed} \quad (1)$$

The resulting corrected intensity values were divided by the slope (m), derived from the calibration curve, which provides the amount of resorufin hydrolyzed in nM ($[P]_t$, **Equation 2**).

$$\frac{I_{hydrolysed}}{m} = [P]_t \quad (2)$$

The reaction rate coefficient (k_{non}) of the non-catalyzed reaction (autohydrolysis) was calculated using **Equation 3**, which was derived from the integration of the differential representation of a first order reaction.

$$k_{non} = \frac{-\ln(1 - \frac{[P]_t}{[S]_0})}{t} \quad (3)$$

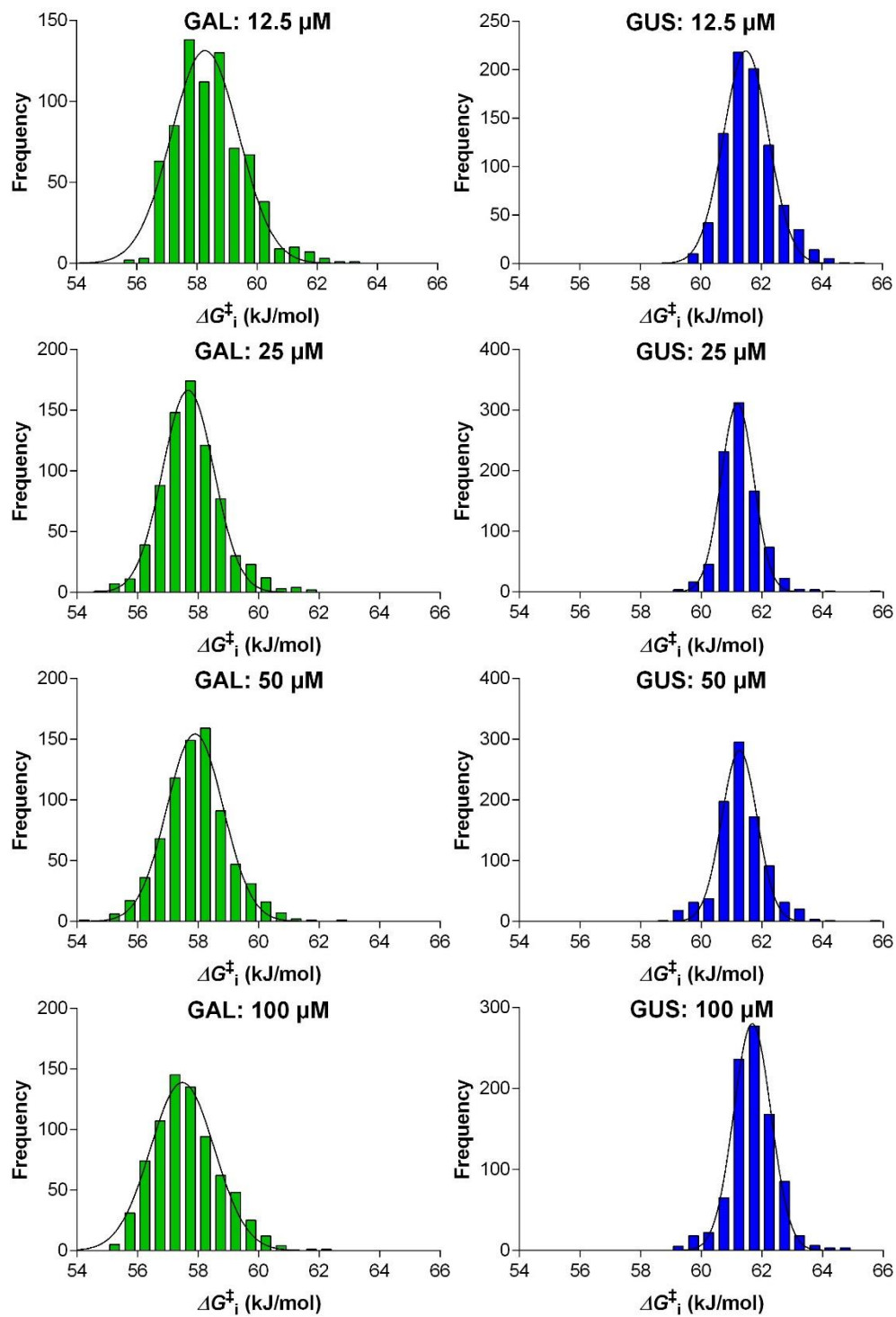
$[S]_0$ is the starting concentration of the substrate (100 μM , at $t=0$) and t the incubation time of the substrate in seconds. Inserting k_{non} into **Equation 4** gives the half-life of the substrate in solution.

$$t_{1/2} = \frac{\ln 2}{k_{non}} \quad (4)$$

The activation energy (ΔG^\ddagger) for the uncatalyzed reaction is given as:

$$\Delta G^\ddagger = -\ln\left(\frac{k_{non} h}{k_B T}\right) RT \quad (5)$$

Distribution of ΔG^\ddagger in GAL and GUS



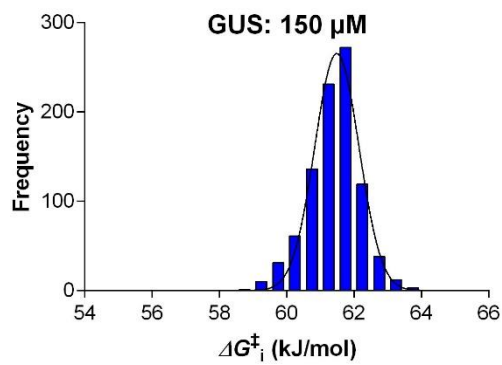


Figure S2: Distribution of the activation energy ΔG^\ddagger in a population of single GAL (green) and GUS (blue) molecules determined at various $[S]$. ΔG^\ddagger_i was calculated according to Eq. 6. The frequency $(f(\Delta G^\ddagger)/c)$ is the number of enzyme molecules per bin (0.5 kJ/mol) divided by the total number of enzyme molecules.

XI. Summary and Conclusions

This thesis builds on photon-upconversion nanoparticles (UCNPs) as background-free luminescent labels in bioaffinity assays using antibodies as recognition elements. UCNPs are nanocrystals that can absorb two or more near-infrared (NIR) photons and emit light with higher energy (anti-Stokes emission). The NIR excitation drastically reduces the measurement background by avoiding autofluorescence and minimizing light scattering. Together with a high photostability and constant emission (no blinking), UCNPs have become an excellent label for many bioanalytical applications. The aim of this work was to develop UCNP-based assays with the possibility to perform a single-molecule (digital) readout.

The first part of the thesis describes the development of immunoassays from a historical perspective and explains the fundamental building blocks needed for affinity assays. Various assay formats are described. The structure, function, and preparation of antibodies is explained. Alternative recognition labels like aptamers and molecularly imprinted polymers (MIPs) are critically discussed, and important label types are examined in detail. Cornerstones in the immunoassay development are highlighted using selected examples from the literature. The definition, advantages, and challenges of digital (single-molecule) affinity assays are discussed with respect to different label types, such as enzymes, small molecular labels, and nanoparticles.

The first research article describes the development of an immunoassay for counting individual molecules of the cancer biomarker prostate-specific antigen (PSA) with UCNPs coupled to an anti-PSA antibody. Individual UCNPs bound to a PSA molecule were visualized using a modified epifluorescence microscope that was equipped with a 980 nm-laser. The PSA concentration was determined in a digital way by counting the number of luminescent spots visible in a defined area of the microplate. Synthesis of the detection conjugate was optimized with respect to minimizing the aggregation of the nanoparticles, and the quality was controlled using agarose gel electrophoresis.

The digital upconversion-linked immunosorbent assay (ULISA) reached a low limit of detection (LOD) of 1.2 pg/mL (42 fM) and covered three orders of magnitude for PSA spiked in 25% blood serum, which was approximately 10× more sensitive than commercial ELISA kits. It was demonstrated that the digital readout is superior to the conventional analog readout of the same microtiter plate using a plate reader equipped with a 980 nm-laser, which resulted in an LOD of 20.3 pg/mL (700 fM, 17× higher LOD). A combination of both readout methods increased the working range to four orders of magnitude from 1 pg/mL to 10,000 pg/mL. The compatibility with standard microplate assay procedures and the high sensitivity make the

Summary and Conclusions

ULISA a powerful alternative to existing assays and will have a substantial impact in the future.

The second research article focused on the surface modification of UCNPs to reduce non-specific binding, while simultaneously increasing the sensitivity of the PSA detection by exploiting the strong affinity of streptavidin towards biotin. A linker consisting of neridronate, a bisphosphonate that strongly coordinates to lanthanide ions, was chosen to anchor a long polyethylene glycol (PEG) spacer with an incorporated alkyne group at the other end. The alkyne group was used for the covalent immobilization of streptavidin azide onto the UCNPs, *via* a copper-catalyzed click reaction.

Like the ULISA with antibody-UCNP conjugates, the digital ULISA with streptavidin-PEG-UCNPs improved the analog readout by a factor of 16. The strong affinity between biotin and streptavidin led to a 50× higher sensitivity compared to the former assay, which led to a subfemtomolar LOD of 800 aM (~50,000 PSA molecules in 100 μL sample) in 25% blood serum. The results obtained for real patient samples were in excellent agreement with results obtained from a standard method based on electrochemiluminescence (Elecsys, Roche).

In Research article 3, the unique photophysical properties of UCNPs were exploited for the immunochemical labeling of a cancer marker on the surface of cells. We demonstrated that UCNP labeling is compatible with standard fluorescence labeling techniques but achieves unsurpassed signal to background ratios. We designed and characterized three different SA-UCNP conjugates and compared the results with a standard fluorescence-based readout using SA conjugated to 5(6)-carboxyfluorescein (SA-FAM).

It was found that our previously established SA-PEG-neridronate-UCNPs showed the highest specific binding and, at the same time, the lowest non-specific signal among the three tested SA-UCNP conjugates. The signal-to-background ratio of SA-PEG-neridronate-UCNPs was 319, a 50-fold increase compared to the SA-FAM conjugate (signal to background of 6). Control experiments confirmed the specificity of the UCNP staining. The results demonstrated that UCNPs are a valuable addition to the existing repertoire of immunochemical labeling techniques.

Research article 4 focuses on the analysis of enzyme kinetics at the single-molecule level. This research is closely related to the digital immunoassay established by the company Quanterix (Chapter IV.6.2). The conventional transition state theory (TST) is used to analyze and explain the reaction rates of enzymes. However, it does not account for static heterogeneity and dynamic effects in proteins, revealed by single-molecule measurements. We analyzed the reaction rates of individual β-D-galactosidase (GAL) and β-D-glucuronidase (GUS) molecules in large arrays of femtoliter-sized wells, revealing a static heterogeneity. The reaction rate

distributions gave access to the intrinsic distributions of the free energy of activation (ΔG^\ddagger) of GAL and GUS.

A broader distribution of ΔG^\ddagger was found for GAL than for GUS, which is potentially caused by the multiple catalytic reaction pathways of GAL as a hydrolase and transglycosylase. Different catalytic reactions of GAL require more catalytically potent conformations for individual enzyme molecules in the enzyme population compared to GUS. Reaction rates of single enzyme molecules do not change over time (10 min). This indicates that each enzyme molecule has a broader set of conformations than it can access during catalysis. We adapted the TST for these findings by assuming transition state ensembles that can not only drive the enzymatic catalysis but also channel the reaction pathway.

The aim of this thesis was to employ UCNPs as labels for highly sensitive immunoassays. With the first two research articles, the digital ULISA was successfully introduced and set the foundation for a new generation of digital immunoassays. It was further shown that UCNPs are exceptional labels for the immunochemical labeling of cells. Especially the low background of the UCNP label could have significant impact on tissue diagnostics in the (near) future.

XII. Zusammenfassung und Fazit

Die vorliegende Arbeit basiert auf der Verwendung von Photonen-aufkonvertierenden Nanopartikeln (engl.: photon-upconversion nanoparticle, UCNP) als optische Markierungen in Antikörper-basierten Bioaffinitätstests (oder Bioaffinitätsassays). UCNPs sind Nanokristalle, die zwei oder mehrere Photonen im Nahinfrarotbereich (NIR) absorbieren und daraufhin Licht mit höherer Energie emittieren (anti-Stokes Emission). Durch die NIR Anregung wird die Autofluoreszenz der Matrix unterdrückt und die Streuung des Anregungslichtes minimiert, so dass der Messhintergrund drastisch reduziert wird. In Kombination mit der hohen Photostabilität und konstanten Emission (kein Blinken) sind UCNPs zu hervorragenden Markierungen für viele bioanalytische Anwendungen geworden. Das Ziel dieser Arbeit war die Entwicklung von UCNP-basierten Assays, die zudem die Möglichkeit zum Einzelmolekülnachweis von Analyten bieten (digitales Auslesen).

Der erste Teil dieser Arbeit beschreibt die Entwicklung von Immunoassays aus historischer Sicht und erklärt die grundlegenden Bestandteile, die für Affinitätsassays benötigt werden. Es werden verschiedene Formate von Immunoassays beschrieben. Die Struktur, Funktion und Herstellung von Antikörpern wird erläutert, zudem werden alternative Erkennungselemente wie Aptamere und molekular geprägte Polymere (engl.: molecularly imprinted polymers, MIPs) ausführlich diskutiert. Besondere Meilensteine in der Entwicklung von Immunoassays werden unter Verwendung von ausgewählten Beispielen aus der Literatur hervorgehoben. Die Definition, Vorteile und Herausforderungen von digitalen (Einzelmolekül) Affinitätsassays werden anhand von verschiedenen Markierungsarten wie Enzymen, molekularen Markern und Nanopartikeln diskutiert.

Die erste Originalarbeit beschreibt die Entwicklung eines Immunoassays, der auf dem Zählen einzelner Moleküle des Krebsmarkers Prostata-spezifisches Antigen (PSA) beruht. Individuelle UCNPs, die an PSA Moleküle gebunden waren, wurden unter einem modifizierten Epifluoreszenzmikroskops, das mit einem 980 nm-Laser ausgestattet wurde, sichtbar gemacht. Anschließend wurde die PSA-Konzentration digital ermittelt, indem die Anzahl an lumineszenten Punkten in einem definierten Bereich eines Mikrowells gezählt wurde. Die Synthese der Nachweismarkierungen wurde optimiert, um die Aggregation der Partikel zu minimieren, und die Qualität der Konjugate wurde durch Agarose-Gelelektrophorese kontrolliert.

Der UCNP-basierte digitale Immunoassay (engl.: upconversion-linked immunosorbent assay, ULISA) erreichte eine Nachweisgrenze (engl.: limit of detection, LOD) von 1,2 pg/mL (42 fM) in 100 μ L Probenvolumen und ermöglichte es, die PSA Konzentration über einen Bereich von

Zusammenfassung und Fazit

drei Größenordnungen in 25% Blutserum zu bestimmen. Damit war der digitale ULISA ca. 10× sensitiver als kommerzielle ELISA-Tests. Um den Vorteil des digitalen Auslesens zu zeigen, wurde der PSA Assay zudem mit einem Mikrotiterplatten-Lesegerät, welches mit einem 980 nm-Laser ausgestattet war, gemessen (analoges Auslesen). Die analoge Auslesemethode erreichte eine LOD von 20,3 pg/mL (700 fM) und war somit 17× höher, als das digitale Zählen der Partikel. Eine Kombination beider Auslesemethoden vergrößerte den Arbeitsbereich des Assays auf vier Größenordnungen von 1 pg/mL bis 10.000 pg/mL. Die Kompatibilität mit herkömmlichen Assayprotokollen und die hohe Sensitivität machen den ULISA zu einer vielversprechenden Alternative zu etablierten Immunoassays.

Die zweite Originalarbeit konzentriert sich auf die Oberflächenmodifikation von UCNPs, um gleichzeitig die unspezifische Bindung der Partikel zu reduzieren und die Sensitivität der PSA-Bestimmung weiter zu verbessern. Dabei wurde die starke, nicht-kovalente Interaktion zwischen Streptavidin (SA) und Biotin ausgenutzt. Zunächst wurde ein langer Polyethylenglykol (PEG)-Linker synthetisiert, der an einem Ende ein Bisphosphonat (Neridronat) trug und an dem anderen ein Alkin. Das Bisphosphonat diente dabei als Anker zwischen dem PEG und dem UCNP, da es eine starke Komplexbindung zu den Lanthanoid-Ionen an der Oberfläche des Partikels ausbilden kann. Die Alkin-Gruppe wurde dann für die kovalente Immobilisierung von SA durch eine Kupfer-katalysierte Click-Reaktion mit SA-Azid verwendet.

Wie der zuvor beschriebene ULISA, verbesserte auch hier die digitale Auslesemethode den analogen Modus um einen Faktor von 16. Die starke Interaktion zwischen den SA-PEG-neridronat-UCNPs und Biotin führte zu einer 50× höheren Sensitivität, im Vergleich zum ULISA mit Antikörper-gekoppelten UCNPs, was eine LOD im sub-femtomolaren Bereich ermöglichte (800 aM, ~50.000 PSA Moleküle in 100 µL, in 25% Blutserum). Der ULISA mit Serumproben echter Patienten zeigte eine hervorragende Korrelation mit einer Referenzmethode, die auf Chemilumineszenz beruhte (Elecsys, Roche).

In der dritten Originalarbeit wurden die einzigartigen photophysikalischen Eigenschaften von UCNPs für die spezifische Markierung eines Brustkrebsmarkers an der Oberfläche von Zellen genutzt. Es wurde gezeigt, dass das spezifische Anfärben mit SA-funktionalisierten UCNPs kompatibel mit konventionellen Markierungsmethoden ist, jedoch ein unübertroffenes Signal-zu-Hintergrund Verhältnis bietet. Es wurden drei verschiedene SA-basierte UCNP Konjugate hergestellt und die Ergebnisse der immunochemischen Färbung mit einer fluoreszenten Verbindung aus SA und 5(6)-Carboxyfluorescein (SA-FAM) verglichen.

Die bereits zuvor beschriebenen SA-PEG-Neridronat-UCNPs zeigten die höchste spezifische Bindung und gleichzeitig das niedrigste unspezifische Signal unter den drei getesteten SA-UCNP Nachweisreagenzien. Somit konnte ein sehr hohes Signal-zu-Hintergrund Verhältnis

von 319 erreicht werden, welches 50× höher war als die Standardmethode mit SA-FAM (Signal-zu-Hintergrund von 6). Kontrollexperimente mit Zelllinien, die den Krebsmarker nur geringfügig exprimieren, bestätigten die Spezifität der SA-PEG-Neridronat-UCNPs. Die Ergebnisse zeigen, dass UCNPs eine vielversprechende Erweiterung zum bereits bestehenden Portfolio an Markierungstechniken für die Immunhistochemie darstellen.

Die vierte Originalarbeit beschäftigt sich mit Enzymkinetiken auf der Einzelmolekülebene. Diese Arbeit ist eng mit dem digitalen Immunoassay der Firma Quanterix (Kapitel IV.6.2) verwandt. Die konventionelle Theorie des Übergangszustandes (engl.: transition state theory, TST) wird verwendet, um die Reaktionsgeschwindigkeiten von Enzymen zu bestimmen. Jedoch berücksichtigt die konventionelle TST weder die statische Heterogenität noch dynamische Effekte innerhalb einer Enzympopulation, die durch Einzelmolekülexperimente nachgewiesen worden sind. In dieser Arbeit wurden einzelne Moleküle der β -D-Galactosidase (GAL) und β -D-Glucuronidase (GUS) in Arrays, die aus zehntausenden Femtoliter-großen Wells bestehen, eingeschlossen und deren Reaktionsraten analysiert. Die Ergebnisse zeigen, dass eine statische Heterogenität in den Geschwindigkeiten der Enzyme innerhalb einer Population vorliegt. Die Verteilung der Reaktionsraten wurde verwendet, um die intrinsischen Verteilungen der freien Aktivierungsenergie (ΔG^\ddagger) von GAL und GUS zu bestimmen.

GAL zeigte eine breitere Verteilung von ΔG^\ddagger als GUS, was darauf zurückzuführen sein könnte, dass GAL mehrere katalytische Funktionen aufweist als GUS. So kann GAL neben der hydrolytischen Spaltung von Laktose, auch die Transglycosylierung von Laktose zu Allolaktose katalysieren. Diese verschiedenen Funktionalitäten benötigen—im Gegensatz zu GUS—mehr katalytisch aktive Konformationen, die einzelne GAL-Moleküle innerhalb einer Population einnehmen können. Da die Reaktionsraten einzelner Enzymmoleküle über einen langen Zeitraum (10 min) konstant sind, lässt sich daraus schließen, dass jedes Enzymmolekül eine größere Ausstattung an möglichen Konformationen besitzt, als es während der Katalyse einnehmen kann. Die TST wurde insoweit angepasst, dass TST Ensembles nicht nur die enzymatische Katalyse, sondern auch deren potentielle Reaktionswege berücksichtigen.

Das Ziel dieser Arbeit war es UCNP-basierte Nachweisreagenzien für hochsensitive Immunoassays zu entwickeln. Mit den ersten beiden Artikeln wurde der nachweisstarke digitale ULISA eingeführt und legte den Grundstein für eine neue Generation von digitalen Immunoassays. Im dritten Artikel wurde die Vielseitigkeit der synthetisierten UCNP-Markierungen anhand des immunochemischen Nachweises von Krebsmarkern auf Zellen gezeigt. Besonders das hohe Signal-zu-Hintergrund Verhältnis von UCNPs könnte künftig einen starken Einfluss auf die Histologie haben.

XIII. Acknowledgments

My deepest gratitude goes first and foremost to my supervisor Dr. Hans-Heiner Gorris, whose knowledge and expertise shaped my scientific thinking. Further, I thank him for the exciting topic and his exceptional support during my work.

I wish to extend my gratitude to Prof. Dr. Antje Bäumner for the opportunity to work at this institute.

My warmest thanks go to (Asst. Prof.) Dr. Zdenek Farka, who visited Regensburg 8x during 2015-2020. Because of his immense knowledge about immunoassays and his black belt in Origin, I could learn handy tricks that made my research much more comfortable. But he was not only a colleague; he became a friend. I enjoyed visiting all the museums in Regensburg and Brno with him, listening to street musicians, and having many Burgers, some Tatratea and of course salad with him. I will always remember the (epic) one game per week challenge.

I am honored to have met Dr. Antonín Hlaváček. None of this would have been possible without his exceptional skills in nanoparticle synthesis. I am looking forward to continuing to work with him.

I am grateful for the time I could spend with Julian Brandmeier, and Dr. Riikka Peltomaa, especially our cooking sessions, and “Wine Wednesdays” were a highlight.

I have had the great privilege of working with a lot of highly skilled professionals like (Dr.) Timo Raith, Dr. Karin Rustler, Dr. Uliana Kostiv, Matej Pastucha, Zuzanna Mikušová. I hope we will meet again.

Special thanks go to Nicole Guber, who was always a great help with administrative issues and made my life easier.

I would like to thank Dr. Vishal Kale and Chiara de Rosa for the great time we had in the lab.

Furthermore, I thank all the students that visited our lab for research internships, Bachelor or Master thesis: Vera Zhao, Lisa Schmauß, Ramona Höflinger, Patrick Recum, Sonja Kunz, Susanne Dechantsreiter, Lucia Birner and Eva Hecht.

My gratitude goes to Prof. Dr. Petr Skládál, who always welcomed me in his group and helped us to improve our publications with his experiences as an editor.

I would like to thank Simone Rink, Christian Griesche, Franziska Beck, Meike Bauer, for the delightful time we had during our coffee breaks and cooking events.

Acknowledgments

My sincerest gratitude goes to my family, who has always supported and encouraged me.

Of course, I thank all members of the Fachschaft Chemie for the fantastic time we had, especially at the yearly “Hüttenfahrt.”

XIV. Eidesstattliche Erklärung

Ich erkläre hiermit an Eides statt, dass ich die vorliegende Arbeit ohne unzulässige Hilfe Dritter und ohne Benutzung anderer als der angegebenen Hilfsmittel angefertigt habe; die aus anderen Quellen direkt oder indirekt übernommenen Daten und Konzepte sind unter Angabe des Literaturzitats gekennzeichnet.

Weitere Personen waren an der inhaltlich-materiellen Herstellung der vorliegenden Arbeit nicht beteiligt. Insbesondere habe ich hierfür nicht die entgeltliche Hilfe eines Promotionsberaters oder anderer Personen in Anspruch genommen. Niemand hat von mir weder unmittelbar noch mittelbar geldwerte Leistungen für Arbeiten erhalten, die im Zusammenhang mit dem Inhalt der vorgelegten Dissertation stehen.

Die Arbeit wurde bisher weder im In- noch im Ausland in gleicher oder ähnlicher Form einer anderen Prüfungsbehörde vorgelegt.

Regensburg, 06.05.2020

Ort, Datum

Unterschrift